

Rochester Institute of Technology

RIT Digital Institutional Repository

Theses

8-11-2017

Enhancing Near Zero Volt Storage Tolerance of Lithium-ion Batteries

Kyle R. Crompton
krc3429@rit.edu

Follow this and additional works at: <https://repository.rit.edu/theses>

Recommended Citation

Crompton, Kyle R., "Enhancing Near Zero Volt Storage Tolerance of Lithium-ion Batteries" (2017). Thesis. Rochester Institute of Technology. Accessed from

This Dissertation is brought to you for free and open access by the RIT Libraries. For more information, please contact repository@rit.edu.

R.I.T

Enhancing Near Zero Volt Storage Tolerance of Lithium-ion Batteries

by

Kyle R. Crompton

A dissertation submitted in partial fulfillment of the requirements
for the degree of Doctorate of Philosophy in Microsystems Engineering

Microsystems Engineering Program
Kate Gleason College of Engineering

Rochester Institute of Technology
Rochester, New York
August 11th, 2017

Enhancing Near Zero Volt Storage Tolerance of Lithium-ion Batteries
by
Kyle R. Crompton

Committee Approval:

We, the undersigned committee members, certify that we have advised and/or supervised the candidate on the work described in this dissertation. We further certify that we have reviewed the dissertation manuscript and approve it in partial fulfillment of the requirements of the degree of Doctor of Philosophy in Microsystems Engineering.

Brian J. Landi, PhD Date
Associate Professor of Chemical Engineering
Dissertation Advisor

Patricia Taboada-Serrano, PhD Date
Assistant Professor of Chemical Engineering

Reginald E. Rogers, PhD Date
Assistant Professor of Chemical Engineering

Michael W. Forney, PhD Date
Member of Technical Staff at The Aerospace Corporation

Stephen Boedo, PhD Date
Professor of Mechanical Engineering

Certified by:

Bruce Smith, PhD Date
Director, Microsystems Engineering Program

Abstract

Kate Gleason College of Engineering
Rochester Institute of Technology

Degree: Doctor of Philosophy

Program: Microsystems Engineering

Authors Name: Kyle R. Crompton

Advisors Name: Brian J. Landi, PhD

Dissertation Title: Enhancing Near Zero Volt Storage Tolerance of Lithium-ion Batteries

There are inherent safety risks associated with inactive lithium ion batteries leading to greater restrictions and regulations on shipping and storage. Maintaining all cells of a lithium ion battery at near zero voltage with an applied fixed resistive load is one promising approach which can lessen (and potentially eliminate) the risk of a lithium ion battery entering thermal runaway when in an inactive state. However, in a conventional lithium ion cell, a near zero cell voltage can be damaging if the anode electrochemical potential increases to greater than the potential where dissolution of the standard copper current collector occurs (i.e. ~ 3.1 V vs. Li/Li^+ at room temperature). Past approaches to yield lithium ion cells that are resilient to a near zero volt state of charge involve use of secondary active materials or alternative current collectors which have anticipated tradeoffs in terms of cell performance and cost.

In the the present dissertation work the approach of managing the amount of reversible lithium in a cell during construction to prevent the anode potential from increasing to greater than ~ 3.1 V vs. Li/Li^+ during near zero volt storage is introduced. Anode pre-lithiation was used in $\text{LiCoO}_2/\text{MCMB}$ pouch cells to appropriately manage the amount of reversible lithium so that there is excess reversible lithium compared to the cathodes intercalation capacity (reversible lithium excess cell or RLE cell). RLE $\text{LiCoO}_2/\text{MCMB}$ cells maintained 99% of their original capacity after three, 3-day and three, 7-day storage periods at near zero volts under fixed load. A $\text{LiCoO}_2/\text{MCMB}$ pouch cell fabricated with a pre-lithiated anode also maintained its original discharge performance after three, 3-day storage periods under fixed load at 45°C . The strong recharge performance after near zero volt storage is attributed to the anode potential remaining below the copper dissolution potential during near zero volt storage as informed by reference electrode measurements. Pulse discharge measurements were performed and show that double layer capacitance likely plays a major role in determining the behavior of electrode potentials during near zero volt storage. To further the viability of the anode pre-lithiation method in $\text{LiCoO}_2/\text{MCMB}$ cells, stabilization coatings on the cathode materials are being investigated to increase the tolerance of the cathode to the low potentials it may experience during near zero volt storage of an RLE lithium ion cell. Results show that an AlPO_4 coating prevents cation exchange in the cathode crystal structure and substantially

increases the cathode's resilience to low electrochemical potentials. Investigations into applying anode pre-lithiation to cells utilizing LiNiCoAlO₂ (NCA) cathodes have also been initiated and found to maintain the anode potential below the copper dissolution potential during near zero volt storage. RLE NCA/MCMB cells showed strong recharge performance and improved rate capability retention over a conventional NCA/MCMB cell after ten, 3-day near zero volt storage periods. Scale up of reversible lithium management to NCA/MCMB x3450 pouch cells was achieved using bath lithium addition and rendered a cell that retained 100% of its discharge performance after a 14 day period at near zero volts under fixed load. The near zero volt storage tolerance of lithium ion cells utilizing an advanced, high energy density lithium rich cathode material (0.49Li₂MnO₃·0.51LiNi_{0.37}Co_{0.24}Mn_{0.39}O₂ or HE5050) has also been studied and found to be high at room temperature without the need for anode pre-lithiation. HE5050/MCMB cells maintained ~100% of their discharge capacity after five, 3-day and five, 7-day near zero volt storage periods at room temperature. HE5050/MCMB also maintained ~99% of their discharge capacity after two, 3-day near zero volt storage periods at 40°C. The high first cycle loss and lower intercalation potential of the HE5050 cathode lead to the anode potential remaining <2.8 V vs. Li/Li⁺ during near zero volt storage and as such, no copper dissolution is expected to be occurring. Finally, Carbon Nanotube (CNT) papers have been shown to be stable up to high potentials vs. Li/Li⁺ and thus, using them as an anode current collector in place of standard copper can generate lithium ion cells that can tolerate near zero volt storage. However, CNT papers suffer from significant irreversible loss due to their high surface area. An Al₂O₃ coating deposited by atomic layer deposition is investigated for its effect in reducing the irreversible losses of a CNT paper. The Al₂O₃ coating was found to reduce irreversible loss by 55% over 50 cycles and still serve as an effective current collector for a graphitic anode composite.

Acknowledgements

To start, I would like to thank all of my committee members for committing their time and efforts to me through the completion of my PhD in Microsystems Engineering.

Advisor: Dr. Brian J. Landi

Committee Members: Dr. Michael W. Forney, Dr. Patricia Taboada-Serrano and Dr. Reginald Rogers.

A special thanks to my advisor, Dr. Brian Landi, who has been an excellent mentor and provided an outstanding opportunity for me at RIT.

I would like to thank my parents as well as my brother and his fiancé (soon to be sister-in-law, I'm so excited for you guys!) for offering me support and encouragement while always keeping me grounded.

I would like to thank all our lab members for their help and support along the way, including those that have moved on to bigger and better things. In no particular order; Nathaniel Cox, Andrew Bucossi, Mike Forney, Jamie Rossi, Jason Staub, Stephen Polly, Andrew Merril, Matthew Ganter, Christopher Schaueremann, Karen Soule, Anthony Leggiero, Ivan Puchades, Martin Dann, Aaron Rape, Sarah Frisco, Paul Thomas and Thomas Mastrangelo.

Also I would like to thank all the staff over the years that closely support all of our on-going efforts; Stephanie Hart, Jim Smith, Paul Allen and Holly Rollins.

Another special mention goes out to Andrew Bucossi, Karen Soule, Jamie Ellis, Jason Staub and Nathaniel Cox, whom I've grown close with over the years and they have been great friends and co-workers.

Another special mention goes out to Andrew Bucossi, Nathaniel Cox and Jason Staub for being absolutely hilarious people and helping to keep the stress down in the cubicles.

A particular thanks goes out to Dr. Mike Forney, who was an excellent mentor my first 2 years in the PhD program and encouraged me to go into battery research.

A big thanks to undergraduate researcher Mike Hladky, whose hard work, great attitude, and dedication on several of my projects helped push progress and contributed to multiple publications.

I would also like to extend my gratitude to the SUNY Geneseo Physics department, especially Dr. Charlie Freeman, Dr. Ed Pogozeleski, Dr. George Marcus, Dr. Aaron Steinhauer, Dr. Stephen Padalino, and Dr. James McLean for being outstanding instructors and preparing me so well for graduate study.

Another thanks to Dr. Lloyd Zilch for serving as my mentor at NSWC Crane during the summer of 2015. The projects he gave me to work on and the exposure to the

government/industry interface helped to broaden my technical experience and career perspective during graduate school and prepare me for the next steps after graduation.

Another thanks to Dr. Corey Love at the Naval Research Laboratories for hosting me as a researcher in the summer of 2016. The projects he exposed me too helped to significantly broaden my technical experience and career perspective, and he continues to be a great mentor and collaborator.

Another thanks to all my Crossfit coaches and martial arts instructors over the last four years for helping me stay sane and healthy.

And finally a big thanks to all of my friends over the years, way too many to list here, for making life interesting and helping me grow as a person.

Contents

Abstract	iii
Acknowledgements	v
1. Introduction	1
1.1 Lithium ion battery components, function and reference electrodes	2
1.2 Amount of reversible lithium in a cell	7
1.3 Safety risks associated with transporting and storing lithium ion batteries	9
1.4 Risk vs. State of charge and potential of state of charge limitations to increase safety	10
1.5 Challenges facing state of charge limitations.....	15
1.5.1 Challenge of determining the state of charge of a lithium ion cell.....	15
1.5.2 Overdischarge risk of state of charge limitation.....	16
1.6 Near zero volt storage	16
1.6.1 Potential of zero volt storage for inactive safety and charge limitation controllability enhancement	16
1.6.2 Degradation mechanisms to overcome during overdischarge of conventional cells to near zero volts	17
1.7 Past approaches to near zero volt storage tolerance and overdischarge protection	21
1.7.1 Anode current collector replacements	22
1.7.2 Secondary electrode materials with intermediate potentials	24
1.7.3 Secondary cathode materials with high first cycle loss	25
1.8 Opportunities for an improved approach to near zero volt storage tolerance	26
2. Dissertation Overview	28
3. Standard Experimental methods	30
3.1 Lithium ion battery standard fabrication.....	30
3.1.1 Reference electrodes in pouch cells	31
3.1.2 Arbin Cyclers and cycling protocols	32
3.1.3 Materials Analysis Techniques	33
4. Reversible lithium management by anode pre-lithiation of $\text{LiCoO}_2/\text{MCMB}$ lithium ion cells as an alternative approach to near zero volt storage tolerance	34
4.1 Composite Fabrication and cycling protocols.....	35
4.2 Electrode Asymptotic Potential	36
4.3 Pre-lithiation process and resulting effect on behavior of electrode potentials during normal charge and discharge	37
4.4 Electrode potential behavior during near zero volt storage of an RLE cell	41
4.5 Performance retention after near zero volt storage of RLE and conventional cells	43
4.6 Effect of near zero volt storage on rate capability and long term cycling	48
4.7 High Temperature testing of near zero volt storage tolerance of RLE cells	50
4.8 Pulse discharge study of RLE lithium ion cell discharged to zero volts	55

4.9	Studying degradation of LiCoO ₂ during near zero volt storage and improving its tolerance to the near zero volt storage condition with AlPO ₄ coating.....	61
4.9.1	Experimental methods.....	62
4.9.2	Results and Discussion.....	64
4.9.3	Conclusions.....	75
4.10	Studying EAP vs. amount of reversible lithium added to the cell	76
4.11	Applying anode pre-lithiation method to NCA/MCMB cells	78
4.11.1	Experimental Methods and Results.....	78
4.12	Scale up of reversible lithium management to x3450 pouch cells	82
5.	Use of high first cycle loss, high energy density lithium rich cathode materials to enable near zero volt storage tolerance.....	90
5.1	Introduction.....	90
5.2	Experimental.....	91
5.3	Results and discussion	94
5.4	Electrode behavior during fixed resistive load near zero volt storage	96
5.5	Discharge Performance retention after repeated periods of near zero volt storage.....	99
5.6	Effects of near zero volt storage on cell rate capability and long term cycling	104
5.7	Elevated temperature testing.....	106
5.8	Conclusions.....	109
6.	Al ₂ O ₃ coating of CNT paper current collectors	112
6.1	Introduction.....	112
6.2	Experimental.....	113
6.3	Results and Discussion	116
6.4	Conclusions.....	125
7.	Dissertation Conclusions and Major Contributions	127
8.	Appendix A: Supplemental Information for Chapter 5	130
9.	Appendix B: Supplemental information for Chapter 4.9.....	142
10.	Appendix C: Optical Cell study of lithium metal deposition	151
11.	Publications, Presentations and Awards.....	156
11.1	Journal Publications.....	156
11.2	Patents.....	156
11.3	Major Conference Presentations	156
11.4	Awards.....	156
12.	References.....	157

List of Figures

Figure 1: (a) Schematic of cell function during charge of conventional LCO/MCMB cell. The pink arrows represent lithium ion flow and the red arrow represents electron flow. (b) 1st cycle charge cell voltage and electrode potentials of conventional LCO/MCMB cell. (c) Schematic of cell function during discharge of conventional LCO/MCMB cell. The pink arrows represent lithium ion flow and the red arrow represents electron flow. (d) 1st cycle discharge cell voltage and electrode potentials of conventional LCO/MCMB cell. (e) 5th cycle charge cell voltage and electrode potentials of conventional LCO/MCMB cell. (f) 5th cycle discharge cell voltage and electrode potentials of conventional LCO/MCMB cell. *Reproduced from Ref [173] with permission from the Royal Society of Chemistry 6

Figure 2: Time elapsed between nail impact and thermal runaway event for NCM-LCO/Graphite cells at difference SoC. *Reproduced from ref [33] with permission from the Electrochemical Society 10

Figure 3: Max temperature increase for NCM-LCO cells at difference SoC. *Reproduced from ref [33] with permission from the Electrochemical Society 11

Figure 4: Max pressure rate increase for NCM-LCO cells at difference SoC. *Reproduced from ref [33] with permission from the Electrochemical Society 11

Figure 5: Characteristic thermal runaway parameters from Accelerated Rate Calorimetry on NCA/graphite cells. (a) Onset cell temperature of thermal runaway. (b) Maximum cell temperature. (c) Amount of produced gas (d) Main detected gas components. [A.W. Golubkov, S. Scheikl, R. Planteu, G. Voitic, H. Wiltsche, C. Stangl, G. Fauler, A. Thaler, V. Hacker, RSC Adv. 5 (2015) 57171–57186.] - Published by the Royal Society of Chemistry. 12

Figure 6: Oxygen release at difference lithiation states: (a) NCA powder upon heating to 600 °C and (b) LFP powder in electrolyte upon heating to 350 °C. [A.W. Golubkov, S. Scheikl, R. Planteu, G. Voitic, H. Wiltsche, C. Stangl, G. Fauler, A. Thaler, V. Hacker, RSC Adv. 5 (2015) 57171–57186.] - Published by the Royal Society of Chemistry. 13

Figure 7: Characteristic thermal runaway parameters from Accelerated Rate Calorimetry on LiFePO4/graphite cells. (a) Onset cell temperature of thermal runaway. (b) Maximum cell temperature. (c) Amount of produced gas (d) Main detected gas components. [A.W. Golubkov, S. Scheikl, R. Planteu, G. Voitic, H. Wiltsche, C. Stangl, G. Fauler, A. Thaler, V. Hacker, RSC Adv. 5 (2015) 57171–57186.] - Published by the Royal Society of Chemistry. 13

Figure 8: DSC profiles of chemically delithiated Li_xCoO_2 at a heating rate of 5 °C/min *Reproduced from [Y. Baba, S. Okada, J.I. Yamaki, Solid State Ionics 148 (2002) 311–316.] with permission from Elsevier 14

Figure 9: (a) 5th cycle discharge and fixed load step (grey shading) cell voltage and electrode potentials plotted vs. cell capacity. (b) 5th cycle discharge and fixed load step (grey shading) cell voltage and electrode potentials plotted vs. time. Red shading represents anode potential range in which copper dissolution occurs. (c) Schematic of cell function in the near zero volt condition. Orange arrows represent copper ion flow. Red arrow represents electron flow through external

circuit. (d) Linear sweep voltammogram of copper foil. Red shaded region represents potential range in which copper dissolution occurs. 19

Figure 10: (a) Image of the arrangement of the separator, cathode, anode and reference Li electrode in the pouch cell. (b) Cross sectional schematic of assembled pouch cells placed between restraint plates for testing. *Reproduced from Ref [173] with permission from the Royal Society of Chemistry..... 31

Figure 11: (a) Schematic of 0.25 mAh charge of a conditioned, discharged cell. (b) Schematic depicting disassembly of cell and discarding cathode. (c) Schematic of reassembly for partially lithiated anode with fresh cathode in a new cell. *Reproduced from Ref [173] with permission from the Royal Society of Chemistry 38

Figure 12: (a) 1st cycle charge cell voltage and electrode potentials of RLE cell. Labeled voltages represent anode potential and full cell voltage at the beginning of charge. (b) 1st cycle discharge cell voltage and electrode potentials of RLE cell. Labeled voltages represent the cathode and anode potentials at the end of discharge. (c) Schematic of cell condition at the end of discharge to a cutoff volt of 3.0 volts showing the cathode fully intercalated and the anode not fully depleted of reversible lithium. *Reproduced from Ref [173] with permission from the Royal Society of Chemistry..... 40

Figure 13: (a) 5th cycle discharge and fixed load step (grey shading) cell voltage and electrode potentials plotted vs. cell capacity of RLE cell. (b) 5th cycle discharge and fixed load step (grey shading) cell voltage and electrode potentials plotted vs. time of RLE cell. Red shading represents anode potential range in which copper dissolution occurs. (c) Schematic of RLE cell function in the near zero volt condition. Pink arrows represent lithium ion flow, the red arrow represent electron flow through internal circuit. *Reproduced from Ref [173] with permission from the Royal Society of Chemistry 42

Figure 14: (a) Cycling schedule flow chart depicting the duration and number of cycles and storage periods. (b) Discharge profiles of a conventional cell prior to zero volt storage and after one, two and three, 3-day near zero volt storage periods. (c) Discharge profile of the conventional cell electrode potentials as measured by a lithium metal reference prior to near zero volt storage and after three, 3-day near zero volt storage periods. (d) Discharge profiles of an RLE cell prior to zero volt storage and after one, two and three, 3-day near zero volt storage periods. (e) Discharge profile of the RLE cell electrode potentials as measured by a lithium metal reference prior to near zero volt storage and after three, 3-day near zero volt storage periods. *Reproduced from Ref [173] with permission from the Royal Society of Chemistry 44

Figure 15: (a) Cycling schedule flow chart. (b) Discharge profiles of an RLE cell prior to near zero volt storage and after 1, 2 and 3 7-day near zero volt storage periods. (c) Discharge profile of the RLE cell electrode potentials as measured by a lithium metal reference prior to near zero volt storage and after 3, 7-day near zero volt storage periods. *Reproduced from Ref [173] with permission from the Royal Society of Chemistry 46

Figure 16: (a) Cycling schedule flow chart showing flow of conditioning, storage, rate testing and low earth orbit (LEO) cycling. (b) Discharge profiles of RLE and conventional cell at different

discharge rates. Rate study done after a 3-day storage period (near zero volt storage for the RLE cell and open circuit storage for the conventional cell). (c) End of discharge voltages for 30% depth of discharge (DOD) low earth orbit (LEO) cycling of the RLE and conventional cell.
 *Reproduced from Ref [173] with permission from the Royal Society of Chemistry 49

Figure 17: (a) Cycling schedule flow chart summarizing room temperature conditioning, cycling at 45°C, and near zero volt storage testing at 45°C. (b) 7th cycle discharge and fixed load step (grey shading) cell voltage and electrode potentials plotted vs. time of RLE cell with 1.2 M LiPF₆ 3:7 EC:EMC v/v electrolyte at 45°C. (c) 7th cycle discharge and fixed load step (grey shading) cell voltage and electrode potentials plotted vs. time of RLE cell with 1.2 M LiPF₆ 3:7 EC:EMC v/v VC 2% w/w electrolyte at 45°C. (d) 9th cycle discharge and fixed load step (grey shading) cell voltage and electrode potentials plotted vs. time of RLE cell with 1.2 M LiPF₆ 3:7 EC:EMC v/v electrolyte at 45°C. (e) 10th cycle discharge and fixed load step (grey shading) cell voltage and electrode potentials plotted vs. time of RLE cell with 1.2 M LiPF₆ 3:7 EC:EMC v/v VC 2% w/w. electrolyte at 45°C. storage periods at 45°C. 53

Figure 18:(a) Discharge profiles of an RLE with 1.2 M LiPF₆ 3:7 EC:EMC v/v electrolyte cell prior to zero volt storage, and after one, two and three, 3-day near zero volt storage periods at 45°C. (b)) Discharge profiles of an RLE with 1.2 M LiPF₆ 3:7 EC:EMC v/v VC 2% w/w electrolyte cell prior to zero volt storage, and after one, two and three, 3-day near zero volt storage periods at 45°C. 55

Figure 19: Cell voltage and electrode potentials of a LiCoO₂/MCMB cell with a lithium reference electrode during a pulse discharge to 0 volts cell voltage..... 56

Figure 20: (a) Measured cathode potential vs. Li/Li⁺ and open circuit potential vs. Li/Li⁺ obtained from RC element fitting at a point about halfway through the pulse discharge test. (b) The overpotential and change in overpotential as a function of time corresponding to the leftmost C/10 discharge pulse in a. (c) Measured cathode potential vs. Li/Li⁺ and open circuit potential vs. Li/Li⁺ obtained from RC element fitting at the end of the pulse discharge test (last 3 pulses). (d) The overpotential and change in overpotential as a function of time corresponding to the leftmost C/10 discharge pulse in c. 58

Figure 21: (a) Measured anode potential vs. Li/Li⁺ and open circuit potential vs. Li/Li⁺ obtained from RC element fitting at a point about halfway through the pulse discharge test. (b) The overpotential and change in overpotential as a function of time corresponding to the leftmost C/10 discharge pulse in a. (c) Measured anode potential vs. Li/Li⁺ and open circuit potential vs. Li/Li⁺ obtained from RC element fitting at the end of the pulse discharge test (last 3 pulses). (d) The overpotential and change in overpotential as a function of time corresponding to the leftmost C/10 discharge pulse in c. 60

Figure 22: (a) SEM micrograph of as-received LiCoO₂. (b) SEM micrograph of LiCoO₂ after AlPO₄ coating process 65

Figure 23: Discharge profiles of conditioning cycles 1,3,5,7 and 9 for uncoated LiCoO₂ (top) and AlPO₄ coated LiCoO₂ (bottom) 66

Figure 24: (a) Cycling schedule of coin cells with as-received LiCoO₂ cathode vs. Lithium metal. Numbers after conditioning represent cycles (charge to 147 mAh/g_{LiCoO₂} extraction and discharge to 3.0 V vs. Li/Li⁺). (b) Constant current discharge to 3.0 V vs. Li/Li⁺ and fixed load over-insertion curve of cycle 10, 11, 13, 16 and 19 for coin cell with as-received LiCoO₂ cathode vs. Lithium metal (c) Fixed resistive load, 5% (7mAh/g_{LiCoO₂}) over-insertion step of cycles 10, 11, 13, 16 and 19 for coin cell with as-received LiCoO₂ cathode vs. Lithium metal. (d) Constant current 0.7 mA/g_{LiCoO₂} charge to 3.0 V vs. Li/Li⁺ and 14 mA/g_{LiCoO₂} charge to 147 mAh/g_{LiCoO₂} of cycles 10, 11, 13, 16 and 19 for coin cell with as-received LiCoO₂ cathode vs. Lithium metal. (e) Zoom in of first 5 mAh/g_{LiCoO₂} of charge of as-received LiCoO₂ for cycles 10, 11, 13, 16, 19. 68

Figure 25: (a) Constant current discharge to 3.0 V vs. Li/Li⁺ and fixed resistive load over-discharge curve of cycle 10, 11, 13, 16 and 19 for coin cell with 1.0 % w/w AlPO₄ coated LiCoO₂ cathode vs. Lithium metal (b) Fixed resistive load, 5% (7mAh/g_{LiCoO₂}) over-insertion step of cycles 10, 11, 13, 16 and 19 for coin cell with 1.0 % w/w AlPO₄ coated LiCoO₂ cathode vs. Lithium metal. (c) Constant current 0.7 mA/g_{LiCoO₂} charge to 3.0 V vs. Li/Li⁺ and 14 mA/g_{LiCoO₂} charge to 147 mAh/g_{LiCoO₂} of cycles 10, 11, 13, 16 and 19 for coin cell with 1.0 % w/w AlPO₄ coated LiCoO₂ cathode vs. Lithium metal. (d) Zoom in of the first 5 mAh/g_{LiCoO₂} of charge of 1.0 % w/w AlPO₄ coated LiCoO₂ for cycles 10, 11, 13, 16 and 19..... 72

Figure 26: (a) X-ray Diffraction (XRD) pattern of as-received LiCoO₂ before (bottom) and after (top) 20 cycles including 10, 5% over-insertion steps by fixed resistive load. (b) X-ray Diffraction (XRD) pattern of AlPO₄ coated LiCoO₂ before (bottom) and after (top) 20 cycles including 10, 5% over-insertion steps by fixed resistive load. 74

Figure 27: (a) Picture of 4-electrode coin cell construction. (b) Plot of the Electrode Asymptotic Potential (EAP) of a LiCoO₂/MCMB lithium ion cell as a function of the amount of lithium added to the cell as a percentage of cell capacity. 77

Figure 28: (a) Electrode potentials and cell voltage during 5th C/10 discharge and 3-day fixed load storage plotted against cell capacity for an RLE NCA/MCMB cell. (b) Electrode potentials and cell voltage during 5th C/10 discharge and 3-day fixed load storage plotted against cell capacity for a conventional NCA/MCMB cell..... 80

Figure 29: (a) Discharge profile of RLE NCA/MCMB cell prior to near zero volt storage and after 5 and 10, 3-day near zero volt storage periods. (b) Discharge profile of conventional NCA/MCMB cell prior to near zero volt storage and after 5 and 10, 3-day near zero volt storage periods..... 81

Figure 30: Discharge energy (normalized to cycle 1) of RLE and conventional cells after ten, 3-day near zero volt storage periods. 82

Figure 31: (a) Schematic of bath cell configuration used for formation cycling and reversible lithium addition. (b) Picture of electrode connection method for bath cell showing the z-fold electrode/separator stack connected by clips and the lithium metal electrode which consist of lithium metal pressed onto a copper wire. (c) Cell voltage, anode and cathode potentials during the 1st C/10 charge and discharge cycle followed by a C/10 charge to 4.2 V cell voltage. (d)

Cathode potential vs. lithium reference electrode, cathode potential vs. lithium source and anode potential vs. lithium reference electrode during the first addition of 25.5 mAh of reversible lithium to the electrode stack. 83

Figure 32: Cell Voltage, cathode and anode potential during 2 cycles of C/10 charge and discharge of cell electrode stack in bath cell after 1st addition of 25.5 mAh of reversible lithium from lithium source electrode. After the second C/10 charge and discharge a fixed resistive load of 105 Ohms is applied to the electrode stack of the cell by the Arbin Cycler (gray shaded region). 85

Figure 33: (a) Cathode potential vs. lithium reference electrode, cathode potential vs. lithium source and anode potential vs. lithium reference electrode during the second addition 25.5 mAh of reversible lithium to the electrode stack. (b) Cell Voltage, anode and cathode potentials during the application of a fixed load of 105 Ohms to the electrode stack of the cell after the second addition of 25.5 mAh of reversible lithium. 86

Figure 34: (a) Cathode potential vs. lithium reference electrode, cathode potential vs. lithium source and anode potential vs. lithium reference electrode during the third addition 25.5 mAh of reversible lithium to the electrode stack. (b) Cell Voltage, anode and cathode potentials during the application of a fixed load of 105 Ohms to the electrode stack of the cell after the third addition of 25.5 mAh of reversible lithium. 87

Figure 35: (a) Photograph of pouch cell with a resistor of 120 Ohms applied to the cell and an external analog voltmeter monitoring cell voltage. (b) Cell voltage, anode potential and cathode potential as monitored by the Arbin cycler during 14-day period with a resistor applied to the pouch cell shown in part a. 88

Figure 36: Overlay of cell voltage, cathode potential and anode potential during the C/10 discharge before and after a 14-day period in a near zero volt state with and applied resistor. 89

Figure 37: (a) Electrode potentials and cell voltage during first charge with a constant current (CC) of 0.6 mA. (b) Electrode potentials and cell voltage during the first discharge with CC of 0.6 mA. 95

Figure 38: (a) Electrode potentials and cell voltage during 5th 1.2 mA constant current (CC) discharge and 3-day fixed resistive load storage plotted against cell capacity. (b) Electrode potentials and cell voltage during 5th 1.2 mA CC discharge and 3-day fixed resistive load storage plotted against time. The red dashed line represents the threshold electrochemical potential at which copper dissolution from the anode will occur. 98

Figure 39: (a) Flowchart of cycling regime for testing the tolerance of the HE5050/MCMB cell to 3 day near zero volt storage periods. (b) 1.2 mA constant current (CC) discharge curves of HE5050/MCMB cell prior to and after 1, 2, 3, 4, and 5 seventy two hour, near zero volt storage periods. 100

Figure 40: (a) HE5050/MCMB cell voltage profile during the 5th cycle discharge and first 3-day near zero volt storage period under fixed resistive load (solid red line) and the cell voltage profile during the charge following the near zero volt storage period (dotted blue line). Dashed line

indicates discharge/charge capacity of each step (b) Discharge capacity (including capacity from the 1.2 mA constant current discharge step to 2.0 V cell voltage and the 3-day fixed resistive load step) plotted with the charge capacity of the cell charge on subsequent cycle after the near zero volt storage period..... 102

Figure 41: (a) Flowchart of cycling regime for testing the tolerance of the HE5050/MCMB cell to 7 day near zero volt storage periods. (b) 1.2 mA constant current (CC) discharge curves of HE5050/MCMB cell prior to and after 1, 2, 3, 4, and 5 seven day, near zero volt storage periods. 103

Figure 42: (a) Flow chart of cycling schedule for testing the effects of near zero volt storage of HE5050/MCMB cells on their rate capability and long term cycling stability compared to cell stored at open circuit. (b) Discharge profiles of HE5050/MCMB cell stored at open circuit for three days and HE5050/MCMB cell stored at near zero volts for three days at 1.2 mA, 6 mA, 12 mA and 60 mA discharge current (i.e. C/10, C/2, C and 5C discharge rates based on rated cell capacity). (c) End of discharge voltages of HE5050/MCMB cell stored at open circuit for three days and HE5050/MCMB cell stored at near zero volts for three days under 30% depth of discharge low earth orbit (LEO) cycling. (d) Discharge voltage profile of the 1st, 200th and 500th LEO cycle of the HE5050/MCMB cell stored at open circuit for three days and HE5050/MCMB cell stored at near zero volts for three days..... 105

Figure 43: (a) Flowchart of testing regime for testing of near zero volt storage tolerance of HE5050/MCMB cells at 40 °C. (b) Discharge profile of HE5050/MCMB cell with Li reference electrode at 0.09 mA at room temperature. (c) Discharge profile of HE5050/MCMB cell with Li reference electrode at 0.09 mA at 40 °C. (d) Plot of reference electrode data for cycle 7. Gray shaded area on left is the constant current discharge to 2.0 V cell voltage. Non-shaded are on right is fixed resistive load step. The red dashed line represents the threshold value that the anode potential would need to increase to for copper dissolution to occur. (e) 0.09 mA constant current (CC) discharge curves of HE5050/MCMB cell prior to and after 1 and 2 3-day, near zero volt storage periods at 40°C. 107

Figure 44: Flow diagram of processing steps of commercial MWCNT sheet materials to remove amorphous carbon and residual metal catalyst and coated with ~3 nm of Al₂O₃. 114

Figure 45: a. First cycle insertion of lithium into CNT paper electrodes. b.) Cumulative irreversible loss plotted against cycle index for a CNT paper electrode coated with Al₂O₃ and a bare CNT paper electrode. c.) Extraction voltage profile of (top) Al₂O₃ coated CNT paper electrode and (bottom) bare CNT paper electrode..... 117

Figure 46: XRD pattern of the bare MWCNT and Al₂O₃-MWCNT before cycling (top) and after cycling (bottom)..... 120

Figure 47: (a) Raman spectra of bare MWCNT before cycling (bottom) and after cycling (top) vs. Li metal in a coin cell. Spectra shown is representative of the average peak ratios observed for the Raman spectra of 5 different spots on the material. (b) Raman spectra of Al₂O₃-MWCNT before cycling (bottom) and after cycling (top) vs. Li metal in a coin cell. Spectra shown is

representative of the average peak ratios observed for the Raman spectra of 5 different spots on the material.	121
Figure 48: Voltage profile of lithium extraction from Al ₂ O ₃ -MWCNT (top) and bare MWCNT (bottom) at 15 mA/g, 30 mA/g, 75 mA/g and 150 mA/g.....	123
Figure 49: (a) First cycle insertion voltage profiles of MCMB composite coated onto bare MWCNT or Al ₂ O ₃ -MWCNT. (b) Extraction voltage profiles for cycles 1-5 of MCMB composited coated onto Al ₂ O ₃ -MWCNT (top) and MCMB composite coated onto bare MWCNT (bottom). (c) Plot of cumulative irreversible loss as a function of the cycle number for MCMB composite coated onto bare MWCNT or Al ₂ O ₃ -MWCNT.	124
Figure 50: Extraction voltage profiles at rates of 30, 60 and 150 mA/g _{electrode} of MCMB composite coated onto Al ₂ O ₃ -MWCNT (top) and MCMB composite coated onto bare MWCNT (bottom).	125
Figure 51: (a) First charge and discharge of HE5050/Li coin cell at an effective C/20 rate. (b) First charge and discharge of MCMB/Li coin cell at an effective C/20 rate.	130
Figure 52: (a) Depiction of the cell after cell construction, white circles represent lithium ions. (b) Depiction of cell condition after the first charge. Red “X” symbols indicate reversible lithium lost to SEI formation. (c) Depiction of cell condition after the first discharge.	131
Figure 53: (a) Depiction of HE5050/MCMB cell after the first discharge. This is also representative of the cell condition after all constant current discharges (b) Depiction of HE5050/MCMB cell after the second charge. This is also representative of the cell condition after all constant current charges. (c) Depiction of HE5050/MCMB cell after the second discharge. This is also representative of the cell condition after all constant current discharges.	133
Figure 54: 1.2 mA constant current (CC) discharge curves of HE5050/MCMB cell prior to and after 1, 2, 3, 4, and 5 seventy two hour, near zero volt storage periods.	136
Figure 55: (a) Overlay of reference electrode measurements for the constant current discharge and fixed load, near zero volt storage period of HE5050/MCMB cell tested with 3-day near zero volt storage periods. (b) Overlay of reference electrode measurements for the constant current discharge and fixed load, near zero volt storage period of HE5050/MCMB cell tested with 7-day near zero volt storage periods.	137
Figure 56: 1.2 mA constant current (CC) discharge curves of HE5050/MCMB cell prior to and after 1, 2, 3, 4, and 5 seventy two hour, near zero volt storage periods.	138
Figure 57: Discharge capacity (including capacity from the 1.2 mA constant current discharge step to 2.0 V cell voltage and the 7-day fixed load step) plotted with the charge capacity of the cell charge on subsequent cycle after near zero volt storage period.	138
Figure 58: Voltage plotted as a function of time for prototype HE5050/MCMB pouch cell discharged and then stored at open circuit for 3 days.	139

Figure 59: Reference electrode data of HE5050/MCMB cell first discharged at constant current (leftmost unshaded region). Then a fixed resistive load is applied for 72 hours (gray shaded region), then the cell is left at open circuit (rightmost unshaded region) 139

Figure 60: 0.09 mA constant current (CC) discharge curves of HE5050/MCMB cell prior to and after 1 and 2 3-day, near zero volt storage periods at 40°C. 140

Figure 61: Overlay of reference electrode measurements for the constant current discharge cell tested with 3-day near zero volt storage periods at 40°C after cycle 7 and 8. 140

Figure 62: Overlay of reference electrode measurements for the constant current discharge and fixed load, near zero volt storage period of HE5050/MCMB cell tested with 3-day near zero volt storage periods at 40°C. 141

Figure 63: (At 40°C) Discharge capacity (including capacity from the 0.09 mA constant current discharge step to 2.0 V cell voltage and the 3-day fixed load step) plotted with the charge capacity of the cell charge on subsequent cycle after near zero volt storage period. 141

Figure 64: First Charge voltage profiles of bare LiCoO₂ and AlPO₄ coated LiCoO₂..... 142

Figure 65: (a) Discharge voltage profiles for cycle 1,5,10,15 and 20 of bare LiCoO₂ cycled vs. Li metal in a coin cell from 3.0-4.5 V vs. Li/Li⁺. (b) Discharge voltage profiles for cycle 1,5,10,15 and 20 of AlPO₄ coated LiCoO₂ cycled vs. Li metal in a coin cell at a constant current from 3.0-4.5 V vs. Li/Li⁺. 142

Figure 66: (a) SEM micrographs of pristine LiCoO₂ prior to cycling and after cycling (20 cycles including 10, 5% over-insertion steps by fixed resistive load after discharge to 3.0 V vs. Li/Li⁺). (b) SEM micrographs of AlPO₄ coated LiCoO₂ prior to cycling and after cycling (20 cycles including 10, 5% over-insertion steps by fixed resistive load after discharge to 3.0 V vs. Li/Li⁺). 143

Figure 67:(a) Voltage profiles of cycles 1-9 of charge of as-received LiCoO₂ with a constant current of 14 mA/g_{LiCoO₂} to a limit of 140 mAh/g_{LiCoO₂}. (b) Voltage profiles of cycles 1-9 of discharge of as-received LiCoO₂ with a constant current of 14 mA/g_{LiCoO₂} to 3.0 V vs. Li/Li⁺... 145

Figure 68: (a) Voltage profiles of cycles 1-9 of charge of 1 wt% AlPO₄ coated LiCoO₂ with a constant current of 14 mA/g_{LiCoO₂} to a limit of 140 mAh/g_{LiCoO₂}. (b) Voltage profiles of cycles 1-9 of discharge of 1 wt% AlPO₄ coated LiCoO₂ with a constant current of 14 mA/g_{LiCoO₂} to 3.0 V vs. Li/Li⁺..... 146

Figure 69: (a) Constant current discharge curve to 3.0 V vs. Li/Li⁺ of cycle 10-19 for coin cell with as-received LiCoO₂ cathode vs. Lithium metal (b) Fixed resistive load, 5% (7mAh/g_{LiCoO₂}) over-insertion step of cycles 10-19 for coin cell with as-received LiCoO₂ cathode vs. Lithium metal..... 147

Figure 70: (a) Constant current 0.7 mA/g_{LiCoO₂} charge to 3.0 V vs. Li/Li⁺ and 14 mA/g_{LiCoO₂} charge to 147 mAh/g_{LiCoO₂} of cycles 10-19 for coin cell with as-received LiCoO₂ cathode vs.

Lithium metal. (b) Zoom in of the first 5 mAh/g_{LiCoO₂} of recharge of as-received LiCoO₂ for cycles 10-19. 148

Figure 71: (a) Constant current discharge curve to 3.0 V vs. Li/Li⁺ of cycle 10-19 for coin cell with 1 w% AlPO₄ coated LiCoO₂ cathode vs. Lithium metal (b) Fixed resistive load, 5% (7mAh/g_{LiCoO₂}) over-insertion step of cycles 10-19 for coin cell with 1 w% AlPO₄ coated LiCoO₂ cathode vs. Lithium metal. 149

Figure 72: (a) Constant current 0.7 mA/g_{LiCoO₂} charge to 3.0 V vs. Li/Li⁺ and 14 mA/g_{LiCoO₂} charge to 147 mAh/g_{LiCoO₂} of cycles 10-19 for coin cell with 1 w% AlPO₄ coated LiCoO₂ cathode vs. Lithium metal. (b) Zoom in of the first 5 mAh/g_{LiCoO₂} of recharge of 1 w% AlPO₄ coated LiCoO₂ for cycles 10-19. 150

Figure 73: Diagram of optical cell setup, the WE on the left is a graphite composite coated onto copper foil, the CE on the right is a LiCoO₂ composite that is oversized so as to be used as a lithium source. The RE on the left is a lithium chip pressed onto copper foil. 151

Figure 74: a.) Optical image (left) and corresponding electrochemical potential (right, red dot shows location of curve that corresponds to optical image) for cell as the electrochemical potential reaches a minimum at ~0.4 hours. b.) Optical image (left) and corresponding electrochemical potential (right, red dot shows location of curve that corresponds to optical image) for cell at 0.75 hours. Optical image (left) and corresponding electrochemical potential (right, red dot shows location of curve that corresponds to optical image) for cell at 1 hour. 153

Figure 75: a.) Optical image (left) and corresponding electrochemical potential (right, red dot shows location of curve that corresponds to optical image) for cell 2 hours. b.) Optical image (left) and corresponding electrochemical potential (right, red dot shows location of curve that corresponds to optical image) for cell at 4 hours. Optical image (left) and corresponding electrochemical potential (right, red dot shows location of curve that corresponds to optical image) for cell at 8 hours. 154

1. Introduction

As society transitions to renewable energy sources and expanded use of electrical energy, energy storage in a reliable and safe manner is becoming more paramount. For many portable applications, electrochemical energy storage using lithium ion batteries is currently the premier method due to the enhanced rechargeable chemistry. Compared to other designs (i.e. NiCd, Ni-H, etc.) lithium ion has higher energy density, cycle life and highly tunable performance characteristics.[1,2] There are many efforts underway to enhance lithium ion battery performance to align with future application needs,[3] however, as energy density increases, the associated safety risks also increase.[4]

When in a user-*inactive* state, the safety of lithium ion batteries could be improved in an easily regulatable way by application of a resistor to discharge them to a near zero volt (i.e. $<10\text{mV}$), completely discharged state. In a completely discharged, near zero volt state the safety risks associated with lithium ion batteries decreases substantially. Additionally unlike in lithium ion cells in a mid-range state of charge (i.e. 10-90%) (for which there is currently no method that can rapidly, reliably and accurately determine the state of charge in the field), the near zero volt state of a lithium ion cell with an applied resistor can be easily monitored or checked. Such a capability introduces significant controllability that overcomes the need to trust manufacturers to comply with low state of charge limitations for shipping.[5] Thus, maintaining user-inactive lithium ion cells in a near zero volt state can lead to significant improvements in safety when cells are stored or shipped.

However, conventional lithium ion cells are significantly damaged if discharged to a near zero volt state. Several methods to create advanced lithium ion cells that can tolerate

a near zero volt or over-discharged state have been pursued and will be discussed in more detail in section 1.7, but all involve material substitutions or additions that can lead to increased cell costs, reduced cell performance, operational complications and/or safety concerns. Thus, identification, understanding, and demonstration of a more advantageous way to render advanced lithium ion cells tolerant to a near zero volt state is necessary to improve the future feasibility of maintaining user-*inactive* lithium ion cells in a near zero volt state with an applied resistor to controllably improve their safety during storage or shipping.

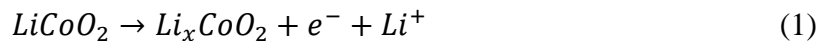
The following sections 1.1-1.2 provide a brief introduction to some basic concepts of lithium ion battery components and function. Section 1.3-1.4 introduces some of the safety risks associated with lithium ion batteries. Section 1.5 will discuss current challenges with implementing state of charge limitations to increase safety of inactive lithium ion batteries. Section 1.6 will introduce the concept of near zero volts storage in greater detail and chapters 1.7 and 1.8 will discuss past approaches to enabling near zero volt storage or over-discharge tolerance and the opportunity for developing alternative approaches to near zero volt tolerance.

1.1 Lithium ion battery components, function and reference electrodes

Conventional lithium ion batteries employ crystalline materials which allow lithium ion intercalation/de-intercalation within the interstitial layers or spaces. The predominant active electrode materials have been a lithiated metal oxide for the cathode (positive electrode) and graphitic carbon as the anode (negative electrode). The active materials are combined with a binder (e.g. polyvinylidene fluoride (PVDF)) and conductive additives (e.g. carbon black, graphite, etc.) prior to being deposited onto metal foil current

collectors. The electrodes are electrically isolated from each other in the battery by a polymer separator, most often consisting of a microporous polypropylene/polyethylene laminate that allows for lithium ion diffusion and migration.[2] An ionically conductive and electrically insulating electrolyte, most commonly consisting of a lithium salt dissolved in organic solvents(s), is wetted into the separator/electrodes.

During the charge of a cell, an externally applied voltage difference causes lithium ions to migrate from the cathode to the anode. The migration of lithium ions results in lithium ions de-intercalating from the cathode and intercalating into the anode. In conjunction electrons flow from the cathode to the anode through an external circuit. The half-cell reaction of a representative LiCoO_2 cathode is represented by equation 1 and the total half-cell reaction of a graphitic anode is represented by equation 2. Briefly, in an electrochemical cell, each half-cell reaction has an associated change of Gibbs free energy. Gibbs free energy can be thought of as the energy available in a system to perform work. By convention a positive change in free energy represents an absorption of energy (environment doing work on the system) and a negative change represents the release of energy (system doing work on the environment). The change in Gibbs free energy can be related to the electrostatic potential of the reaction by equation 3, where E is the reaction potential of a half-cell reaction, F is the Faraday constant, and n is the charge constant.[6]



$$\Delta G = -nFE \quad (3)$$

In an electrochemical cell, the overall reaction is made up of the two individual half-cell reactions. Each half-cell reaction has its own ΔG that contributes to the overall

cell potential. Additionally, when Butler-Volmer reaction kinetics are considered, the following current-potential relationship can be formed (equation 4). Essentially, this equation relates the overpotential (different between electrode potential and equilibrium potential, $E - E_{eq}$) to the cell current by taking into account the reaction rate constants and the changing of energy barriers by an externally applied potential/load, which may be different for each electrode. $C_o(0, t)$ and $C_R(0, t)$ represent surface concentrations of oxidizing or reducing species (in this case occupied lithium sites or vacant lithium sites). C_o^* and C_R^* represent bulk concentrations of oxidizing or reducing species, and i_0 represents the exchange current. F is the faraday constant, R is the gas constant, and T is the temperature. This equation, or a modified version of this equation, is used in describing almost all reactions in electrochemistry[6] and is in the case of lithium ion cells is typically used to represent the flux of lithium ions through the surfaces of active particles in electrode composites[7]. Double layer capacitance also plays a significant role in the electrode kinetics, and can be represented by a capacitor which has a current potential relationship according to equation 5.

$$i = i_0 \left[\frac{C_o(0,t)}{C_o^*} e^{-\alpha \frac{F}{RT}(E-E_{eq})} - \frac{C_R(0,t)}{C_R^*} e^{(1-\alpha) \frac{F}{RT}(E-E_{eq})} \right] \quad (4)$$

$$i = C \frac{d(E-E_{eq})}{dt} \quad (5)$$

It is not possible to experimentally de-convolute each electrode potential during testing (although it can be done theoretically in some cases), and so instead the potential of half reactions is measured against a standard reference. In the case of lithium ion batteries, lithium metal is the most commonly used quasi-reference electrode (will be referred to just as a “reference” electrode throughout the following chapters) to measure electrode potentials vs. the Li/Li⁺ redox couple. Quasi-reference electrodes are chosen so

that their effective composition, and therefore their potential, does not change during testing and they won't contaminate the electrolyte with unwanted ion species.[6] Lithium metal used as a quasi-reference electrode contains an effectively infinite amount of lithium ions, and therefore its effective composition does not change throughout testing.

Lithium ion cell function during charge is depicted in Figure 1a and measured cell voltage and electrode potentials during charge are shown in Figure 1b. The cell configuration for measurement of electrode potentials with a lithium metal reference electrode will be discussed in section 3.1.1. As shown in Figure 1b, as the cell charges on the first cycle, the electrochemical potential of the cathode vs. Li/Li^+ increases (absorbing energy) as lithium ions de-intercalate from it. The electrochemical potential of the anode, on the other hand, decreases (releasing energy) as lithium ions are intercalated into it. As a result, the cell voltage, which is the difference between the cathode and anode electrochemical potentials, increases until charge is stopped at the chosen cutoff voltage.

When the cell is discharged by applying an external load between the electrodes, lithium ions diffuse from the anode to the cathode due to the electrochemical potential difference between the electrodes. In conjunction, electrons flow through the external load from the anode to the cathode. The cell function during discharge is depicted in Figure 1c and the measured cell voltage and electrode potentials during charge are shown in Figure 1d. As shown in Figure 1d, as the cell discharges, the electrochemical potential of the cathode vs. Li/Li^+ decreases as lithium ions intercalate into it. The electrochemical potential of the anode, on the other hand, increases as lithium ions de-intercalate from it. As a result, the cell voltage decreases until discharge is stopped at the cutoff voltage (3 V cell voltage in this case).

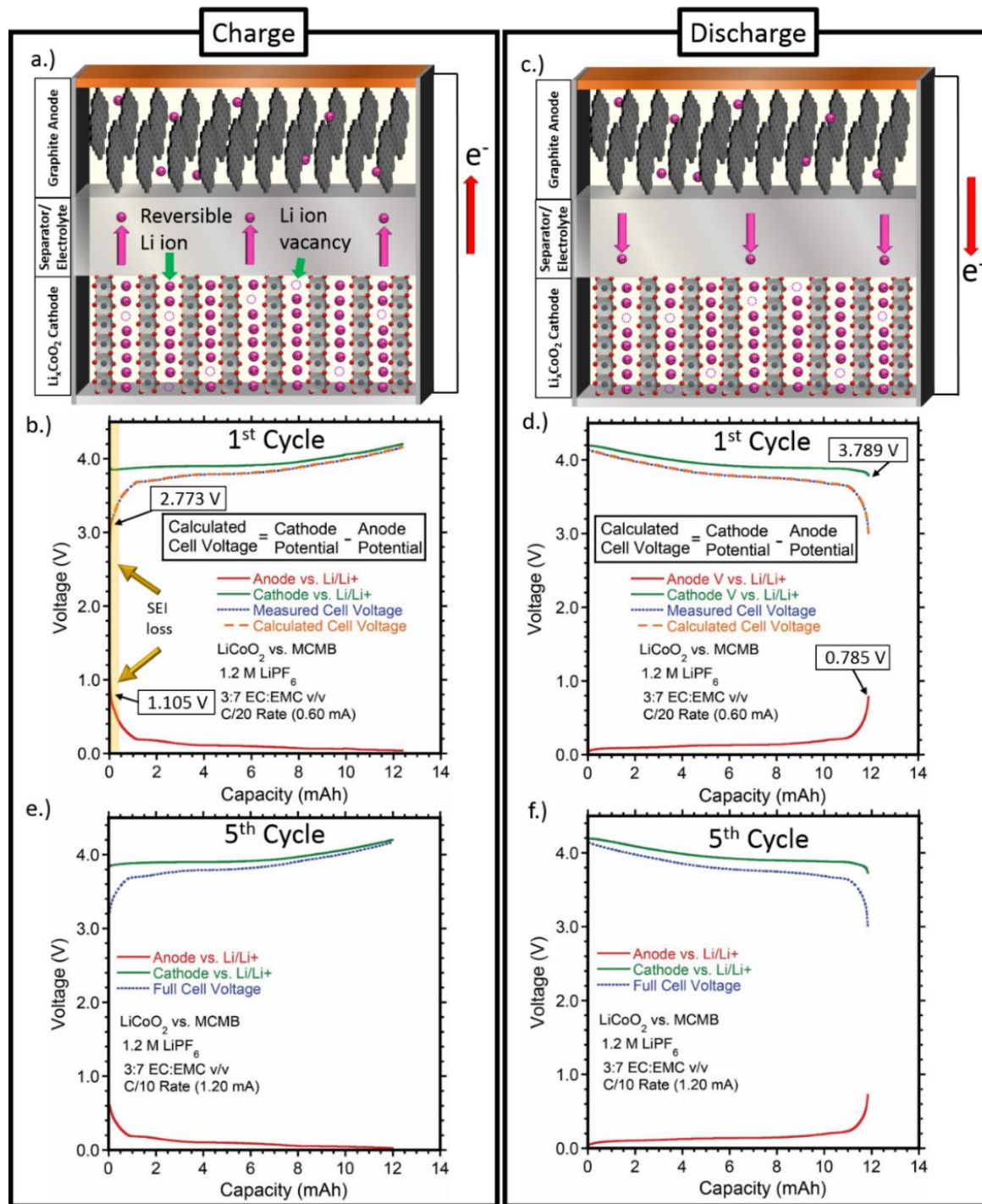


Figure 1: (a) Schematic of cell function during charge of conventional LCO/MCMB cell. The pink arrows represent lithium ion flow and the red arrow represents electron flow. (b) 1st cycle charge cell voltage and electrode potentials of conventional LCO/MCMB cell. (c) Schematic of cell function during discharge of conventional LCO/MCMB cell. The pink arrows represent lithium ion flow and the red arrow represents electron flow. (d) 1st cycle discharge cell voltage and electrode potentials of conventional LCO/MCMB cell. (e) 5th cycle charge cell voltage and electrode potentials of conventional LCO/MCMB cell. (f) 5th cycle discharge cell voltage and electrode potentials of conventional LCO/MCMB cell. *Reproduced from Ref [173] with permission from the Royal Society of Chemistry

Reference electrode tests allows for independent measurement of each electrode potential as well as the cell voltage during cell cycling. Knowing the electrochemical potential of each electrode during testing can give important insights into the intercalation state, performance, and degradation modes of the individual electrodes. In order to ensure that the reference electrode measurements are consistent with the observed cell voltage, the difference between the measured electrode potentials was compared to the measured cell voltage throughout cycling. An example is shown in Figure 1b and d and as shown, the calculated cell voltage is nearly identical to the measured cell voltage throughout charge and discharge with a magnitude of difference of <8 mV.

1.2 Amount of reversible lithium in a cell

When a conventional LiCoO_2 /graphite lithium ion cell is assembled, the cathode is inherently fully intercalated with lithium while the anode contains no lithium. In an idealized view of lithium ion cell function, during charge, the same amount of lithium ions will be de-intercalated from the cathode as are intercalated into the anode. Then, upon discharge, the same amount of lithium that flowed from the cathode to the anode on the charge will de-intercalate from the anode and intercalate into the cathode. This amount of lithium that can flow from the anode to the cathode during discharge will herein be defined as *the amount of reversible lithium in the cell*.

In real lithium ion cell function, during the first charge of a cell side reactions with the electrolyte occur at the surface of the anode active material. The breakdown products of these reactions form a passivation layer on the anode active particles, called the Solid Electrolyte Interface (SEI).[8–13] When the SEI is fully formed, it prevents any further side reactions between the electrolyte and the anode active materials. During the formation

of the SEI layer, lithium ions *irreversibly* form into reaction products instead of *reversibly* intercalating into the anode material. For graphite anodes used in the present study, this loss amounts to ~5-8% of the lithium ions inserted on the first cycle (as measured by half-cell data). As a result, the amount of lithium that can be de-intercalated from the anode upon discharge is less than what was initially intercalated, *resulting in a decrease in the amount of reversible lithium in the cell.*

The LiCoO₂ cathode used in the present study, on the other hand, has a first cycle capacity loss of ~2-3% (as measured by half-cell data), meaning it can intercalate ~97-98% of the lithium ions that were de-intercalated from it on the first charge. Since the loss of reversible lithium during anode SEI formation is greater than the loss of cathode capacity, *it can be expected that the amount of reversible lithium in the cell will be less than that required to fully intercalate the cathode with lithium upon discharge.*

As shown in Figure 1d, the electrochemical potential of the anode increases rapidly to 0.785 V vs. Li/Li⁺ at the end-of-discharge while the electrochemical potential of the cathode remains high in its normal range at 3.789 V vs. Li/Li⁺. This increase in anode potential indicates that the anode is mostly depleted of reversible lithium while the cathode is *not* fully intercalated with lithium at the end of discharge. This is consistent with the expectation that the cell will not have enough reversible lithium to fully intercalate the cathode at the end of discharge in this conventional cell. After four cycles, the cell charges and discharges with nearly the same capacity during cycle 5 as shown in Figure 1e-f, indicating that all passivation layers have formed and the cell is cycling stably. If anode materials with higher first cycle loss than graphite such as silicon[14–21] and

germanium[22–25] are used in alternative cells, the initial loss of reversible lithium is more dramatic.

1.3 Safety risks associated with transporting and storing lithium ion batteries

During storage or shipment of user-inactive lithium ion batteries, manufacturer defects or abuse of lithium ion cells within a battery can lead to a thermal runaway event.[26–42] Thermal runaway results from several internal exothermic reactions that are initiated by overheating of a cell that can result from internal short, rapid charge/discharge, overcharge, external heating, or other abuse condition. The exothermic reactions include SEI decomposition, electrolyte reaction with the electrodes, decomposition of active materials and electrolyte decomposition.[26–39] Thermal runaway can result in a dangerous fire or explosion that can propagate to other nearby cells.[40,41] In the case of a large battery consisting of many lithium ion cells, or many batteries stored together, propagation can lead to a very dangerous event with severe damage including explosion, fire, and venting of toxic gases.[42] Several research efforts to mitigate safety risks while lithium ion batteries are in a user-*active* state have been reported.[42–65] Internal to lithium ion cells, shut-down separators to prevent ion flow upon overheating,[43,44] cathode coatings to suppress exothermic release,[45–49] non-flammable electrolytes to avoid electrolyte combustion[43,50–56,56,57] and redox shuttle additives to prevent overcharge[43,58–65] have been investigated. External to cells during normal operation, battery management systems (BMS) to avoid abuse of cells, blocking diodes to prevent inadvertent charge or discharge, current limiting fuses to prevent rapid charge or discharge, and bypass diodes to prevent overcharge/overdischarge of a “weak” cell in a battery pack

have all been investigated or are currently used.[42,43] In the case of entering dangerous operating conditions, positive temperature coefficient devices (PTCs) to block or reduce current upon overheating and current interrupt devices (CIDs) to block current in the case of over-pressure have been used or are currently in use.[42,43]

1.4 Risk vs. State of charge and potential of state of charge limitations to increase safety

As the state of charge of a lithium ion cell increases, it has been shown that the risk of thermal runaway correspondingly increases. In the case of nail penetration, Reichert *et al*[33] showed that for NCM-LCO 18650 cells, as state of charge decreased, the onset time for thermal runaway increased (or never occurred for 0% and 25% state of charge) as shown in Figure 2. Additionally, the max temperature increase of the cells decreased substantially at 0% state of charge (see Figure 3) and the max pressure rate increase decreased as state of charge decreased (see Figure 4).

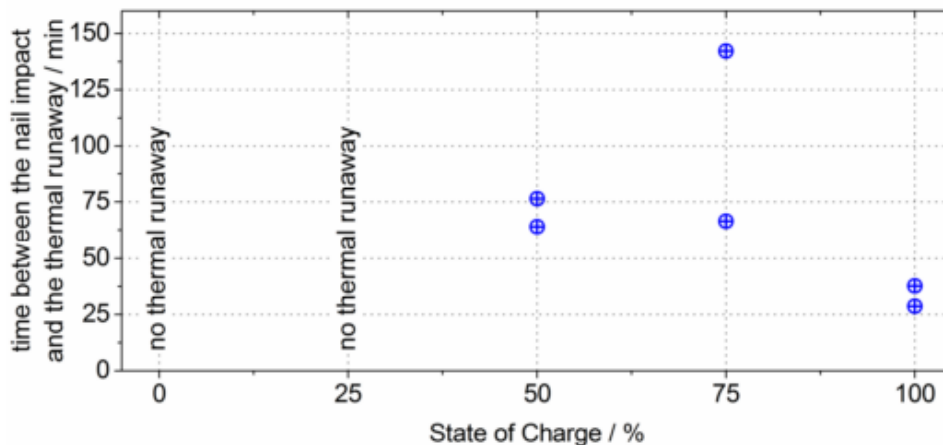


Figure 2: Time elapsed between nail impact and thermal runaway event for NCM-LCO/Graphite cells at difference SoC. *Reproduced from ref [33] with permission from the Electrochemical Society

Golubkov *et al*[34] showed with accelerate rate calorimetry (ARC), thermal stability of 18950 NCA/Graphite and LFP/Graphite cells increases as the state of charge

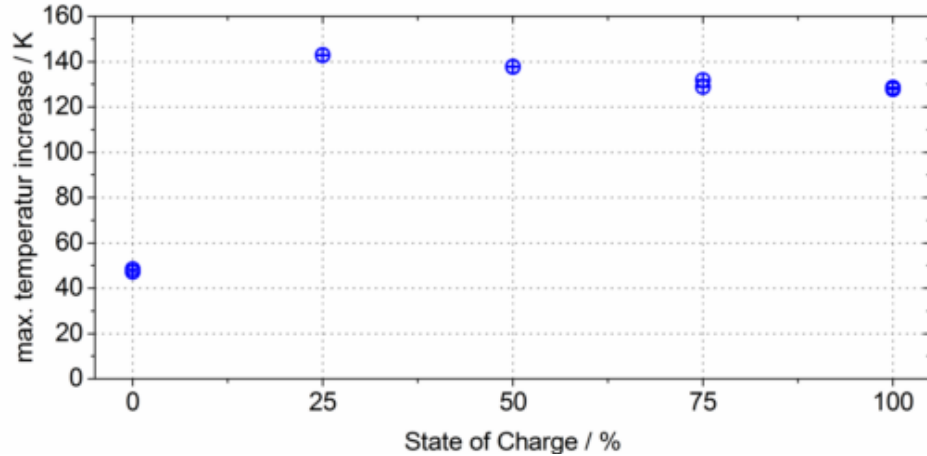


Figure 3: Max temperature increase for NCM-LCO cells at difference SoC. *Reproduced from ref [33] with permission from the Electrochemical Society

decreases. As shown in Figure 5a, the onset temperature of thermal runaway in NCA/graphite 18650 increases as the state of charge of the cell decreases. At a 0% state of charge, the cell must be heated to ~ 160 °C to initiate thermal runaway, whereas at 50% state of charge, the cell must be heated to only ~ 140 °C to initiate thermal runaway. As shown in Figure 5c, the amount of gas evolved also substantially decreases as the state of charge decreases when the cell is heated. Lastly, as shown in Figure 5d, the content of H_2 increases to $\sim 20\%$ of evolved gas when the state of charge is $\geq \sim 25\%$. It is well known that H_2 gas is highly flammable. The content of CO gas, a poison, increases to about 40% when

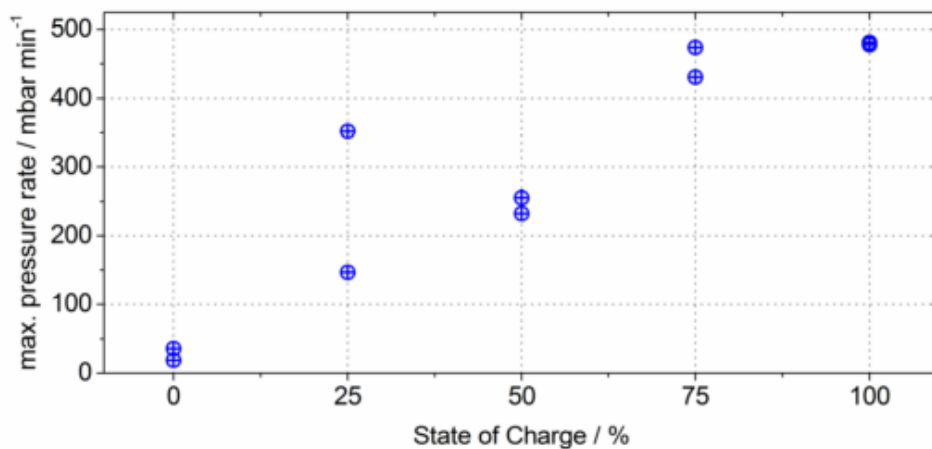


Figure 4: Max pressure rate increase for NCM-LCO cells at difference SoC. *Reproduced from ref [33] with permission from the Electrochemical Society

the state of charge is $\geq 50\%$. At 0% state of charge, the only component of the gas is CO_2 , which is far more benign than CO or H_2 . Thus, 18650 NCA/graphite cells can be considered much safer in lower states of charge, especially 0% state of charge.

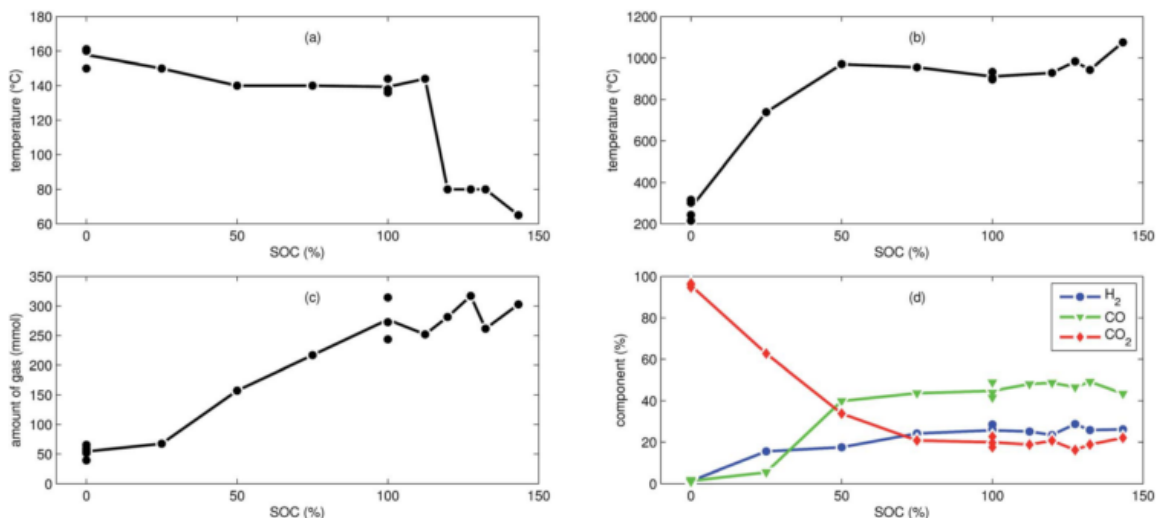


Figure 5: Characteristic thermal runaway parameters from Accelerated Rate Calorimetry on NCA/graphite cells. (a) Onset cell temperature of thermal runaway. (b) Maximum cell temperature. (c) Amount of produced gas (d) Main detected gas components. [A.W. Golubkov, S. Scheickl, R. Planteu, G. Voitc, H. Wilsche, C. Stangl, G. Fauler, A. Thaler, V. Hacker, *RSC Adv.* 5 (2015) 57171–57186.] - Published by the Royal Society of Chemistry.

Golubkov *et al*[34] also performed ARC on LiFePO_4 /graphite cells and found similar results to the NCA/graphite cells. Figure 7a shows the onset temperature for thermal runaway in LiFePO_4 /graphite 18650 cells increases from 80 °C to 200 °C when the charge state decreases from 125% to 25%. As with NCA/graphite cells, the maximum temperature observed in LiFePO_4 /graphite cells during an ARC test decreased as the state of charge decreased as shown in Figure 7b. In contrast to NCA/Graphite cells, LiFePO_4 /graphite evolved more gas at 0% state of charge than in any of the other charge states as shown in Figure 7c. However, it was 100% CO_2 , a fairly benign gas. Similar to NCA/graphite cells, the percentage of H_2 gas and CO gas increased as the state of charge of LiFePO_4 /graphite cells increased. Thus, it can be concluded that like NCA/graphite cells, for LiFePO_4 /graphite, lower states of charge are safer than high states of charge.

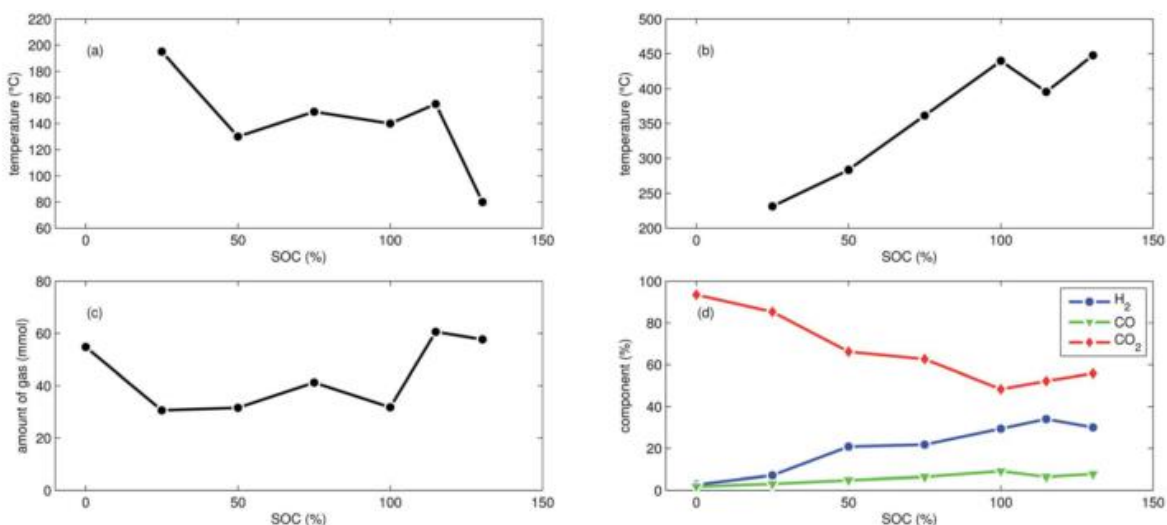


Figure 7: Characteristic thermal runaway parameters from Accelerated Rate Calorimetry on LiFePO₄/graphite cells. (a) Onset cell temperature of thermal runaway. (b) Maximum cell temperature. (c) Amount of produced gas (d) Main detected gas components. [A.W. Golubkov, S. Scheikl, R. Planteu, G. Voitic, H. Wiltse, C. Stangl, G. Fauler, A. Thaler, V. Hacker, RSC Adv. 5 (2015) 57171–57186.] - Published by the Royal Society of Chemistry.

One of the primary reasons for the increased stability at low states of charge is the increase in thermal stability of common cathode materials. Two important facets of the stability of the cathodes is their exothermic heat release and oxygen release. Exothermic

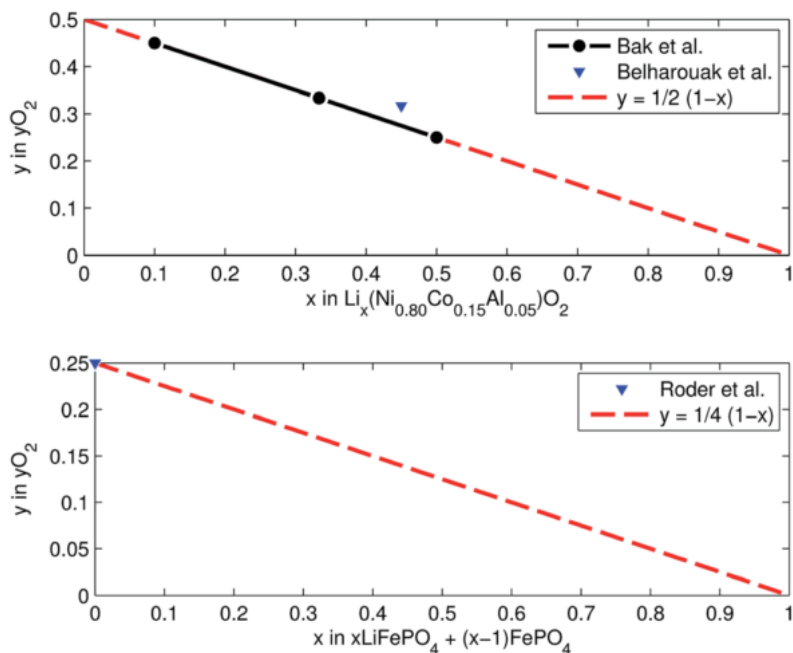


Figure 6: Oxygen release at different lithiation states: (a) NCA powder upon heating to 600 °C and (b) LFP powder in electrolyte upon heating to 350 °C. [A.W. Golubkov, S. Scheikl, R. Planteu, G. Voitic, H. Wiltse, C. Stangl, G. Fauler, A. Thaler, V. Hacker, RSC Adv. 5 (2015) 57171–57186.] - Published by the Royal Society of Chemistry.

heat release adds to the thermal runaway feedback loop and oxygen release provides fuel for combustion reactions. Golubkov *et al*[34] summarized past work with a simple linear model (see Figure 6a and b) describing oxygen release from NCA and LiFePO_4 when heated at different states of charge. As shown in Figure 6a and b, both NCA and LiFePO_4 release less oxygen in higher states of lithium intercalation (discharged state in lithium ion cell). The same result has been shown for $\text{Li}_x\text{Ni}_{1/3}\text{Mn}_{1/3}\text{Co}_{1/3}\text{O}_2$ [66] and LiMnPO_4 .[67] In addition to reduced exothermic release at higher states of lithium intercalation (corresponding to a low state of charge in a full lithium ion cells), Baba *et al*[68] showed with differential scanning calorimetry (DSC) that LiCoO_2 , one of the most commonly used cathode materials, undergoes substantially less exothermic heat release in higher states of lithium intercalation(See Figure 8). The same result has been shown for LiMnPO_4 .[67] and $\text{Li}_x\text{Ni}_{1/3}\text{Mn}_{1/3}\text{Co}_{1/3}\text{O}_2$.[66] Thus, cathode materials undergo significantly less exothermic reaction and release less oxygen when in a high state of lithium intercalation which contributes significantly to the increased safety of cells at low states of charge.

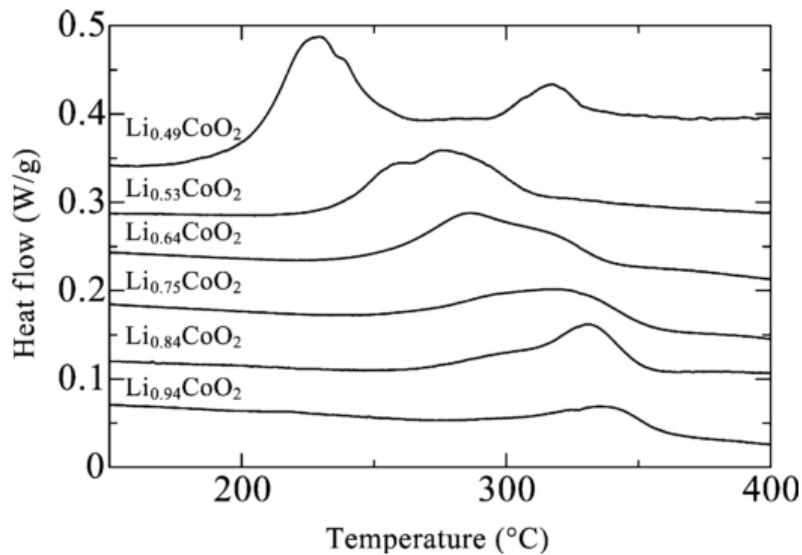


Figure 8: DSC profiles of chemically delithiated Li_xCoO_2 at a heating rate of $5\text{ }^\circ\text{C}/\text{min}$ *Reproduced from [Y. Baba, S. Okada, J.I. Yamaki, *Solid State Ionics* 148 (2002) 311–316.] with permission from Elsevier

Other factors contributing to the increase in safety of cells with the decrease in state of charge is less heat produced by an internal short (due to less stored charge energy), decrease in exothermic release upon heating from de-lithiated graphite anodes[69], and less lithium metal exposed when the graphite anode combusts.[34] *Overall, all of the described factors contribute to lithium ion cells generally being much safer when in a low state of charge. Therefore, state of charge limitation on lithium ion batteries to be transported could be a viable approach to safer transport provided state of charge determination is possible in the field. However, as will be discussed in the following section, there is currently no accurate, reliable and rapid way to determine the state of charge of a lithium ion cell in the field.*

1.5 Challenges facing state of charge limitations

1.5.1 Challenge of determining the state of charge of a lithium ion cell

While some efforts have been made to yield a rapid, cheap and accurate way to determine the state of charge of lithium ion cells[5,70,71], there is currently no widely accepted method to rapidly and accurately determine the state of charge of a cell in the field. Measuring the open circuit voltage of a cell is insufficient, as between 10-90% state of charge, the open circuit voltage will vary little (e.g. 0.4 V in LiCoO₂/MCMB cells). Additionally, cell history, ambient conditions and cell construction parameters/materials can all effect the open circuit voltage for a given state of charge of a cell.[5] Thus, implementing state of charge limitations on lithium ion cells to be shipped or stored will rely on trust of manufacturers to comply with them. When it comes to large assets and especially risk of human life, however, trust is not sufficient. Rapid, accurate assessment

of a safe state of charge of a cell in the field is a necessity to insure compliance with a state of charge limitation.

1.5.2 Overdischarge risk of state of charge limitation

In addition to state of charge determination, discharging lithium ion cells to low states of charge increases the risk of them entering an overdischarged state during transport due to self-discharge[72–84] or cell mismanagement. Such an overdischarged state risks damaging internal components of the cells (most significantly dissolution of the copper current collector of the anode[85–91], as will be discussed in more detail in section 1.6.2) which can cause significant degradation in the cell’s recharge performance or render it unusable.

1.6 Near zero volt storage

1.6.1 Potential of zero volt storage for inactive safety and charge limitation controllability enhancement

If lithium ion cells could be modified in such a way that complete discharge to a near zero volt state of charge did not damage internal components, the motivation of rendering lithium ion batteries safe to transport and resolving both the implementation challenge of state-of-charge limitations and overdischarge risk could be realized. In a representative scenario, after a cell is discharged to a low state of charge, an appropriately sized resistor (i.e. one which won’t discharge the cell too rapidly or too slowly) can be applied to the cell to further discharge it towards the ideal case of no stored charge energy and a cell voltage of near zero volts. As summarized in sections 1.4 and 1.5, the very low state of charge will increase safety of the cell by increasing onset temperatures of exothermic reactions and preventing a rapid discharge resulting from an internal or external

short (due to near zero potential difference between the electrodes). Additionally, the state of charge could be easily checked by a handheld voltmeter since the cell voltage will be near zero volts. Thus, discharging and storing lithium ion cells at a near zero volt state of charge has the potential to significantly decrease associated safety risks and allow for highly controllable implementation of a state of charge restriction on lithium ion batteries that are to be transported or stored.

The key to implementing such a promising approach in the near future is to accomplish near zero volt storage resilience of lithium ion cells with little to no modification to a conventional design. This would be a stark contrast to past approaches that require modifications to cell design and use of unconventional materials that can reduce cell quality and performance while increasing cost. Thus, an alternative approach that requires no modification to conventional cell construction parameters or use of unconventional materials will need to be developed.

1.6.2 Degradation mechanisms to overcome during overdischarge of conventional cells to near zero volts

Understanding the electrode potential behavior during cell overdischarge towards near zero volts by an applied fixed load can lead to identification of an alternative approach to developing lithium ion cells that are tolerant to near zero volt storage. As an example, a conventional 12 mAh LiCoO₂/graphite pouch cell, which has been conditioned for 5 cycles, has a fixed load of 2.5 kOhm applied to the cell by an Arbin cycler after discharge to 3.0 V to simulate a resistor placed between the leads of the cell, similar to what could be achieved in a practical storage or transportation situation. The value of the applied load is designed so that at 3.0 V cell voltage, the initial current would be equivalent to a C/10 (1.2 mA) discharge rate. The fixed load step is applied for a total of three days to represent an extended period of near zero volt storage.

3-electrode data for the 5th cycle during discharge is shown as a function of discharge capacity in Figure 9a and a function of time in Figure 9b. As shown in Figure 9a and b, during the C/10 discharge (first ~12 mAh or ~10 hours) the cell current is constant and the electrode potentials exhibit their normal discharge behavior. At ~12 mAh, (~10 hours), the cell reaches 3.0 V and the fixed load (2.5 kOhm) step is initiated and the cell undergoes a transient period as it discharges to near zero volts. As shown in Figure 9b, the cell voltage decreases to <0.4 V in the first hour which under the fixed load corresponds to a cell current of <0.16 mA. During the first hour the cathode potential decreases initially, but then recovers to ~3.6 V vs. Li/Li⁺ while the anode potential increases rapidly up to ~3.4 V vs. Li/Li⁺. Both electrodes plateau at these potentials for ~2 hours. The cathode then decreases and asymptotes to within 10 mV of anode potential at ~3.2 V vs. Li/Li⁺. Once the cell reaches this point, the cell voltage is <10 mV and the cell current is <4 μA (C/3000) which is considered to be a quasi-equilibrium state. The quasi-equilibrium state remains for the remainder of the 3-day step under fixed load. The electrode potentials slightly decrease during this time by about 0.1 V to ~3.1 V vs. Li/Li⁺ and the cell voltage decreases to ~3 mV.

The initial decrease and subsequent recovery of the electrochemical potential of the cathode during the transient period may not be expected, but similar results have been observed in prior work.[92] The decrease and recovery of the cathode potential may be due to the effects of double layer capacitance or several non-ideal effects such as changing

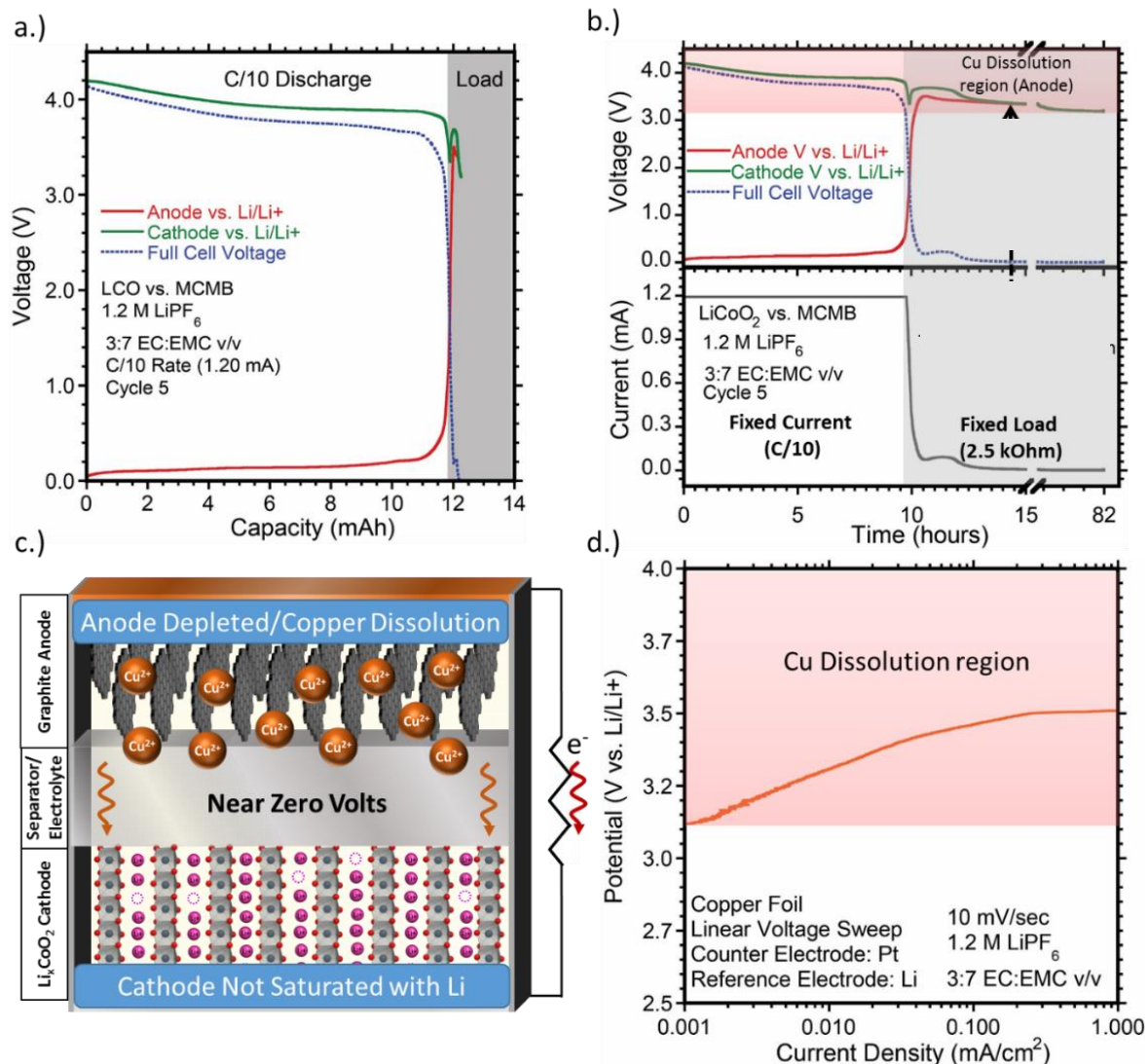


Figure 9: (a) 5th cycle discharge and fixed load step (grey shading) cell voltage and electrode potentials plotted vs. cell capacity. (b) 5th cycle discharge and fixed load step (grey shading) cell voltage and electrode potentials plotted vs. time. Red shading represents anode potential range in which copper dissolution occurs. (c) Schematic of cell function in the near zero volt condition. Orange arrows represent copper ion flow. Red arrow represents electron flow through external circuit. (d) Linear sweep voltammogram of copper foil. Red shaded region represents potential range in which copper dissolution occurs.

ionic activities, the effects of reaction rate constants or non-faradaic processes as the cell current decreases. Regardless, the cathode potential remaining in its normal range for several hours and intercalating 0.5 mAh of additional lithium at ~3.6 V vs. Li/Li⁺ during the fixed load step supports that the cathode can still intercalate more lithium in its normal potential range after the normal discharge.

The rapid rise in potential of the anode when the fixed load is applied is consistent with the anode being mostly depleted of intercalated lithium ions and highly polarizable at the end of discharge. The major concern with the rise in anode potential is the onset of copper dissolution of the copper into the electrolyte can occur as depicted in Figure 9c.

Figure 9d is a representative linear sweep voltammogram which quantifies the copper dissolution process. The test uses a polished copper working electrode, polished platinum counter electrode and lithium reference electrode. The potential of the copper foil is swept in the positive direction at 10 mV/s from the open circuit voltage (OCV) of ~ 3.1 V vs. Li/Li⁺. As can be seen, an oxidative current from copper foil initiates at a potential of ~ 3.1 V vs. Li/Li⁺ and reaches current densities of ~ 0.01 mA/cm² at 3.3 V vs. Li/Li⁺, ~ 0.1 mA/cm² at 3.4 V vs. Li/Li⁺ and ~ 1.0 mA/cm² at 3.5 V vs. Li/Li⁺. The oxidative current is primarily attributed to copper ions stripping off the surface of the copper foil resulting in soluble cations, consistent with previous studies.[89,93–95]

It is important to note here that determined values of the onset potential for copper dissolution can vary since the choice of an oxidative current density threshold is arbitrary and non-faradaic process can contribute to the oxidative current. Additionally, the exact value of the onset of copper dissolution can be affected by factors such as ambient conditions and electrolyte composition. In the present work, 3.1 V vs. Li/Li⁺ will be assigned for interpretation purposes as below this value, no oxidative current was observed in the linear sweep voltammogram in Figure 9d, and therefore, no copper dissolution is expected to be occurring.

The adverse effects from copper ions being present in the electrolyte will lead to side reactions with the electrolyte, competitive reduction processes with lithium ions, and

copper dendrite formation which can lead to internal shorting. Each of these effects can cause significant damage to the cell and reduce its recharge capacity and performance.[85–91] *Thus, for cells to be tolerant to near zero volt storage, cell design must be modified or different materials used to avoid the copper dissolution degradation mechanism.*

1.7 Past approaches to near zero volt storage tolerance and overdischarge protection

There have been several past approaches to make lithium ion cells resilient to the general case of overdischarge. Many approaches to general overdischarge protection can be applied to a near zero volt storage scenario. However, approaches to protect a cell from overdischarge to a *negative* cell voltage, such as redox shuttle additives,[60,65] cannot be applied to a near zero volt scenario and thus are not considered.

Many past approaches to near zero volt storage or overdischarge protection have made use of predicting a zero crossing potential (ZCP)[96–99] at which the electrode potentials meet when a cell is discharged to zero volts. Although rigorous descriptions of how the ZCP is predicted are absent, examination of prior art suggests that the ZCP has been predicted based on attempting to match and extrapolate half-cell (vs. Li metal) constant current discharge profiles of each electrode. For fixed load storage of cells at near zero volts, the predicted ZCP is regarded as the potential of the electrodes throughout the duration of the fixed load storage period.

The ZCP method is unlikely to accurately represent the true transient behavior of the electrode potentials when a fixed load is applied. Loss due to SEI formation, Incomplete intercalation of the anode (due to excess anode used to prevent plating), electrode composite variation and any other non-ideal effects that arise can be difficult to

account for in predicting the behavior of the electrode potentials during a near zero volt state. Additionally, in a practical near zero volt storage situation where a fixed load is applied, the cell current decreases to very low levels (e.g. $\sim C/1,000$ - $C/10,000$ rate) when the cell voltage approaches zero volts. As a result, half-cell discharge profiles resulting from more typical, constant discharge rates (e.g. $C/10$, $C/20$) are not good predictors of the behavior of the electrode potentials when the cell voltage (and cell current) approaches zero. Lastly, under fixed load storage at near zero volts, the concept of a ZCP is not physically accurate as the electrode potentials do not ever cross each other and the cell never actually reaches zero volts. Rather, the electrode potentials asymptote towards an intermediate potential and the cell gets to a near zero volt state. Thus, use of a ZCP prediction is insufficient for accurately characterizing electrode behavior during near zero volt storage under fixed load. Instead, approaches to near zero volt storage should make use of reference electrode measurements to accurately and definitively characterize the behavior of the electrode potentials.

1.7.1 Anode current collector replacements

One strategy to avoid copper dissolution in a near zero volt state has been to employ alternative anode current collectors which do not undergo dissolution at higher potentials vs. Li/Li^+ . Voltammetry studies, similar to the one shown in Figure 9d, have been done previously[93,94,100,101] on potential current collector replacement materials. The voltammetry studies can determine the electrochemical stability of a current collector replacement in the potential range of interest. Potential current collector replacements must demonstrate increased stability at high potentials vs. Li/Li^+ (i.e. $> 3.5\text{V}$) as well as low potentials vs. Li/Li^+ (i.e. 5-1000 mV). Some metals, like aluminum,^{85,94-98} that are stable

at high potentials vs. Li/Li^+ will alloy with lithium at low potentials in conventional LiPF_6 electrolytes. This would lead to pulverization of the anode current collector during normal cycling. Titanium, Titanium alloys, Nickel, Nickel alloys and stainless steel have all been patented[96,97] as potential current collector replacements because they meet the high and low potential stability requirements.

Titanium foils are showing promise in commercially developed near zero volt storage capable cells[107] as an anode current collector. However, tradeoffs exist with titanium foils in that they are typically thicker than standard copper foils and can cost substantially more due to increased extraction and processing costs.[108] These tradeoffs can reduce both the volumetric and gravimetric energy density of the cells while increasing cell cost. Additionally, bulk titanium is more than an order of magnitude more resistive than copper, which may limit the rate capability of cells, especially in large format or wound cells. Despite these tradeoffs, lithium ion cells with titanium anode current collectors represent the main competing zero volt tolerant lithium ion cell technology.

Carbon nanotube[109,110] and graphene free-standing electrodes may also be potential current collector replacements due to their high chemical stability. Anodes made purely of other carbon allotropes have already been demonstrated to generate cells that can tolerate fixed load, near zero volt[111] and overdischarge[112] conditions. However, lower bulk electrical conductivity, coulombic efficiency issues from SEI formation on nanoscale surface, and higher cost are disadvantages of the nanocarbon-based current collectors compared to copper.[110]

In addition to replacing copper current collectors with a more stable material, another strategy to protect cells during near zero volt/overdischarge conditions is to

passivate copper current collectors and prevent dissolution at high potentials vs. Li/Li⁺. One approach is the use of succinonitrile as an electrolyte additive to passivate the copper current collector and prevent its corrosion.[89] However, succinonitrile additive has also been shown to significantly increase the impedance of cells during cycling[113] which can limit rate capability. Formation of nitrile compounds on the surface of copper foil before electrode fabrication[114] has also shown promise, but it is unclear what effect a nitrile coating might have on the charge transfer resistance between the copper current collector and anode composite. Future approaches to inhibit corrosion of the copper current collector, with minimal effect on battery performance, may present a viable pathway to near zero volt storage resilient cells.

1.7.2 Secondary electrode materials with intermediate potentials

Use of secondary active materials in the cathode that have a discharge potential below the copper dissolution potential can protect a cell in a near zero volt scenario. Such a secondary material can force the cathode potential to be less than the copper dissolution potential during overdischarge. In a near zero volt storage situation, this effect can keep the anode potential less than the copper dissolution potential, thus preventing copper dissolution. Li₂MoO₄[92,99,115] as an additive to a LiCoO₂ cathode has been demonstrated to work in this regard and protect cells during overdischarge. Several other secondary cathode materials, like LiS₂ and V_xO_y, with the appropriate intercalation potentials exist and have been patented.[92,116]

Use of secondary active materials in the anode with intermediate charge/discharge potentials has also been patented[96] as a method to protect cells during overdischarge. Specifically, the secondary active material would have an intermediate de-intercalation

potential that is greater than the potential where the cathode can begin to degrade and less than the copper dissolution potential. The secondary active material would contain additional active lithium that, upon overdischarge, would begin de-intercalating lithium as soon as the graphite was depleted of lithium. In concept, this will keep the anode potential less than the copper dissolution potential during overdischarge. It will also prevent the cathode potential from decreasing to the point where it can begin to degrade. The stability of the many suggested secondary materials in the low anode potential range during normal operation, namely transition metal oxides, is a major operational concern in pursuing this approach.[117]

Overall, no widely available validation or experimental data exists on many of the patented secondary active materials. Thus, the resilience to multi-day near zero volt storage and impact on performance during normal operation is unclear. Additionally, adding an amount of secondary active materials with intermediate charge/discharge potentials will likely decrease cell energy density by lowering the average discharge voltage and/or electrode specific capacity.

1.7.3 Secondary cathode materials with high first cycle loss

Another strategy towards fabricating cells with resilience to overdischarge is to generate a lithium ion cell with a higher ratio of reversible lithium to cathode capacity by using high first cycle loss cathode additives. Li_2NiO_2 can deliver ~300 mAh/g of lithium on the first charge and then its decomposition products can only intercalate ~70-100 mAh/g when the discharge is stopped at 3.0 V vs. Li/Li^+ . [118–120] Use of Li_2NiO_2 as a secondary cathode material has been shown to protect cells from overdischarge.[121] The higher ratio of reversible lithium to cathode capacity leads to the anode not being depleted and the

cathode approaching full intercalation at the end of discharge. Additionally, the breakdown products of Li_2NiO_2 have a lower discharge potential and act as a secondary active material in the cathode like those described in section 1.7.2. As a result, the anode potential does not reach the copper dissolution potential during overdischarge.

Although a promising approach, Li_2NiO_2 as a secondary active material in the cathode has been shown to lead to substantial gas evolution during initial charging and at high temperatures.[120] Gas evolution can cause severe and potentially dangerous swelling of cells during the conditioning process or during normal use. It has also been shown that Li_2NiO_2 additive will increase the fade rate of a LiCoO_2 /graphite cell.[90] Additionally, the breakdown products of Li_2NiO_2 will likely decrease the energy density of the cell due to their lower capacity and discharge voltage compared to many common cathode materials like LiCoO_2 .

Thus, operational concerns exist regarding the use of Li_2NiO_2 as a secondary active material in the cathode to protect the cell during overdischarge. These concerns include potential for substantial gas evolution or side reactions, effect on cycling stability, and impact on energy density. Other secondary active materials like Li_6CoO_4 [122] or additives like Li_2O [123] that have a high first cycle charge/discharge capacity ratio may protect cells during overdischarge in the same manner as Li_2NiO_2 . However, they will have a similar potential impact on energy density and may have other tradeoffs or operational concerns.

1.8 Opportunities for an improved approach to near zero volt storage tolerance

In light of the numerous anticipated performance and cost tradeoffs of past and current approaches to near zero volt storage tolerance, it is highly desirable to identify an

alternative method that avoids significant tradeoffs in performance and cost of lithium ion cells. Such a method would increase implementability of near zero volt tolerant cells which can impact the rapid and widespread adoption of lithium ion cells that are safer to transport. In the present dissertation work, the method of modifying the amount of reversible lithium during lithium ion cell construction to prevent high anode potential during a near zero volt state and render the cell tolerant to that state, with no other modifications to cell design, is studied and its feasibility is demonstrated.

2. Dissertation Overview

The goal of this work is to develop an approach to enabling near zero volt storage tolerance in lithium ion cells that makes use of only conventional materials and typical cell construction parameters. Identified approaches are evaluated with electrochemical measurements to study the effect of each approach in preventing damaging conditions inside cells during near zero volt storage and understand the underlying electrochemical processes occurring during near zero volt storage. Additionally, post-mortem materials analysis is utilized to study active material degradation mechanisms. Construction and testing of prototype lithium ion cells is used to test the effects of near zero volt storage on long term and high rate cycling in lithium ion cells modified to tolerate near zero volt storage.

The dissertation is organized into five primary research focus areas based on impact prioritization of research tasks. The following numbered list contains the primary research focus areas.

1. Applying reversible lithium management to lithium ion cells using anode-pre-lithiation
2. Study cathode degradation mechanisms during over-insertion of lithium into LiCoO_2 cathode materials and study the effect of a nanoscale AlPO_4 coating on stabilizing the LiCoO_2 against lithium over-insertion
3. Scaling reversible lithium management approach to X3450 pouch cells using a bath lithium addition technique

4. Using a high-energy density, high first cycle loss lithium rich cathode material to enable near zero-volt storage tolerance in lithium ion cells
5. Study of Al_2O_3 coating on CNT paper current collectors to reduce the irreversible losses that inhibit their implementation as a chemically stable anode current collector that can enable near zero volt storage tolerance

Chapter 3 discusses standard experimental techniques used for fabrication of lithium ion cells, use of reference electrodes in lithium ion cells, standard cycling protocols, and materials analysis techniques used. Chapter 4 describes research into reversible lithium management to enable near zero-volt storage tolerance in lithium ion cells with anode pre-lithiation as the reversible lithium management technique. Chapter 5 describes research into use of a high energy density lithium rich cathode material with high first cycle loss to enable near zero volt storage tolerance. Chapter 6 discusses research into using a nanometer scale Al_2O_3 coating on CNT current collectors to reduce their irreversible losses during cycling which prevent their effective implementation as anode current collector replacements. Chapter 7 discusses dissertation conclusions, Chapter 8 contains supplemental information for Chapter 5, Chapter 9 contains supplemental information for Section 4.9, and Chapter 10 discusses an optical cell study on lithium deposition on graphite anodes. Chapter 11 contains publications, patents and awards achieved during the dissertation work, and Chapter 12 contains references.

3. Standard Experimental methods

3.1 Lithium ion battery standard fabrication

Lithium ion battery electrodes are prepared via a slurry coating process to coat the active material composite onto a current collector (typically a metal foil). In short, the components of the electrode composite, including the active material, a conductive additive (usually graphite, amorphous carbon, or other carbon allotrope) and binder material (often polyvinylidene fluoride (PVDF)) are mixed into an organic solvent (most commonly N-methyl pyrrolidone (NMP)) to form a slurry. The slurry is then cast onto a current collector (typically aluminum foil for the cathode and copper foil for the anode) by a doctor blade on one or both sides of the foil. The composite is dried in a vacuum oven, then calendared to compress the composite. Electrodes are then punched from the prepared composites and assembled into cells.

The active materials used in the cathode and anode have a defined specific capacity, which is the amount of lithium they can reversibly intercalate/de-intercalate per gram of the material over a particular potential range. LiCoO_2 cathode material for instance has a specific capacity of ~ 140 mAh/g when cycled between the potentials 3.0-4.2 V vs. Li/Li^+ . Graphite anode material has a practical specific capacity of 300-330 mAh/g when cycled between 0.005-1.5 V vs. Li/Li^+ . Depending on the mass loading of the composite (mg/cm^2), electrodes will have a corresponding areal capacity (mAh/cm^2).

Cells are assembled in an argon glove box maintained at <1 ppm O_2 and <1 ppm water or in a dry room to minimize water contamination of the cell. An electrolyte solution consisting of a lithium salt dissolved in an organic solvent or combination of organic solvents (1.2M LiPF_6 in 3:7 volume ratio of ethylene carbon (EC) and ethyl methyl carbonate (EMC) is a common formulation) is injected prior to sealing the laminate. An

Arbin BT2000 cycler is used for cycling the cells. For cells with a reference electrode, the cell voltage and the electrochemical potential of each electrode with respect to the reference are measured independently throughout cycling. For testing, pouch cells are compressed between restraint plates as depicted in Figure 10b. A rubber slab was placed on one side of the cell in the restraint plates to ensure even pressure and comply with expansion and contraction of the cell upon cycling. Testing is done at room temperature unless otherwise specified.

3.1.1 Reference electrodes in pouch cells

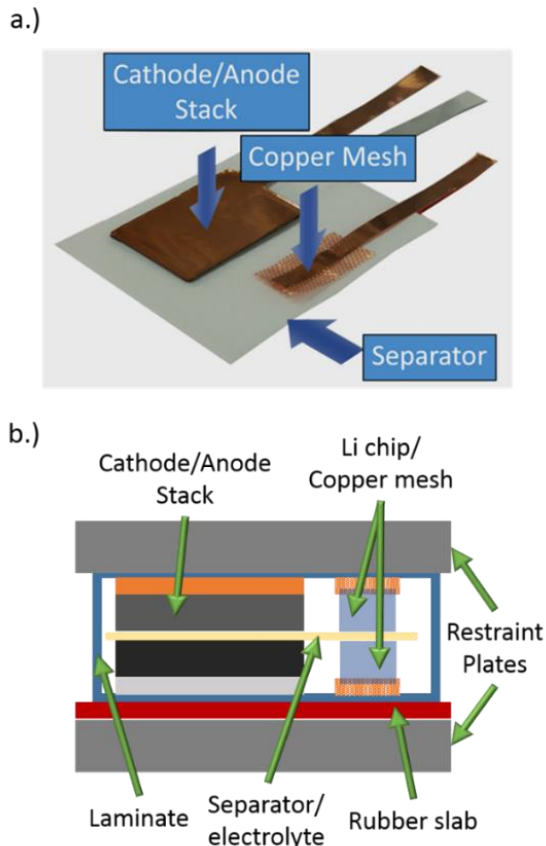


Figure 10: (a) Image of the arrangement of the separator, cathode, anode and reference Li electrode in the pouch cell. (b) Cross sectional schematic of assembled pouch cells placed between restraint plates for testing. *Reproduced from Ref [173] with permission from the Royal Society of Chemistry

A lithium metal reference electrode is used to measure the individual electrochemical potential of the cathode and anode during cycling. The design used in the present work, as shown in Figure 10a and b places the reference electrode on either side of the cathode/anode stack in the pouch cell, which is a setup that has been used successfully by others.[89,90] As shown in Figure 10b, the reference electrode used in this study consists of a lithium metal foil pressed onto copper mesh that is ultrasonically welded to a copper tab. The lithium-Cu mesh is placed on both sides of the separator to ensure good contact with the electrolyte soaked separator when the cell is compressed between restraint plates during testing, as depicted in Figure 10b.

3.1.2 Arbin Cyclers and cycling protocols

Arbin cyclers are capable of constant current cycling by application of a varying potential according to equation 5, often done in terms of C-rate (1C = complete charge/discharge in 1 hour, 2C = complete charge/discharge in 30 minutes, etc.). The cyclers can also perform constant voltage by applying a varying current according to equation 6, the simplified Ohms's law. . The cyclers can also applied a fixed load, such as would be accomplished by an applied resistor, by maintaining R constant according to equation 6.

$$V = IR \tag{6}$$

The Arbin cyclers also have auxiliary voltage measurements, which can be used to individually measure the voltage between any chosen electrodes. In the case of a cell with a reference electrode like that shown in Figure 10, the potential difference between all three electrodes can be measured independently. The voltage is measured by applying a high

impedance (about 10 GOhm) between the electrode and measuring the resulting current flow. The magnitude of the current is <1 nA, so the resulting perturbation of the electrochemical system is negligible.

3.1.3 Materials Analysis Techniques

Several materials analysis techniques are used for pre- and post-processing and well as pre-cycling and post-mortem. The techniques include;

- **Scanning Electron Microscopy (SEM)** for 2D visualization of micro, meso and nanoscale features of materials
- **X-ray Diffraction (XRD)** for examining the crystal structure of cathode and anode active materials to monitor changes or index crystal structure. Also used to examine the packing of carbon nanotube bundles
- **Raman Spectroscopy** for analyzing phonon modes of materials, primarily to characterize defects in carbon nanotubes

4. Reversible lithium management by anode pre-lithiation of LiCoO₂/MCMB lithium ion cells as an alternative approach to near zero volt storage tolerance

Based on the discussion in section 1.6 and 1.7 it can be expected that anode pre-lithiation prior to cell assembly will increase the amount of reversible lithium in a cell, which should change the behavior of the electrode potentials during near zero volt storage. Hypothetically, a cell having more reversible lithium than necessary to fully lithiate the cathode upon discharge will prevent the anode potential from increasing to the copper dissolution potential upon fixed load discharge to near zero volts. If the amount of pre-lithiation is minimal, damage to the cathode, which can result from a low cathode potential during near zero volt storage,[96] can also be minimized or mitigated. Thus, anode pre-lithiation is a potentially effective approach to realize lithium ion cells that are highly tolerant to near zero volt storage.

Anode pre-lithiation does not introduce unconventional materials or necessitate change in the battery construction parameters, so such an approach can avoid the anticipated trade-offs of the current and past approaches to near zero volt storage tolerance described in section 1.7. Additionally, anode pre-lithiation in concept could be applied to a range of different active material combinations, since there are no operational concerns related to secondary active material stability or reactions with the primary active material.

Pre-lithiation of a graphite anode has also been shown to have the additional benefit of improving performance of conventional cells[124–126] which can help to reduce the cost/benefit ratio. Also, it may eliminate the need for formation cycling,[127] which could serve to reduce manufacturing costs. Thus, addition of anode pre-lithiation to the battery

manufacturing process may not substantially increase the cost of lithium ion cells and could improve general performance in addition to enabling near zero volt storage tolerance.

Additionally, several methods of pre-lithiation with potential for industrial scalability exist. Use of Stabilized Lithium Metal Powder (SLMP)[128] has been shown to be an effective way to pre-lithiate anodes.[129] Electrochemical pre-lithiation such as bath pre-lithiation has also been developed and is a promising option that is scalable.[130–132] Therefore, industrially scalable pre-lithiation methods exist and could be utilized for large scale production.

4.1 Composite Fabrication and cycling protocols

In the present work, the anode was prepared by mixing MCMB's into a slurry with SuperC™ Carbon Black, SFG-6 and PVDF (Solvay) in a 93:0.3:2.7:4 w/w ratio using N-methyl-1-Pyrrolidone (NMP) as the solvent. The PVDF was dissolved first in the NMP and then the conductive additive and active material was added in succession with intermediate mixing steps. All mixing was done with a Thinky AR-100 planetary mixer. The slurry was coated onto a 20 μm thick copper foil using a doctor blade. The composite was then dried overnight in a vacuum oven at 90 °C and then calendared to a composite density of $\sim 1.2 \text{ g/cm}^3$. The cathode was prepared by mixing LiCoO_2 (MTI Corp) into a slurry with SuperC™ Carbon Black, SFG-6 and PVDF (Solvay) in a 90:5:5 w/w ratio. The mixing procedure was the same as described for the anode using N-methyl-1-Pyrrolidone (NMP) as the solvent. The cathode slurry was coated onto a 20 μm aluminum foil using a doctor blade. The composite was dried overnight in a vacuum oven at 90 °C and then calendared to a composite density of $\sim 2.2 \text{ g/cm}^3$.

The cathode is loaded at $\sim 19.3 \text{ mg/cm}^2$ of LiCoO_2 giving an areal capacity of $\sim 2.7 \text{ mAh/cm}^2$. The anode is loaded at $\sim 10 \text{ mg/cm}^2$ of MCMB/SFG-6, giving an areal capacity of $\sim 3.0 \text{ mAh/cm}^2$ (conservatively using 300 mAh/g as the capacity of the active material). The area of the electrodes used is 4.5 cm^2 , giving a total cathode capacity of $\sim 12.2 \text{ mAh}$ and an anode capacity of $\sim 13.5 \text{ mAh}$. The 10% excess of anode capacity compared to the cathode is common practice to reduce the risk of lithium plating on the anode during cycling.[133]

For pouch cells used in the present study, each cycle of experimental cells with a reference electrode utilized a charge step which referenced a cathode potential maximum of $4.2 \text{ V vs. Li/Li}^+$. The potential of the cathode vs. Li/Li^+ was selected as the control for the upper charge limit to ensure that for all experimental 3-electrode cells in the present study, the cathode is charged to the same degree independent of anode variation. The stability of LiCoO_2 is known to be sensitive to the degree which it is charged to, particularly when overcharged.[134] Therefore, utilizing the cathode potential vs. Li/Li^+ as the upper charge limit helps eliminate the degree of cathode charge as a variable affecting the cell's cycling performance. Prototype cells and cells constructed for anode pre-lithiation that do not employ a reference electrode utilized a cell voltage of 4.1 V as the upper charge limit, which is a standard charge cutoff voltage for a $\text{LiCoO}_2/\text{MCMB}$ lithium ion cell. All cells were discharged to 3.0 V cell voltage, which is a standard cutoff value for a $\text{LiCoO}_2/\text{MCMB}$ cell.

4.2 Electrode Asymptotic Potential

As shown in Figure 9b, after a period of time the electrode potentials asymptote to within a small potential difference of each other and no longer change significantly (cell

reaches quasi-equilibrium state). It is therefore convenient to define a single potential that is representative of the minimally varying potential of both electrodes when the cell is in the quasi-equilibrium state. This quantity will be defined herein as the electrode asymptotic potential (EAP) and is described by equation 7 where V_C is the cathode potential vs. Li/Li⁺ and V_A is the anode potential vs. Li/Li⁺.

$$EAP = \frac{V_C - V_A}{2} + V_A \quad \text{when } (V_C - V_A) < \psi \quad (7)$$

The threshold potential difference ψ is chosen to represent when the cell reaches a quasi-equilibrium state in which the electrode potentials no longer change significantly. ψ may have to be defined differently for different cell configurations, fixed load values and active materials used. The value of ψ is chosen to be 10 mV in the present study. Once the electrode potential difference reaches ψ , the EAP drifts by only ~0.1 V during the remaining 66 hours of the fixed load period, indicating that 10 mV is a sufficient choice for ψ in the present case.

4.3 Pre-lithiation process and resulting effect on behavior of electrode potentials during normal charge and discharge

In the present work, a lab-scale pre-lithiation method using a sacrificial cathode is used for demonstration of the approach. A LiCoO₂/MCMB cell is built with a pre-lithiated anode. All cells described herein are fabricated with the same construction parameters described in section 4.1 and 4.2. Figure 11 illustrates the process that was used (in a dry Argon glove box maintained at < 1.0 ppm Oxygen and <1.0 ppm water) to increase the amount of reversible lithium present in a cell for near zero volt storage evaluation.

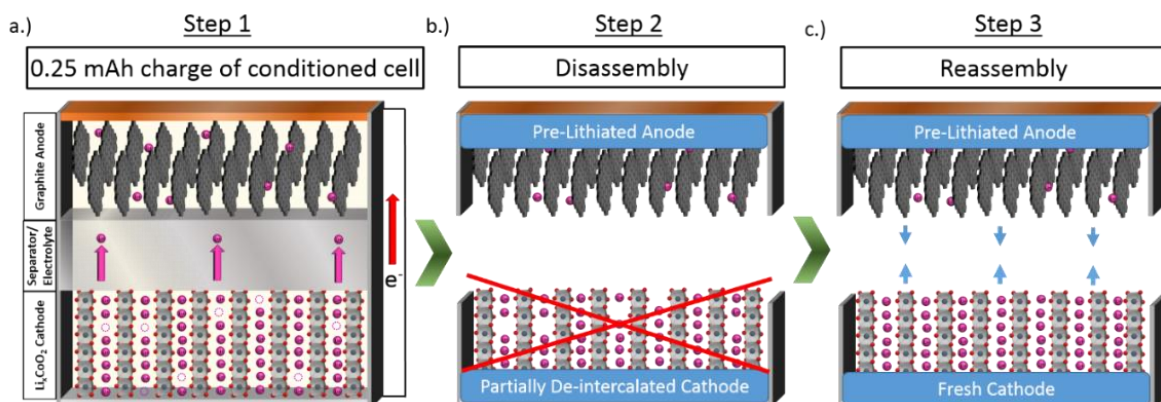


Figure 11: (a) Schematic of 0.25 mAh charge of a conditioned, discharged cell. (b) Schematic depicting disassembly of cell and discarding cathode. (c) Schematic of reassembly for partially lithiated anode with fresh cathode in a new cell. *Reproduced from Ref [173] with permission from the Royal Society of Chemistry

Initially, a LiCoO₂/MCMB pouch cell was constructed (without a lithium reference electrode) and was cycled at a C/10 rate twice from 3.0-4.1 V cell voltage then partially charged by 0.25 mAh as depicted in Figure 11a. At this state of cycling, the SEI layer on the anode will be formed and the MCMB will be partially (~2% of its capacity) lithiated, whereas the cathode is partially depleted of lithium (see Figure 11a).

As depicted in Figure 11b and c, the cell was then disassembled and the partially-lithiated anode was reassembled into a cell with a fresh LiCoO₂ cathode (and a reference electrode in this step – not shown in Figure 11c) which is intrinsically fully lithiated. Since the cathode is fully lithiated, the SEI is already formed on the anode and the anode has some lithium intercalated into it, it can be expected that the resulting cell will have more reversible lithium than is required to fully intercalate the cathode upon discharge. This will be referred to as a reversible lithium excess (RLE) cell condition.

The RLE cell with a lithium reference electrode was conditioned by cycling once at a C/20 rate and then four times at a C/10 rate. The cell was charged and discharged in the same manner as described in section 1.6.2 between 3.0 V full cell voltage and a cathode potential of 4.2 V vs. Li/Li⁺. The first cycle charge and discharge curves of the RLE cell,

including the electrode potentials as measured by a lithium reference electrode, are shown in Figure 12a and b, respectively. It is observed that the increase of the amount of reversible lithium has changed the behavior of the electrodes during normal charge and discharge. At the start of the charge, the anode potential is ~ 700 mV vs. Li/Li⁺ lower than the conventional cell (i.e. 0.374 V RLE vs. 1.105 V conventional) and as a result the cell voltage is ~ 700 mV vs. Li/Li⁺ higher during the initial stage of charge (i.e. 3.46 V RLE vs. 2.77 V conventional). The lower anode potential at the beginning of charge is consistent with it being partially lithiated upon cell assembly. At the end of charge it is important to note that since the anode potential is greater than 0.0 V vs. Li/Li⁺ (i.e. ~ 50 mV), it still has sufficient capacity to intercalate all lithium during the charge. This indicates that despite pre-lithiation of the anode prior to final cell assembly, no lithium plating is likely to be occurring (See Chapter 10).

At the end of discharge, the cathode potential is ~ 350 mV lower in the RLE cell than in the conventional cell (3.360 V RLE vs. 3.789 V conventional). The lower cathode potential at the end of discharge indicates that at this point the cathode is approaching full intercalation as depicted in Figure 12c. The anode potential is also ~ 350 mV lower in the RLE cell than in the conventional cell at the end of discharge (0.355 V RLE vs. 0.785 V conventional). The lower anode potential at the end of discharge indicates that at this point the anode is not fully depleted of reversible lithium as depicted in Figure 12c.

Thus, the process of using a pre-lithiated anode manifests itself in changes to the behavior of the electrode potentials during normal charge and discharge. This is expected to impact the resulting transient behavior of the electrode potentials and the cell's EAP during near zero volt storage under fixed load.

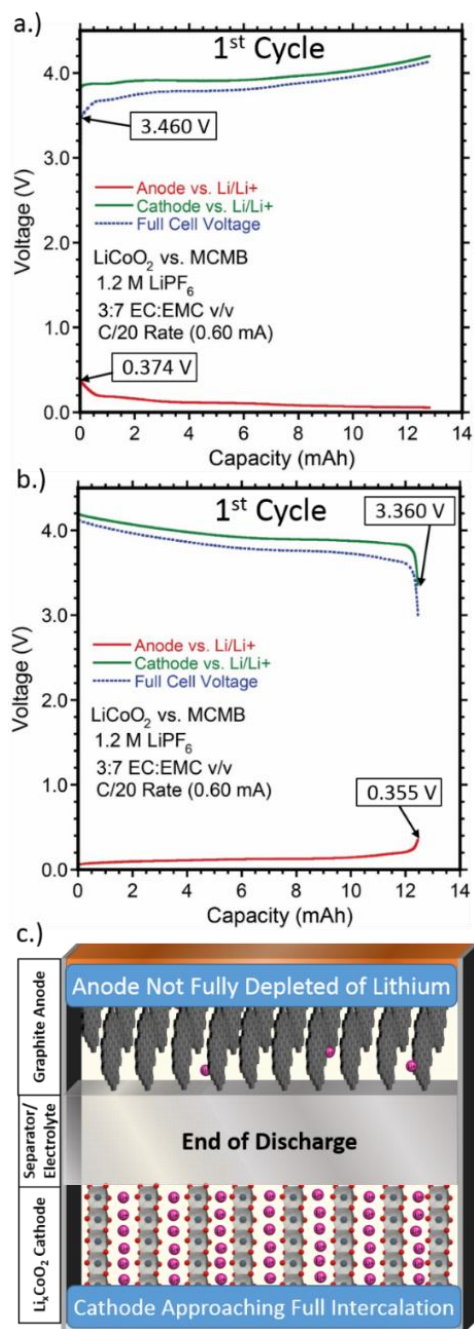


Figure 12: (a) 1st cycle charge cell voltage and electrode potentials of RLE cell. Labeled voltages represent anode potential and full cell voltage at the beginning of charge. (b) 1st cycle discharge cell voltage and electrode potentials of RLE cell. Labeled voltages represent the cathode and anode potentials at the end of discharge. (c) Schematic of cell condition at the end of discharge to a cutoff volt of 3.0 volts showing the cathode fully intercalated and the anode not fully depleted of reversible lithium. *Reproduced from Ref [173] with permission from the Royal Society of Chemistry

4.4 Electrode potential behavior during near zero volt storage of an RLE cell

After the C/10 discharge to 3.0 V cell voltage on the 5th conditioning cycle of the RLE cell, a constant load of 2.5 kOhms was applied to the cell to discharge it to near zero volts (i.e. actual voltage reaches 1-3 mV). The fixed load was applied for three days to represent an extended near zero volt storage period.

The 3-electrode data during the 5th cycle discharge is shown as a function of discharge capacity in Figure 13a and a function of time in Figure 13b. As shown in Figure 13b, during the C/10 discharge (first 10 hours) the cell current is constant and the electrode potentials exhibit their normal discharge behavior. At ~10 hours, the cell reaches 3.0 V and the fixed load (2.5 kOhm) step is initiated. Under fixed load, the RLE cell, like the conventional cell described in section 0, undergoes a transient period as it discharges to near zero volts. As shown in Figure 13b, the cell voltage decreases to <0.1 V in the first two hours which under the fixed load corresponds to a cell current of <0.04 mA. During the first two hours the cathode potential initially decreases to ~1.3 V vs. Li/Li⁺ and then increases to ~1.4 V vs. Li/Li⁺. The anode potential initially increases to ~0.6 V vs. Li/Li⁺, then decreases to ~0.5 V vs. Li/Li⁺ as the cell current decreases. The anode potential then increases to >1.0 V vs. Li/Li⁺ after 2 hours at fixed load. After the first 2 hours the potential of both electrodes increases until they asymptote to within 10 mV of each other at ~1.9 V vs. Li/Li⁺ realizing the EAP for this cell. As with the conventional cell described in section 0, at this point the cell voltage is <10 mV and the cell current is <4 μ A (C/3000) which is considered a quasi-equilibrium state. The quasi-equilibrium state remains for the final 67

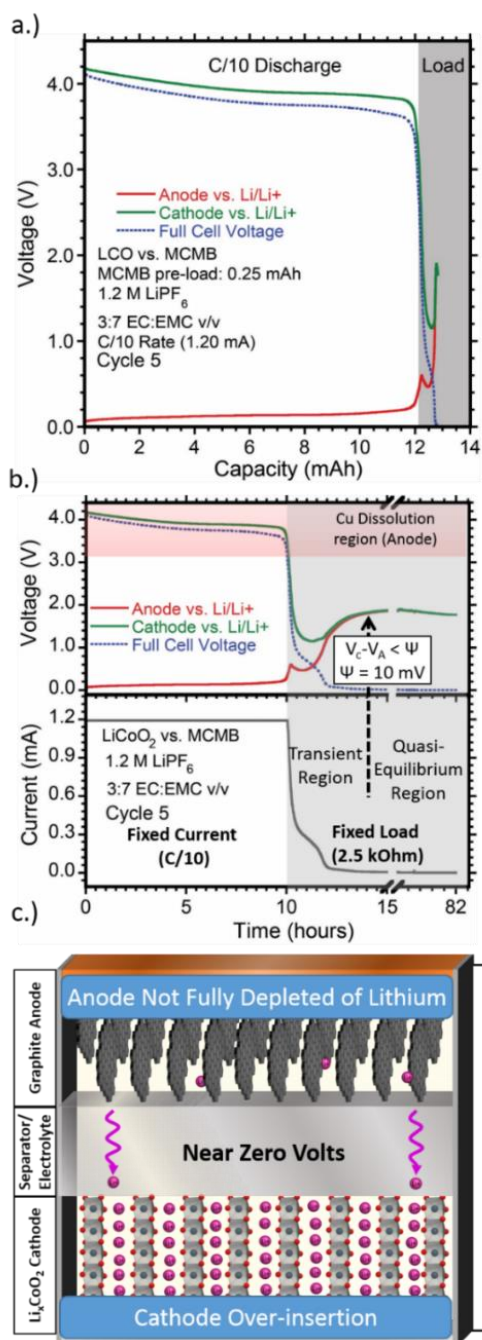


Figure 13: (a) 5th cycle discharge and fixed load step (grey shading) cell voltage and electrode potentials plotted vs. cell capacity of RLE cell. (b) 5th cycle discharge and fixed load step (grey shading) cell voltage and electrode potentials plotted vs. time of RLE cell. Red shading represents anode potential range in which copper dissolution occurs. (c) Schematic of RLE cell function in the near zero volt condition. Pink arrows represent lithium ion flow, the red arrow represent electron flow through internal circuit. *Reproduced from Ref [173] with permission from the Royal Society of Chemistry

hours of the fixed load step. The EAP increases to ~ 2.0 V vs. Li/Li⁺ then decreases back to ~ 1.9 V vs. Li/Li⁺ during this period.

The initial decrease of the cathode potential below its normal operating potential range without recovery at ultra-low cell currents is attributed to the cathode being fully intercalated with lithium during the overdischarge and possibly undergoing over-insertion as depicted in Figure 13c. Apparent intercalation of ~ 0.7 mAh of additional charge into the cathode (Figure 13a) during the fixed load step may be due to cathode degradation processes since it primarily occurs at < 1.636 V vs. Li/Li⁺, where LiCoO₂ has been reported to degrade in an equilibrium condition.[135,136]

The anode potential staying below 2.0 V vs. Li/Li⁺ during the transient period and the EAP of the cell being ≤ 2.0 V vs. Li/Li⁺ indicates that the anode is not fully depleted of intercalated lithium in the near zero volt state of charge, as depicted in Figure 13c. Importantly, the anode potential stays well below ~ 3.1 V vs. Li/Li⁺ during the entire fixed load near zero volt storage period. This suggests that the design is stable for such near zero volt storage in that no copper dissolution is expected to be occurring.

4.5 Performance retention after near zero volt storage of RLE and conventional cells

The performance retention after near zero volt storage of the RLE cell described in section 4.3-4.4 and the conventional cell described in section 1.6.2 was compared using the cycling regime depicted in Figure 14a. After conditioning cycles, a fixed load of 2.5 kOhm was applied to each of the cells for three days to store them at near zero volts (the first load application corresponding to the data shown in Figure 9 and Figure 13). Each cell was then charged at a C/200 rate to 3.0 V cell voltage to gradually bring the cell back to its

normal voltage range, as has been done in testing of commercial near zero volt capable cells using a titanium current collector.[137] Then each cell was charged at a C/10 rate to

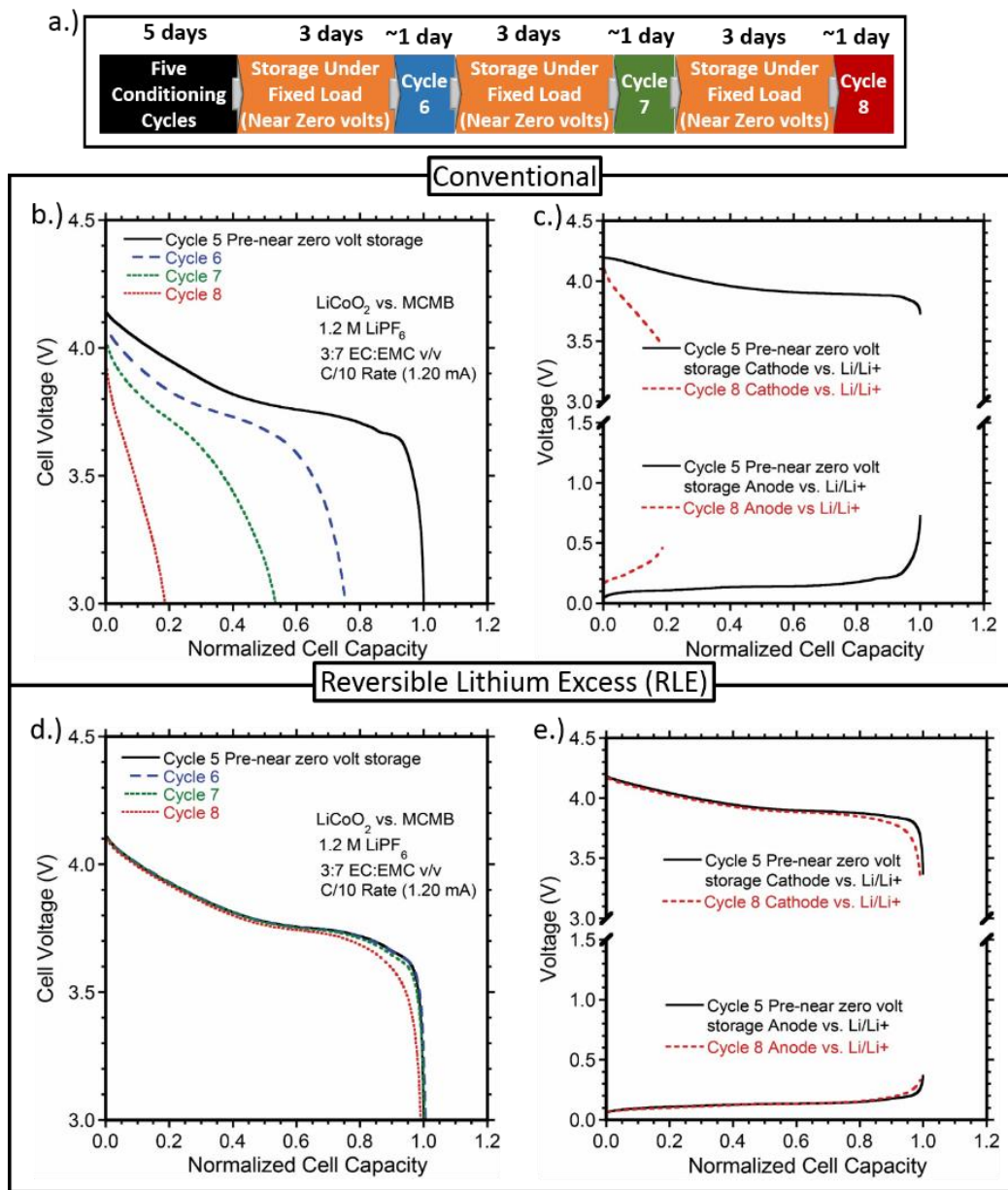


Figure 14: (a) Cycling schedule flow chart depicting the duration and number of cycles and storage periods. (b) Discharge profiles of a conventional cell prior to zero volt storage and after one, two and three, 3-day near zero volt storage periods. (c) Discharge profile of the conventional cell electrode potentials as measured by a lithium metal reference prior to near zero volt storage and after three, 3-day near zero volt storage periods. (d) Discharge profiles of an RLE cell prior to zero volt storage and after one, two and three, 3-day near zero volt storage periods. (e) Discharge profile of the RLE cell electrode potentials as measured by a lithium metal reference prior to near zero volt storage and after three, 3-day near zero volt storage periods. *Reproduced from Ref [173] with permission from the Royal Society of Chemistry

a cathode potential of 4.2 V vs. Li/Li⁺ and then discharged at C/10 to 3.0 V cell voltage. Then, the fixed load was again applied and the cycle repeated.

The discharge profiles of the conventional cell before and after intermediate 3-day fixed load, near zero volt storage periods are plotted in Figure 14b. As shown, the conventional cell fades rapidly on cycle 3 to <20% of its original capacity with significant degradation in the discharge voltage characteristics. As shown in Figure 14c both the cathode and anode discharge behavior in the conventional cell was degraded by the near zero volt storage period. The reference electrode measurements show that both electrodes lose all typical discharge characteristics and demonstrate substantial capacity loss. In comparison, Figure 14d shows that the RLE cell exhibits minimal capacity fade by delivering ~99% of its original discharge capacity after the third, 3-day near zero volt storage period. Additionally, only a minor fade in the average discharge voltage of 25 mV was observed. Such a drastic improvement in performance retention over the conventional cell is attributed to the fact that as measured by the reference electrode, the potential of the anode never exceeds 2.0 V vs. Li/Li⁺ during each near zero volt storage period. This is well below the assigned copper dissolution potential of 3.1 V vs. Li/Li⁺ and as such no copper dissolution is expected to be occurring.

Three-electrode measurements of the RLE cell on the cycle prior to near zero volt storage and after the third, 3-day near zero volt storage period are shown in Figure 14e. During cycle 3, the cathode discharge potential of the RLE cell fades slightly throughout the discharge and at the end of discharge, the potential drop-off is more gradual. The anode discharge potential on the other hand does not notably change at all throughout the majority

of the discharge. Only a slight rounding of the potential curve at the end of discharge is observed.

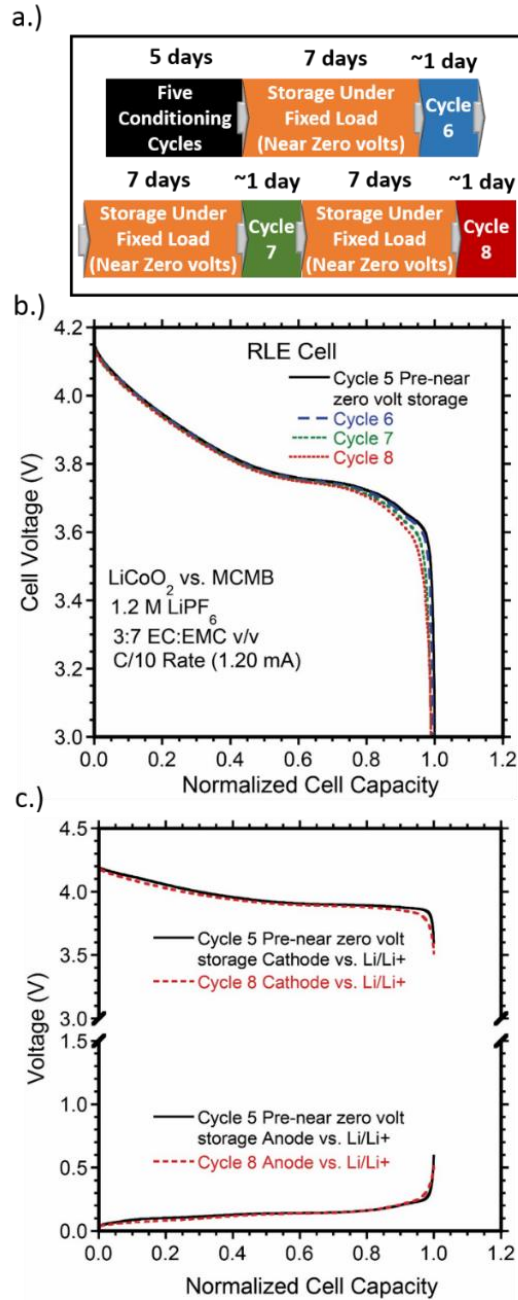


Figure 15: (a) Cycling schedule flow chart. (b) Discharge profiles of an RLE cell prior to near zero volt storage and after 1, 2 and 3 7-day near zero volt storage periods. (c) Discharge profile of the RLE cell electrode potentials as measured by a lithium metal reference prior to near zero volt storage and after 3, 7-day near zero volt storage periods. *Reproduced from Ref [173] with permission from the Royal Society of Chemistry

Thus, the minor fade of the RLE cell observed is primarily attributed to fade in the cathode discharge performance. Fade in the cathode discharge performance likely results from the cathode potential decreasing to less than the cited degradation potential of 1.636 V vs. Li/Li⁺ during the transient period of fixed load storage. However, high performance retention reflects that this damage is minimal and that a cell constructed in the manner of an RLE cell has high tolerance for near zero volt storage conditions.

A second RLE type cell constructed in the same manner as that described in section 4.1 and 4.3 was cycled in the same regime as described in section 4.5 but with 7-day fixed-load near zero volt storage periods instead of 3-day periods (depicted in Figure 15a). The benefit of this test is to further investigate the potential of RLE type cells for longer term storage at near zero volts. The resulting discharge profiles before and after each intermediate storage period are shown in Figure 15b. As shown, with 99% capacity retention and an average discharge voltage fade of only 16 mV after the third, 7-day storage period at near zero volts, the cell showed nearly identical capacity and discharge voltage retention as the RLE cell stored at near zero volts for 3-day periods. As with the cell stored for 3-day periods, the minor fade of the RLE cell stored at near zero volts for 7-day periods is primarily attributed to fade in the cathode performance as shown in Figure 15c by reference electrode measurements.

Lack of increase in the fade rate of the RLE cell with the increase in storage period time at near zero volts is attributed to the fact that most electrochemical processes occur during the transient period (first ~4-5 hours) of fixed load storage. After that, the cell reaches a quasi-equilibrium state and very little current flows. Thus, it is likely that even longer storage periods will have little to no impact on the fade rate of the cell and that the

main factor effecting cell fade rate is the number of times the cell is overdischarged to near zero volts.

4.6 Effect of near zero volt storage on rate capability and long term cycling

Conventional and RLE LiCoO₂/MCMB cells were constructed (without reference electrodes) with the same construction parameters as described in section 4.1 and 4.3. The cycling schedule for the cells is shown in the flow chart in Figure 16a. The cells were cycled between 3.0-4.1 V and conditioned with 1 cycle at a C/20 rate followed by 4 cycles at a C/10 rate. After the 5th cycle discharge the RLE cell was stored at near zero volts with a 2.5 kOhm load applied to the cell for 3 days. The conventional cell on the other hand was stored at open circuit (OC) for 3 days after the 5th cycle discharge.

After the 3-day storage period, the RLE cell was charged to 3.0 V at a C/200 rate, then both the RLE and conventional cells underwent a rate study in which the charge rate was held constant at C/10 and the discharge rate was varied to C/10, C/2, C and 5C as shown in Figure 16b. The data indicates that the rate capability of the RLE cell is nearly identical to the conventional cell, confirming that the 3-day storage period at near zero volts did not have a negative effect on the rate capability of the cell.

After the rate study, the conventional and RLE cells were charged at C/10 and then put on 30% depth of discharge (DOD) low earth orbit (LEO) cycling. The cycling regime consists of a ~C/2.9 charge to a 4.1 V constant voltage step for 54 minutes followed by a C/2 discharge for 36 minutes. The end of discharge voltages are shown for each cell in Figure 16c. The RLE cell cycles with the same stability as the conventional cell for 500 cycles, indicating that the 3-day near zero volt storage period had no significant effect on the RLE cell's cycling stability for 31 days of cycling. The benefit of the rate study and

LEO cycling is to show that in addition to discharge capacity and voltage retention at a C/10 discharge rate, the discharge rate performance and long term cycling stability of an

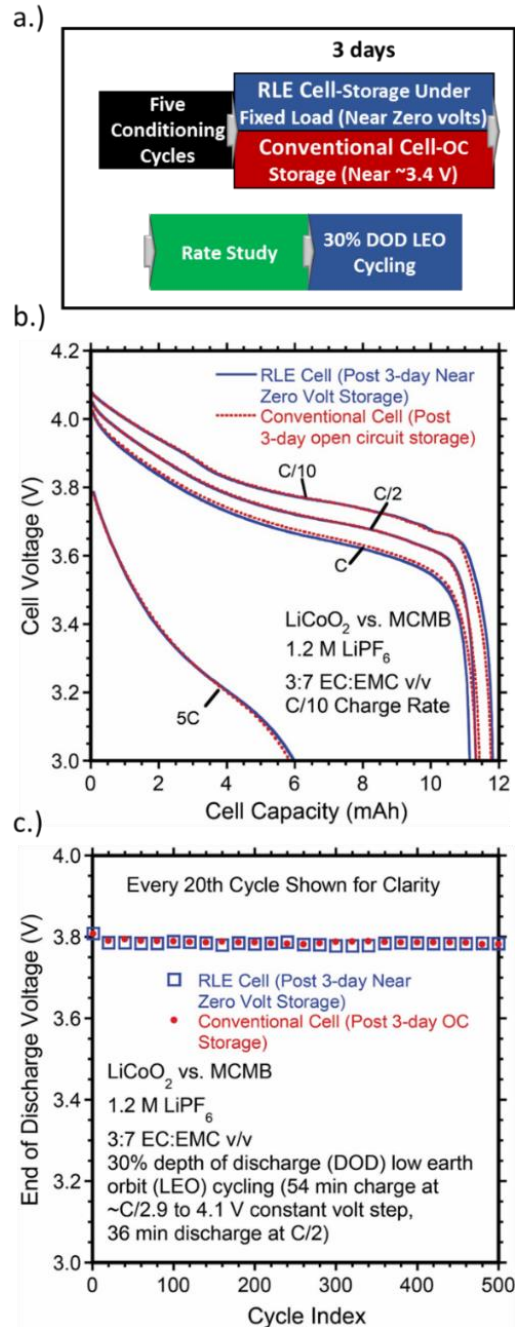


Figure 16: (a) Cycling schedule flow chart showing flow of conditioning, storage, rate testing and low earth orbit (LEO) cycling. (b) Discharge profiles of RLE and conventional cell at different discharge rates. Rate study done after a 3-day storage period (near zero volt storage for the RLE cell and open circuit storage for the conventional cell). (c) End of discharge voltages for 30% depth of discharge (DOD) low earth orbit (LEO) cycling of the RLE and conventional cell. *Reproduced from Ref [173] with permission from the Royal Society of Chemistry

RLE cell is not reduced by an extended near zero volt storage period.

4.7 High Temperature testing of near zero volt storage tolerance of RLE cells

The ambient temperature that cells are exposed to *in operando* can vary drastically from room temperature. Cells present in implanted medical devices will constantly experience a temperature of 98.6 °F (~37 °C) and cells being transported or stored may experience a range of temperatures from -20°F – 130°F (-30-54 °C). SEI layers on the active anode materials lose stability at elevated temperatures.[138] It has been shown that at room temperature, oxidative stripping of the SEI layer can begin at an anode potential 2.1 V vs. Li/Li⁺ of in LiPF₆ electrolytes.[139] Thus, it is anticipated that oxidative stripping of SEI may become more severe or initiate at lower anode potentials with loss of stability at elevated temperature. Electrolyte additives that have been used to stabilize the SEI layer on various anode materials may help to address this issue.[140–162] Additionally, at high temperatures the dissolution potentials of metal substrates may decrease. For example the copper dissolution potential at 37 °C has been reported to be 2.8 V vs. Li/Li⁺, [107] lower than that observed in the present work which was done at room temperature.

Oxidative stripping of SEI at elevated temperatures has been shown to have significant consequences for commercially available near zero volt storage capable cells that use a titanium anode current collector.[107] Specifically, a commercial LiCoO₂/Graphite lithium ion cell employing a titanium anode current collector, which can tolerate near zero volt storage at room temperature (98.6% capacity retention), fails to suitably tolerate near zero volt storage conditions at 37 °C (73.5% capacity retention) due to anode SEI decomposition.[107] Decomposition of the SEI layer during a near zero volt

storage period means that the SEI must reform during the recharging of the cell. SEI reformation will lead to further loss of reversible lithium in a cell, which will lead to reduced discharge capacity of the cell.[85]

In comparison, a LiNiCoO₂/graphite cell using a titanium anode current collector demonstrated high tolerance to near zero volt storage at 98.6 °F (~37 °C) with ~100% performance retention after storage under fixed load.[107] This improved performance retention was attributed to the lower discharge potential of LiNiCoO₂. The lower potential likely leads to a lower anode potential during the transient period and a lower EAP. This effect may help prevent oxidative stripping of the SEI layer that has been destabilized by the higher temperature.

RLE LiCoO₂/MCMB pouch cells with reference electrodes were constructed in the same manner as that described in section 4.1 and 4.3 with a pre-lithiated anode. In the case of these cells one used a 1.2 M LiPF₆ 3:7 EC:EMC v/v electrolyte and another used a 1.2 M LiPF₆ 3:7 EC:EMC v/v electrolyte with 2% w/w vinylene carbonate (VC). VC was used since it has been shown to significantly improve the cycling stability of LiCoO₂/graphite cells at elevated temperature.[161]

High temperature testing of RLE LiCoO₂/MCMB cells was done by restraining a cell in a metal test fixture that was placed on top of a hot plate. A thermocouple was placed next to the cell in the test fixture and connected to the Arbin cycler which is outfitted with external temperature measurement capability. The temperature experienced by the cell was monitored throughout testing. The cell was cycled 5 times at room temperature under the same cycling conditions as described in section 4.4 and then set to an open circuit condition. The hot plate was then used to heat the metal test fixture to 45°C. The metal

test fixture was given ~2 hours to equilibrate at the elevated temperature, then the cell was cycled twice at a C/10 rate, as depicted in the flow chart in Figure 17a. After the seventh cycle discharge, a fixed load of 2.5 kOhm was applied to the cell for 3 days. The resulting behavior of the electrode potentials plotted vs time is shown in Fig 17b for the cell with baseline electrolyte and in Fig 17c for the cell with 2% w/w VC additive.

As shown in Figure 17b and c, for both cells during the first 2 hours of the fixed load step, the cell voltage quickly drops to <20 mV. In the cell without VC added to the electrolyte, as shown in Fig 17b, the cathode potential drops to ~1.8 V vs. Li/Li⁺ and then recovers up to ~1.9 V vs. Li/Li⁺. The anode potential rapidly increases to ~1.5 V vs. Li/Li⁺, where it plateaus briefly, then it increases to ~1.9 V vs. Li/Li⁺. After the first two hours of fixed load storage, the electrode potentials are at ~1.9 V vs. Li/Li⁺, where after ~5 hours of the fixed load step, they asymptote to within 10 mV of each other at ~1.9-2.0 V vs. Li/Li⁺, realizing the EAP for this cell and reaching a quasi-equilibrium state. The electrode potentials stay at ~2.0 V vs. Li/Li⁺ for the remainder of the fixed load storage period. In the cell with VC additive, as shown in Fig 17c, the cathode potential drops to ~1.2 V vs. Li/Li⁺ and then recovers up to ~1.5 V vs. Li/Li⁺. The anode potential steadily increases to ~1.5 V vs. Li/Li⁺. After the first two hours of fixed load storage, the electrode potentials increase to ~1.7 V vs. Li/Li⁺, where after ~11 hours of the fixed load step, they asymptote to within 10 mV of each other at ~1.75 V vs. Li/Li⁺, realizing the EAP for this cell and reaching a quasi-equilibrium state. The electrode potentials stay at ~1.75 V vs. Li/Li⁺ for the remainder of the fixed load storage period. The behavior of the electrode potentials at elevated temperature is very similar for both electrolytes with and without VC additive.

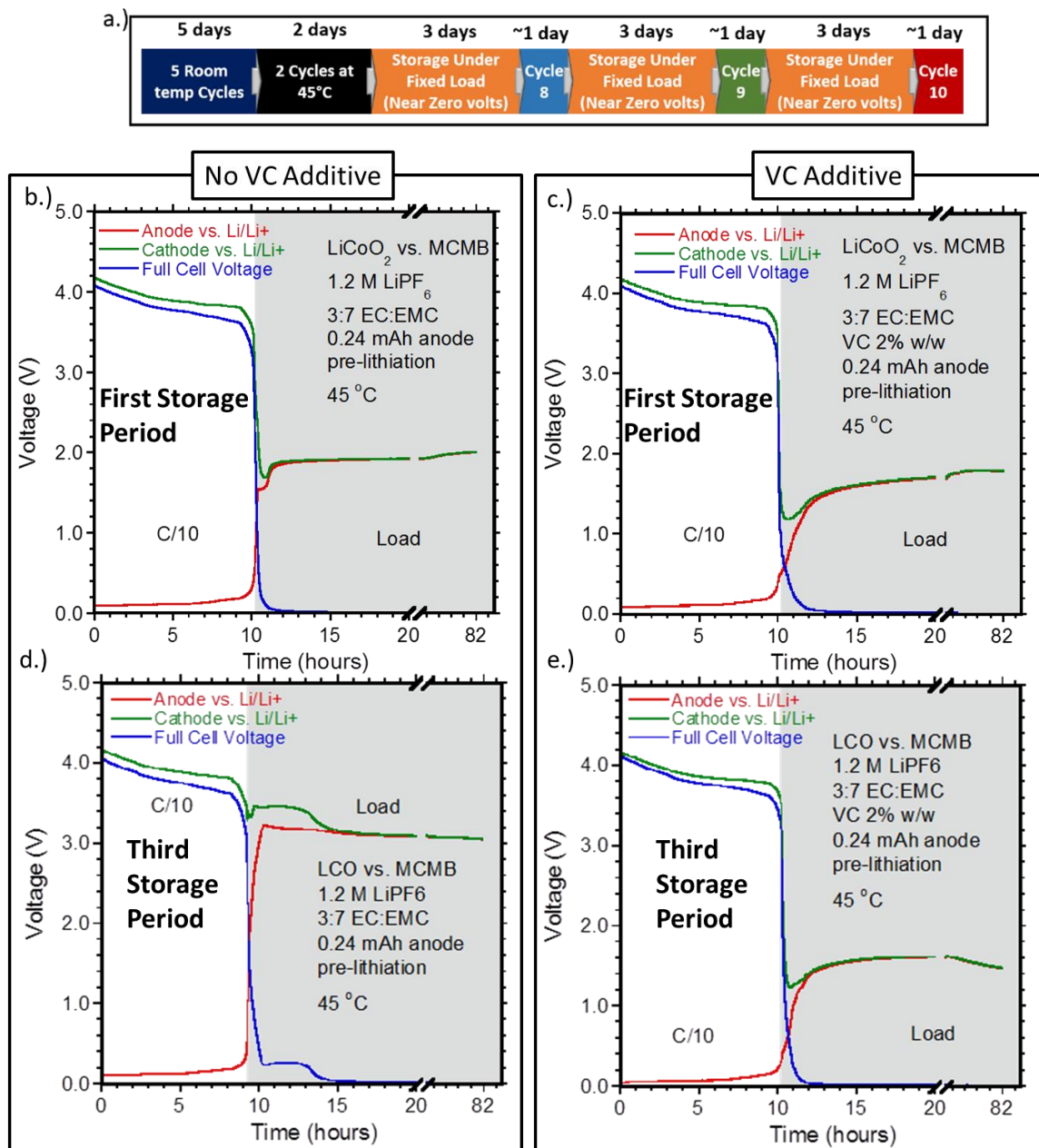


Figure 17: (a) Cycling schedule flow chart summarizing room temperature conditioning, cycling at 45°C, and near zero volt storage testing at 45°C. (b) 7th cycle discharge and fixed load step (grey shading) cell voltage and electrode potentials plotted vs. time of RLE cell with 1.2 M LiPF₆ 3:7 EC:EMC v/v electrolyte at 45°C. (c) 7th cycle discharge and fixed load step (grey shading) cell voltage and electrode potentials plotted vs. time of RLE cell with 1.2 M LiPF₆ 3:7 EC:EMC v/v VC 2% w/w electrolyte at 45°C. (d) 9th cycle discharge and fixed load step (grey shading) cell voltage and electrode potentials plotted vs. time of RLE cell with 1.2 M LiPF₆ 3:7 EC:EMC v/v electrolyte at 45°C. (e) 10th cycle discharge and fixed load step (grey shading) cell voltage and electrode potentials plotted vs. time of RLE cell with 1.2 M LiPF₆ 3:7 EC:EMC v/v VC 2% w/w. electrolyte at 45°C. storage periods at 45°C.

Importantly, the transient anode potential and EAP of the cell are low enough that no

copper dissolution can be expected to be occurring.

The third 3-day near zero volt storage period of the RLE cells without and with 2% w/w VC additive are shown in Figure 17d and Figure 17e, respectively. As can be seen, in the cell without VC additive, the anode potential rapidly increases during the fixed load near zero volt storage period and plateaus at ~ 3.2 V vs. Li/Li⁺, indicative of substantial copper dissolution. The change in electrode behavior from the first near zero volt storage period can be attributed to loss of reversible lithium due to SEI instability at the high temperature. The cell with VC additive, on the other, displays electrode potential behavior during the third near zero volt storage period that is almost identical to the first near zero volt storage period, indicating no loss of reversible lithium due to the high temperature. Importantly, the cell's transient period anode potential and EAP are low enough that no copper dissolution can be expected to be occurring.

The discharge performance retention of the RLE cells without and with 2% w/w VC electrolyte additive at 45°C is plotted in Figure 18a and b, respectively. As shown, the discharge performance retention of the RLE cell without VC additive is not as good as the discharge performance retention at room temperature, with only 74% capacity retention after three, 3-day near zero volt storage periods. The loss of performance can be attributed to loss of reversible lithium during high temperature cycling and copper dissolution during the third, 3-day near zero volt storage period.

The RLE cell with VC additive has very similar discharge performance retention to the cell without 2% w/w VC additive tested at room temperature. After three, 3-day storage periods at 45°C under fixed load at near zero volts, the cell discharged with 103% of the cell capacity prior to near zero volt storage under fixed load with no decrease in

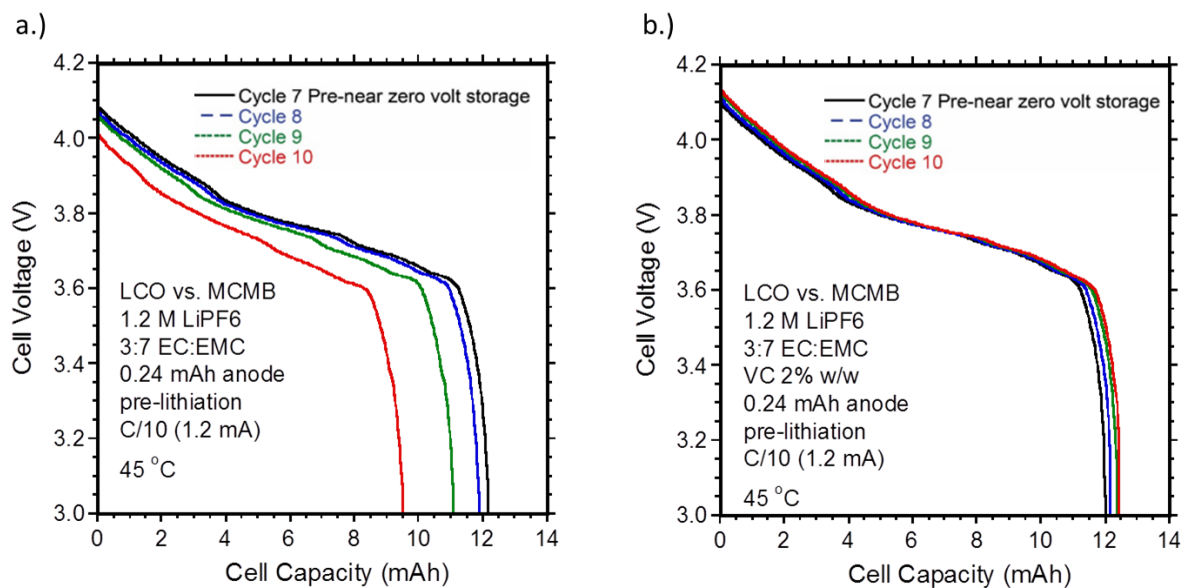


Figure 18:(a) Discharge profiles of an RLE with 1.2 M LiPF₆ 3:7 EC:EMC v/v electrolyte cell prior to zero volt storage, and after one, two and three, 3-day near zero volt storage periods at 45°C. (b) Discharge profiles of an RLE with 1.2 M LiPF₆ 3:7 EC:EMC v/v VC 2% w/w electrolyte cell prior to zero volt storage, and after one, two and three, 3-day near zero volt storage periods at 45°C.

average discharge voltage. The strong performance retention is attributed to the cell's EAP remaining at ~1.6-1.7 V vs. Li/Li⁺ for each fixed load storage period, so no copper dissolution is expected to be occurring during any of the near zero volt storage periods. Thus, anode pre-lithiation is a viable approach to near zero volt storage tolerance at elevated temperatures which can impact batteries used in implanted medical devices and cells experiencing high temperatures during transit or storage.

4.8 Pulse discharge study of RLE lithium ion cell discharged to zero volts

Pulse Discharge testing of a LiCoO₂/MCMB cell with a pre-lithiated anode was performed in order to further understand the electrochemical processes occurring during near zero volt storage in an RLE cell. A 1.35 mAh LiCoO₂/MCMB lithium ion pouch cell was constructed with the anode pre-lithiated in the same manner as described in section 4.1. The cell was charged and discharged 10 times between 3.0 and 4.1 V at a C/10 rate. After the 10th charge, the cell underwent a pulse discharge step that consisted of a 60

second, C/10 discharge pulse followed by a 60 second open circuit step. Figure 19 shows the cell voltage and measured electrode potentials of the pulse discharge step. As shown, the discharge behavior was similar to that shown in Figure 12, but the discharge took 20 hours total due to the 60 second rest step between each 60 second discharge.

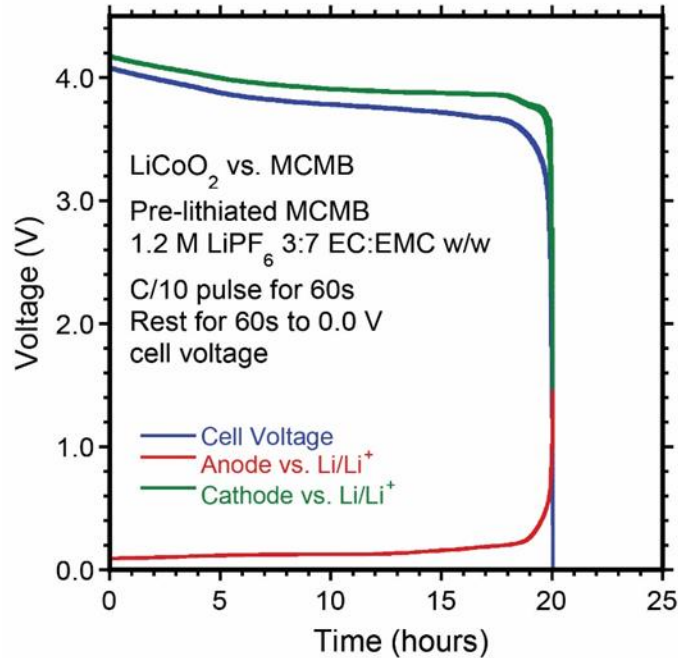


Figure 19: Cell voltage and electrode potentials of a LiCoO₂/MCMB cell with a lithium reference electrode during a pulse discharge to 0 volts cell voltage.

Figure 20a shows the measured cathode potential of three pulse discharge iterations about halfway through the pulse discharge step. Also shown is the open circuit potential at each point in time. The open circuit potential is determined by fitting the potential profile during the 60 second open circuit step with an RC element (resistor and capacitor in parallel) to estimate what the open circuit potential would be in the cell were kept at open circuit for an infinite amount of time. A linear relationship between the estimated open circuit potential of cathode at each 60 second rest step was assumed. The fitting was done using the Wolfram Mathematica FindFit function.

As shown in Figure 20a, during a current pulse about halfway through the discharge, the potential of the cathode initially decreases by about 6 mV within ~1 second of the start of the discharge pulse. The rapid initial drop can be attributed to the series resistance of the electrode. After the initial decrease, the potential decreases in a non-linear manner with a gradual decrease in the magnitude of the slope. The current pulse at about halfway through discharge is representative of the current pulses up to about the last 10% of discharge.

Figure 20b shows the overpotential (i.e. difference between the open circuit and measured potential) and the change in overpotential with time corresponding to the leftmost C/10 pulse discharge shown in Figure 20a. The measured potential was fit with an RC element to smooth the curve. As shown, the overpotential decreases from an initial value of -5.6 mV to -7.5 mV while the change of the overpotential with time (labeled dV/dt in Figure 20b) increases from an initial value of -0.08 mV/s to -0.01 mV/s. The increase in overpotential over the span of the discharge pulse is consistent with the current contribution from faradaic intercalation and de-intercalation of lithium ions (which can be described by Butler-Volmer kinetics, equation 4 in section 1.1) is increasing over the course of the discharge pulse. The decrease in magnitude of dV/dt over the span of the discharge pulse on the other hand is consistent with the current contribution from double layer capacitance (which can be represented by a capacitor, equation 5 in section 1.1) decreasing as the discharge pulse progresses.

Figure 20c shows the last three discharge pulses of the pulse discharge step that end when the cell voltage reaches zero volts. Compared to Figure 20a, the voltage swing of the cathode potential during each current pulse and subsequent open circuit is much larger

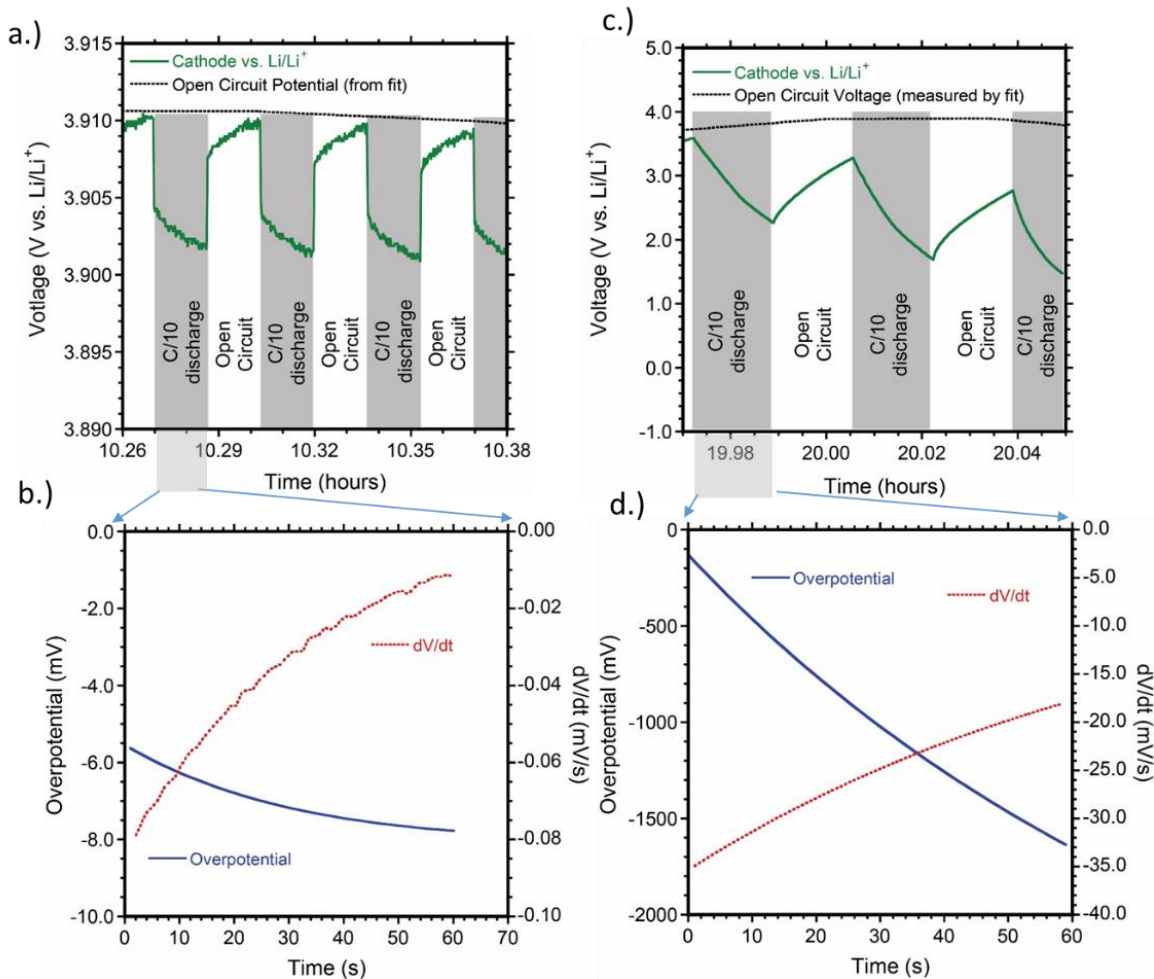


Figure 20: (a) Measured cathode potential vs. Li/Li⁺ and open circuit potential vs. Li/Li⁺ obtained from RC element fitting at a point about halfway through the pulse discharge test. (b) The overpotential and change in overpotential as a function of time corresponding to the leftmost C/10 discharge pulse in a. (c) Measured cathode potential vs. Li/Li⁺ and open circuit potential vs. Li/Li⁺ obtained from RC element fitting at the end of the pulse discharge test (last 3 pulses). (d) The overpotential and change in overpotential as a function of time corresponding to the leftmost C/10 discharge pulse in c.

(~1.0 V compared to 0.008 V) at the end of discharge than at ~50% state of charge. Figure 20d shows the overpotential and change in overpotential with time (dV/dt) corresponding to the leftmost discharge pulse shown in Figure 20c. As shown, the overpotential decreases from an initial value of -150 mV to -1700 mV over the span of the discharge pulse while dV/dt increases from -35 mV/s to -18 mV/s over the course of the discharge pulse.

The much larger overpotential during the discharge pulse at the end of discharge compared to at ~50% state of charge is consistent with the LiCoO₂ active material

approaching saturation at the end of discharge. In the Butler-Volmer framework, saturation corresponds to the concentrations (C in equation 4 of section 1.1) of the vacant sites of the LiCoO_2 cathode decreasing significantly at the end of discharge. Such a decrease in concentration leads to a much larger overpotential necessary to achieve the applied current values, consistent with what is shown in Figure 20d. Additionally, the much larger dV/dt value shown in Figure 20d compared to that of Figure 20b is consistent with the contribution to electrode current from double layer capacity being much larger at the end of discharge than at 50% state of charge.

Figure 21a shows the measured anode potential and calculated open circuit potential for three 60s discharge pulses with 60s open circuit steps between them at about 50% state of charge (Same discharge pulses shown in Figure 20a). Figure 21b shows the overpotential and change of overpotential with time (labeled dV/dt in Figure 21a) corresponding to the leftmost discharge pulse shown in Figure 21a. As shown, the overpotential increases from 0.4 mV to 1.6 mV over the course of the discharge pulse. The change in overpotential with time decreases from 0.037 mV/s to 0.010 mV/s over the course of the discharge pulse. Such a result is similar to that observed in the cathode during the same discharge pulse. The increasing magnitude of the overpotential is consistent with increasing current contribution from intercalation and de-intercalation reactions. The decreasing magnitude of dV/dt over the span of the discharge pulse is consistent with a decreasing current contribution from the double layer capacitance of the electrode throughout the discharge pulse.

Figure 21c shows the last three discharge pulses of the discharge step that end when the cell voltage reaches 0.0 V. Similar to the cathode, the magnitude of the voltage swings

in much greater than during the discharge pulses at 50% state of charge (~300 mV compared to 1.5 mV). Figure 21d shows the overpotential and change in overpotential with time (dV/dt) corresponding to the leftmost discharge pulse shown in Figure 21c. As shown, the overpotential increases from an initial value of 75 mV to a final value of 210 mV while dV/dt decreases from an initial value of 2.5 mV/s to 2.0 mV/s over the span of the discharge pulse. The much higher magnitude of the overpotential shown in Figure 21d compared to that shown in Figure 21b is consistent with a significantly decreased

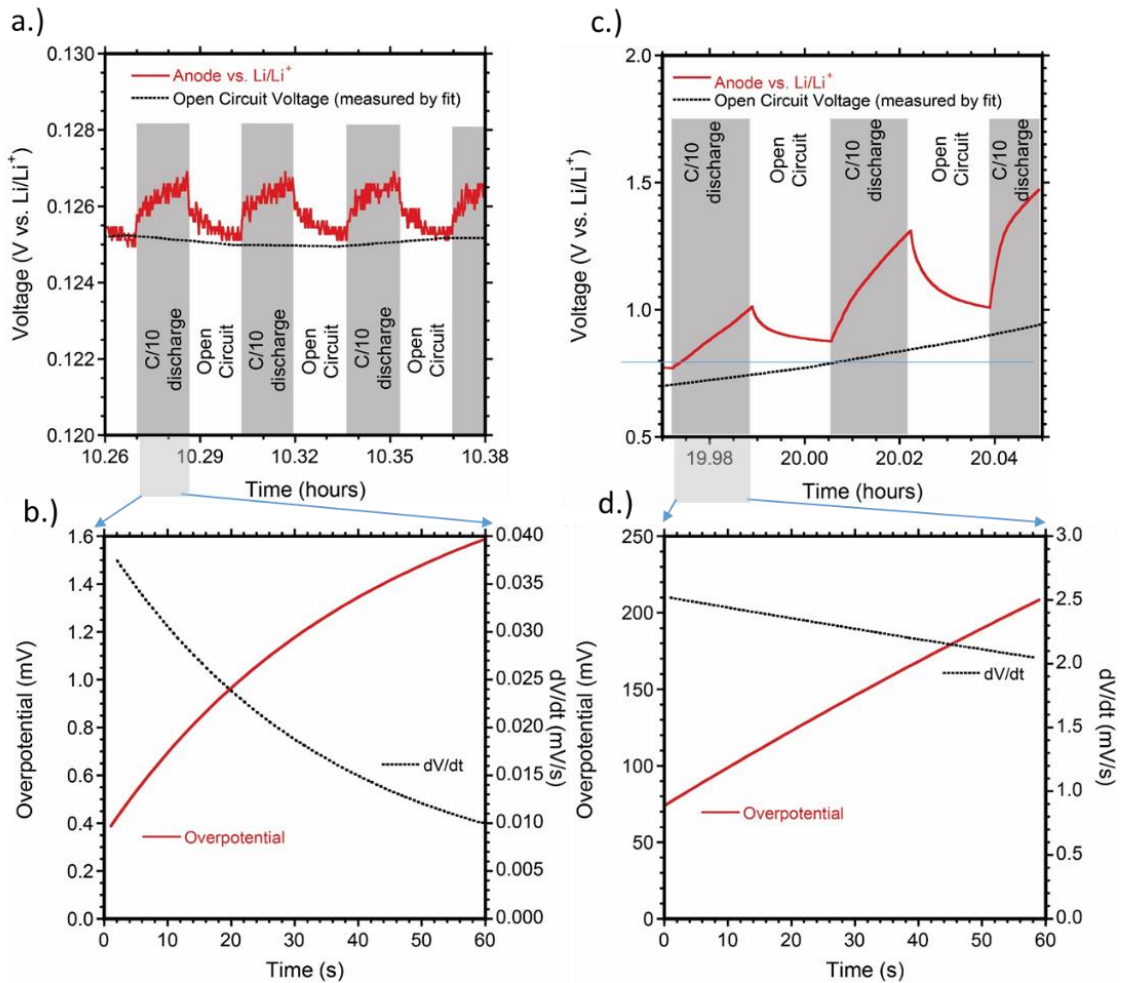


Figure 21: (a) Measured anode potential vs. Li/Li^+ and open circuit potential vs. Li/Li^+ obtained from RC element fitting at a point about halfway through the pulse discharge test. (b) The overpotential and change in overpotential as a function of time corresponding to the leftmost C/10 discharge pulse in a. (c) Measured anode potential vs. Li/Li^+ and open circuit potential vs. Li/Li^+ obtained from RC element fitting at the end of the pulse discharge test (last 3 pulses). (d) The overpotential and change in overpotential as a function of time corresponding to the leftmost C/10 discharge pulse in c.

concentration of occupied lithium sites (C in equation 4 of section 1.1) in the graphite particles of the anode at the end of discharge compared to at ~50% state of charge. Decreased concentration of lithium vacant sites is consistent with the anode approaching depletion of lithium ions as the cell discharges to zero volts. The much higher magnitude of dV/dt throughout the discharge pulse compared to at 50% state of charge is also consistent with greater current contribution from double layer capacitance as the cell approaches zero volts.

Collectively, the results and analysis presented in this section suggest that non-faradaic double layer capacitance plays a significant role in dictating the transient behavior of electrode potentials when a cell is discharged to near zero volts. This is due to the concentration of cathode vacant sites and anode lithium occupied sites decreasing substantially as the cell nears zero volts, consistent with saturation and lithium depletion, respectively. Such a result can inform on ways to further improve the approach of reversible lithium management to enable near zero volt storage tolerance in lithium ion cells.

4.9 Studying degradation of LiCoO_2 during near zero volt storage and improving its tolerance to the near zero volt storage condition with AlPO_4 coating

As-discussed in section 4.4-4.5, over-insertion of the cathode is possible in a RLE type cell during near zero volt storage, and such over-insertion can degrade the performance of the material. Thus, identifying ways to stabilize the cathode material against over-insertion of lithium are needed to further improve the resistance of the cathode to near zero volt storage conditions in an RLE cell.

AlPO₄ coated on the surface of cathode active particles has been shown to improve the stability of several cathode active materials.[49,163–166] In particular several studies have shown that the AlPO₄ coated on the surface of LiCoO₂ particles stabilizes LiCoO₂ against charge to high potentials >4.2 V vs. Li/Li⁺. [46–48,167–172] Such stabilizing effects may extend to over-insertion of lithium into the cathode and thus AlPO₄ coating on the surface of LiCoO₂ could have a dual utility of enhancing overdischarge *and* overcharge tolerance of advanced lithium ion cells with added reversible lithium.

In this section, a solution deposited coating of AlPO₄ onto LiCoO₂ particles is tested for its utility in improving the tolerance of LiCoO₂ to over-insertion of lithium at potentials <3.0 V vs. Li/Li⁺. Half-cell testing in coin cells is used to study the effect of an AlPO₄ coating to stabilize a LiCoO₂ cathode discharge performance against a 5% over-insertion of lithium by fixed resistive load. X-ray Diffraction (XRD) is used to investigate the crystal structure change of as-received LiCoO₂ and AlPO₄ coated LiCoO₂ after 10 repeated charge/discharge cycles to 5% over-insertion of lithium. A mechanism is proposed to explain the utility of AlPO₄ coatings to enhance the tolerance of LiCoO₂ to over-insertion of lithium.

4.9.1 Experimental methods

AlPO₄ coating

Coating of LiCoO₂ particles (MTI corporation) with AlPO₄ was done following a previously described procedure targeting 1.0 %w/w of AlPO₄ coated on the surface of the LiCoO₂ particles.[171,172] The procedure includes dissolving 0.0996 g of (NH₄)₂HPO₄ and 0.2832 g Al(NO₃)₃·9H₂O in 30 mL deionized H₂O by magnetic stir bar mixing. After a white suspension formed, 9.2 g of LiCoO₂ was added to the mixture and the mixture was

covered and stirred overnight. Then, the water was evaporated under stirring at about 70°C followed by the solid mixture was dried in a vacuum oven for 4 hours at 100°C. After drying, the powder was subsequently hand ground with an agate mortar and pestle before and after being fired in a furnace at 700°C in air for 5 hours.

Electrode fabrication

Electrode coatings were prepared by mixing LiCoO₂ (As-received or AlPO₄ coated) into a slurry with superC™ carbon black and Solef® PVDF in a 90:5:5 mass ratio using N-methyl-1-pyrrolidone (NMP) as the solvent. The slurry preparation consisted of dissolving polyvinylidene fluoride (PVDF) in NMP, followed by mixing in the carbon black and then addition of the LiCoO₂ (As-received or AlPO₄ coated) with intermediate mixing steps. Mixing steps were each performed for 20 minutes using a Thinky AR-100 planetary mixer. The composite slurry was coated onto a 20 μm aluminum foil using a doctor blade. The coated cathode was dried overnight in a vacuum oven at 100°C and then calendared to a composite density of ~1.7 g/cm³. The final active material areal loading was 18.6 mg/cm² resulting in an areal capacity of 2.6 mAh/cm² using 140 mAh/g_{LiCoO₂} specific capacity.

Electrochemical testing

Electrodes were punched into 0.65 cm diameter disks and built into 2032 coin cells with Li metal as the counter electrode. The electrolyte used was 1.2 M LiPF₆ 3:7 ethylene carbonate (EC):ethyl methyl carbonate (EMC) w/w and a Celgard 2325 separator. All assembly was performed in a dry argon glovebox maintained at <1.0 ppm oxygen and <1.0 ppm water. Cycling of the coin cells was done with an Arbin BT2000 cycler at room temperature (23 °C).

Material analysis

For post-mortem analysis, coin cells were disassembled in a dry argon glovebox and electrodes were rinsed with excess EMC. After rinsing, the electrodes were dried under vacuum for 2 hours before being taken out of the glovebox. X-ray diffraction (XRD) was performed with a Bruker D2 Phaser powder x-ray diffractometer with a $\text{Cu } \alpha$ 1.54184 Å x-ray source. The step size was set to 0.0081167 degrees in the 2θ scale with 1.0 second collection time at each step. The electrode was placed on a sample holder that was rotated at a rate of 1.0 rotation/second. Background subtraction was done using Bruker software. Scanning electron microscopy (SEM) was done with a Hitachi S-900 at an accelerating voltage of 2 kV. Samples were applied directly to the brass stub by using double-sided carbon tape.

4.9.2 Results and Discussion

Figure 22a shows scanning electron micrographs of as-received LiCoO_2 and Figure 22b shows the LiCoO_2 after the AlPO_4 coating process. As shown in Figure 22a, the surface of the as-received LiCoO_2 has some observed features including cracks, indents and partially detached fragments but is visibly smooth in between features. As shown in Figure 22b, the surface of the LiCoO_2 changes substantially after coating with surface depositions leading to roughened microscale appearance at an equivalent SEM magnification. The observed surface depositions are consistent with previous studies that used a similar AlPO_4 coating process.[167,169,172] Consistent with prior studies,[46–48,167–172] the quality of the AlPO_4 coating is confirmed based upon the stability to overcharge for LiCoO_2 to a 4.5 V vs. Li/Li^+ cutoff voltage (See Figure 65). Thus, the

resulting coating has an overcharge-stabilizing effect which could also be beneficial to overdischarge.

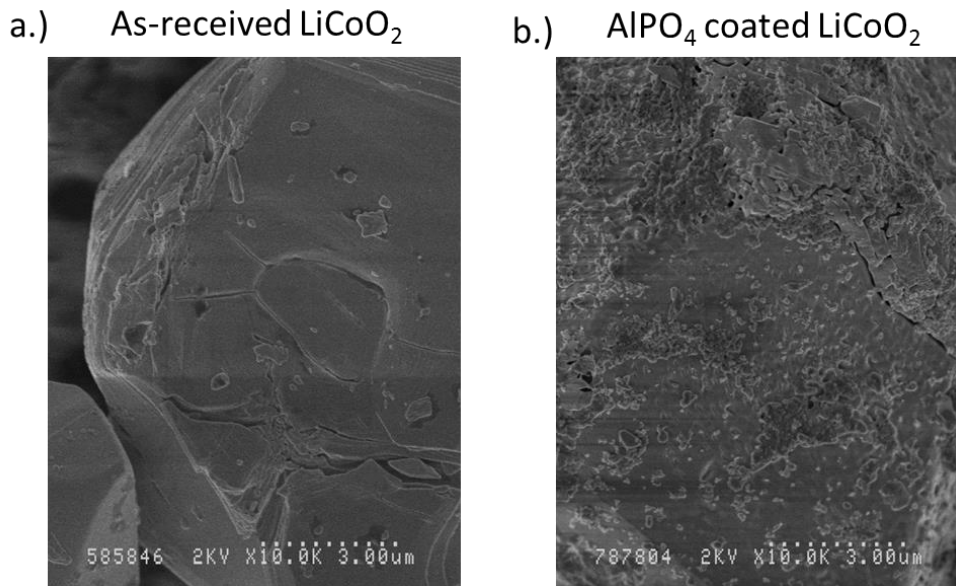


Figure 22: (a) SEM micrograph of as-received LiCoO_2 . (b) SEM micrograph of LiCoO_2 after AlPO_4 coating process

Coin cells were constructed with an as-received or AlPO_4 coated LiCoO_2 working electrode and lithium metal counter electrode. Coin cells were charged to 140 mAh/gLiCoO_2 extraction capacity and discharged to 3.0 V vs. Li/Li^+ . The charge cut off was based on the gravimetric specific capacity of the LiCoO_2 (accounting for the 1.0 % w/w of AlPO_4 in the coated LiCoO_2) so that both as-received and AlPO_4 coated LiCoO_2 were de-lithiated to the same degree during charge regardless of difference in overpotential that is caused by the AlPO_4 coating (See Figure 64). LiCoO_2/Li cells were charged and discharged 10 times to a 140 mAh/gLiCoO_2 extraction limit and 3.0 V vs. Li/Li^+ insertion limit at 14 mA/gLiCoO_2 to condition the cells. The discharge voltage profiles for every other cycle from 1-9 of as-received LiCoO_2 and AlPO_4 coated LiCoO_2 are shown in Figure 23 (The charge and discharge voltage profiles for all cycles 1-9 are shown in Figure 67 and Figure 68, respectively. Every other cycle is shown here for clarity). As shown, both the as-received

LiCoO₂ and AlPO₄ coated LiCoO₂ materials were measured to insert about 133 mAh/g_{LiCoO₂} on the first cycle and then ~138 mAh/g_{LiCoO₂} for cycles 3,5,7 and 9. The voltage profile greater than 100 mAh/g_{LiCoO₂} insertion capacity to 129 mAh/g_{LiCoO₂} is more rounded for the AlPO₄ coated LiCoO₂ than the as-received LiCoO₂ during the first cycle, but for each subsequent cycle the discharge voltage curves become more similar between samples.

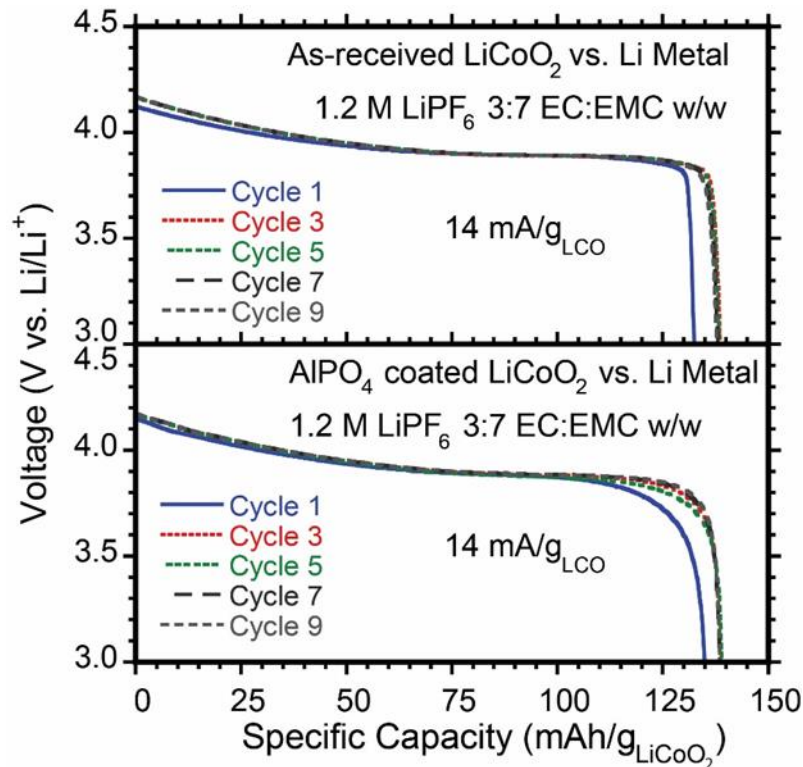


Figure 23: Discharge profiles of conditioning cycles 1, 3, 5, 7 and 9 for uncoated LiCoO₂ (top) and AlPO₄ coated LiCoO₂ (bottom)

Figure 24a shows the cycling schedule used to test the effect of lithium over-insertion on LiCoO₂ cathodes. After the nine conditioning cycles shown in Figure 23 the tenth condition cycle with the same conditions as the first 9 was applied. After the 10th cycle constant current discharge to 3.0 V vs. Li/Li⁺, a fixed resistive load was applied to the cell by the Arbin cycler until 7 mAh/g_{LiCoO₂} additional lithium was inserted into the LiCoO₂. The additional discharge of 7 mAh/g_{LiCoO₂} (5% of cathode discharge capacity)

was selected to mimic a representative cell design in which about 5% reversible lithium is added to the cell.[173] A fixed resistive load was chosen to mimic an external/internal short in a full cell or gradual self-discharge of a cell that is stored. The value of the load was ~35 kOhm but specific to each cell active mass (due to mass variations of 0.06 mg, leading to a variation in load of about 5 Ohm) and designed to give a 14 mA/g_{LiCoO₂} current at a cell voltage of 3.0 volts. After the fixed load step, the LiCoO₂ electrode was recharged to 3.0 V vs. Li/Li⁺ at 0.7 mA/g_{LiCoO₂} (~C/200) and then charged at a constant 14 mA/g_{LiCoO₂} rate to a total charge limit of 147 mAh/g_{LiCoO₂} (includes both 0.7 mA/g_{LiCoO₂} and 14 mA/g_{LiCoO₂} constant current steps). The charge limit compensates for 7 mAh/g_{LiCoO₂} over-insertion and effectively charges the LiCoO₂ to the same 140 mAh/g_{LiCoO₂} extraction limit for each cycle. The cells were then discharged to 3.0 V vs. Li/Li⁺ at 14 mA/g_{LiCoO₂} before a fixed resistive load was again applied to the cell until 7 mAh/g_{LiCoO₂} additional charge passed.

The cycling was repeated 8 more times and after the 10th application of a fixed load, both cells were recharged to 3.0 V vs. Li/Li⁺ at 0.7 mA/g_{LiCoO₂} to complete the test. Figure 24b shows the voltage profile of the 14 mA/g_{LiCoO₂} constant current discharge to 3.0 V vs. Li/Li⁺ and fixed load step to 7 mAh/g_{LiCoO₂} additional charge passed of the as-received LiCoO₂ for cycle 10, 11, 13, 16 and 19 (corresponding to the cycle prior to overdischarge testing, and after 1, 3, 6 and 9 fixed load, 7 mAh/g_{LiCoO₂} over-insertion steps). The discharge profiles of all cycles 10-19 are shown in Figure 69a, with every other cycle shown here for clarity. As shown, the discharge voltage plateau of the as-received LiCoO₂ prior to overdischarge cycling becomes less pronounced, with cycling leading to rounding of the profile towards the end of discharge, consistent with prior studies.[136]

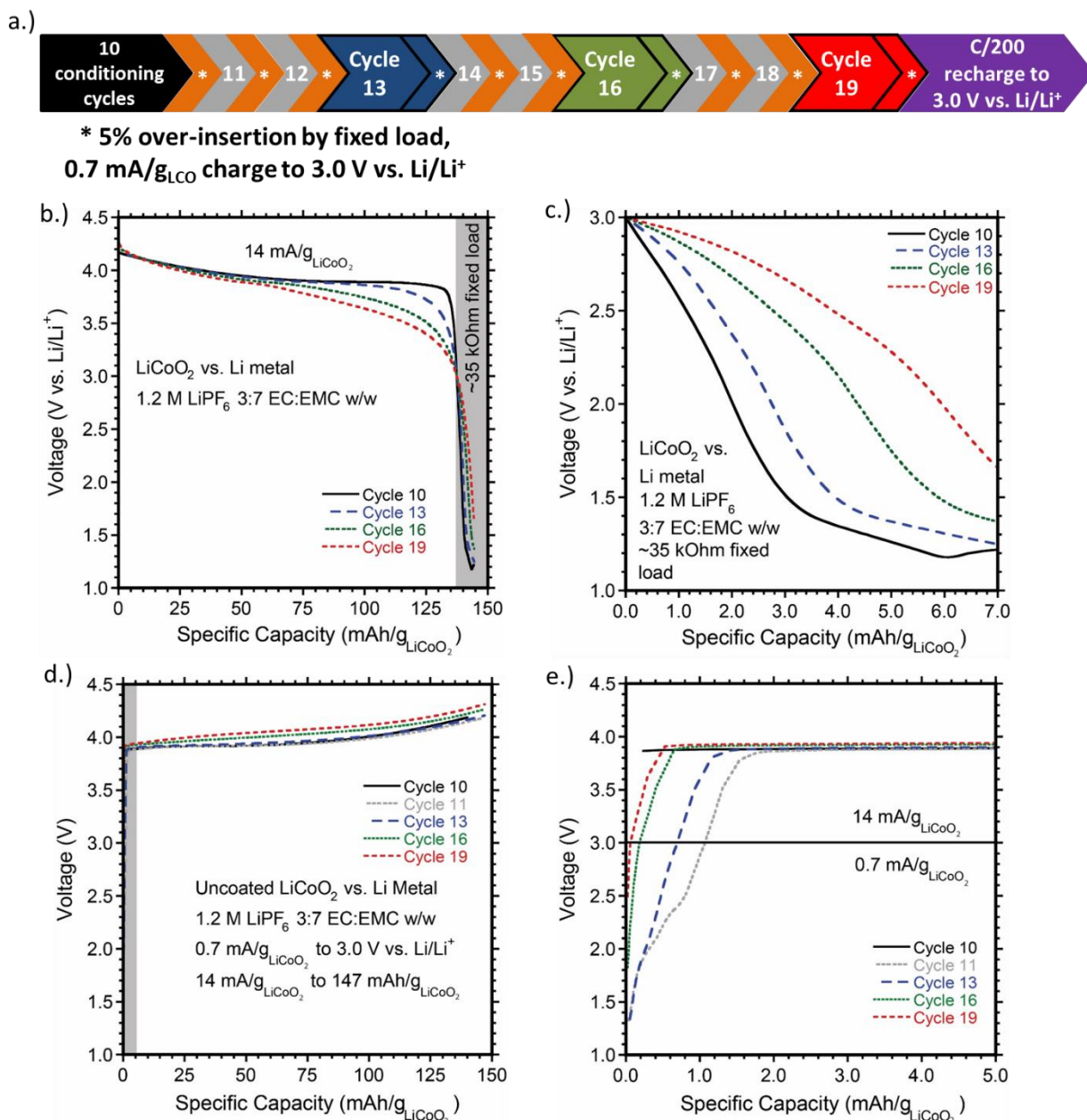


Figure 24: (a) Cycling schedule of coin cells with as-received LiCoO₂ cathode vs. Lithium metal. Numbers after conditioning represent cycles (charge to 147 mAh/g_{LiCoO₂} extraction and discharge to 3.0 V vs. Li/Li⁺). (b) Constant current discharge to 3.0 V vs. Li/Li⁺ and fixed load over-insertion curve of cycle 10, 11, 13, 16 and 19 for coin cell with as-received LiCoO₂ cathode vs. Lithium metal (c) Fixed resistive load, 5% (7mAh/g_{LiCoO₂}) over-insertion step of cycles 10, 11, 13, 16 and 19 for coin cell with as-received LiCoO₂ cathode vs. Lithium metal. (d) Constant current 0.7 mA/g_{LiCoO₂} charge to 3.0 V vs. Li/Li⁺ and 14 mA/g_{LiCoO₂} charge to 147 mAh/g_{LiCoO₂} of cycles 10, 11, 13, 16 and 19 for coin cell with as-received LiCoO₂ cathode vs. Lithium metal. (e) Zoom in of first 5 mAh/g_{LiCoO₂} of charge of as-received LiCoO₂ for cycles 10, 11, 13, 16, 19.

Such a change in the discharge profile of the cathode is unfavorable for lithium ion cell function as it leads to a decreased average cell voltage. Thus, the over-insertion steps at

the end of each cycle are affecting unfavorable changes in the discharge characteristics of the cathode.

As shown in Figure 24b after the fixed load is applied during cycle 10, 13, 16 and 19, the voltage of the cell decreases to about 1.2-1.6 V vs. Li/Li⁺. Figure 24c shows a zoomed in plot of the discharge voltage profiles from Figure 24b during the fixed resistive load over-insertion step for cycles 10, 13, 16 and 19, with the x-axis set to reflect only the insertion capacity during the fixed load step. All cycles are shown in Figure 69b but a selection is shown here for clarity. As shown, during the first application of a fixed load during the tenth cycle, the potential of the LiCoO₂ cathode decreases until beginning to plateau at about 1.4 V vs. Li/Li⁺. Based on previous work by Shu *et al.*, [136] the initial decrease in electrode potential may be attributed to the formation of a metastable phase, Li_{1+x}Co^{II}Co^{III}O_{2-y} (0 < x, 0 ≤ y). After the potential of each electrode decreases to about 1.4 V vs. Li/Li⁺, there is a plateau that ranges from 1.3-1.4 V vs. Li/Li⁺. The prior work of Shu *et al.* [136] showed that the plateau results from the formation of Li₂O and high valence cobalt compounds Li_xCoO_y (where x > 1.0 and y < 2.0). [136] As shown for cycles 13, 16 and 19 in Figure 24c, the features of the voltage profile change significantly compared to cycle 10 as the LiCoO₂ is repeatedly over-inserted. The plateau at around 1.3-1.4 V vs. Li/Li⁺ becomes much less pronounced and by cycle 19, the plateau is no longer present. All insertion reactions during the fixed load, 7 mAh/g_{LiCoO₂} over-insertion step occur at potentials >1.5 V vs. Li/Li⁺, which is a change consistent with previous work [136] and is indicative of permanent crystal structure changes in the cathode active material. [136]

Figure 24d shows the voltage profiles of the full recharge step of cycles 10, 11, 13, 16 and 19. The charge profiles of all cycles 10-19 are shown in Figure 70a, with a selection

of cycles shown here for clarity. As shown, cycle 13 is nearly the same as the charge curve prior to overdischarge testing. Cycle 16 and 19, however, begin to show an increase in the potential of the charge plateau as well as a ~50 mV increase in the initial polarization of the cell when it begins the 14 mA/g_{LiCoO₂} charge step. Such an increase in the charge potential may indicate that material transformations have led to an increase in charge transport resistance in the LiCoO₂ cathode as a result of repeated over-insertion of 7 mA/g_{LiCoO₂} at <3.0 V vs. Li/Li⁺.

Figure 24e shows a zoomed in view of the first 5 mAh/g_{LiCoO₂} of charge for cycles 10, 11, 13, 16 and 19. All cycles are shown in Figure 70b, but a selection is shown here for clarity. As shown, compared to cycle 10 which is a recharge after a normal discharge to 3.0 V vs. Li/Li⁺, during cycle 11, which is after a fixed load over-insertion, there are plateau-like features at ~2.0 V vs. Li/Li⁺ and 2.4 V vs. Li/Li⁺. Based on prior work,[136] where similar plateaus were observed, the plateaus may reflect a reaction between Li₂O and Co, Li₂O and CoO or Li₂O and Co₃O₄ that may have formed during the over-insertion of lithium. Regardless, the extraction of charge at <3.0 V vs. Li/Li⁺ suggests that some of the crystal transformations that occurred during lithium over-insertion may be partially reversible.[136] As shown in Figure 24e, in the initial charging stage after over-insertion for cycles 13, 16 and 19 the plateau features disappear and the amount of lithium extracted at potentials <3.86 V vs. Li/Li⁺ (where the charging plateau of LiCoO₂ begins) decreases from ~1.8 mAh/g_{LiCoO₂} to ~0.4 mAh/g_{LiCoO₂}. The decrease in lithium extraction with each over-insertion of lithium indicates that the oxide crystal structure has undergone irreversible transformations during lithium over-insertion[136].

Figure 25a shows the discharge to 3.0 V vs. Li/Li⁺ and fixed load step to 7 mAh/g_{LiCoO₂} additional charge passed of the AlPO₄ coated LiCoO₂ for cycle 10, 11, 13, 16 and 19 (corresponding to the cycle prior to overdischarge testing, and after 3, 6 and 9 fixed load, 7 mAh/g_{LiCoO₂} over-insertion steps). The discharge profiles of all cycles 10-19 are shown in Figure 71a, but a selection of cycles is shown here for clarity. As shown, the discharge profile of the AlPO₄ coated LiCoO₂ is nearly the same after 9 fixed load, 7 mAh/g_{LiCoO₂} overdischarge periods. This subtle rounding in the discharge voltage profile is in contrast to the more significant discharge voltage profile change observed for as-received LiCoO₂ shown in Figure 24b and thus, the AlPO₄ coating is suppressing changes to the LiCoO₂ cathode that lead to unfavorable changes of the discharge voltage profile.

Figure 25b shows a zoom in of the voltage profile of the fixed resistive load, 7 mAh/g_{LiCoO₂} over-insertion step of the AlPO₄ coated LiCoO₂ for cycles 10, 11, 13, 16, and 19. All cycles are shown in Figure 71b but a selection is shown here for clarity. The voltage profile plateaus at 1.3-1.4 V vs. Li/Li⁺, similar to the as-received LiCoO₂, indicating that the AlPO₄ coating is not likely changing the material transformations that are occurring during over-insertion of lithium. As shown, the features of the voltage profile changes to a much lesser extent than those of the as-received LiCoO₂ shown in Figure 24c. Insertion reactions between 1.5-3.0 V vs. Li/Li⁺ increase from 2.0 to 4.5 mAh/g_{LiCoO₂} from cycle 10 to 19, about 50% less than that of the as-received LiCoO₂. In the AlPO₄ coated LiCoO₂ sample, the plateau region around 1.3-1.4 V vs. Li/Li⁺ is maintained in all overdischarge profiles in contrast to the as-received LiCoO₂, where it was no longer present in cycle 19. Therefore, the AlPO₄ coating is suppressing the permanent crystal structure

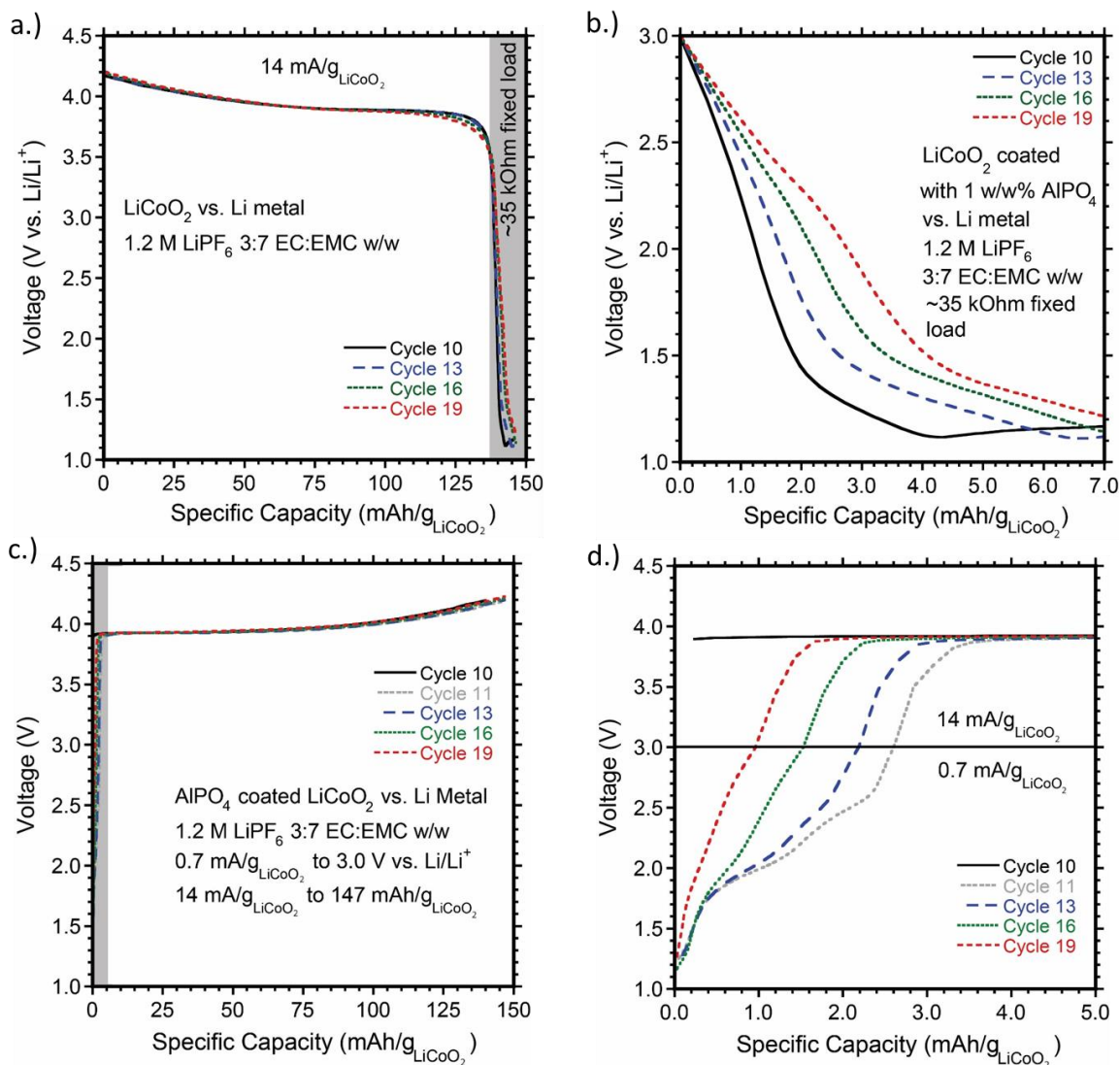


Figure 25: (a) Constant current discharge to 3.0 V vs. Li/Li^+ and fixed resistive load over-discharge curve of cycle 10, 11, 13, 16 and 19 for coin cell with 1.0 % w/w AlPO_4 coated LiCoO_2 cathode vs. Lithium metal (b) Fixed resistive load, 5% ($7\text{mAh/g}_{\text{LiCoO}_2}$) over-insertion step of cycles 10, 11, 13, 16 and 19 for coin cell with 1.0 % w/w AlPO_4 coated LiCoO_2 cathode vs. Lithium metal. (c) Constant current $0.7\text{ mA/g}_{\text{LiCoO}_2}$ charge to 3.0 V vs. Li/Li^+ and $14\text{ mA/g}_{\text{LiCoO}_2}$ charge to $147\text{ mAh/g}_{\text{LiCoO}_2}$ of cycles 10, 11, 13, 16 and 19 for coin cell with 1.0 % w/w AlPO_4 coated LiCoO_2 cathode vs. Lithium metal. (d) Zoom in of the first $5\text{ mAh/g}_{\text{LiCoO}_2}$ of charge of 1.0 % w/w AlPO_4 coated LiCoO_2 for cycles 10, 11, 13, 16 and 19.

changes that lead to permanent changes in the voltage profile of lithium over-insertion reactions into LiCoO_2 at $<3.0\text{ V vs. Li/Li}^+$. [136]

Figure 25c shows the charge voltage profiles of the AlPO_4 coated LiCoO_2 for cycles 10, 13, 16 and 19 (corresponding to the cycle prior to overdischarge testing, and after 3, 6

and 9 fixed load, 7 mAh/g_{LiCoO₂} overinsertion steps). All cycles are shown in Figure 72a but a selection is shown here for clarity. As shown, the charge voltage profile is nearly identical for all cycles shown, with a <10 mV increase in the initial charge polarization of the cell is observed on cycle 19, which is about 40 mV less than in the as-received LiCoO₂. This result is consistent with the AlPO₄ coating suppressing irreversible changes to the LiCoO₂ cause by repeated over-insertion of lithium that lead to the more significant increase in initial cathode polarization in the as-received LiCoO₂ compared to the AlPO₄ coated cathode.

Figure 25d shows a zoomed in view of the first 5 mAh/g_{LiCoO₂} of charge for cycles 10, 11, 13, 16 and 19 for the 1.0 %w/w AlPO₄ coated LiCoO₂. All cycles are shown in Figure 72b, but a selection is shown here for clarity. Similar to the as-received LiCoO₂, compared to cycle 10, which is a recharge after a normal discharge to 3.0 V vs. Li/Li⁺, in cycle 11, which is after a fixed load over-insertion, there are plateau-like features at ~2.0 V vs. Li/Li⁺ and 2.4 V vs. Li/Li⁺. Compared to the as-received LiCoO₂, in the AlPO₄ coated LiCoO₂, the plateau features extend to a greater extraction capacity on cycle 11 and more lithium is extracted at potentials less than the beginning of the extraction plateau of LiCoO₂ at ~3.88 V vs. Li/Li⁺ (~3.2 mAh/g_{LiCoO₂} for AlPO₄ coated vs. ~1.5 mAh/g_{LiCoO₂} for as-received). In cycles 13, 16 and 19, the extraction capacity below 3.88 V vs. Li/Li⁺ remains higher in the AlPO₄ coated LiCoO₂ compared to the as-received LiCoO₂. Additionally, plateaus at ~2.0 and ~2.4 V vs. Li/Li⁺ remain in cycle 13 in the AlPO₄ coated LiCoO₂, where in the as-received LiCoO₂ (Figure 24c) no plateau features were present in cycle 13. Thus, the result again indicates that the AlPO₄ coating is suppressing irreversible crystal structure changes in the LiCoO₂ cause by over-insertion of lithium.[136]

Collectively, the results shown in Figure 25 indicate that a 1.0 %w/w AlPO_4 coating on LiCoO_2 stabilizes the LiCoO_2 against detrimental material changes caused over-insertion of lithium at potentials <3.0 V vs. Li/Li^+ .

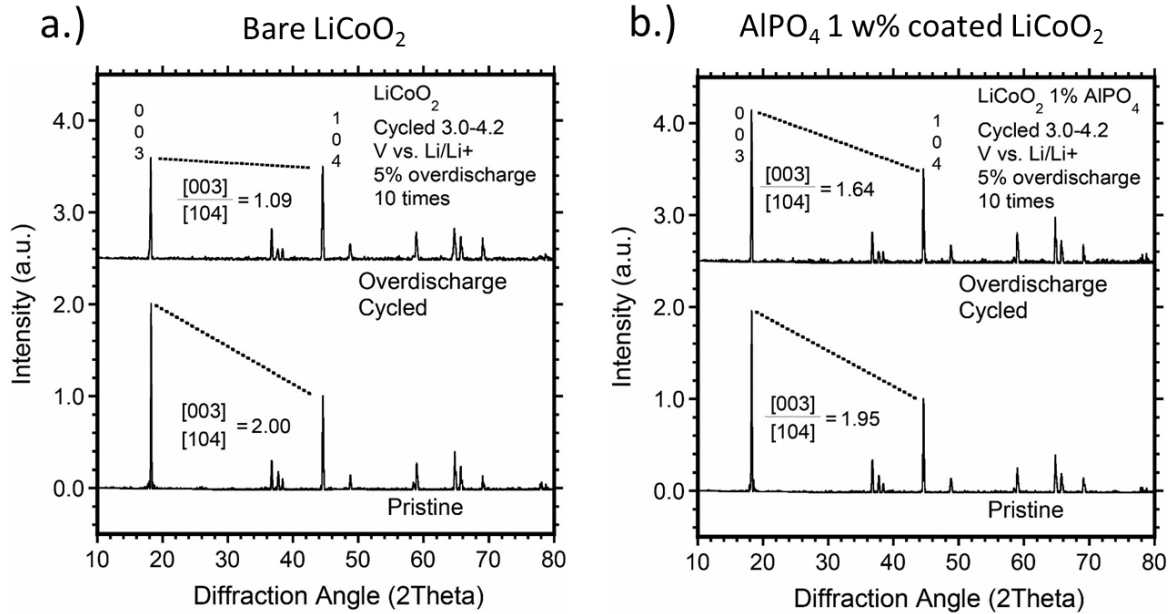


Figure 26: (a) X-ray Diffraction (XRD) pattern of as-received LiCoO_2 before (bottom) and after (top) 20 cycles including 10, 5% over-insertion steps by fixed resistive load. (b) X-ray Diffraction (XRD) pattern of AlPO_4 coated LiCoO_2 before (bottom) and after (top) 20 cycles including 10, 5% over-insertion steps by fixed resistive load.

Figure 26a shows the XRD patterns for pristine as-received LiCoO_2 and as-received LiCoO_2 after the testing described in the previous sections detailed in Figure 23a. In a pristine state, the XRD pattern of as-received LiCoO_2 on the bottom of Figure 26a is typical of LiCoO_2 in the $R\bar{3}M$ space group.[174,175] After over-insertion cycling of as-received LiCoO_2 , the relative intensity of the $\{003\}$ peak decreases significantly, with the ratio of $\{003\}$ peak to the $\{104\}$ peak decreasing from 2.00 to 1.09. Figure 26b shows the XRD patterns of AlPO_4 coated LiCoO_2 in a pristine state and after over-insertion cycling. As shown, the relative intensity of the $\{003\}$ peak decreases to a lesser extent than in the as-

received LiCoO₂. The ratio of the {003} peak to the {104} peak decreases from 1.95 to 1.64, about 84% of its original relative intensity compared to 55% for as-received LiCoO₂.

Previously, Wang *et al*[174] demonstrated with simulations that a decrease in the relative intensity of the {003} peak for layered LiCoO₂ indicates cation exchange between the cobalt and lithium ions in the octahedral layers. A prior study by Gummow and Thackeray[175] also interpreted a lower relative intensity of the {003} peak as cation mixing between octahedral layers based Reitveld refinements of time of flight neutron diffractometry and XRD. The change in relative intensity of the {003} peak in the XRD pattern in the present work supports that cation exchange in the octahedral layers of LiCoO₂ occurs during over-insertion of lithium. The greater decrease in relative intensity of the {003} peak in the as-received LiCoO₂ compared to the AlPO₄ coated LiCoO₂ after 10 repeated lithium over-insertion steps suggests that the AlPO₄ coating suppresses irreversible cation exchange between lithium and cobalt ions. The cation exchange may be occurring as part of the formation of high valence cobalt compounds and Li₂O during over-insertion of lithium or as a consequence of the formation of high valence cobalt compounds and Li₂O. Thus, the AlPO₄ coating may either be increasing the reversibility of cation exchange or suppressing the cation exchange process.

4.9.3 Conclusions

Stabilization of cathode active materials to over-insertion of lithium is necessary to improve the tolerance of advanced lithium ion cells with excess reversible lithium compared to cathode capacity to overdischarge or near zero volt conditions, such as an RLE cell. The present work has demonstrated that coating LiCoO₂ active particles with AlPO₄ improves tolerance to over-insertion of lithium. Cycling versus lithium metal in

coin cells shows that AlPO_4 coating changes the potential profile of lithium insertion as well as improves the reversibility of lithium insertion reactions <3.0 V vs. Li/Li^+ . Ten repetitions of over-insertion of lithium to an excess of 5% of the 3.0-4.2 V vs. Li/Li^+ capacity of LiCoO_2 shows that the AlPO_4 coated LiCoO_2 maintains its original charge/discharge potential characteristics significantly better than as-received LiCoO_2 . XRD data shows that the AlPO_4 coating effects a lessened decrease in the relative intensity of {003} peak of $R\bar{3}M$ space group after repeated lithium over-insertion. This result supports that the mechanism by which the AlPO_4 coating improves the tolerance of LiCoO_2 to over-insertion is suppression of irreversible cation exchange between the octahedral layers during over-insertion of lithium into LiCoO_2 . This is considering that no major deformations were observed by SEM after cycling (see Figure 66). Overall, the present results show that AlPO_4 coating of LiCoO_2 active particles is a promising method to improve the overdischarge and overcharge tolerance of advanced lithium ion cells with excess reversible lithium compared to the cathode capacity.

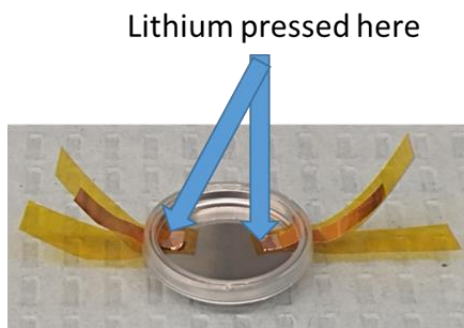
4.10 Studying EAP vs. amount of reversible lithium added to the cell

A 0.9 mAh, 4-electrode coin cell with an MCMB counter electrode, LiCoO_2 working electrode, a lithium metal auxiliary electrode and a lithium metal reference electrode (see Figure 27a) was constructed in order to measure the Electrode asymptotic potential of a cell as a function of how much reversible lithium was added to the cathode/cathode anode pair. The MCMB and LiCoO_2 electrodes were fabricated in the same manner as described in section 4.1. Before electrolyte addition and final cell assembly, lithium metal was pressed onto the copper tabs shown in Figure 27a inside a dry Argon glove box maintained

at <1 ppm oxygen and <1 ppm water to form the lithium metal auxiliary electrode and lithium metal reference electrode.

The cell was cycled 5 times 3.0-4.1 V at a C/10 constant current for conditioning. Then, after the 5th discharge lithium was added galvanostatically at a C/100 rate to the cathode from the auxiliary lithium metal electrode until the cathode potential was 3.0 V vs. Li/Li⁺. Then, a fixed load of 33.333 kOhm was applied between the LiCoO₂ cathode and MCMB anode for 2 days. Following this, 0.018 mAh of reversible lithium was added from the auxiliary lithium metal electrode to the cathode at a C/100 rate and then the load was applied again between the LiCoO₂ cathode and MCMB anode. This process was repeated until the test was stopped.

a.)



b.)

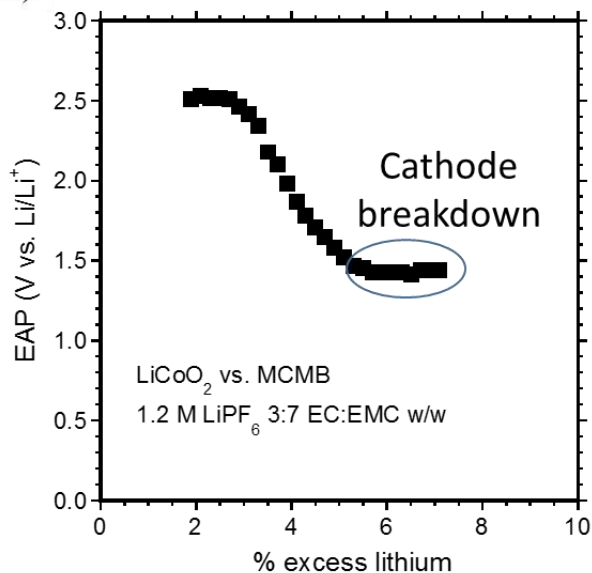


Figure 27: (a) Picture of 4-electrode coin cell construction. (b) Plot of the Electrode Asymptotic Potential (EAP) of a LiCoO₂/MCMB lithium ion cell as a function of the amount of lithium added to the cell as a percentage of cell capacity.

As shown in Figure 27b, the initial EAP is 2.5 V vs. Li/Li⁺ at 2% excess lithium added (during cathode insertion step at C/100) to the cell. As reversible lithium is added to the LiCoO₂/MCMB electrode pair, the EAP decreases until at 5% excess lithium

addition to the cell, the EAP stops changing at 1.4 V vs. Li/Li⁺, which can be attributed to the insertion plateau of LiCoO₂ that is shown in Figure 24c corresponding to the formation of Li₂O[136]. Collectively, this test shows that the EAP of a cell can be set to value sufficient to not damage either electrode during near zero volt storage. The amount of lithium added to the cell can vary by up to 1-2% of cell capacity and still be sufficient, which can help relax manufacturing controls and lower costs of implementation.

4.11 Applying anode pre-lithiation method to NCA/MCMB cells

4.11.1 Experimental Methods and Results

The anode pre-lithiation approach to near zero volt storage tolerance of lithium ion cells was applied to another common electrode pairing, a LiNiCoAlO₂ (NCA) cathode and a MCMB anode. Cathodes slurries were prepared by mixing LiNiCoAlO₂, SuperC and PVDF in a 92:4:4 ratio using NMP as the solvent. PVDF was first dissolved, followed by the addition of SuperC and then addition of LiNiCoAlO₂. A 20 minute mixing step after the addition of each component was carried out using a Thinky planetary mixer. After final mixing the slurry was coated onto an aluminum foil with a doctor blade at a loading of 15 mg/cm² yielding an areal capacity of 2.7 mAh/cm².

The anode was prepared by mixing MCMB's into a slurry with SuperCTM Carbon Black, SFG-6 and PVDF (Solvay) in a 93:0.3:2.7:4 w/w ratio using N-methyl-1-Pyrrolidone (NMP) as the solvent. The PVDF was dissolved first in the NMP and then the conductive additive and active material was added in succession with intermediate mixing steps. All mixing was done with a Thinky AR-100 planetary mixer. The slurry was coated onto a 20 μm thick copper foil using a doctor blade. The composite was then dried overnight in a vacuum oven at 90 °C and then calendared to a composite density of ~1.2

g/cm^3 . The anode is loaded at $\sim 10.4 \text{ mg/cm}^2$ of MCMB/SFG-6, giving an areal capacity of $\sim 3.1 \text{ mAh/cm}^2$ (conservatively using 300 mAh/g as the capacity of the active material). The area of the electrodes used is 4.5 cm^2 , giving a total cathode capacity of $\sim 12.2 \text{ mAh}$ and an anode capacity of $\sim 13.95 \text{ mAh}$. The 15% excess of anode capacity compared to the cathode is common practice to reduce the risk of lithium plating on the anode during cycling and manage the first cycle loss of the NCA.[133]

Electrochemical testing

Experimental 3 electrode pouch cells were constructed with lithium reference electrodes and a 1.2 M LiPF_6 3:7 EC:EMC v/v electrolyte. A lithium metal reference was placed to the side of the cathode/anode stack in the same configuration as shown in Figure 10b. The RLE cell was constructed with an anode that was pre-lithiated in the same manner as described in section 4.3. Cells were cycled between 3.0 V cell voltage and 4.3 V vs. Li/Li^+ cathode potential. Each cell was cycled for 1 cycle at $C/20$ then 4 cycles at $C/10$ to condition the cell. After the 5th cycle discharge, a fixed load of $2.5 \text{ k}\Omega$ was applied to the cell.

The 5th cycle discharge and fixed load step of the RLE and conventional NCA/MCMB cells is shown in Figure 28a and b, respectively. As shown in Figure 28b, that the EAP of the conventional is 3.21 V vs. Li/Li^+ , which is high enough that some copper dissolution from the anode current collector can be expected. As shown in Figure 28a, in the RLE cell, the EAP is decreased to 2.63 V vs. Li/Li^+ , which is low enough (see Figure 9d) that no copper dissolution is expected to be occurring.

The recharge performance of the RLE and conventional cell was tested with the testing protocol shown in Figure 29a. The cell was cycled for 5 cycles from 3.0 V cell voltage to 4.3 V vs. Li/Li⁺ cathode potential, as discussed above, to complete formation. After the 5th cycle discharge, a fixed load of 2.5 kOhm was applied for the three days (corresponding to data shown in Figure 28). Afterwards, the cells were recharged at a C/200 rate until the cell voltage reached 3.0 V to gradually bring the cell back into its normal voltage range. A very gradual initial charge after near zero volt storage like that done in the present work has been done previously during testing of commercial near zero volt capable cells[137] and previous near zero volt storage studies.[173] The cell was then cycled at C/10 and after the discharge, a 2.5 kOhm load was again applied and the cycle repeated.

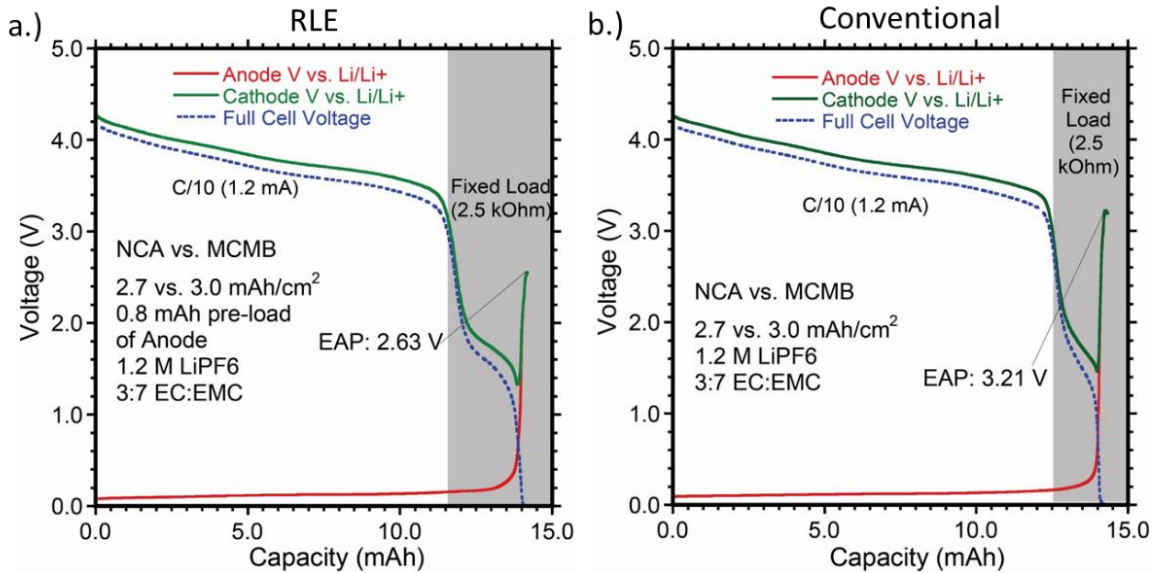


Figure 28: (a) Electrode potentials and cell voltage during 5th C/10 discharge and 3-day fixed load storage plotted against cell capacity for an RLE NCA/MCMB cell. (b) Electrode potentials and cell voltage during 5th C/10 discharge and 3-day fixed load storage plotted against cell capacity for a conventional NCA/MCMB cell.

As shown by the data in Figure 29a and b, both the RLE and conventional cells showed strong recharge performance after 10, 3 day near zero volt storage periods under

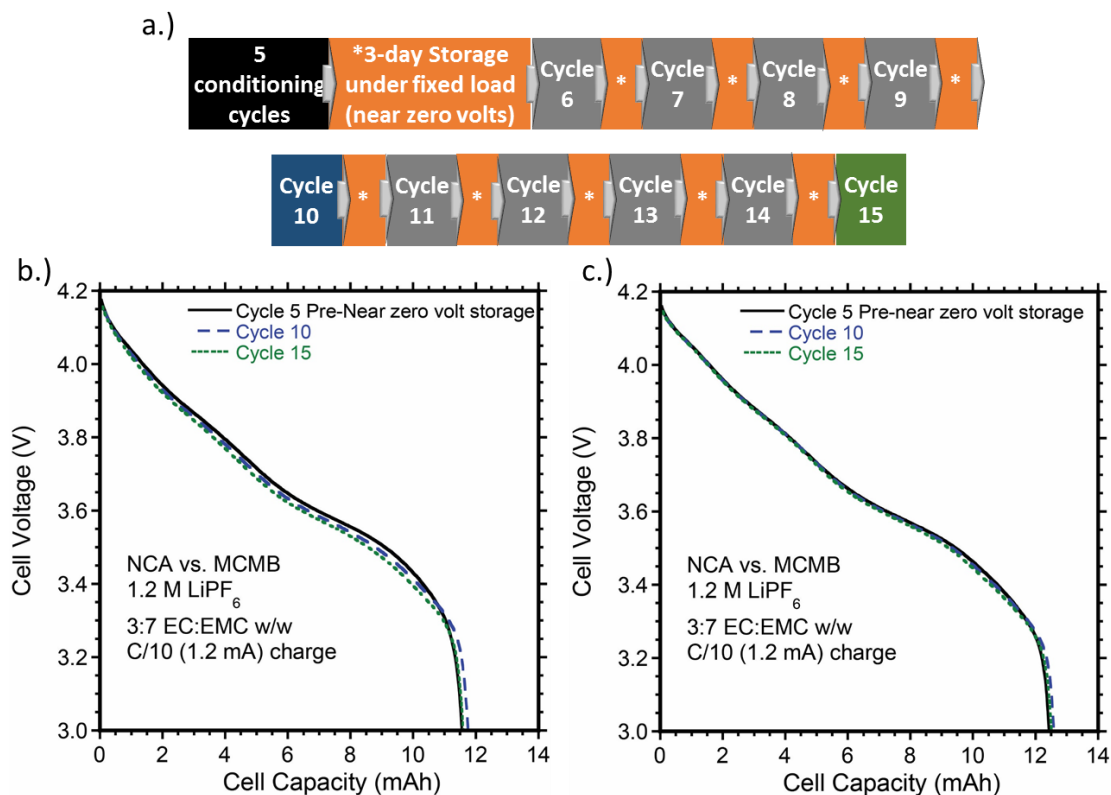


Figure 29: (a) Discharge profile of RLE NCA/MCMB cell prior to near zero volt storage and after 5 and 10, 3-day near zero volt storage periods. (b) Discharge profile of conventional NCA/MCMB cell prior to near zero volt storage and after 5 and 10, 3-day near zero volt storage periods.

fixed load. Each cell maintained $\sim 100\%$ of its discharge performance. However, a cyclers error resulted in the conventional cell being charged at $C/200$ for nearly the entire charge period for several of the testing cycles, which may be unduly making the discharge performance appear better than it is.

Following the 10, 3-day near zero volt storage periods, each cell underwent a rate study in which the charge rate was held constant at $C/10$ and the discharge rate was changed from $C/10$ to $C/5$, $C/2$, C , $2C$ and $5C$. The resulting normalized discharge energy at each discharge rate is plotted in Figure 30. As shown, the RLE maintained a higher discharge energy than the conventional cell at a $2C$ and $5C$ discharge rate, indicating that the near

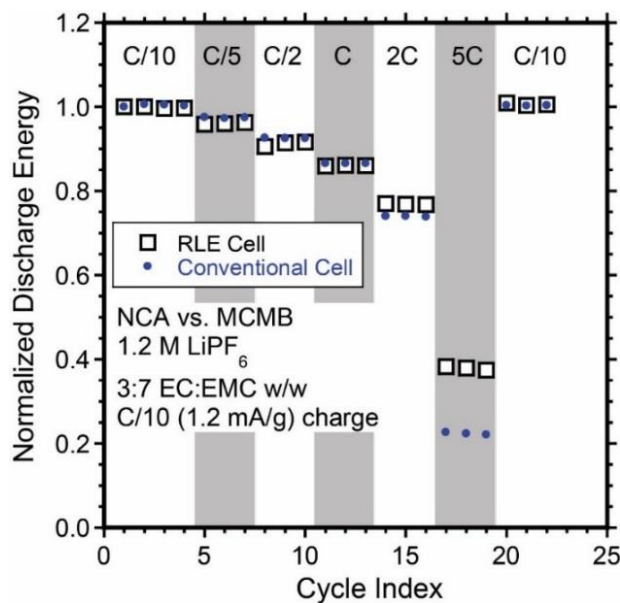


Figure 30: Discharge energy (normalized to cycle 1) of RLE and conventional cells after ten, 3-day near zero volt storage periods.

zero volt storage periods may have reduced the rate capability of the conventional cell while not degrading the RLE cell.

4.12 Scale up of reversible lithium management to x3450 pouch cells

To demonstrate the scalability of using reversible lithium management during the construction of a lithium ion cell to enable tolerance to near zero volt storage, a reversible lithium modification method was developed that can be integrated into the SoLith® semi-automated pouch cell construction line in the Battery Prototyping Center at the Rochester Institute of Technology. Specifically, a 5-electrode bath cell was developed in which the z-folded electrode stack of the cathode and anode was removed from the SoLith® semi-automated pouch cell construction line after stacking of the cathode, anode and separator and tab welding. As shown in the photograph in Figure 31a the electrode/separator stack was clipped onto copper electrical leads that were anchored through a bottle screw-cap by epoxy. Three additional copper electrical leads were anchored to the bottle screw cap and

lithium metal was pressed to their ends. Two of the lithium metal electrodes were placed normal to the broad face of the electrode/separator stack and will be referred to as the lithium source electrodes. The 3rd lithium metal electrode was placed in plane with the electrode/separator stack and served as a reference electrode. The screw cap was then secured to its corresponding bottle made from high density polyethylene. The bottle was filled with 1.2 M LiPF₆ electrolyte to a level such that all electrodes were fully immersed in electrolyte as depicted in Figure 31b.

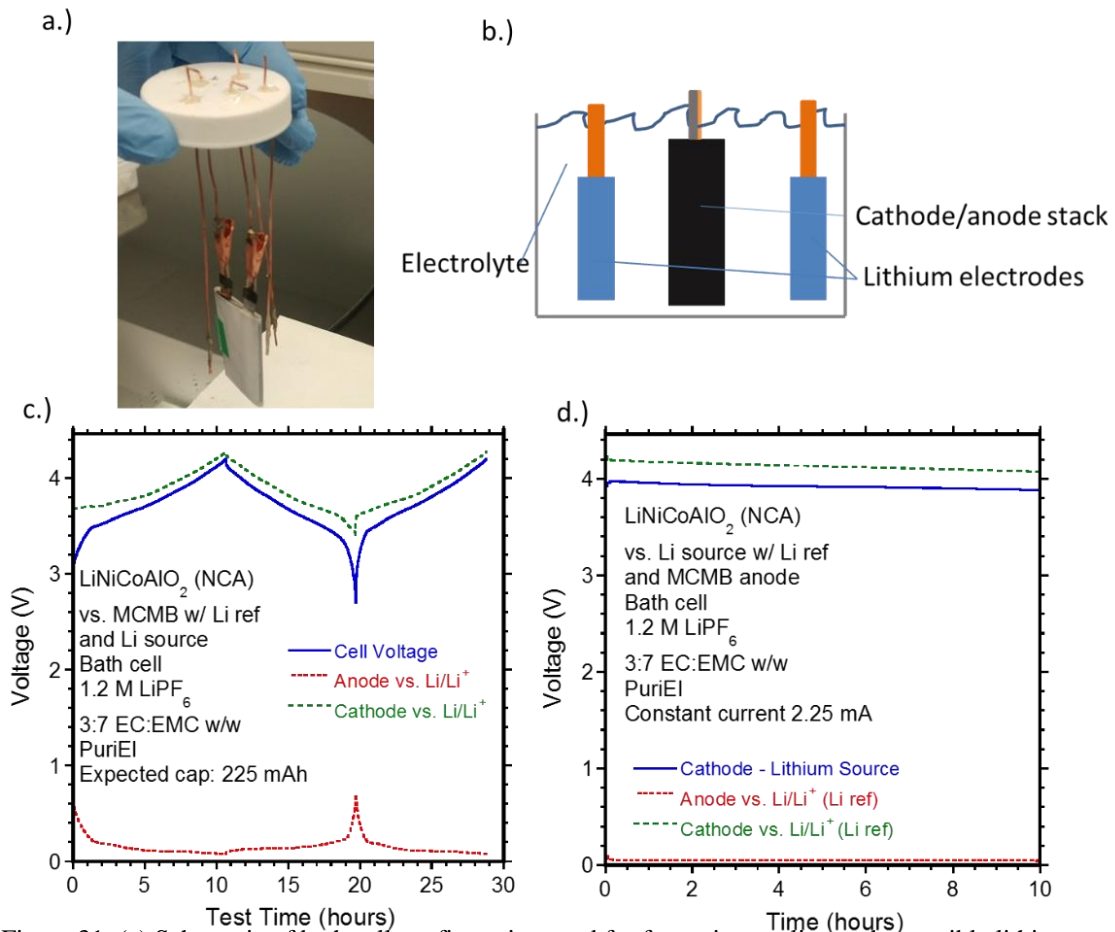


Figure 31: (a) Schematic of bath cell configuration used for formation cycling and reversible lithium addition. (b) Picture of electrode connection method for bath cell showing the z-fold electrode/separator stack connected by clips and the lithium metal electrode which consist of lithium metal pressed onto a copper wire. (c) Cell voltage, anode and cathode potentials during the 1st C/10 charge and discharge cycle followed by a C/10 charge to 4.2 V cell voltage. (d) Cathode potential vs. lithium reference electrode, cathode potential vs. lithium source and anode potential vs. lithium reference electrode during the first addition of 25.5 mAh of reversible lithium to the electrode stack.

Figure 31c shows the cell voltage, cathode potential and anode potential profiles for the first charge, discharge and charge of the electrode/separator stack after cell assembly. As shown, the electrode potential profiles match what is expected under similar cycling conditions for MCMB[176] and NCA[177] indicating the cell setup is valid. The first cycle coulombic efficiency is 80%, which is lower than the normally observed 90% first cycle coulombic efficiency for this material combination but may be due to more anode surface exposure in the bath electrode than in a typical lithium ion cell.

Figure 31d shows the cathode vs. Li source, cathode vs. Li reference and anode vs. Li reference during the first addition of reversible lithium in an amount of 10% (25.5 mAh) of the expected electrode/separator stack capacity (which will be the expected cell capacity after final cell construction). The addition is done at a current of 2.25 mA over 10 hours to mitigate resistance in the electrolyte arising from relatively large diffusion distances (~1 cm) between the lithium source electrodes and the electrode/separator stack. Lithium is added to the cathode since the cathode is at a high potential (>4.0 V vs. Li/Li⁺) after charging the electrode/separator stack leading to low risk of lithium plating. As shown in Figure 31d, the cathode potential decreases linearly from ~4.1 V vs. Li/Li⁺ to ~4.05 V vs. Li/Li⁺ over the 10 hour lithium addition step, consistent with lithium intercalation.

Figure 32 shows 2 charge and discharge cycles of the electrode/separator stack after the lithium addition step. As shown, the cell initially charges with ~25 mAh of capacity after the lithium addition consistent with the amount of reversible lithium added to the electrode/separator stack. Such consistency indicates that nearly all added reversible lithium was intercalated into the cathode active material rather than being lost to side reactions.

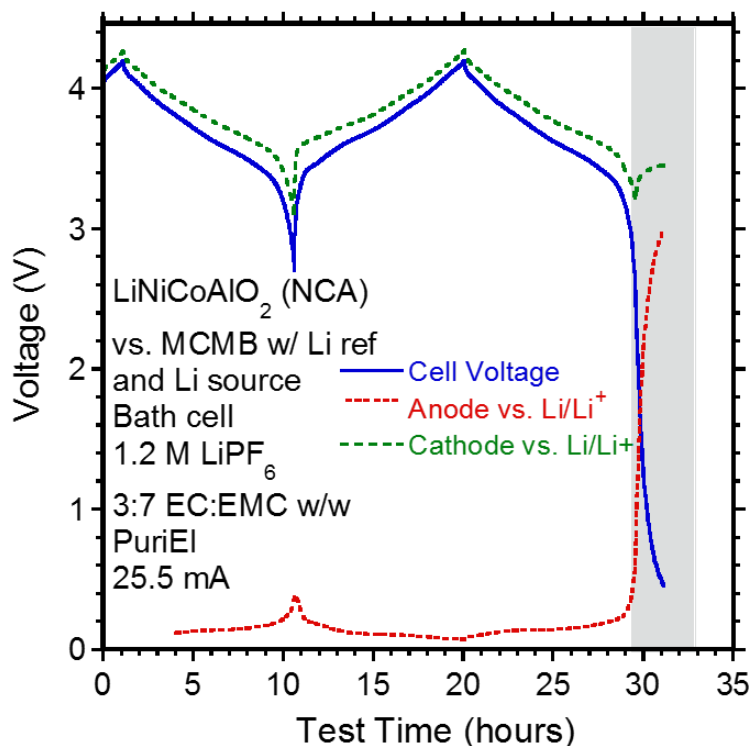


Figure 32: Cell Voltage, cathode and anode potential during 2 cycles of C/10 charge and discharge of cell electrode stack in bath cell after 1st addition of 25.5 mAh of reversible lithium from lithium source electrode. After the second C/10 charge and discharge a fixed resistive load of 105 Ohms is applied to the electrode stack of the cell by the Arbin Cycler (gray shaded region).

At the end of the first discharge shown in Figure 32, the anode potential is ~0.5 V vs. Li/Li⁺, lower than that in the discharge prior to the lithium addition step shown in Figure 31c, consistent with more reversible lithium present as discussed in section 4.3. However, as shown in Figure 32 after the second charge/discharge and application of a fixed resistive load the anode potential increases to 3.0 V vs. Li/Li⁺, at which point the resistive load was removed to prevent copper dissolution. Such an increase in the anode potential indicates that more reversible lithium is needed in the system to lower the EAP to an acceptable value less than the copper dissolution potential.

Figure 33a shows the cathode vs. Li source potential, cathode vs. Li reference potential, and anode vs. Li reference potential during the second addition of 25.5 mAh of reversible lithium to the electrode/separator stack. The lithium addition was performed after the fixed load step shown in Figure 32 was ended. As shown, the cathode potential decreases during the 10 hour lithium addition step, consistent with intercalation of lithium ions. As shown in Figure 33b however, when a fixed resistive load is again applied, the cathode and anode potentials trend towards an EAP of >3.0 V vs. Li/Li^+ , so the fixed load was removed after about 2 minutes after application.

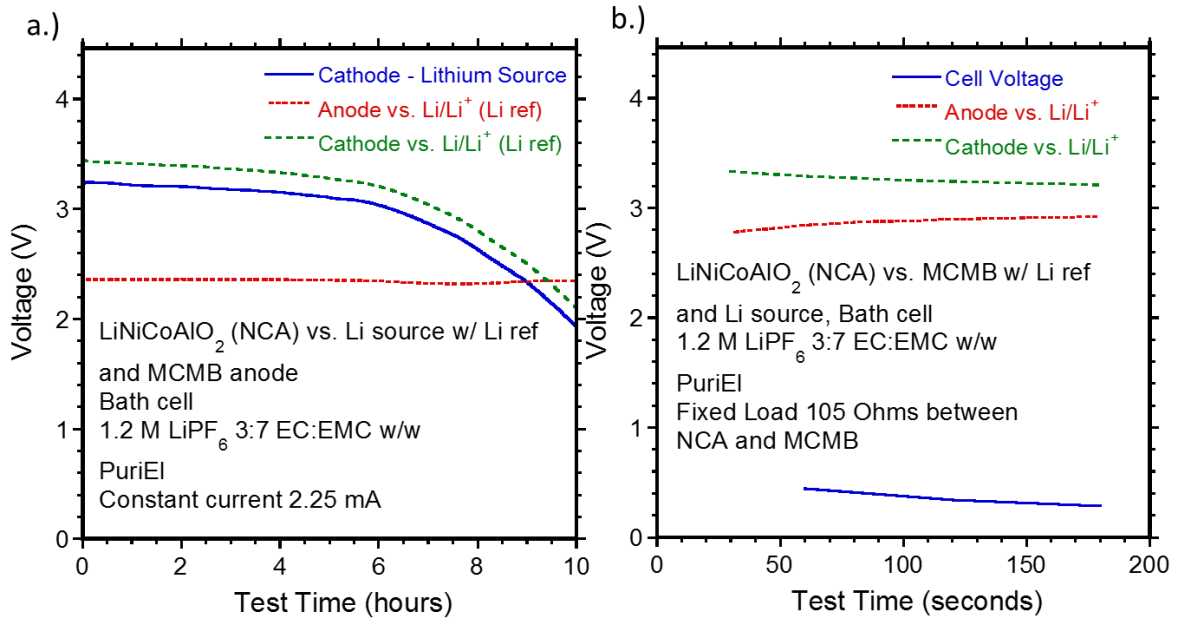


Figure 33: (a) Cathode potential vs. lithium reference electrode, cathode potential vs. lithium source and anode potential vs. lithium reference electrode during the second addition 25.5 mAh of reversible lithium to the electrode stack. (b) Cell Voltage, anode and cathode potentials during the application of a fixed load of 105 Ohms to the electrode stack of the cell after the second addition of 25.5 mAh of reversible lithium

A third lithium addition step was performed and the cathode vs. Li source potential, cathode vs. Li reference potential, and anode vs. Li reference potential are shown in Figure 34a. As shown, the cathode potential vs. the Li reference electrode plateaus at ~ 1.9 V vs. Li/Li^+ over the 10 hour lithium addition step. Following the lithium addition step, a fixed

resistive load of 105 Ohms was applied to the electrode/separator stack, and the cell voltage, anode and cathode potential are shown in Figure 34b. As shown, the EAP of the cell is now at ~ 2.1 V vs. Li/Li^+ , which is sufficiently less than the copper dissolution potential.

After the third lithium addition step and determination of a sufficient EAP, the electrode/separator stack was removed from the electrolyte bath and re-inserted into the SoLith® semi-automated pouch cell line to construct it into an x3450 pouch cell. A reference electrode was inserted into the pouch cell to enable measurement of the electrode potentials in the cell.

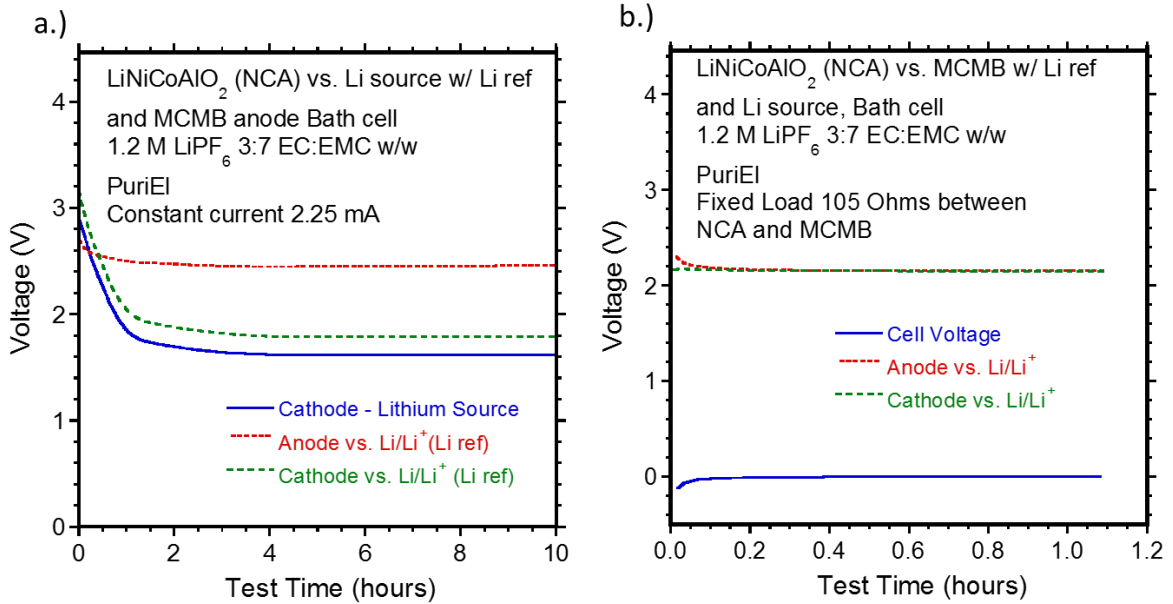


Figure 34: (a) Cathode potential vs. lithium reference electrode, cathode potential vs. lithium source and anode potential vs. lithium reference electrode during the third addition 25.5 mAh of reversible lithium to the electrode stack. (b) Cell Voltage, anode and cathode potentials during the application of a fixed load of 105 Ohms to the electrode stack of the cell after the third addition of 25.5 mAh of reversible lithium

The as-constructed pouch cell was cycled 3 times at C/10 between 2.7-4.2 V cell voltage and then an external resistor (120 Ohm) attached to an analog voltmeter (See Figure 35a) was applied to the cell after the third discharge. The resistor remained on the cell for 14 days, during which time the potential of the cathode, anode and cell were monitored by an Arbin BT2000 cyler. The cell voltage, cathode potential and anode potential during the 14-day period with an applied resistor is shown in Figure 35b. As shown, the EAP of the cell is about 2.2 V vs. Li/Li⁺, in close agreement with that measured in the bath cell (Figure 34b) and is very stable over the 14-day period. Importantly, the EAP is less than 3.1 V vs. Li/Li⁺, so no copper dissolution is expected to be occurring.

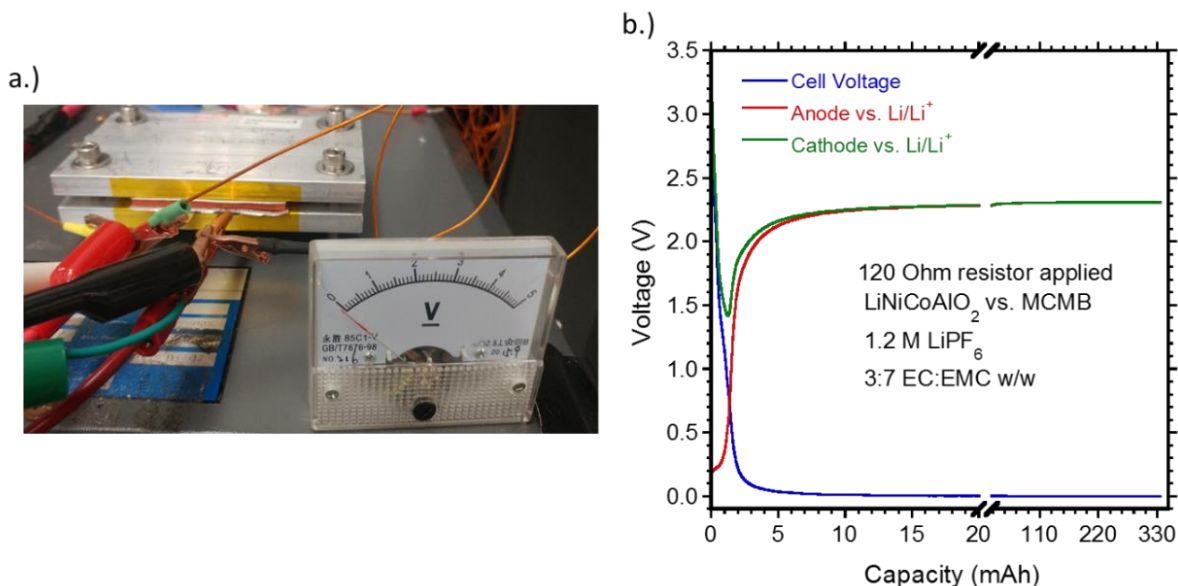


Figure 35: (a) Photograph of pouch cell with a resistor of 120 Ohms applied to the cell and an external analog voltmeter monitoring cell voltage. (b) Cell voltage, anode potential and cathode potential as monitored by the Arbin cyler during 14-day period with a resistor applied to the pouch cell shown in part a.

Figure 36 shows an overlay of the cathode potential, anode potential and cell voltage for the discharge before the 14 day period at near zero volts under fixed resistive load and after the 14 day period at near zero volts under fixed resistive load. As shown,

the voltage profiles are nearly identical, indicating that in this X3450 pouch cell that underwent reversible lithium management during construction did not lose discharge capacity after being stored at near zero volts for 14 days. Thus, scaling up of the reversible lithium management approach to near zero volt storage was successful in construction a cell-phone size battery that was high tolerant to a 14 day near zero volt storage period after construction.

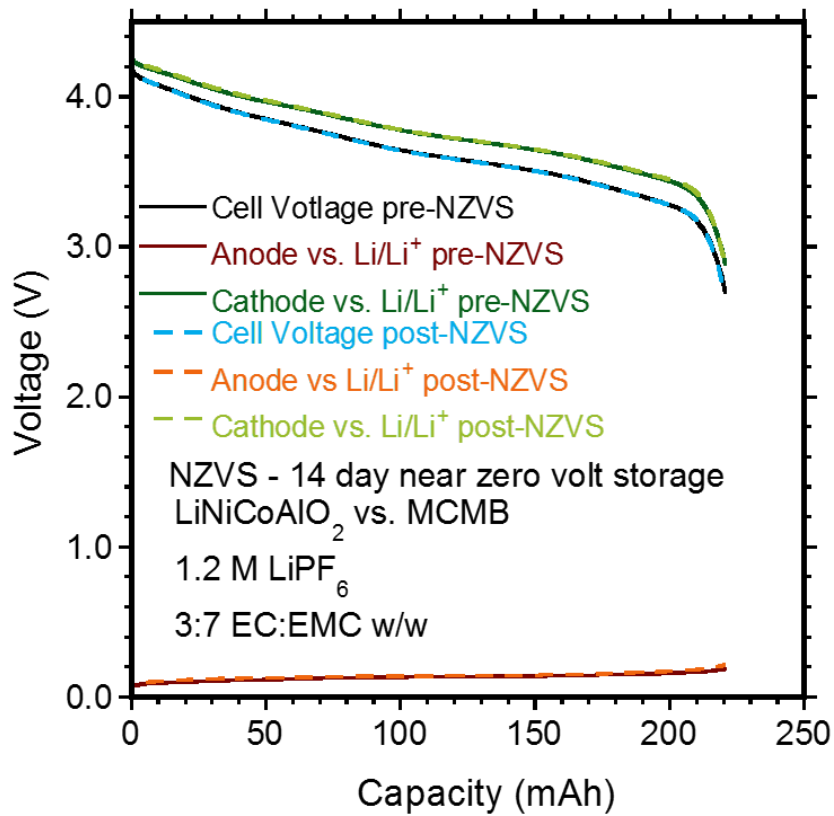


Figure 36: Overlay of cell voltage, cathode potential and anode potential during the C/10 discharge before and after a 14-day period in a near zero volt state with and applied resistor.

5. Use of high first cycle loss, high energy density lithium rich cathode materials to enable near zero volt storage tolerance

The following chapter is adapted from K. R. Crompton, J. W. Staub, M. P. Hladky, and B. J. Landi, "Lithium rich cathode/graphite anode combination for lithium ion cells with high tolerance to near zero volt storage," *J. Power Sources*, vol. 343, pp. 109–118, 2017. Figures in this chapter and Chapter 8 are reprinted with permission from Elsevier.

5.1 Introduction

Lithium rich cathode materials exhibit a high first cycle loss[178] which could potentially be used to generate a cell with excess reversible lithium. Lithium rich cathode materials have already generated significant interest in recent years due to their increased energy densities over current state of the art cathode materials[178]. In the present work, the effect of a lithium rich cathode's first cycle loss to maintain the anode potential less than the copper dissolution potential during near zero volt storage under fixed resistive load is investigated. Reference electrode measurements are utilized to investigate the behavior of the electrode potentials of a Li-rich/graphite lithium ion cell during extended near zero volt storage periods under fixed resistive load. The electrode potential behavior during the transient period in which the cell discharges to near zero volts is measured and the electrode asymptotic potential (EAP) of the cell is characterized once the cell reaches a quasi-equilibrium, near zero volt state. The recharge performance of the 3-electrode Li-rich/graphite cells after several multi-day near zero volt storage periods is also reported. Conventional 2-electrode pouch cells are tested for the effects of a 3-day near zero volt storage period under fixed resistive load on cell discharge rate capability and longer term cycling stability compared to cells stored at open circuit. Lastly, elevated temperature

testing is also performed to determine the near zero volt storage tolerance of Li-rich/graphite cells at 40°C.

5.2 Experimental

Electrode preparation

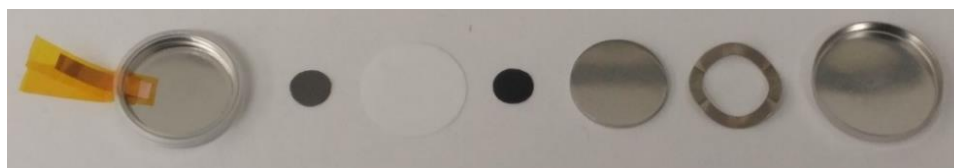
Cathodes were prepared by mixing TODA HE5050 ($0.49\text{Li}_2\text{MnO}_3 \cdot 0.51\text{LiNi}_{0.37}\text{Co}_{0.24}\text{Mn}_{0.39}\text{O}_2$) into a slurry with SuperC™ Carbon Black, TIMREX® SFG-6 and Solef® PVDF in an 86:2:4:8 mass ratio using N-methyl-1-Pyrrolidone (NMP) as the solvent. The slurry preparation consisted of dissolving Polyvinylidene Fluoride (PVDF) in NMP, followed by mixing in the conductive additives (Carbon Black and SFG-6) and then addition of the HE5050 with intermediate mixing steps. Mixing steps were each performed for 20 minutes using a Thinky AR-100 planetary mixer. The composite slurry was coated onto a 20 μm aluminum foil using a doctor blade. The coated cathode was dried overnight in a vacuum oven at 90°C and then calendared to a composite density of ~1.1 g cm⁻³. The final active material areal loading was 10.7 mg cm⁻² resulting in a first cycle charge areal capacity of 3.26 mAh cm⁻² using the measured 305 mAh g⁻¹ first cycle charge capacity at a 0.1225 mA g⁻¹ (~C/20) extraction rate (See Figure 51a) and a discharge areal capacity of ~2.72 mAh cm⁻² using the measured 254 mAh g⁻¹ discharge capacity at a 0.1225 mA g⁻¹ (~C/20) insertion rate (See Figure 51a). The cathode will be referred to as the HE5050 cathode.

Anodes were prepared by mixing Osaka Gas 25-28 mesocarbon microbead (MCMB) into a slurry with SuperC™ Carbon Black, TIMREX® SFG-6 and Solef® PVDF in a 93:0.3:2.7:4 mass ratio using NMP as the solvent. The slurry preparation consisted of dissolving PVDF in NMP, then by mixing in the conductive additives (Carbon Black and

SFG-6) and then addition of the MCMB with intermediate mixing steps in a Thinky AR-100 planetary mixer. The composite slurry was coated onto a 20 μm copper foil using a doctor blade. The electrode was then dried overnight in a vacuum oven at 90°C and calendared to a composite density of 0.985 g cm^{-3} . The final active material areal loading was 11.23 mg cm^{-2} resulting in a reversible areal capacity of 3.42 mAh cm^{-2} using the measured 311 mAh g^{-1} extraction capacity of the graphite (MCMB, SFG-6) in the composite (See Figure 51b). Using the measured first cycle insertion capacity of 323 mAh g^{-1} (which includes SEI formation) the first cycle anode insertion areal capacity is 3.63 mAh cm^{-2} . The first cycle insertion anode areal capacity is designed to be at least 10% excess (actual is 11%, see Figure 52a) capacity relative to the first cycle charge capacity of the cathode in order for there to be sufficient capacity to accommodate all lithium intercalated into it during the first charge without lithium deposition on the anode. The anode will be referred to as the MCMB anode.

Electrochemical testing

Cells incorporating reference electrodes were constructed using single layer pouch type cells with electrodes of 4.5 cm^2 and the cells were rated at 12 mAh capacity. The cathode and anode were stacked with a Celgard™ separator between them and a 1.2 M LiPF_6 3:7 ethylene carbonate:ethyl methyl carbonate v/v was injected before final sealing of the pouch cell. In the case of pouch cells with a reference electrode, a lithium chip



Picture 1: (a) Electrode potentials and cell voltage during first charge with a constant current (CC) of 0.6 mA. (b) Electrode potentials and cell voltage during the first discharge with CC of 0.6 mA.

pressed into a copper mesh with an ultrasonically bonded copper tab was placed to the side of the cathode/anode stack on both sides of the separator. A schematic of the pouch cell setup can be found in a previous study[173].

In the case of coin cells with a reference electrode, a copper tap was inserted around the gasket that seals the cell with Kapton film on both sides of the tab to electrically isolate it from the lid of the coin cell as shown in Picture 1. A lithium chip was then pressed onto the copper before construction of the coin cell. The coin cell was assembled in the order anode->separator>cathode>spacer>wave spring>case (left to right in Picture 1), all while ensuring that the lithium and copper did not physically contact the coin cell case or electrodes. Lithium chip incorporation, electrolyte injection and final pouch cell sealing/coin cell crimping was done in an Argon glove box maintained at <1 ppm oxygen and <1 ppm water.

Pouch cells were cycled using an Arbin BT-2000 cycler outfitted with auxiliary voltage measurements. The cell voltage, cathode potential and anode potential were all monitored independently during cycling of 3-electrode cells. Cells utilizing a lithium reference electrode were cycled galvanostatically to a cathode potential of 4.6 V vs. Li/Li⁺ and discharged to a full cell voltage of 2.0 V. Utilizing the cathode potential as the charge cutoff point ensures that the cathode is fully utilized but not overcharged. Conventional 2-electrode were cycled between 2.0 and 4.5 V cell voltage. All tests referred to as 3-days in duration constitute a 72-hour period and all tests referred to as 7-days in duration constitute a 168-hour period. All electrochemical tests were performed at room temperature (~21 °C).

The lithium metal reference electrode used in the present work allows for monitoring of the electrochemical potentials of both the cathode and the anode vs. the Li/Li⁺ redox couple during cycling. The present setup is suitable for DC voltage measurements since the measured impedance between the reference electrode and either electrode is ≤ 10.0 kOhm. The Arbin cycler used in the present study uses a ~ 10 GOhm impedance for DC voltage measurements, which would result in a sufficiently low measurement error of ≤ 1.0 μ V caused by the IR drop in the fabricated cell. Additionally, the difference of the measured cathode potential and anode potential deviates by < 8 mV from the measured cell voltage throughout all cycling in the present work, indicating the setup is valid[173].

5.3 Results and discussion

First Cycle charge and discharge

It is well documented that many lithium rich layered cathode materials have a high irreversible capacity loss during the first charge/discharge cycle[179–203] of $\sim 20\%$. In the case of the material used in the present study, the first cycle loss is measured to be 19.7% (see Figure 51a). In comparison, the graphitic anode exhibits a first cycle loss of about 5% due to SEI formation (See Figure 51b). In full cells, the cathode and anode must be capacity matched so that the anode has sufficient capacity to manage all lithium extracted from the cathode on the first cycle charge to avoid lithium deposition. In the present work, the first cycle anode insertion areal capacity (which includes SEI formation and intercalation capacity) is designed to be about 10% (actual is 11%, see Figure 52a) excess of the cathode's first cycle charge capacity. The first charge of the HE5050/MCMB cell shown in Figure 37a requires 13.52 mAh of charge capacity to charge until the cathode reaches 4.6 V vs. Li/Li⁺. As shown in Figure 37a, at the end of the first cycle charge, the

anode electrochemical potential is 28 mV vs. Li/Li^+ , indicating it is not fully intercalated with lithium and confirms the designed excess capacity. Figure 37b shows the first discharge, which delivers 11.3 mAh at the cutoff cell voltage of 2.0 V.

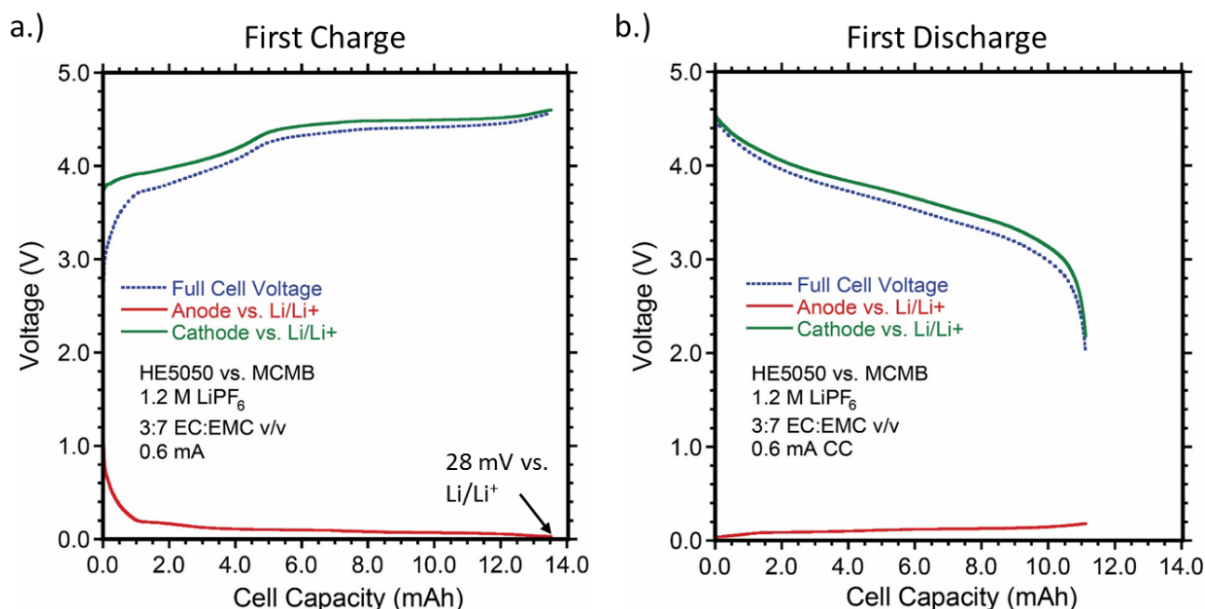


Figure 37: (a) Electrode potentials and cell voltage during first charge with a constant current (CC) of 0.6 mA. (b) Electrode potentials and cell voltage during the first discharge with CC of 0.6 mA.

At the end of discharge, the anode potential remains in its normal 100-200 mV vs. Li/Li^+ range (See Figure 37b) indicating the anode still contains reversible lithium at the end of discharge. The insertion transformations of the cathode that occur between the resulting cathode discharge range of 2.1-4.6 V vs. Li/Li^+ are fully saturated as evidenced by the cathode potential decreasing rapidly at the end of discharge.

Using the calculations detailed in the supplemental information, the amount of reversible lithium in the cell can be tracked throughout cycling based on the charge/discharge capacities of the cell and the amount of lithium consumed by SEI formation on the anode as measured in half-cells. Specifically, after each charge, the amount of lithium consumed by SEI on the anode, as measured by half-cell data, is subtracted from the amount of lithium inserted into the anode on charge (i.e. the cell's

charge capacity) to yield the amount of reversible lithium in the anode after charge. Then, from this calculated amount of reversible lithium in the anode, the amount of lithium extracted from the anode on discharge (i.e. the cell's discharge capacity) is subtracted. The amount of reversible lithium in the anode after discharge of the cell to 2.0 V will be referred to as the amount of excess reversible lithium in the cell. The amount of excess reversible lithium calculated to remain in the anode after the first cycle discharge is 1.85 mAh (See Figure 52c).

5.4 Electrode behavior during fixed resistive load near zero volt storage

Experimental 3-electrode cells were conditioned for 4 additional cycles at a 1.2 mA charge/discharge current (i.e. C/10 based on rated cell capacity) after the first cycle. Following the 5th cycle discharge to 2.0 V, a fixed resistive load of 1.67 kOhm was applied for 72 hours to simulate a resistor being applied across the leads of a battery. A fixed resistive load is selected as a controlled method to decrease the cell potential to a near zero volt state, as it represents a highly implemental approach for practical storage of cells in the field. The load value in the present work was designed to give a 1.2 mA current rate when the cell voltage is at 2.0 V Figure 38a shows the cell voltage and electrode potentials during the 5th cycle discharge and fixed resistive load step plotted as a function of cell capacity. Figure 38b shows the cell potential and electrode potentials during the 5th cycle discharge and fixed resistive load step plotted as a function of time.

As shown in Figure 38b, after the 5th constant current discharge and application of the fixed resistive load, the cell undergoes a transient period in which the cell potential decreases to near zero volts. During the transient period, the potential of the cathode initially decreases to ~1.5 V vs. Li/Li⁺ where it plateaus for the first few hours. The cathode

insertion plateau at ~ 1.5 V vs. Li/Li^+ is an expected feature of layered lithium rich cathode materials as reported in prior work[204].

The anode potential, on the other hand, remains in its normal range of < 300 mV vs. Li/Li^+ for the same first few hours of the transient period. As observed in Figure 38a, an additional 2.29 mAh of discharge capacity is realized during this time of the transient period with the cell voltage plateauing at ~ 1.3 V. The amount of additional discharge is in reasonably close agreement ($\sim 7\%$ difference) to the calculated amount of excess reversible lithium stored in the anode of 2.11 mAh (See Table 1, Equation S1-2, Figure 52-Figure 52, and supplemental discussion). The excess reversible lithium is not extracted during the normal discharge and is only extracted when the cell is overdischarged by an applied fixed resistive load. The slight larger observed amount of excess reversible lithium compared to the calculated amount may be accounted for by the fact that half-cell tests only extracted lithium to 1.5 V vs. Li/Li^+ , not 2.8 V vs. Li/Li^+ , which is where the anode potential increased to during near zero volt storage. Additionally, the half-cell's were cycled at a constant current of $C/20$ and $C/10$, whereas in the full cell during the fixed resistive load step, the current decreases to a much lower value which can be expected to lead to extraction of more reversible lithium from the anode.

After the first 3 hours of the transient period, the anode potential increases significantly and approaches the cathode potential at ~ 1.5 V vs. Li/Li^+ . Figure 38b shows that after the anode reaches ~ 1.5 V vs. Li/Li^+ , the potentials of the electrodes vs. Li/Li^+ both begin to increase. About 10 hours after the fixed resistive load is applied, the electrode potentials asymptote at ~ 2.8 V vs. Li/Li^+ , where they remain for the duration of the fixed resistive load step. At this point, the cell current is < 6 μA ($\sim C/2000$) and the cell can be

considered to be in a quasi-equilibrium state. Despite being in a quasi-equilibrium state, the resistor must remain on the cell, otherwise under an open-circuit condition the cell voltage will recover (see Figure 59). Thus, the resistor is required in a realistic scenario in

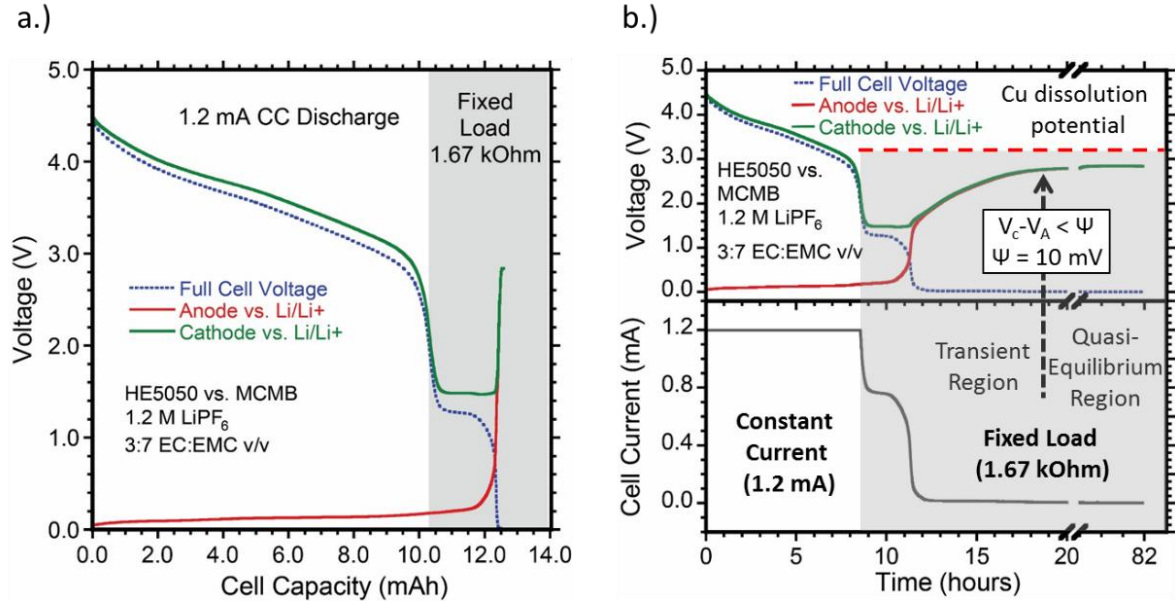


Figure 38: (a) Electrode potentials and cell voltage during 5th 1.2 mA constant current (CC) discharge and 3-day fixed resistive load storage plotted against cell capacity. (b) Electrode potentials and cell voltage during 5th 1.2 mA CC discharge and 3-day fixed resistive load storage plotted against time. The red dashed line represents the threshold electrochemical potential at which copper dissolution from the anode will occur.

order to keep the cell voltage constant at a near zero volt, safe state, to be easily read by a voltmeter.

As detailed in section 4.2, it is useful to define an electrode asymptotic potential (EAP) that is representative of the semi-constant potential of both electrodes when the cell is in a quasi-equilibrium, near zero volt state under fixed resistive load. The EAP is again described by equation 7 in section 4.2. Since the electrode potentials remain fairly constant at ~2.8 V vs. Li/Li⁺ once the cell voltage decreases to less than 10 mV, $\Psi = 10 \text{ mV}$ is a sufficient threshold for defining the EAP of the HE5050/MCMB cell. Importantly, the transient period anode potential and EAP of the cell are below 3.1 V vs. Li/Li⁺, which is

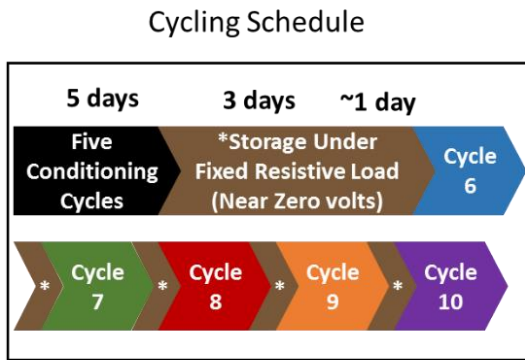
the potential assigned in a previous study at which dissolution of the copper current collector initiates at room temperature[173]. As such, damaging copper dissolution[85–91] is not expected to be occurring in the HE5050/MCMB cell at room temperature during near zero volt storage.

The changes in electrode and cell voltages that are observed in Figure 38 during fixed resistive load testing highlight the importance of reference electrode measurements. The measured increase in the HE5050 and MCMB electrode potentials after the 1.5 V vs. Li/Li⁺ intercalation plateau of the cathode and depletion of the anode results in an EAP of ~2.8 V vs. Li/Li⁺. Predictions based on capacity matching and extrapolation of fixed current half-cell discharge curves of the individual electrodes would not predict the EAP value in the quasi-equilibrium regime. In comparison, the transient behavior and EAP of previously reported LiCoO₂/MCMB cells[36], with or without anode pre-lithiation, are different than the data shown in Figure 2a and 2b for an HE5050/MCMB cell. Thus, the quasi-equilibrium state represents a condition where the cell voltage decreases to <10 mV (with a very low current equivalent to less than C/2000), and the electrode and electrolyte kinetics are no longer influencing the potentials, rather the thermodynamics of the system dominate. The implication of these results is that the active material chosen for the cathode and the amount of reversible lithium of the cell has an effect on the transient behavior and cell EAP. Overall, the benefits of reference electrode measurements in determining the behavior of the electrode potentials during fixed resistive load, near zero volt storage of a lithium ion cell motivate their utility and necessity for future studies.

5.5 Discharge Performance retention after repeated periods of near zero volt storage

The performance retention of the 3-electrode pouch cell after repeated storage periods at near zero volts was tested according to the testing regime described in Figure 39a. After cell conditioning and first application of a fixed resistive load, the cell was recharged with a constant current of 0.06 mA ($\sim C/200$) until the cell voltage reached 2.0 V to bring the cell back into its normal voltage range. A very gradual initial charge after near zero volt storage is done presently to ensure testing is similar to what has been done previously for testing of commercial near zero volt capable cells[137] and in previous near zero volt storage studies[173]. After charging the cell to 2.0 V, it was charged with a constant current of 1.2 mA to 4.6 V vs. Li/Li⁺ cathode potential and discharged with a 1.2 mA constant current to 2.0 V cell voltage. After discharge a 1.67 kOhm load was again applied and the cycle repeated.

a.)



b.)

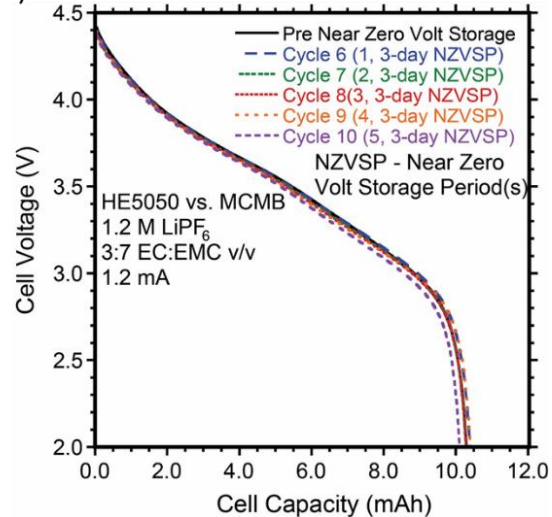


Figure 39: (a) Flowchart of cycling regime for testing the tolerance of the HE5050/MCMB cell to 3 day near zero volt storage periods. (b) 1.2 mA constant current (CC) discharge curves of HE5050/MCMB cell prior to and after 1, 2, 3, 4, and 5 seventy two hour, near zero volt storage periods.

Figure 39b shows the discharge curves for the cycle before near zero volt storage and the cycles after one to five 3-day near zero volt storage periods (NZVSP). The cell maintains >98% of its original capacity (see Figure 54 for zoomed in view of curves) with

only a 22 mV fade in the average discharge voltage after five, 3-day near zero volt storage periods. The performance retention is primarily attributed to the cell's EAP remaining at ~2.8 V vs. Li/Li⁺ for all near zero volt storage periods (See Figure 55a), which is less than the copper dissolution potential assigned in a previous study[173].

The measured discharge performance retention shown in Figure 39b also indicates that the low voltage insertion of the cathode near 1.5 V vs. Li/Li⁺ does not significantly degrade the cathode performance. Furthermore, as observed in Figure 40a, the near zero volt storage coulombic efficiency (NZVSCE) of the cell (calculated by equation 8 where C_{pnzv} is the charge capacity post near zero volt storage, D_{cc} is the discharge capacity of the constant current step, and D_{frl} is the discharge capacity of the fixed resistive load step) of the cell is >99%. Evident in Figure 40b, the NZVSCE value remains essentially constant (>98%) for all subsequent near zero volt storage periods. Thus, charge passed during the fixed resistive load discharge to near zero volts is highly reversible. Overall, observed discharge performance retention demonstrates that high tolerance to repeated near zero volt storage is attainable with an HE5050/MCMB cell.

$$NZVSCE(\%) = \frac{C_{pnzv}}{D_{cc} + D_{frl}} \times 100 \quad (8)$$

A second 3-electrode pouch cell was tested in the same manner as that shown in Figure 39 but with 7-day near zero volt storage periods instead of 3-day storage periods (see Figure 41a). The benefit of this test is to determine if longer storage periods at the beginning of cell life lead to changes in the discharge performance retention of the cell for this chemistry. The EAP of the cell, as with the cell stored for 3-day fixed resistive load periods, remains at ~ 2.8 V vs. Li/Li^+ for each near zero volt storage period (see comparison of voltage curves in Figure 55b), so even with longer storage periods at near zero volts, no copper dissolution is expected to be occurring. Additionally, the NZVSCE for each 7-day fixed resistive load storage period is $>97\%$ (See Figure 57), which is very similar to $>98\%$ observed during 3-day near zero volt storage periods. Thus, increasing the time of the near zero volt storage periods does not significantly decrease the reversibility of charge passed during the fixed resistive load, near zero volt storage period.

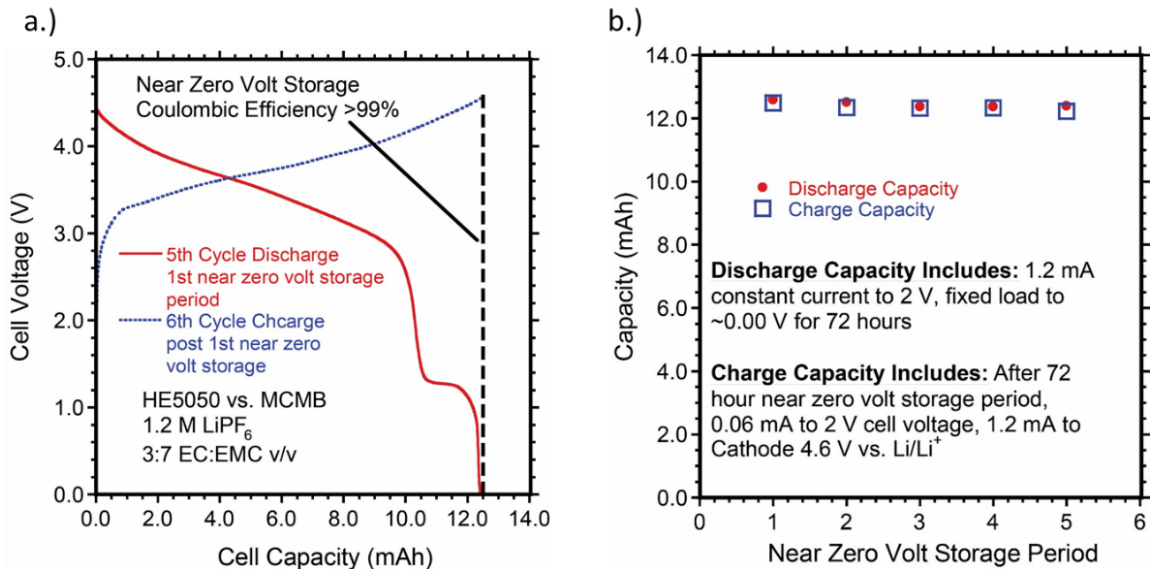


Figure 40: (a) HE5050/MCMB cell voltage profile during the 5th cycle discharge and first 3-day near zero volt storage period under fixed resistive load (solid red line) and the cell voltage profile during the charge following the near zero volt storage period (dotted blue line). Dashed line indicates discharge/charge capacity of each step (b) Discharge capacity (including capacity from the 1.2 mA constant current discharge step to 2.0 V cell voltage and the 3-day fixed resistive load step) plotted with the charge capacity of the cell charge on subsequent cycle after the near zero volt storage period.

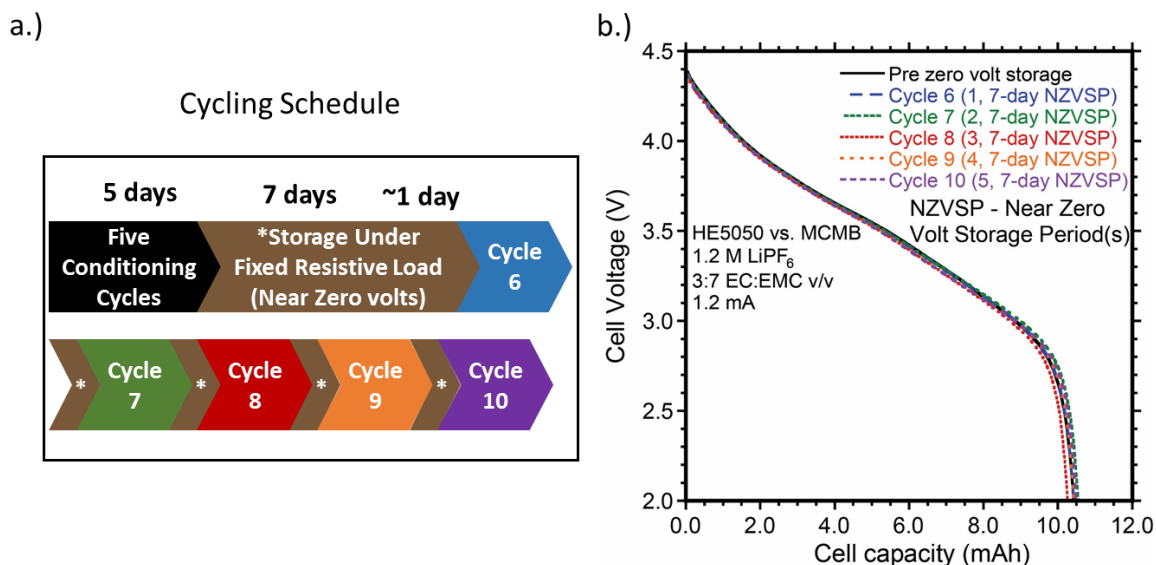


Figure 41: (a) Flowchart of cycling regime for testing the tolerance of the HE5050/MCMB cell to 7 day near zero volt storage periods. (b) 1.2 mA constant current (CC) discharge curves of HE5050/MCMB cell prior to and after 1, 2, 3, 4, and 5 seven day, near zero volt storage periods.

As shown in Figure 41b, the cell maintains nearly 100% of its discharge capacity (see Figure 56 for zoomed in view of curves) with only a 16 mV average discharge voltage fade after 5, 7-day near zero volt storage periods (35 total days of near zero volt storage). Overall, the results suggest that increased storage time of the cell under fixed resistive load does not increase the fade of HE5050/MCMB cells. The high tolerance can be attributed to an EAP sufficiently less than the copper dissolution potential and high reversibility of charge passed during the fixed resistive load, near zero volt step even with the longer storage periods. Similar to prior study of LiCoO₂/MCMB cells which utilized a pre-lithiated anode[173], the dominant electrochemical reactions take place during the transient period of ~10 hours of fixed resistive load storage, and after that, the cell can be considered to be in a quasi-equilibrium state. Collectively, the results suggest that longer storage periods in conditioned cells are not likely to increase the fade rate of discharge performance in the cells after near zero volt storage.

5.6 Effects of near zero volt storage on cell rate capability and long term cycling

Two conventional, 2-electrode HE5050/MCMB pouch cells (not containing reference electrodes, single layer and same composites as the cells described in section 5.2 and 5.4) were constructed and tested according to the flowchart shown in Figure 42a. Cells were cycled for 5 conditioning cycles (one at 0.6 mA constant current and 4 cycles at 1.2 mA constant current) from 2.0-4.5 V cell voltage. After the 5th cycle discharge, one cell was stored at open circuit for 3 days (cell voltage remained from ~3.0-3.1 V, See Figure 58) while the other cell was stored at near zero volts under fixed resistive load for 3 days.

After the 3 day period, the cell stored at near zero volts was recharged to 2.0 V cell voltage at a 0.06 mA (~C/200) constant current. Then, both cells were analyzed by a rate study in which the charge rate was held constant at 1.2 mA and the discharge rate was varied from 1.2 mA, 6.0 mA, 12 mA and 60 mA (i.e. C/10, C/2, 1C and 5C rates based on rated cell capacity of 12 mAh). The benefit of the rate test is to determine if the cell stored at near zero volts for 3-days has equivalent discharge rate capability compared to the cell stored at open circuit, which would indicate the near zero volt storage period is not detrimental to performance.

As shown in Figure 42b, the cell stored at open circuit for 3 days and the cell stored at near zero volts for 3 days had very similar discharge profiles for all tested discharge rates. An increase in capacity retention of about 10% is observed in Fig 6b for the cell stored at near zero volts for 3 days at 1C and 5C rates. Thus, near zero volt storage does

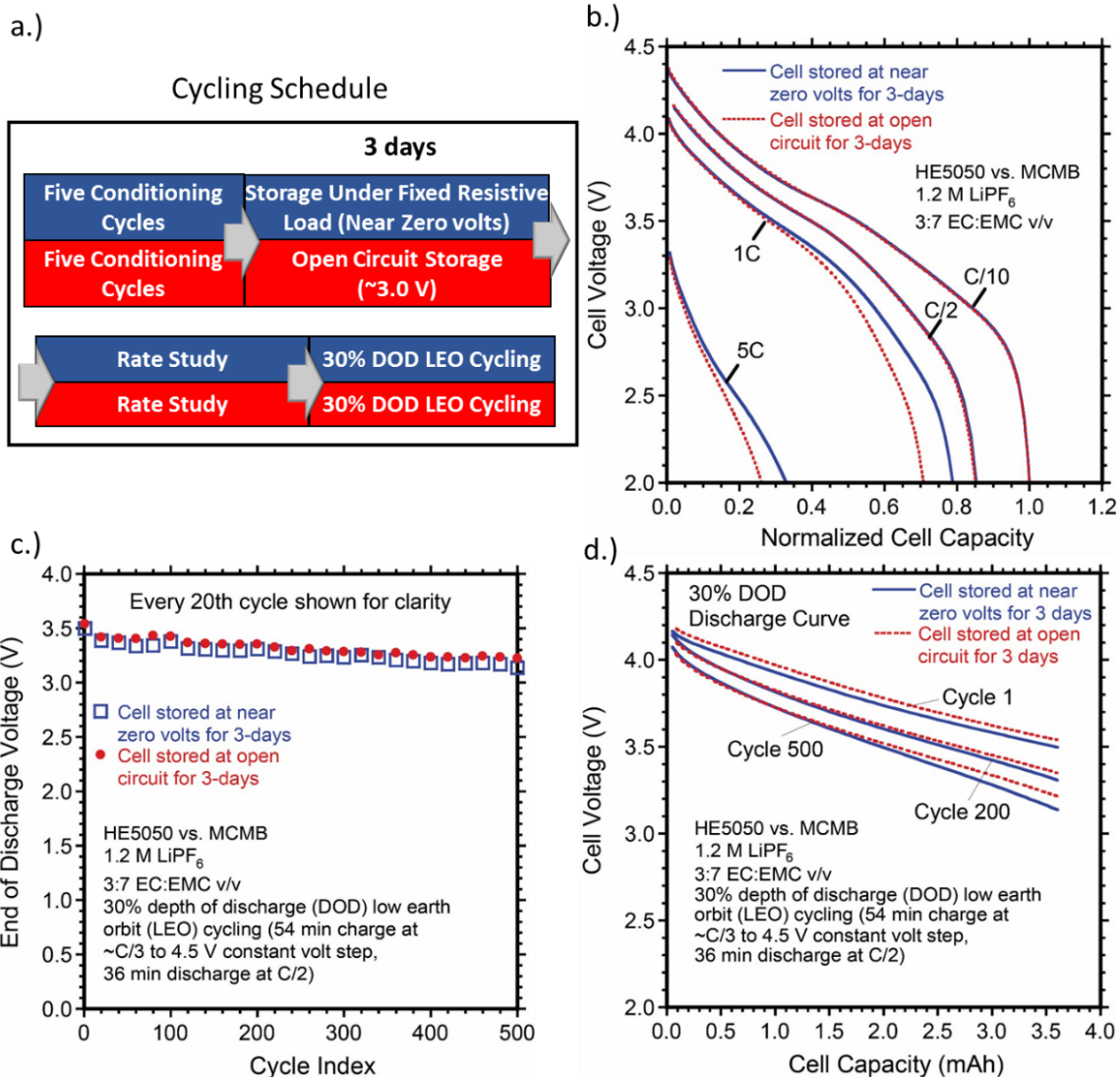


Figure 42: (a) Flow chart of cycling schedule for testing the effects of near zero volt storage of HE5050/MCMB cells on their rate capability and long term cycling stability compared to cell stored at open circuit. (b) Discharge profiles of HE5050/MCMB cell stored at open circuit for three days and HE5050/MCMB cell stored at near zero volts for three days at 1.2 mA, 6 mA, 12 mA and 60 mA discharge current (i.e. C/10, C/2, C and 5C discharge rates based on rated cell capacity). (c) End of discharge voltages of HE5050/MCMB cell stored at open circuit for three days and HE5050/MCMB cell stored at near zero volts for three days under 30% depth of discharge low earth orbit (LEO) cycling. (d) Discharge voltage profile of the 1st, 200th and 500th LEO cycle of the HE5050/MCMB cell stored at open circuit for three days and HE5050/MCMB cell stored at near zero volts for three days.

not have a negative effect on the rate capability of HE5050/MCMB cells, and was even observed to lead to minor improvements at discharge rates $\geq 1C$.

Following the rate study, each of the conventional HE5050/MCMB 2-electrode cells were cycled using a standard 30% depth of discharge (DOD) low earth orbit (LEO)

cycling regime, which involves a 54 minute charge (~C/3 charge to a 4.5 V constant voltage step) followed by a C/2 discharge for 36 minutes. The LEO cycling regime was selected because it represents a rigorous, demanding cycling schedule that will be sensitive to any degradation caused by the near zero volt storage. The benefit of LEO cycling is to determine if the cell stored at near zero volts for 3-days has decreased long term cycling stability compared to the cell stored at open circuit, which would indicate the near zero volt storage period is detrimental to the longevity of the cell.

Figure 42c shows the end of discharge cell voltages for each cycle up to 500 cycles (~1 month of cycling). As observed, the end of discharge voltages are very similar throughout cycling between the cell stored at near zero volts for 3 days and the cell stored in a discharged state at open circuit for 3 days. Figure 42d shows the discharge profiles of the 1st, 200th and 500th cycles, which only display subtle voltage differences. Thus, the 3 day near zero volt storage period at the beginning of life had minimal to no negative effect on longer term cycling stability of the HE5050/MCMB cell. The modest fade observed in both cells is attributed to fade of the HE5050 discharge performance, which is commonly observed in lithium rich cathode materials[179–203].

5.7 Elevated temperature testing

A 3-electrode coin cell was constructed for testing at elevated temperature. The cell was placed into a large metal test fixture which was placed on top of a hot plate. A thermocouple was placed next to the cell to monitor the temperature experienced by the cell at all times during testing. Figure 43a shows a flowchart of the testing regime for the cell. The cell was conditioned 5 times at room temperature 2.0 V cell voltage and 4.6 V

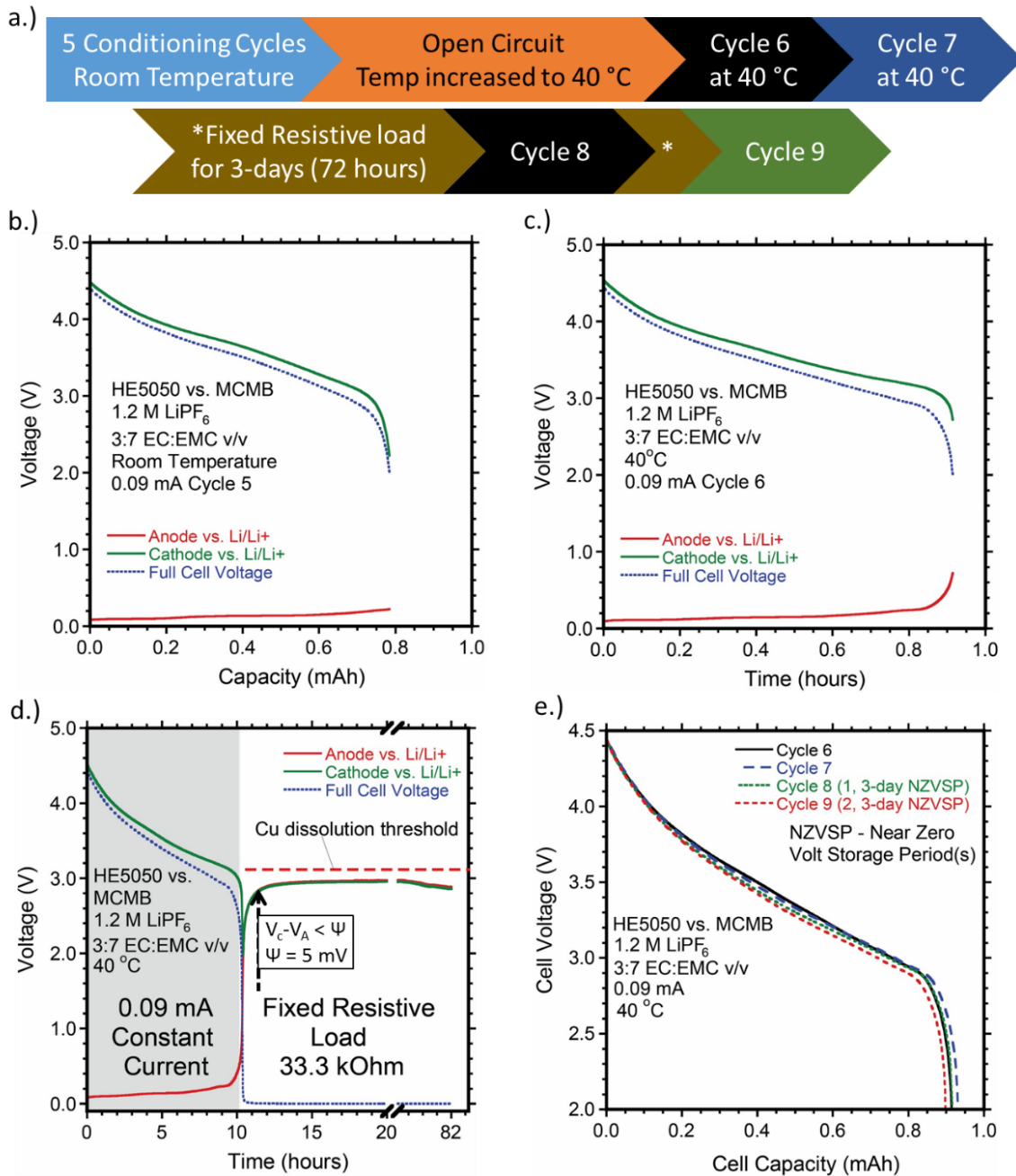


Figure 43: (a) Flowchart of testing regime for testing of near zero volt storage tolerance of HE5050/MCMB cells at 40 °C. (b) Discharge profile of HE5050/MCMB cell with Li reference electrode at 0.09 mA at room temperature. (c) Discharge profile of HE5050/MCMB cell with Li reference electrode at 0.09 mA at 40 °C. (d) Plot of reference electrode data for cycle 7. Gray shaded area on left is the constant current discharge to 2.0 V cell voltage. Non-shaded are on right is fixed resistive load step. The red dashed line represents the threshold value that the anode potential would need to increase to for copper dissolution to occur. (e) 0.09 mA constant current (CC) discharge curves of HE5050/MCMB cell prior to and after 1 and 2 3-day, near zero volt storage periods at 40°C.

vs. Li/Li^+ cathode potential. Then, while the cell was at open circuit, the hot plate setting was gradually increased until the thermocouple steadily read 40 ± 1 °C. Once at 40 °C, the cell was cycled twice to determine the high temperature capacity (cycles 6 and 7).

Figure 43b shows the measured full cell, cathode and anode potentials during discharge at room temperature and Figure 43c shows those corresponding to discharge at 40 °C. As shown in Figure 43b and c, the cell discharged with 0.131 mAh (or 16.7%) additional capacity than it did at room temperature. The reference electrode measurements show that the additional capacity can be attributed to increased intercalation capacity of the cathode in the 2.7-4.6 V vs. Li/Li^+ potential range. Such increased capacity of lithium rich layered materials at elevated temperatures has been observed previously[181,186,189] and is attributed to increased participation of Mn redox reactions during insertion[181].

Figure 43d shows the plot of the cell potential, anode potential and cathode potential as a function of discharge time during cycle 7. The left portion of the plot that is shaded grey is the constant current discharge step and the right portion of the plot that is not shaded is the fixed resistive load step. As shown, after the constant current discharge and application of the fixed resistive load, the cell undergoes a very different transient period than at room temperature. Compared to room temperature cycling, no notable plateau in the cathode potential is observed at 1.5 V vs. Li/Li^+ . The lack of the plateau at 1.5 V vs. Li/Li^+ is attributed to the fact that at 40°C the cathode intercalated significantly more lithium during the constant current discharge compared to room temperature. Therefore, the capacity that was intercalated at 1.5 V vs. Li/Li^+ during the fixed load step at room temperature had already been effectively saturated during the constant current discharge at 40°C.

The HE5050/MCMB cell realizes a potential <5 mV after ~1 hour. The EAP of the cell is measured at about 2.8 V vs. Li/Li⁺ initially, but increases to as high as 2.97 V vs. Li/Li⁺ before decreasing back to about 2.8 V vs. Li/Li⁺. An EAP threshold value of 5 mV is used in this case as the electrode potentials exhibit higher stability at this threshold compared to 10 mV at room temperature. Importantly, the value of the EAP is sufficiently less than 3.1 V vs. Li/Li⁺, so no copper dissolution is expected to be occurring.

Figure 43e shows the discharge curves during cycles 6-9 of the high temperature testing (See Figure 60 for a zoomed in view of the curves). As shown, after the 3-day fixed resistive load, near zero volt step, the cycle 9 discharge (after two, 3-day near zero volt storage periods at 40°C) has only a minor fade in average discharge voltage (36 mV) and capacity (98% of Cycle 6 capacity). The fade is increased over the room temperature cell, and can be attributed to an increased fade rate of the cathode material (See Figure 61). Increased fade rate of lithium rich cathode materials at elevated temperature is a previously observed result[189]. However, the discharge performance retention is excellent at 40°C and can be attributed to (1) a transient period anode potential and EAP less than the copper dissolution potential for both near zero volt storage periods (See Figure 62) and (2) high reversibility of charge passed during fixed resistive load (NZVSCE is ≥100% for both NZVSP, See Figure 63). Overall, the results show that HE5050/MCMB cells have good tolerance to near zero volt storage at elevated temperature, which could have impacts for medical implants and cells that experience elevated temperatures during transit.

5.8 Conclusions

Lithium ion cells have been designed with a lithium rich cathode material appropriately capacity matched with an anode to achieve a cell with excess reversible

lithium relative to the cathode's nominal discharge capacity. Specifically, HE5050/MCMB cells utilized at least 10% excess first charge anode capacity relative to the first cycle charge capacity of the cathode. The excess reversible lithium sourced from the lithium rich cathode combined with its low potential intercalation plateau leads to a cell with a transient period anode potential of <2.8 V vs. Li/Li^+ and an electrode asymptotic potential (EAP) of ~ 2.8 V vs. Li/Li^+ . The EAP value being less than the previously assigned copper dissolution potential of 3.1 V vs. Li/Li^+ resulted in no expected copper dissolution and HE5050/MCMB cells showed excellent discharge performance retention. In particular, cells maintained $>98\%$ of their capacity and showed <22 mV decrease in average discharge voltage after five 3-day and five 7-day near zero volt storage periods. Additionally, conventional 2-electrode pouch cells stored at near zero volts or open circuit for 3-days demonstrated nearly identical discharge rate capability and low earth orbit cycling stability. Testing of the near zero volt storage tolerance of the cell at elevated temperature (40°C) has also shown that the same tolerance to near zero volt storage is achieved for two, 3-day near zero volt storage periods. Overall, the excellent discharge performance retention is attributed to: (1) the anode potential remaining less than the copper dissolution potential throughout the fixed resistive load, near zero volt storage period leading to no expected copper dissolution, (2) the cathode active material not undergoing degradation during the near zero volt storage period as evidenced by its discharge performance retention, and (3) the high observed NZVCE of an experimental cell. Thus, the HE5050/MCMB lithium ion cell is highly tolerant to multi-day near zero volt storage under an applied fixed resistive load with no appreciable effect on cell performance.

Lithium rich cathode materials like HE5050 are of significant interest for their potential to increase the energy density of lithium ion cells over current state of the art. As demonstrated in the present work, near zero volt storage tolerance in an appropriately capacity matched, conditioned full cell represents a significant additional benefit of enhanced user-inactive safety when using lithium rich cathode materials. It is important to recognize that this capability is achieved without the need for secondary active materials, alternative current collectors, or pre-processing steps performed on the electrodes. Overall, while the long term cycling stability of lithium rich cathode materials is still a challenge that needs to be overcome for them to meet current needs, the additional inactive safety capability of near zero volt storage tolerance can help to reduce safety hazards associated with shipping and storing of future, higher energy density lithium ion batteries that utilize these cathode materials.

6. Al₂O₃ coating of CNT paper current collectors

6.1 Introduction

Increasing the gravimetric energy density of lithium ion batteries has been a large focus of research in recent years. Increased gravimetric energy density can have many benefits in aerospace, EV and portable electronics applications[2]. Among several approaches to increasing the gravimetric energy of lithium ion batteries, including thicker composites[109], more energy dense cathode active materials[178] and high capacity alloying anode materials[14–25,129,147,205–216], using carbon nanotube papers as a lightweight current collector replacement, particularly as a replacement for the copper foil of the anode, has been investigated[109].

Carbon nanotube papers have several advantages over standard copper foils. In particular they are roughly an order of magnitude lower areal density and they can contribute up to 100 mAh/g capacity in the 0.005-1.5 V vs. Li/Li⁺ potential range[110]. Carbon nanotube papers can also form a mechanically compliant current collector for materials like silicon[21,129] and germanium[23] thin films, leading to better performance. In addition to all of these benefits of CNT papers, they are also very stable to high potentials (>3.0 V vs. Li/Li⁺)[217] *and when used as the anode current collector could enable lithium ion cells that can withstand over-discharge or prolonged storage at a near zero volt state of charge*[109,173].

However, carbon nanotube papers are known to suffer significant first cycle loss due substantial SEI formation caused by their high surface area.[110] The carbon nanotubes that make up a bulk CNT paper also suffer interlayer instability[110] after repeated cycling which could affect the electrical conductivity of the CNT papers.

Generally, pathways to reduce SEI formation on CNT papers and improve cycling stability are necessary to improve the utility of CNT papers as an effective anode current collector replacement for copper foils.

In this chapter, a nanoscale layer of Al₂O₃ is deposited by atomic layer deposition onto commercial CNT papers and its effect on the lithium ion cycling performance of the CNT papers is investigated. Cycling of the CNT papers vs. Li metal in coin cells is used to investigate charge loss, specific capacity and cycling stability of CNT papers. X-ray diffraction is used to investigate the effect of the Al₂O₃ coating on maintaining crystallinity of the CNT papers during cycling. Raman spectroscopy is used to investigate the effect of the Al₂O₃ coating on defect properties in the CNTs during cycling. Lastly, a mesocarbon microbead (MCMB) anode composite is coated onto the CNT paper and the electrode is tested by cycling vs. Li metal in a coin cell to determine the viability of an Al₂O₃ coated CNT paper as a current collector replacement.

6.2 Experimental

Purification and Al₂O₃ coating of commercial MWCNT sheet material

The purification and coating steps performed on the commercial MWCNT sheet materials obtained from Nanocomp Technologies Inc. are shown in the flowchart in Figure 44. As-received MWCNT sheet material first underwent a thermal oxidation (Ramp-stop from room temperature to 520°C at 10°C/min under flowing dry air) to remove amorphous carbon material which thermally oxidizes at a lower temperature than MWCNT's[218]. The sheet material was then immersed in reagent grade HCl for 30 minutes to remove residual metal catalyst left over from the material synthesis. The material was subsequently rinsed with excess DI H₂O and dried before undergoing another thermal oxidation (ramp-

stop from room temperature to 520°C at 10°C/min under flowing dry air) to remove residual HCl from the material.

Following purification the aluminum oxide (Al_2O_3) coatings were grown at 125°C by atomic layer deposition (ALD) in a commercial Beneq TFS-200 system. The MWCNT sheet was suspended inside the reactor to create a gap between the substrate holder and the

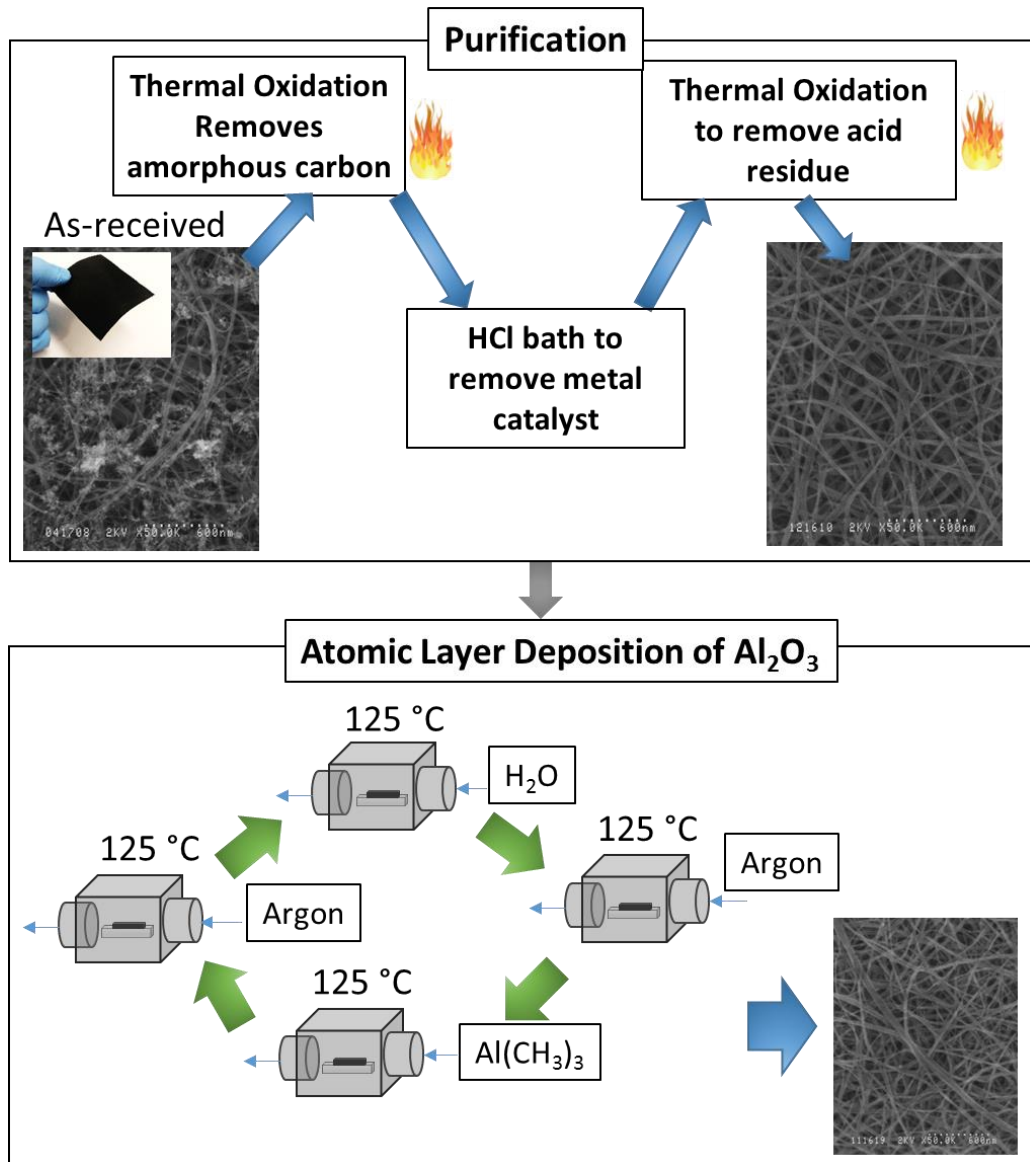


Figure 44: Flow diagram of processing steps of commercial MWCNT sheet materials to remove amorphous carbon and residual metal catalyst and coated with ~3 nm of Al_2O_3 .

bottom surface of the MWCNT sheet, to ensure that both the top and bottom sides are

conformally coated with Al₂O₃. The precursors used were trimethylaluminum (TMA, Al(CH₃)₃) and deionized H₂O for the aluminum and oxygen sources, respectively, and both precursors were kept at 20°C. Ultra-high purity argon (UHP Ar) was used as the carrier gas. Since MWCNT's have a relatively inert surface, water was pulsed first to help with TMA nucleation. Thus, the ALD sequence consisted of the following: H₂O / UHP Ar / TMA / UHP Ar. The exposures for both precursors were 0.15 s, and the purge times were 5 s and 1 s for H₂O and TMA, respectively. The coating thickness targeted was 3 nm based on tool calibration. A prior study has shown that atomic layer deposition onto MWCNTs with similar deposition conditions and distilled H₂O and TMA as pre-cursors leads to a conformal coating of an amorphous Al₂O₃ layer[219]. The Al₂O₃ coated MWCNT paper will be referred to as Al₂O₃-MWCNT paper hence forth.

Electrochemical Testing

Electrodes were built into 2032 coin cells vs. lithium metal with a Celgard separator between them for electrochemical testing. The electrolyte used was a 1.2 M LiPF₆ in 3:7 ethylene carbonate (EC):ethyl methyl carbonate (EMC) w/w. Cells were constructed in a dry, argon filled glove box maintained at <1% oxygen and <1% water. Cycling was performed on an Arbin BT2000 cycler.

MCMB composite electrode fabrication

Mesocarbon microbead (MCMB) composite anodes coated onto MWCNT paper current collectors were prepared by mixing Quallion 25-28 (T13E00-1) MCMB into a slurry with SuperC™ Carbon Black, TIMREX® SFG-6 and Solef® PVDF in a 93:0.3:2.7:4 mass ratio using NMP as the solvent. The slurry preparation consisted of dissolving PVDF in NMP, then by mixing in the conductive additives (Carbon Black and

SFG-6) and then addition of the MCMB with intermediate 20 minute mixing steps in a Thinky AR-100 planetary mixer. The composite slurry was coated onto the MWCNT paper using a doctor blade. The electrode was then dried overnight in a vacuum oven at 100°C and calendared to a composite density of about 1.39 g cm⁻³. The final electrode areal density was 15±1 mg/cm².

Cell disassembly and electrode rinsing

2032 coin cells were disassembled in a dry, argon filled glove box maintained at <1% oxygen and <1% water using a de-crimping tool. The CNT paper electrodes were rinsed in excess EMC and dried in vacuum for 2 hours before analysis.

Material Analysis

Raman spectroscopy was performed using a Jobin Yvon LabRam spectrophotometer with a 633 nm light source and 300 to 3000 cm⁻¹ collection range. X-ray diffraction (XRD) was performed with a Bruker D2 Phaser powder x-ray diffractometer. A Cu k α 1.54184 Å x-ray source was used. The step size was set to 0.0081167 (2 θ) with 1 second collection time at each step. The electrode was placed on a sample holder that was rotated at a rate of 1.0 rotation/second. Background subtraction and smoothing was done using Bruker Diffrac software.

6.3 Results and Discussion

The first cycle insertion of lithium into a bare MWCNT paper and an Al₂O₃-MWCNT paper is shown in Figure 45a. As shown, the voltage profile of the bare MWCNT paper has a plateau at about 1.0 V vs. Li/Li⁺ that extends out to ~1500 mAh/g insertion specific capacity. This plateau is attributed to Solid Electrolyte Interface (SEI) formation on the MWCNT paper[109,110] and is substantial due to the high surface area of the

MWCNTs[109,110]. After 1500 mAh/g_{CNT} of insertion capacity, the voltage decreases to 5.0 mV vs. Li/Li⁺ after an additional 1200 mAh/g_{CNT} insertion specific capacity, resulting in total first cycle insertion specific capacity of 2800 mAh/g_{CNT}. In comparison, the voltage profile of the MWCNT paper coated with Al₂O₃ is very different. Compared to the bare CNT paper, the insertion specific capacity of the plateau observed at ~1.0 V vs. Li/Li⁺ is significantly reduced by about 75% to ~500 mAh/g_{CNT}. After 500 mAh/g_{CNT} of insertion specific capacity, the potential of the Al₂O₃-MWCNT paper decreases to 5 mV vs. Li/Li⁺ after an additional 500 mAh/g_{CNT} of insertion specific capacity, resulting in a total first cycle insertion capacity of 1000 mAh/g_{CNT}.

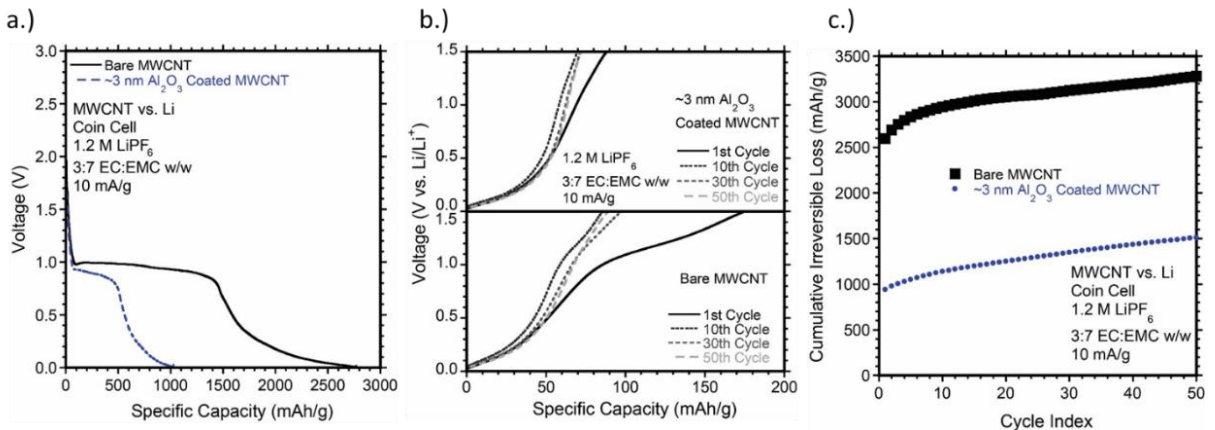


Figure 45: a. First cycle insertion of lithium into CNT paper electrodes. b.) Cumulative irreversible loss plotted against cycle index for a CNT paper electrode coated with Al₂O₃ and a bare CNT paper electrode. c.) Extraction voltage profile of (top) Al₂O₃ coated CNT paper electrode and (bottom) bare CNT paper electrode.

The decrease in specific insertion capacity at the ~1.0 V vs. Li/Li⁺ plateau of MWCNT coated with Al₂O₃ compared to pristine MWCNT is attributed to a significant decrease in SEI formation on the MWCNT paper. Al₂O₃ coatings have resulted in a decrease in SEI formation in Si anodes as well[220]. Significant SEI formation during the first cycle is a major challenge of MWCNT papers as anode current collector replacements in lithium ion batteries. Thus, such a significant reduction of the amount of SEI formation

can have a substantial impact on the feasibility of using MWCNT papers as an anode current collector replacement.

Figure 45b shows the 1st, 10th, 30th and 50th cycle extraction voltage profiles of the bare MWCNT paper and an Al₂O₃-MWCNT paper. The 1st cycle voltage profile of the bare MWCNT shows 170 mAh/g_{CNT} extraction specific capacity, with pseudo-plateaus at ~0.2 mV vs. Li/Li⁺ and ~1.2 V vs. Li/Li⁺, similar to a previous study on single walled carbon nanotube papers[110]. The 10th cycle voltage profile of the bare MWCNT shows a significant decrease in the pseudo-plateau at ~1.2 V vs. Li/Li⁺ compared to the 1st cycle which decreases the extraction capacity to 90 mAh/g_{CNT}. In the 30th cycle the small remnant “shoulder” feature of the profile at ~1.2 V vs. Li/Li⁺ has decreased more and during the 50th cycle is no longer present.

By comparison, the 1st cycle extraction voltage profile of the MWCNT coated with Al₂O₃ profile has only a pseudo-plateau at ~0.2 V vs. Li/Li⁺ with a 90 mAh/g_{CNT} extraction capacity. The 10th cycle voltage profile is very similar, with the extraction capacity decreasing by about 20 mAh/g_{CNT} to 70 mAh/g_{CNT}, with the decrease in overall extraction capacity resulting from a decrease in extraction at potentials >0.5 V vs. Li/Li⁺. The 30th and 50th cycle extraction voltage profiles of the Al₂O₃ coated CNT paper are nearly identical to that of the 10th cycle, indicating stable cycling.

The decrease in the magnitude of the ~1.2 V vs. Li/Li⁺ pseudo-plateau with cycle index in the bare MWCNT paper electrode is consistent with repeated stripping of unstable SEI components followed by re-deposition of new SEI during each insertion step until only stable components of the SEI are present[221]. The absence of the pseudo-plateau in the first cycle extraction voltage profile of the Al₂O₃-MWCNT paper indicates the Al₂O₃

promotes growth of an SEI layer with more stable components during the initial insertion step.

Figure 45c shows the cumulative irreversible loss of the bare MWCNT electrode and Al₂O₃-MWCNT electrode plotted as a function of cycle index. As shown, after 50 cycles the cumulative irreversible loss of the Al₂O₃ coated electrode is about 45% of the cumulative irreversible loss of the bare MWCNT electrode. Thus, after 50 cycles, the Al₂O₃ coating effects a greater than 50% decrease in irreversible losses exhibited by a MWCNT paper electrode. Such an effect can be attributed to the Al₂O₃ layer providing an artificial SEI layer and helping to form a more stable SEI, as shown in prior studies of Al₂O₃ coatings on silicon anodes[220].

Figure 46 compares the X-ray diffraction spectra of bare and Al₂O₃-MWCNT papers before electrochemical cycling (top) and after electrochemical cycling (bottom). As shown in the top of the diagram, a peak appears at about 25 degrees (2-theta) which corresponds to the inter-MWCNT spacing in MWCNT bundles which is roughly the same as graphene plane spacing in graphite[110]. As shown in the top of Figure 46, the peak shape and intensity relative to noise is very similar in the bare MWCNT paper and the Al₂O₃-MWCNT paper, indicating the inter-tube spacing in each sample is very similar. Thus, the Al₂O₃ coating process did not affect the inter-tube spacing CNTs in the coated samples.

The bottom part of Figure 46 shows the XRD pattern of the CNT paper electrodes after the 50 cycles shown in Figure 45. As shown, the peak at about 25 degrees (2-theta) is no longer present for the bare MWCNT paper. In the case of the Al₂O₃-MWCNT paper, the peak is still present, but its intensity relative to noise appears to have decreased while

its width has slightly increased. The presence of the peak indicates that in the MWCNT electrode, the Al_2O_3 improved the interlayer stability of individual CNTs and/or the

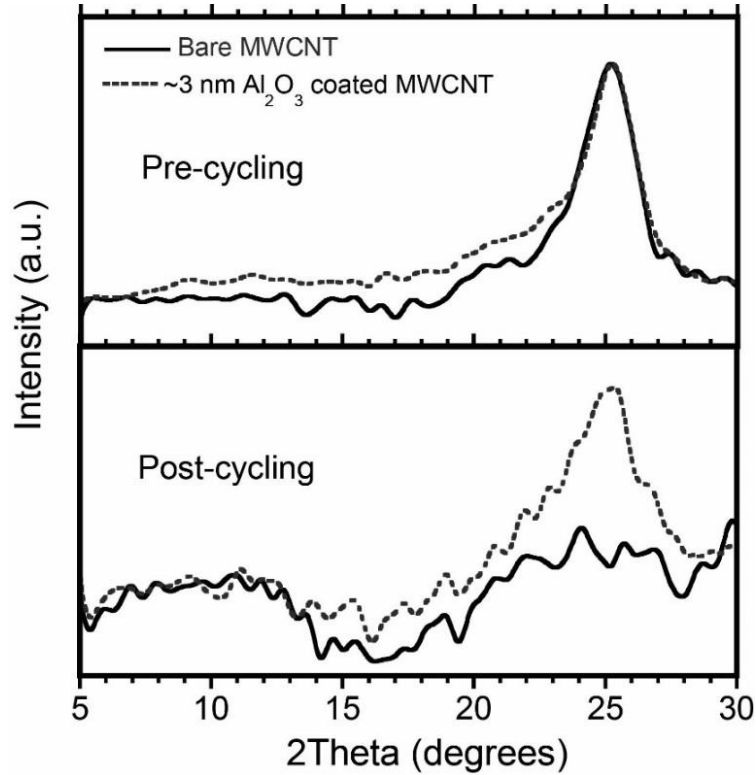


Figure 46: XRD pattern of the bare MWCNT and Al_2O_3 -MWCNT before cycling (top) and after cycling (bottom)

hexagonal close packing of CNT bundles.

Figure 47a shows the Raman spectra of bare MWCNT paper prior to the cycling shown in Figure 45 (bottom) and after cycling (top). As shown, peaks appear at 1320 cm^{-1} , 1600 cm^{-1} and 2640 cm^{-1} . The peak at 1600 cm^{-1} (G-peak) corresponds to longitudinal and latitudinal vibrations of the graphene sub-lattices that make up the concentric walls of the MWCNTs[109,110,218]. The peak at 1320 cm^{-1} (D-peak) corresponds to scattering with a defect site in a cylindrical graphene layer of the MWCNT such as a vacancy or displacement[109,110,218]. The peak at 2640 cm^{-1} (G' peak) corresponds to two photon, 2nd order scattering process[222].

As shown in Figure 47a, after cycling the magnitude of the D-peak relative to the G-peak and G'-peak has increased significantly compared to the sample prior to cycling (D/G ratio 0.2 to 0.9). The increase in the relative intensity of the D-peak indicates that cycling has increased the density of defect sites in the walls of the CNTs, as observed in prior work[110,218]. By comparison, as shown in Figure 47b, in the CNT paper coated with Al₂O₃ the relative intensity of the D-peak increases to a lesser extent (0.2->0.8), indicating the density of defect sites is less in the Al₂O₃-MWCNT paper electrode after cycling compared to the bare MWCNT paper electrode. Thus, the Al₂O₃ coating on the MWCNT paper lessens the creation of defects in the walls of the CNTs during cycling vs. Li metal.

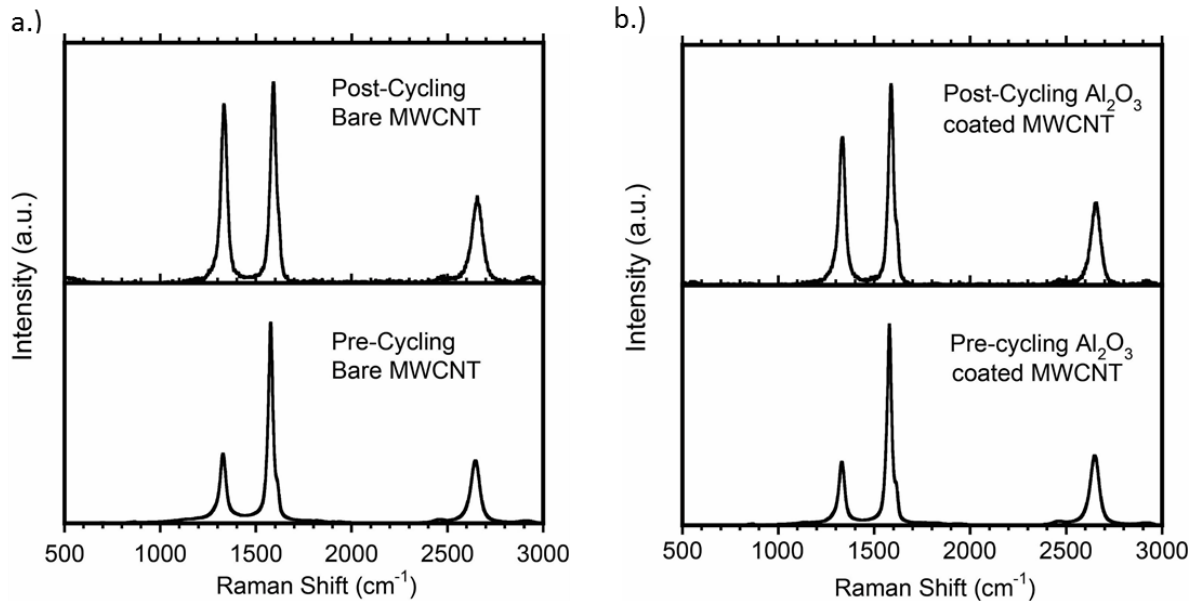


Figure 47: (a) Raman spectra of bare MWCNT before cycling (bottom) and after cycling (top) vs. Li metal in a coin cell. Spectra shown is representative of the average peak ratios observed for the Raman spectra of 5 different spots on the material. (b) Raman spectra of Al₂O₃-MWCNT before cycling (bottom) and after cycling (top) vs. Li metal in a coin cell. Spectra shown is representative of the average peak ratios observed for the Raman spectra of 5 different spots on the material.

Electrochemical rate capability testing

A second set of 2032 coin cells with MWCNT paper electrodes vs. Li metal were constructed to test the effect of Al₂O₃ coatings on the extraction rate capability of the MWCNT paper electrodes. The cells were cycled 5 times between 0.005-1.5 V vs. Li/Li⁺ at 15 mA/g_{CNT} to condition the paper electrodes. Then, the insertion rate was held constant at 15 mA/g_{CNT} and the extraction rate was varied to 15 mA/g_{CNT}, 30 mA/g_{CNT}, 75 mA/g_{CNT}, and 150 mA/g_{CNT}. Figure 48 shows the extraction voltage profiles of Al₂O₃ coated (top) and bare (bottom) MWCNT paper electrodes at the different extraction rates.

As shown in the top part of Figure 48, the extraction voltage profile of the Al₂O₃-MWCNT paper electrode changes little at the different extraction rates up to an effective 2C extraction rate. By comparison, the extraction voltage profile of the bare MWCNT paper electrode has some change at the different extraction rates up to an effective 2C extraction rate. The change in the extraction profile above 1.0 V vs. Li/Li⁺ is likely attributed to continued conditioning of the SEI layer as shown in Figure 45b. Overall, the results show that the Al₂O₃ coating maintains the extraction rate capability of the MWCNT paper electrode up to an effective 2C extraction rate.

MCMB composite was coated on bare MWCNT paper and Al₂O₃-MWCNT paper and testing in coin cells vs. Li metal. The primary purpose of the testing was to evaluate the effect of the thin insulating Al₂O₃ on the performance of a MWCNT paper as a current collector replacement. MCMB vs. Li cells were cycled 5 times from 0.005-1.5 V vs. Li/Li⁺ at 15 mA/g_{electrode}. Figure 49a shows the first cycle insertion of the MCMB on MWCNT (bare and Al₂O₃ coated) current collectors. As shown, the initial insertion curve from ~0.7 V vs. Li/Li⁺ to 0.12 V vs. Li/Li⁺ extends to about 60 mAh/g_{electrode} for the MCMB on an

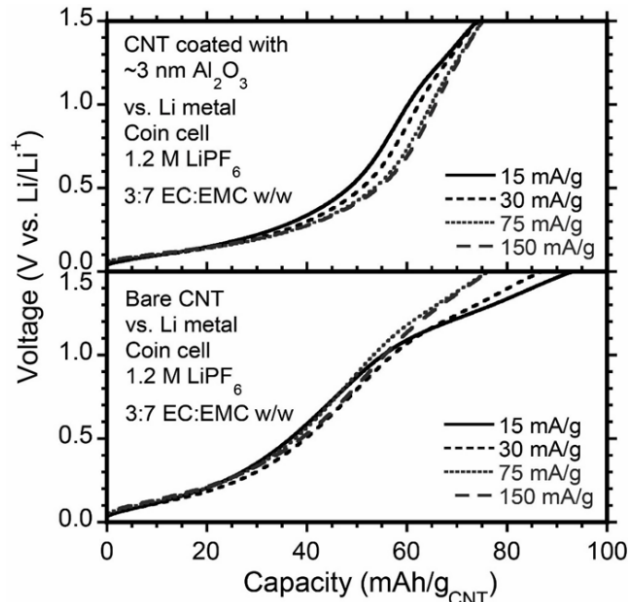


Figure 48: Voltage profile of lithium extraction from Al₂O₃-MWCNT (top) and bare MWCNT (bottom) at 15 mA/g, 30 mA/g, 75 mA/g and 150 mA/g

Al₂O₃-MWCNT current collector compared to 80 mAh/g_{electrode} for MCMB coated on a bare MWCNT current collector. The decrease in insertion capacity in the ~0.7-0.12 V vs. Li/Li⁺ in the electrode with an Al₂O₃-MWCNT current collector can be attributed to the Al₂O₃ coating effecting a decrease in the amount of SEI formed on the electrode.

Figure 49b shows the extraction voltage profile of the MCMB coated on Al₂O₃-MWCNT (top) and bare MWCNT (bottom). As shown, the extraction capacity of both electrodes increases throughout the 5 conditioning cycles. The extraction capacity of the MCMB coated on Al₂O₃-MWCNTs increased from 215 to 284 mAh/g_{electrode}. The extraction capacity of the MCMB coated on bare MWCNT increased 246 to 286 mAh/g_{electrode}. The larger change in extraction capacity in the MCMB coated on Al₂O₃ coated electrode may reflect the need to condition the Al₂O₃ layer[220] with partial Li ion insertion before it forms a an effective connection to the MCMB composite. Overall, after 5 conditioning cycles, the extraction capacity of both electrodes is nearly identical. Thus, the Al₂O₃

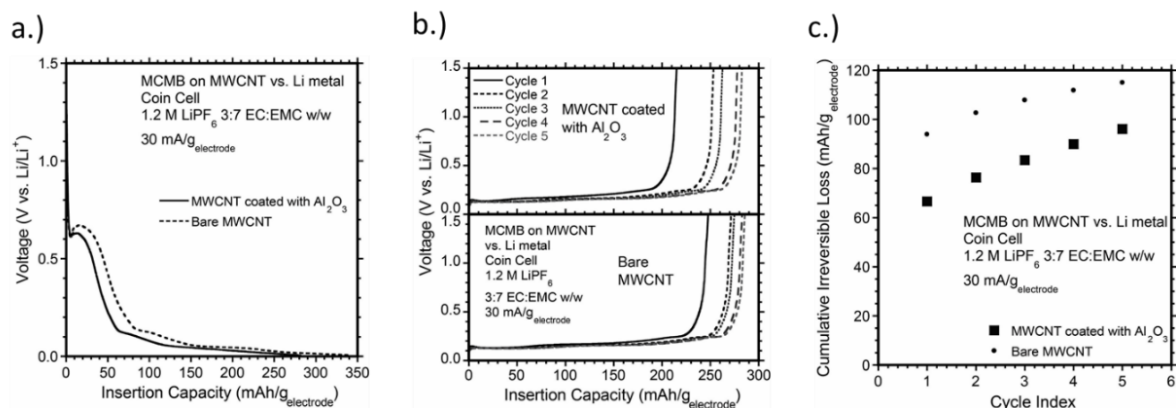


Figure 49: (a) First cycle insertion voltage profiles of MCMB composite coated onto bare MWCNT or Al₂O₃-MWCNT. (b) Extraction voltage profiles for cycles 1-5 of MCMB composited coated onto Al₂O₃-MWCNT (top) and MCMB composite coated onto bare MWCNT (bottom). (c) Plot of cumulative irreversible loss as a function of the cycle number for MCMB composite coated onto bare MWCNT or Al₂O₃-MWCNT.

coating on the MWCNT current collector does not diminish the available capacity of a composite coated on it following conditioning.

Figure 49c shows the cumulative irreversible loss for the first 5 conditioning cycles of the MCMB coated on Al₂O₃-MWCNT and bare MWCNT current collectors. As shown, the cumulative irreversible loss after 5 cycles is 96 mAh/g_{electrode} for the MCMB coated on Al₂O₃-MWCNT current collector and 115 mAh/g_{electrode} for the MCMB coated on a bare MWCNT current collector. The ~17% decrease in cumulative irreversible loss in the anode with a Al₂O₃-MWCNT current collector can be attributed to a reduction in the SEI formation on the CNTs as shown in Figure 45. Thus, an Al₂O₃ coating on a MWCNT current collector decreases irreversible losses of electrodes during conditioning, which again can be attributed to the Al₂O₃ coating effecting the formation of a thinner and more stable SEI layer on the CNTs similar to prior studies of the effect of Al₂O₃ coatings on silicon anodes[220].

After conditioning, the MCMB coated on Al₂O₃-MWCNT current collector and bare MWCNT current collector underwent an extraction rate study in which the insertion rate was held constant at 30 mA/g_{electrode} and the extraction rate was changed to 30

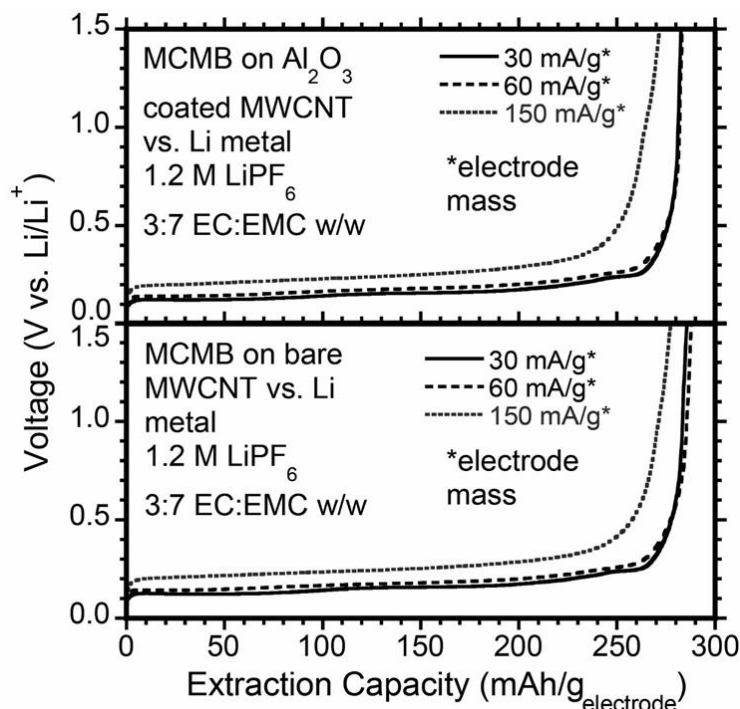


Figure 50: Extraction voltage profiles at rates of 30, 60 and 150 mA/g_{electrode} of MCMB composite coated onto Al₂O₃-MWCNT (top) and MCMB composite coated onto bare MWCNT (bottom).

mA/g_{electrode} (~C/10) to 60 mA/g_{electrode} (~C/5) and 150 mA/g_{electrode} (~C/2). As shown in Figure 50, for each tested rate the voltage profile of the MCMB coated onto Al₂O₃-MWCNT is nearly the same as the voltage profile of the MCMB coated on bare MWCNT. Thus, the Al₂O₃ coating on the MWCNT paper does not affect charge transfer processes between the MWCNT current collector and MCMB composite in a manner detrimental to extraction rate capability.

6.4 Conclusions

The electrochemical performance of a MWCNT paper electrode coated with ~3 nm of Al₂O₃ by atomic layer deposition was characterized and compared to that of a bare MWCNT electrode. Cycling of the MWCNT paper electrodes vs. Li metal in coin cells showed a significant decrease in SEI formation on the first cycle. Additionally, the voltage profiles over 50 cycles suggests that the Al₂O₃ coating results in the deposition of more

stable SEI during the first insertion. Overall, cumulative irreversible loss after 50 cycles was decreased by 55% in the Al₂O₃-MWCNT paper compared to the bare MWCNT paper. XRD analysis indicates that the Al₂O₃ coating improves the interlayer stability and/or hexagonal close packing stability of CNTs after 50 cycles. Raman spectroscopy shows that the Al₂O₃ coating may affect minor suppression of defect formation in the graphene walls of the MWCNTs. Coating Al₂O₃ coated and bare MWCNT paper electrodes with an MCMB composite shows that the Al₂O₃ reduces the cumulative irreversible loss of the MCMB-MWCNT electrode by ~17% after 5 cycles and does not diminish the rate capability of the MCMB-MWCNT electrode. Overall, the present results suggest coating of CNT paper electrodes with thin oxide materials by atomic layer deposition can improve on the irreversible losses observed with CNT materials when cycled in lithium ion cells. Thus, ALD coatings of thin oxides which stabilize the SEI layer may improve the viability of CNT papers as current collector replacements.

7. Dissertation Conclusions and Major Contributions

The work presented in this dissertation represents multiple studies and findings that could have a major impact on the future of how lithium ion cells are constructed, shipped, stored and operated. Use of reversible lithium management in cells constructed from state of the art conventional materials and construction parameters has yielded near zero-volt storage tolerance at both room and high temperature up to 45°C.

In LiCoO₂/MCMB lithium ion cells, reference electrode measurements showed that anode pre-lithiation in appropriate amounts maintains electrode potentials steadily outside their damage zones during prolonged near zero volt storage – a result previously undescribed and not thought feasible according to conventional teachings such as the “zero cross potential”. Pulse discharge studies in LiCoO₂/MCMB cells showed that double layer capacitance plays a significant role in determining the behavior of electrode potentials during near zero volt storage and it was shown that reversible lithium addition can vary by up to 2% of cell capacity while still yielding a sufficient EAP, making manufacture of such cells more feasible. Similar studies could be performed on lithium rich and LiNiCoAlO₂ systems for further optimization beyond what was demonstrated in the present dissertation. Use of a bath lithium addition method successfully enabled scaling up of reversible lithium management to an X3450 LiNiCoAlO₂/MCMB pouch cell that demonstrated high tolerance to a 14-day period at a near zero volt state.

Studies on the over-insertion of lithium into LiCoO₂ and the degradation mechanism it undergoes contributes new understanding to prior work. Use of an AlPO₄ coating on the surface of LiCoO₂ to inhibit the degradation of the LiCoO₂ crystal structure during over-insertion of lithium also represents the first study of its kind and yielded

stabilization of the LiCoO_2 crystal that can further improve near zero volt storage tolerance and general overdischarge tolerance of lithium ion cells with excess reversible lithium.

Studies on the near zero volt electrode potential behavior of cells constructed with a lithium rich cathode material (i.e. HE5050), paired with an MCMB anode, revealed electrode potential behavior that provided a strategy to capitalize on high first cycle loss cathodes. Results demonstrate that the near zero volt storage tolerance for cells utilizing an HE5050 cathode paired with an MCMB anode is viable at both room temperature and 40°C . The EAP for cells containing an HE5050 cathode and MCMB anode remained at $\sim 2.8\text{ V vs. Li/Li}^+$ during all tests. It is expected that if specific applications or testing require a lowering of the EAP, then addition of reversible lithium could be performed following the procedure established herein for $\text{LiCoO}_2/\text{MCMB}$ or $\text{LiNiCoAlO}_2/\text{MCMB}$ cells. However, the major implication of the work using HE5050/MCMB cells in this dissertation found that no lithium addition during fabrication is needed for this active material combination to achieve near zero volt tolerant lithium ion cells, and thus, has the potential to be highly implementable.

Carbon nanotube (CNT) sheets are of interest for near zero volt storage as a replacement anode current collector, but suffer from excessive SEI formation which limits their utility. Therefore, the study of the effect of an Al_2O_3 coating deposited by atomic layer deposition (ALD) on the surface of a purified CNT paper electrode revealed a significant impact on the lithium ion cycling behavior of CNTs. The Al_2O_3 coating results in a 50% reduction in irreversible losses for CNT electrodes after 50 cycles. XRD data for a CNT paper electrode compared to an Al_2O_3 coated sample after cycling showed that the coating preserved the graphene separation feature at 26 degrees 2 theta. Thus, the Al_2O_3

coating leads to an improved interlayer stability in individual CNTs and/or hexagonally close packing of the CNTs into bundles during lithium ion cycling. Optimization of ALD parameters/materials as well as combination of ALD with other SEI stabilization techniques such as electrolyte additives may overcome the irreversible losses associated with CNT materials in lithium ion cells and lead to their implementation as anode current collector replacements.

Overall, in the present dissertation reversible lithium management was applied to lithium ion cells with *three different* cathode active materials and shown to enable high tolerance to near zero volt storage at the beginning of cell life. The approach of reversible lithium management requires no secondary active materials, current collector replacements, or other modifications to typical cell construction parameters. Thus, use of reversible lithium management can enable near zero volt storage tolerance in lithium ion cells while maintaining state of the art performance. The ability to maintain conventional anode current collectors like copper is specifically advantageous compared to the predominant commercial approach of using a titanium anode current collector, which can have tradeoffs in terms of cell performance and cost. Future application of reversible lithium management in other cathode (e.g. LiFePO_4 , $\text{Li}_{1+x}(\text{Ni}_{0.33}\text{Co}_{0.33}\text{Mn}_{0.33})_{1-x}\text{O}_2$, etc.) and anode materials (e.g. Si, Ge, Sn, etc.) can broaden the adoption of near zero volt storage tolerance in lithium ion cells to encompass the range of high energy and high power battery technology.

8. Appendix A: Supplemental Information for Chapter 5

Figure 51a shows the first cycle of an HE5050/Li 2032 type coin cell cycled at an effective C/20 rate. The teal shading indicates the difference between the first cycle extraction and first cycle insertion of the HE5050 cathode, which is attributed to the first cycle loss. Figure 51b shows the first cycle of an MCMB/Li coin cell cycled at an effective C/20 rate. The yellow shading indicates the difference between the first cycle insertion and first cycle extraction, which is the first cycle loss of the anode, resulting from SEI formation.

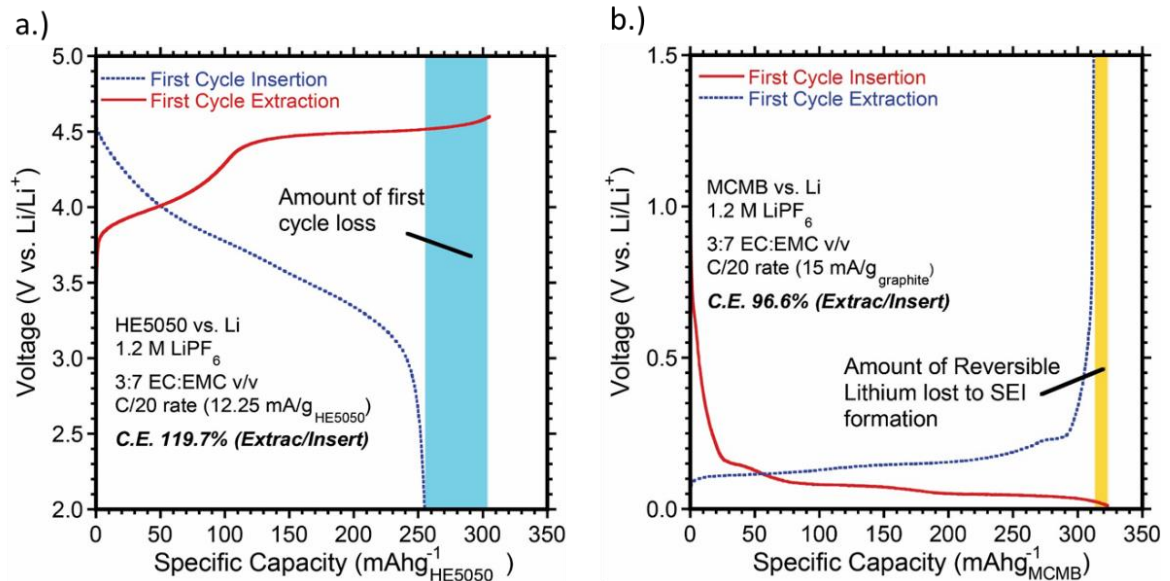


Figure 51: (a) First charge and discharge of HE5050/Li coin cell at an effective C/20 rate. (b) First charge and discharge of MCMB/Li coin cell at an effective C/20 rate.

Figure 52 depicts the lithium tracking details for the 3-electrode pouch cell tested with 3-day near zero volt storage periods. The starting condition of the cell after construction is depicted in Figure 52a. In this condition, the cathode is in a fully lithiated state, while the anode contains no lithium and no SEI has been formed. The areal capacities for both electrodes during the first charge are calculated based on the half-cell data shown

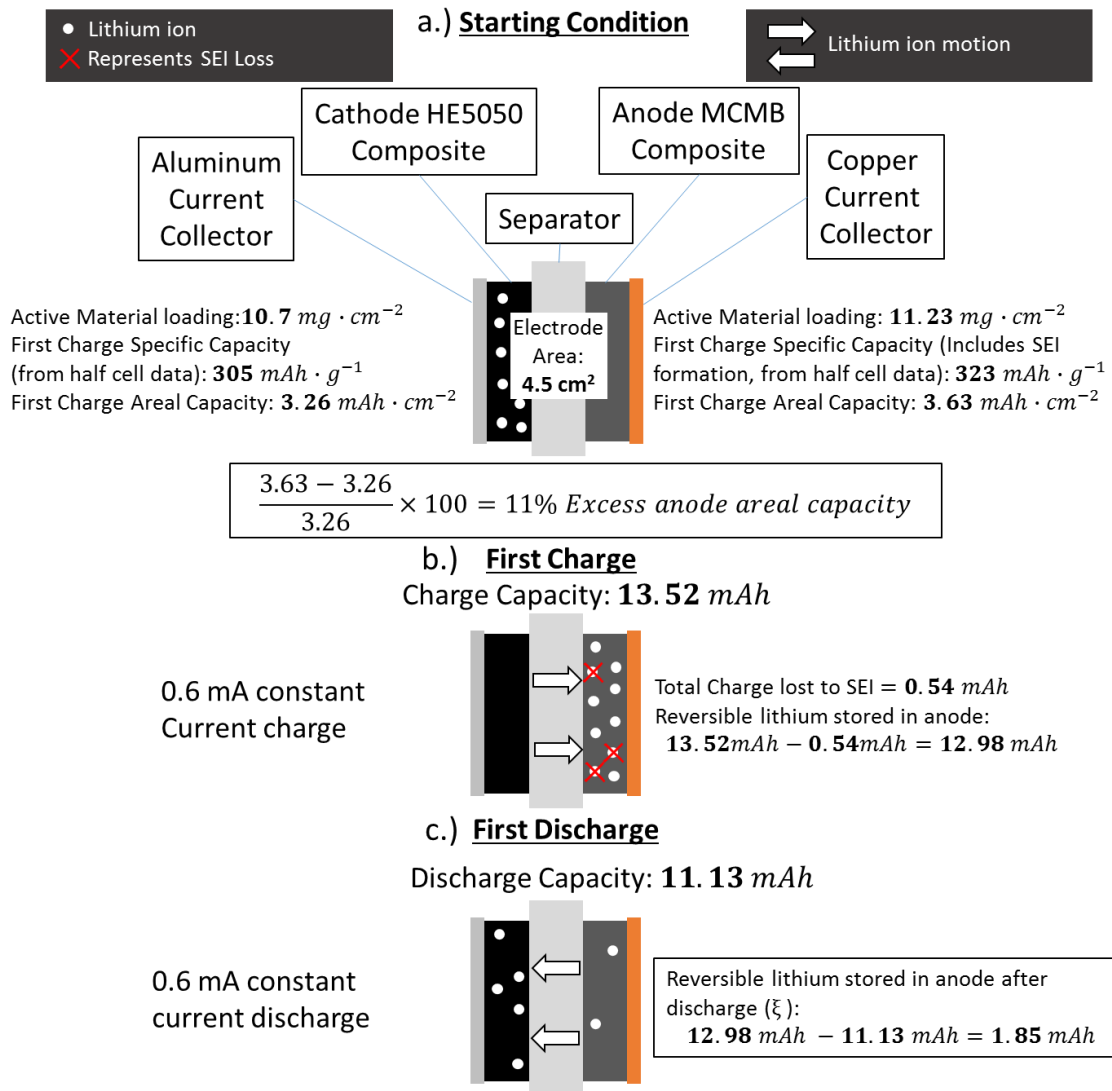


Figure 52: (a) Depiction of the cell after cell construction, white circles represent lithium ions. (b) Depiction of cell condition after the first charge. Red “X” symbols indicate reversible lithium lost to SEI formation. (c) Depiction of cell condition after the first discharge.

in Figure 51. The cathode areal capacity calculated based on the half-cell data shown in Figure 51a includes the first cycle extraction capacity of HE5050 to 4.6 V vs. Li/Li⁺. The anode areal capacity calculated from the first cycle shown in Figure 51b includes both the amount of charge lost to SEI formation and the insertion capacity of the graphite to 5 mV vs. Li/Li⁺. Thus, the areal capacity of the anode for the first charge is 3.63 mAh/cm², which is 11% excess compared to the first charge areal capacity of the cathode.

Figure 52b depicts the end condition of the first constant current charge of the HE5050/MCMB cell. The red “X” over several of the white circles representing lithium depict the reversible lithium consumed in SEI formation on the anode. The amount of lithium consumed by SEI formation is calculated by multiplying the loss per electrode area (as measured by the half-cell shown in Figure 51b) by the area of each electrode used in the pouch cell, since all tests were performed with the same anode coating. The white circles without a red “X” over them represent the amount of reversible lithium in the anode at the end of the charge. This value is calculated by the equation shown to the right of the Figure 52b, which subtracts the amount of lithium lost to SEI from the measured charge capacity of the full cell. Figure 52c depicts the cell condition at the end of the first discharge where the white circles in the anode represent the amount of reversible lithium stored in the anode. This amount of lithium is calculated by the equation shown to the right of Figure 52c which subtracts the measured discharge capacity of the full cell from the amount of reversible lithium calculated to be in the anode at the end of the first charge.

Figure 53 depicts the cell charge and discharge after the first cycle. The values shown in the calculation are specific to the second cycle at a 1.2 mA constant current (~C/10), but the method is general to all cycles after the first cycle. The starting condition

depicted in Figure 53a is after the first discharge, where 1.85 mAh of reversible lithium is calculated to remain in the anode while 11.13 mAh has inserted into the cathode. Figure 53b depicts the cell on the second cycle charge where the measured charge capacity in the cell is 10.73 mAh. The slightly lower charge capacity compared to the amount of lithium that intercalated into the cathode during the first cycle discharge can be attributed to the higher constant current of the second cycle vs. the first, C/10 vs. C/20, respectively (based on the cell's rated capacity). Some lithium is consumed by SEI formation on the second cycle, albeit it is more than an order of magnitude less than the first cycle and that is

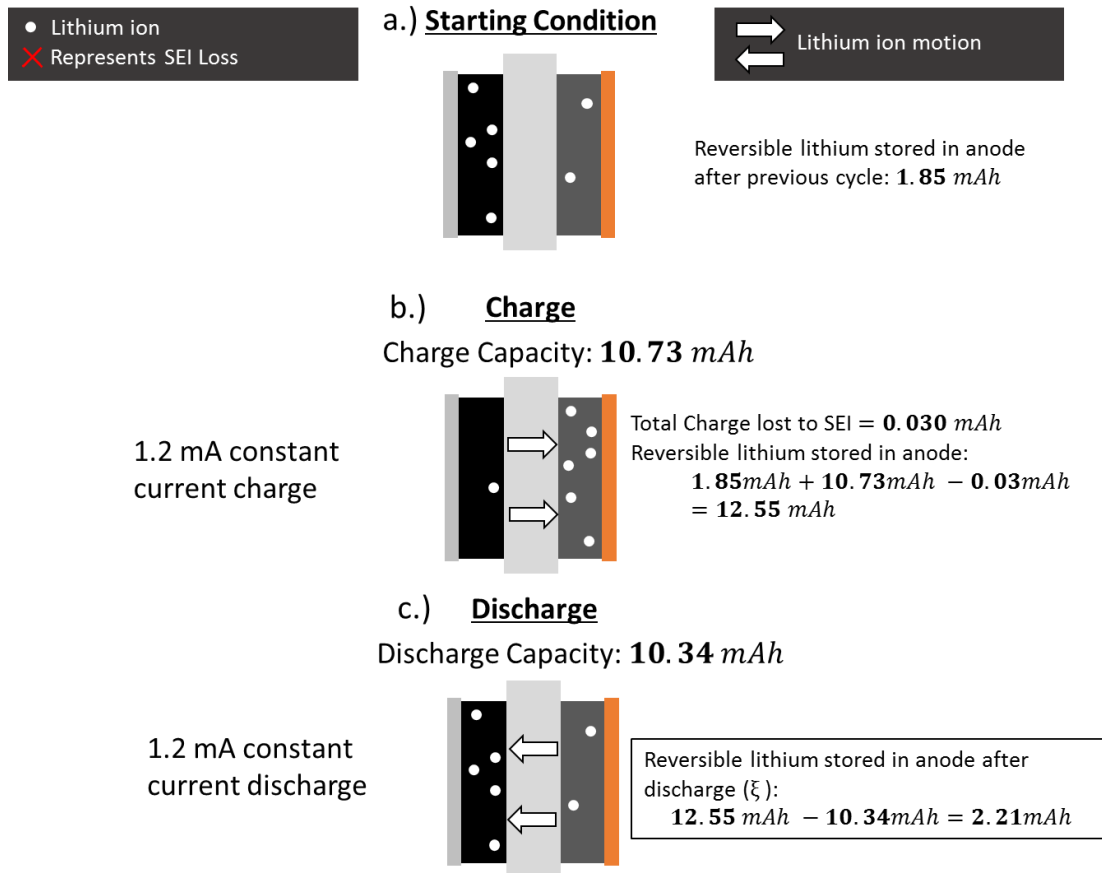


Figure 53: (a) Depiction of HE5050/MCMB cell after the first discharge. This is also representative of the cell condition after all constant current discharges (b) Depiction of HE5050/MCMB cell after the second charge. This is also representative of the cell condition after all constant current charges. (c) Depiction of HE5050/MCMB cell after the second discharge. This is also representative of the cell condition after all constant current discharges.

calculated by the equation on the right side of Figure 53b. Figure 53c depicts the cell after the second cycle discharge, which is similar to Figure 52c, shows that some reversible lithium remains in the anode after the discharge. The lower discharge capacity compared to the charge capacity on the second cycle can be attributed to some loss (~4%) from the HE5050 on the second cycle. By the third cycle, no loss is observed from the HE5050.

The calculations used to determine the amount of reversible lithium in the anode after the discharge step of each cycle are collated by equations S1 and S2, where ξ_i is the amount of excess reversible lithium stored in the anode after discharge on cycle i , C is the charge capacity of the cell, D is the discharge capacity of the cell, and ζ is the loss of reversible lithium due to SEI formation on the anode. The measured charge and discharge capacities of the full cell, the loss due to SEI formation calculated based on half-cell measurements, and the resulting values of reversible lithium stored in the anode after cell discharge are shown in Table 1. After five conditioning cycles, the stabilization of the anode is evident by the significant decrease in SEI loss while maintaining near constant reversible lithium excess of ~2.1 mAh after each discharge.

$$\xi_1 = C - \zeta - D \quad (\text{S1})$$

$$\xi_i = C - \zeta - D + \xi_{i-1} \text{ when } i > 1 \quad (\text{S2})$$

i	ζ	C	D	ξ	
Cycle	SEI Loss on anode (mAh)	Full Cell Charge Capacity (mAh)	Full Cell Discharge Capacity (mAh)	Amount of Excess Reversible lithium in anode at the end of discharge (mAh)	Charge and Discharge Rate (mA)
1	0.537	13.52	11.13	1.85	0.6 (~C/20)
2	0.030	10.73	10.34	2.21	1.2 (~C/10)
3	0.035	10.41	10.53	2.06	1.2 (~C/10)
4	0.029	10.42	10.36	2.09	1.2 (~C/10)
5	0.016	10.33	10.29	2.11	1.2 (~C/10)

Table 1: Summary of lithium tracking results for the first 5 cycles of the cell of Figures 1, 2, and 3. Column 1.) Cycle Index. Column 2.) Expected loss based on calculating the loss per area from half-cell data and multiplying that by the area of the anode in the full pouch cell. Column 3.) Charge capacity of HE5050/MCMB cell. Column 4.) Discharge capacity of HE5050/MCMB cell. Column 5.) Amount of Excess reversible lithium stored in anode of HE5050/MCNM cell as calculated by Equation S1 for Cycle 1 and Equation S2 for Cycle 2-5. Column 6.) Charge and discharge rate for each cycle.

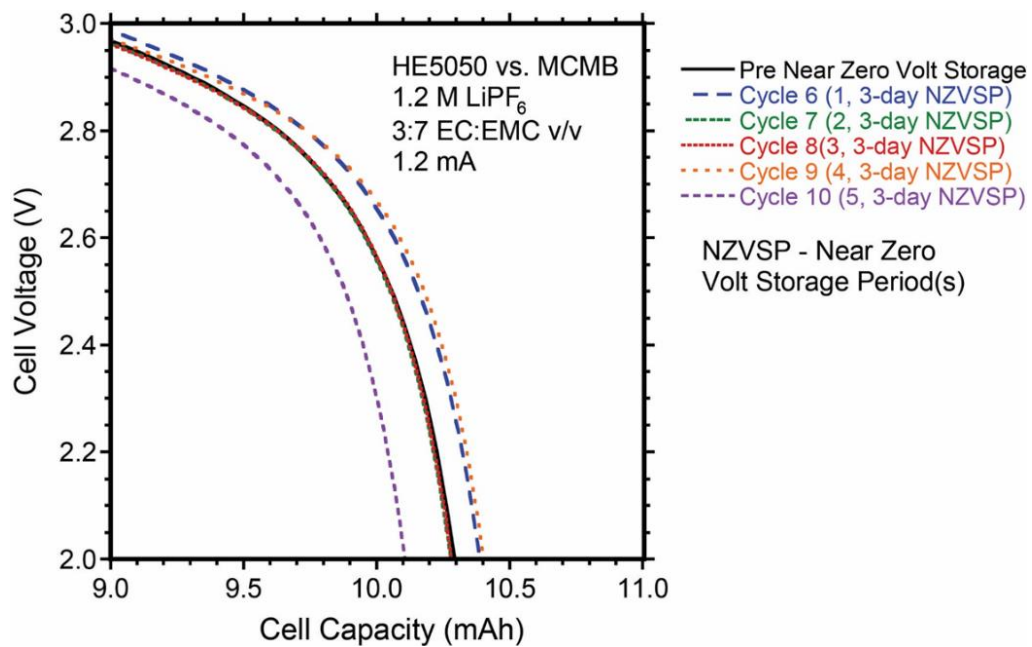


Figure 54: 1.2 mA constant current (CC) discharge curves of HE5050/MCMB cell prior to and after 1, 2, 3, 4, and 5 seventy two hour, near zero volt storage periods.

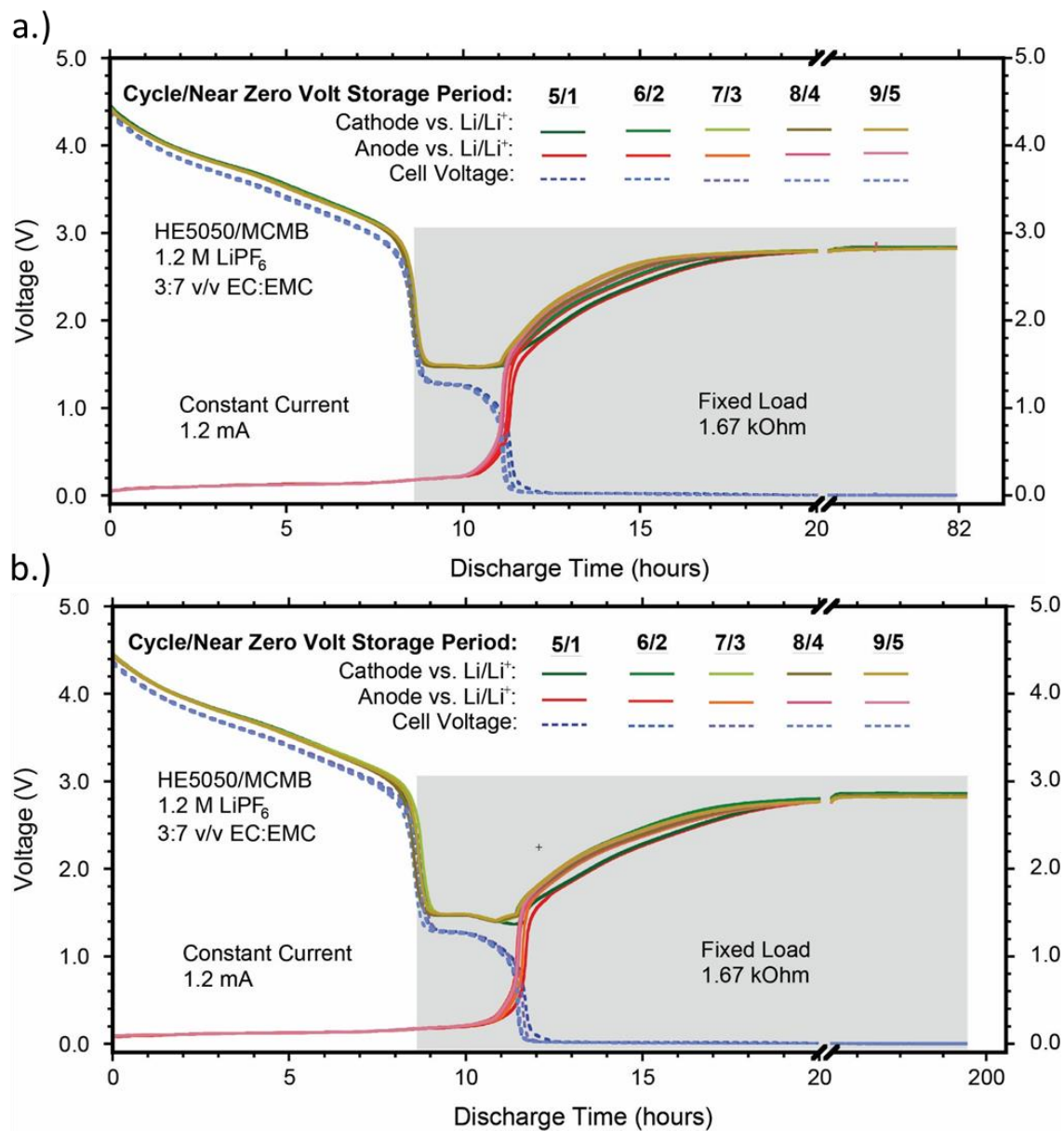


Figure 55: (a) Overlay of reference electrode measurements for the constant current discharge and fixed load, near zero volt storage period of HE5050/MCMB cell tested with 3-day near zero volt storage periods. (b) Overlay of reference electrode measurements for the constant current discharge and fixed load, near zero volt storage period of HE5050/MCMB cell tested with 7-day near zero volt storage periods.

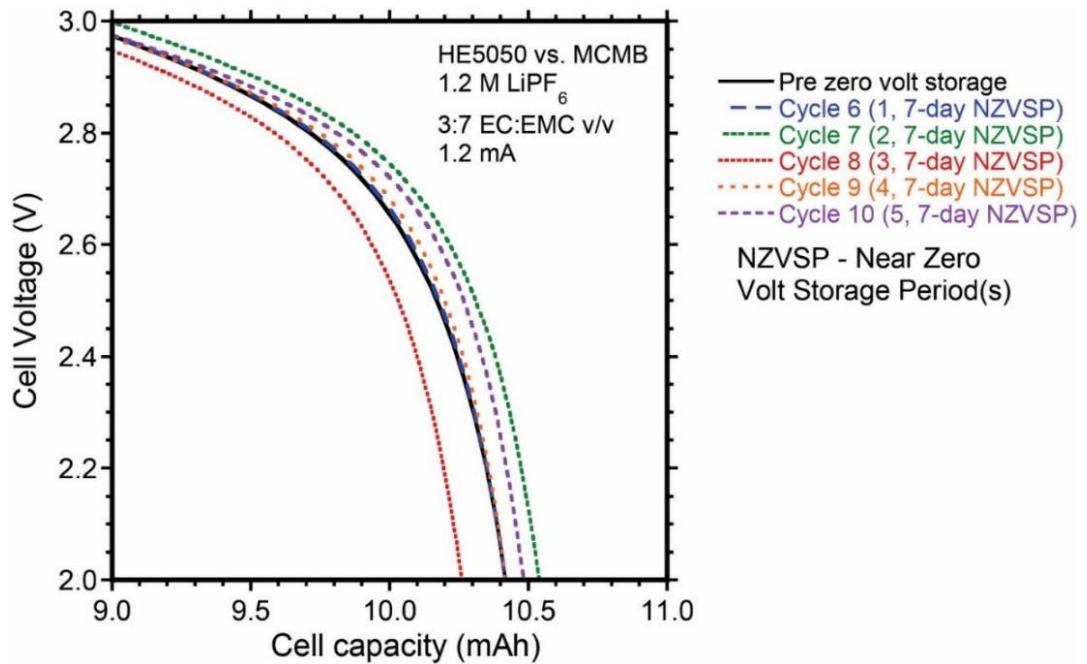


Figure 56: 1.2 mA constant current (CC) discharge curves of HE5050/MCMB cell prior to and after 1, 2, 3, 4, and 5 seventy two hour, near zero volt storage periods.

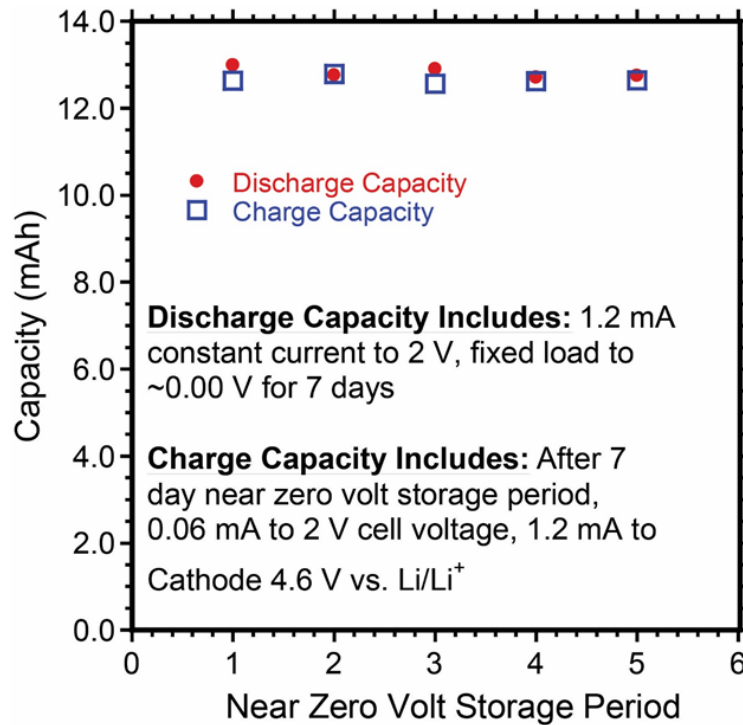


Figure 57: Discharge capacity (including capacity from the 1.2 mA constant current discharge step to 2.0 V cell voltage and the 7-day fixed load step) plotted with the charge capacity of the cell charge on subsequent cycle after near zero volt storage period.

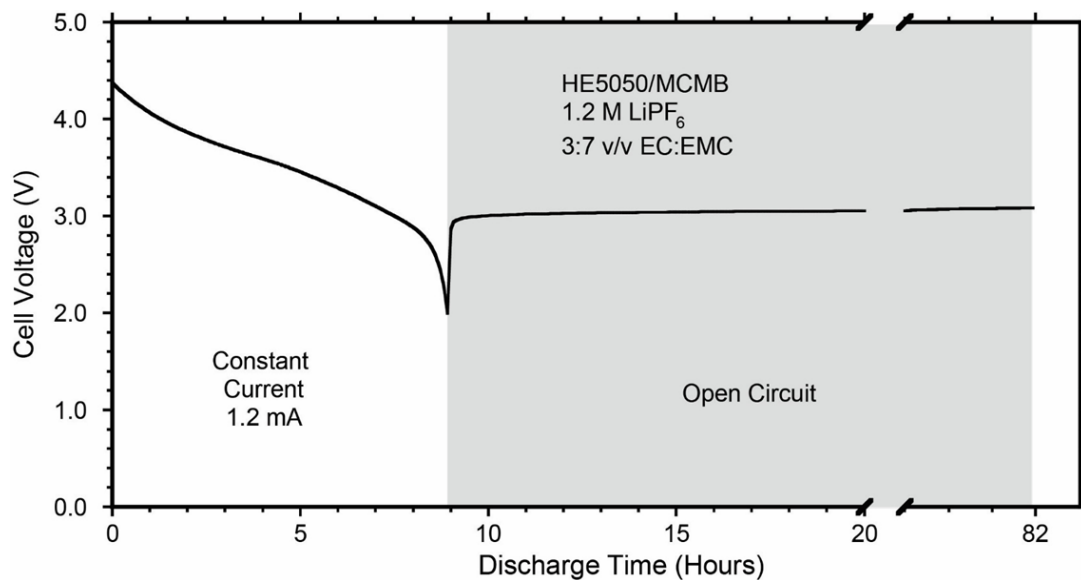


Figure 58: Voltage plotted as a function of time for prototype HE5050/MCMB pouch cell discharged and then stored at open circuit for 3 days.

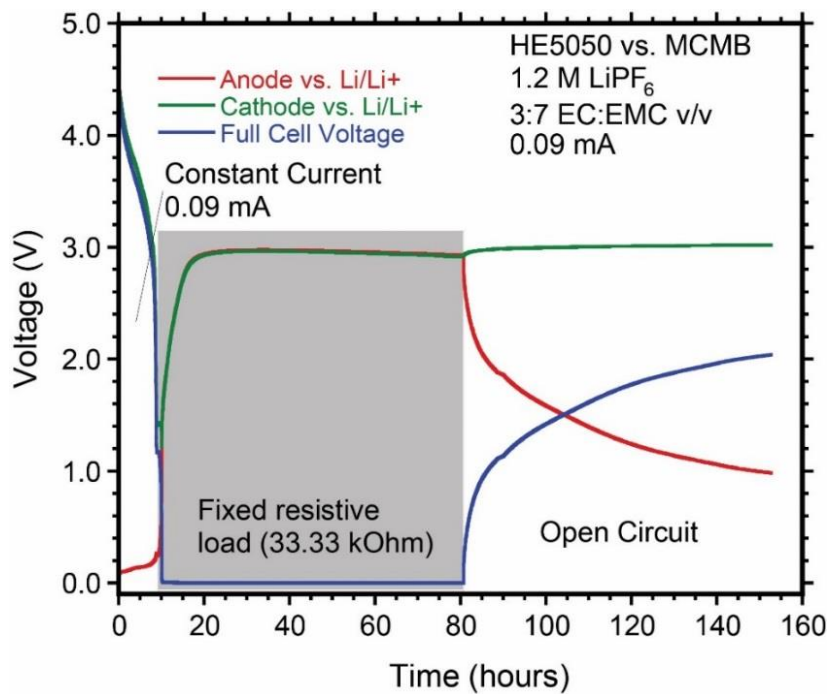


Figure 59: Reference electrode data of HE5050/MCMB cell first discharged at constant current (leftmost unshaded region). Then a fixed resistive load is applied for 72 hours (gray shaded region), then the cell is left at open circuit (rightmost unshaded region)

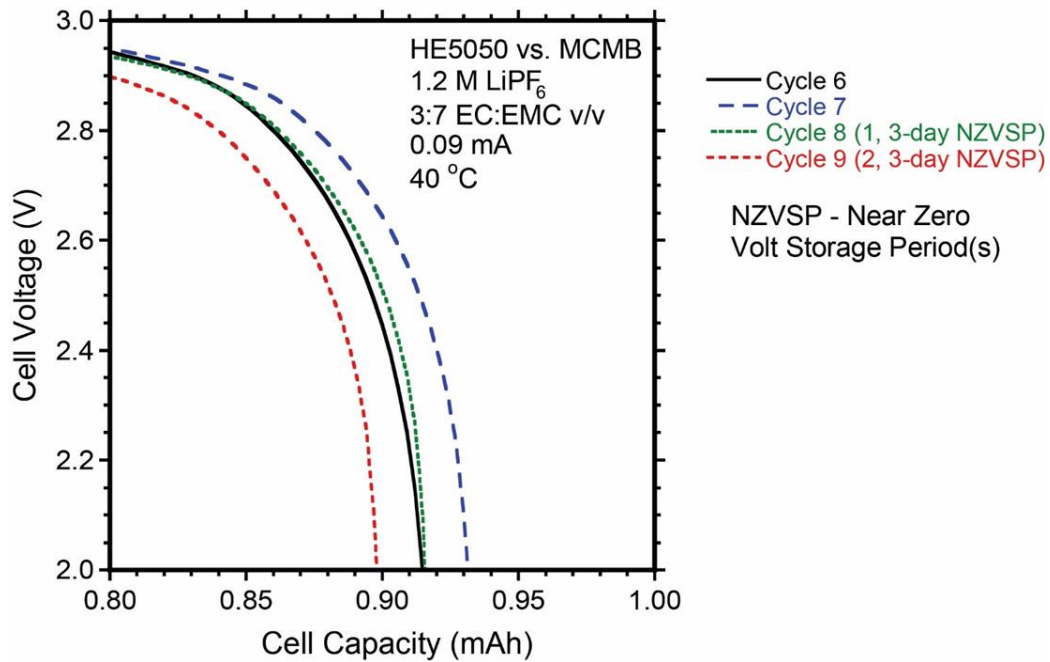


Figure 60: 0.09 mA constant current (CC) discharge curves of HE5050/MCMB cell prior to and after 1 and 2 3-day, near zero volt storage periods at 40°C.

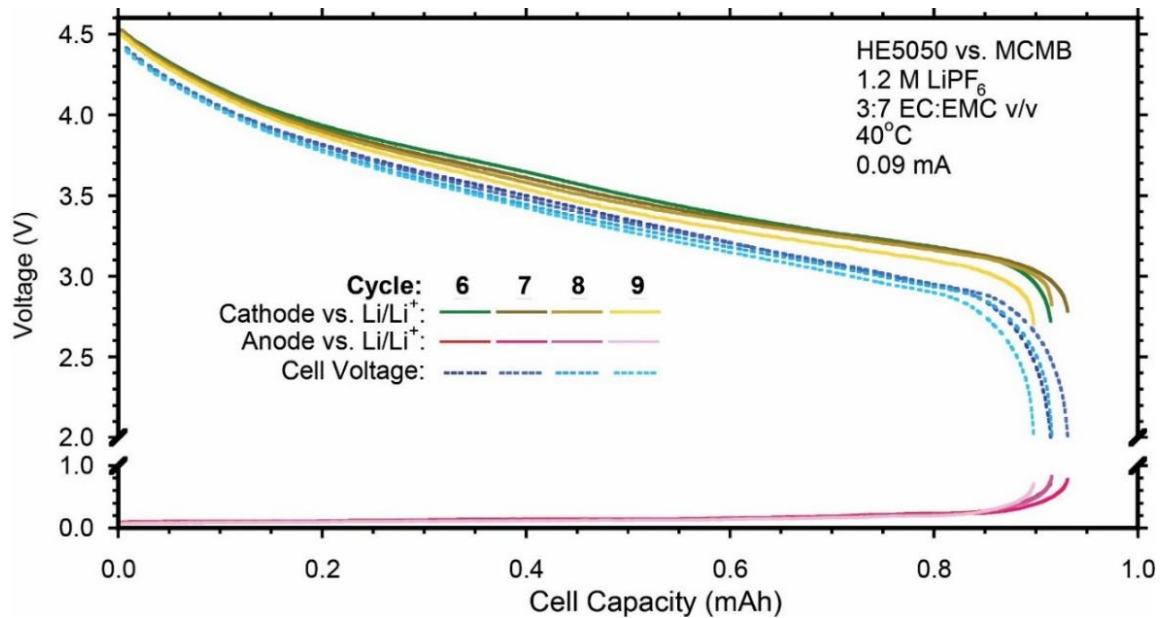


Figure 61: Overlay of reference electrode measurements for the constant current discharge cell tested with 3-day near zero volt storage periods at 40°C after cycle 7 and 8.

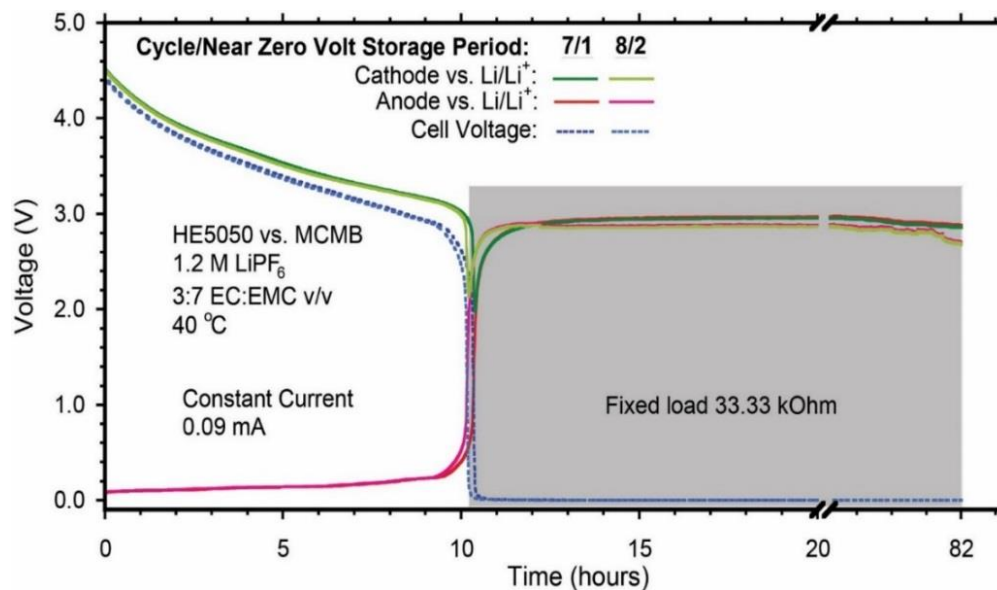


Figure 62: Overlay of reference electrode measurements for the constant current discharge and fixed load, near zero volt storage period of HE5050/MCMB cell tested with 3-day near zero volt storage periods at 40°C.

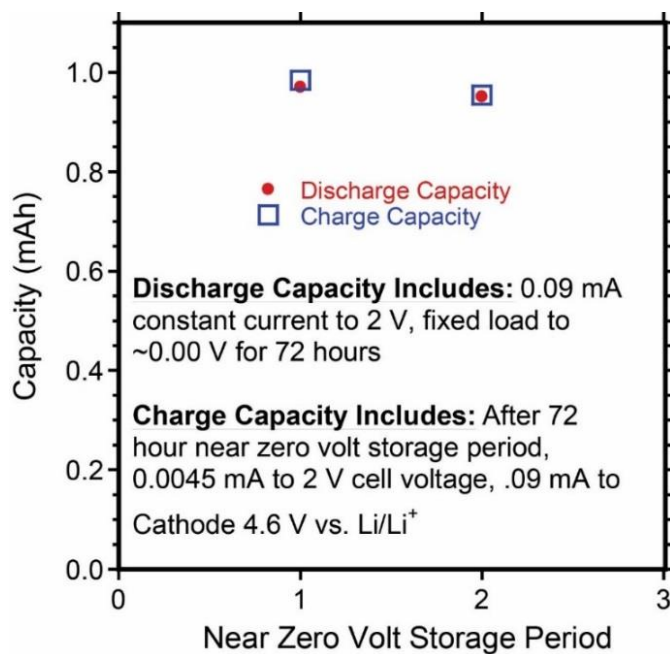


Figure 63: (At 40°C) Discharge capacity (including capacity from the 0.09 mA constant current discharge step to 2.0 V cell voltage and the 3-day fixed load step) plotted with the charge capacity of the cell charge on subsequent cycle after near zero volt storage period.

9. Appendix B: Supplemental information for Chapter 4.9

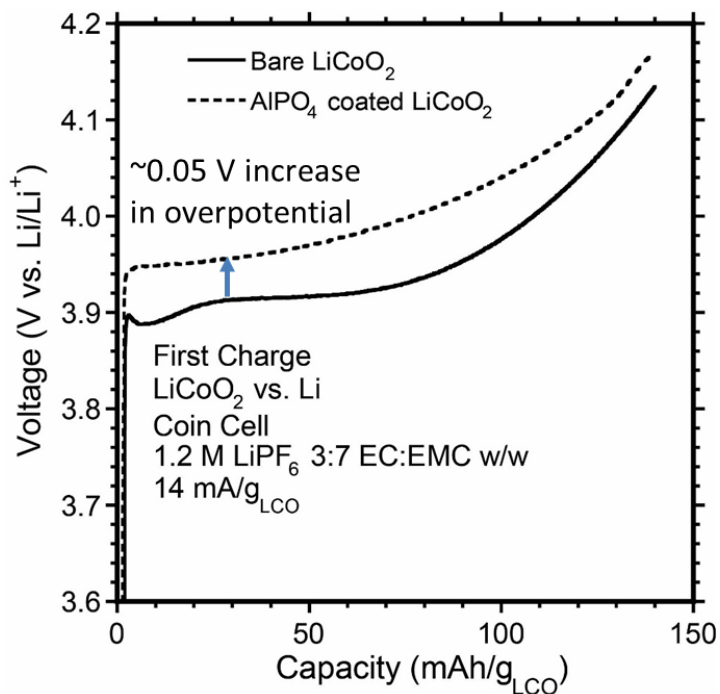


Figure 64: First Charge voltage profiles of bare LiCoO_2 and AlPO_4 coated LiCoO_2

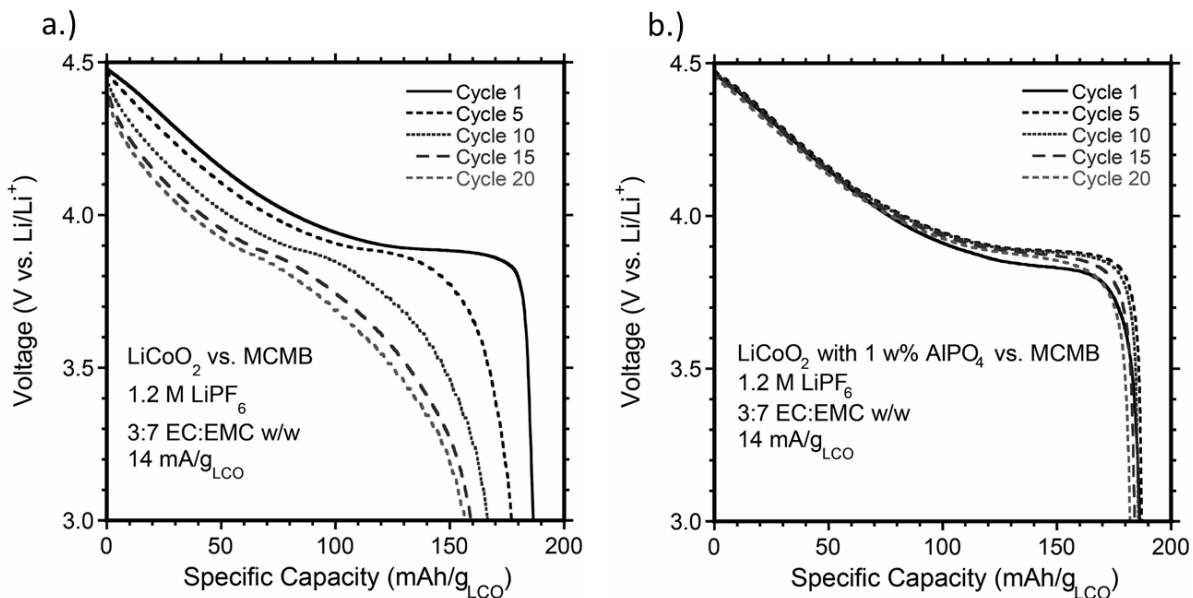


Figure 65: (a) Discharge voltage profiles for cycle 1,5,10,15 and 20 of bare LiCoO_2 cycled vs. Li metal in a coin cell from 3.0-4.5 V vs. Li/Li^+ . (b) Discharge voltage profiles for cycle 1,5,10,15 and 20 of AlPO_4 coated LiCoO_2 cycled vs. Li metal in a coin cell at a constant current from 3.0-4.5 V vs. Li/Li^+ .

Figure 66a shows SEM micrographs of pristine LiCoO_2 cathode composite before 5% over-insertion cycle testing. As shown Figure 66b, after 5% over-insertion cycling the bulk morphology of the LiCoO_2 active particles is not notably changed by the overdischarge cycling. No microscale cracking or severe distortion of the particle surface is observed in the active particles. Buildup of a surface film is observed that is apparently partially burned off by the electron beam of the SEM, indicating it is likely organic deposits caused by solvent breakdown. Also shown in Figure 66a after over-discharge cycling, particles of ~ 10 nm are also observed to form on the surface of the LiCoO_2 particles. Further studies with XPS and EDS analysis is necessary to further understand the nature

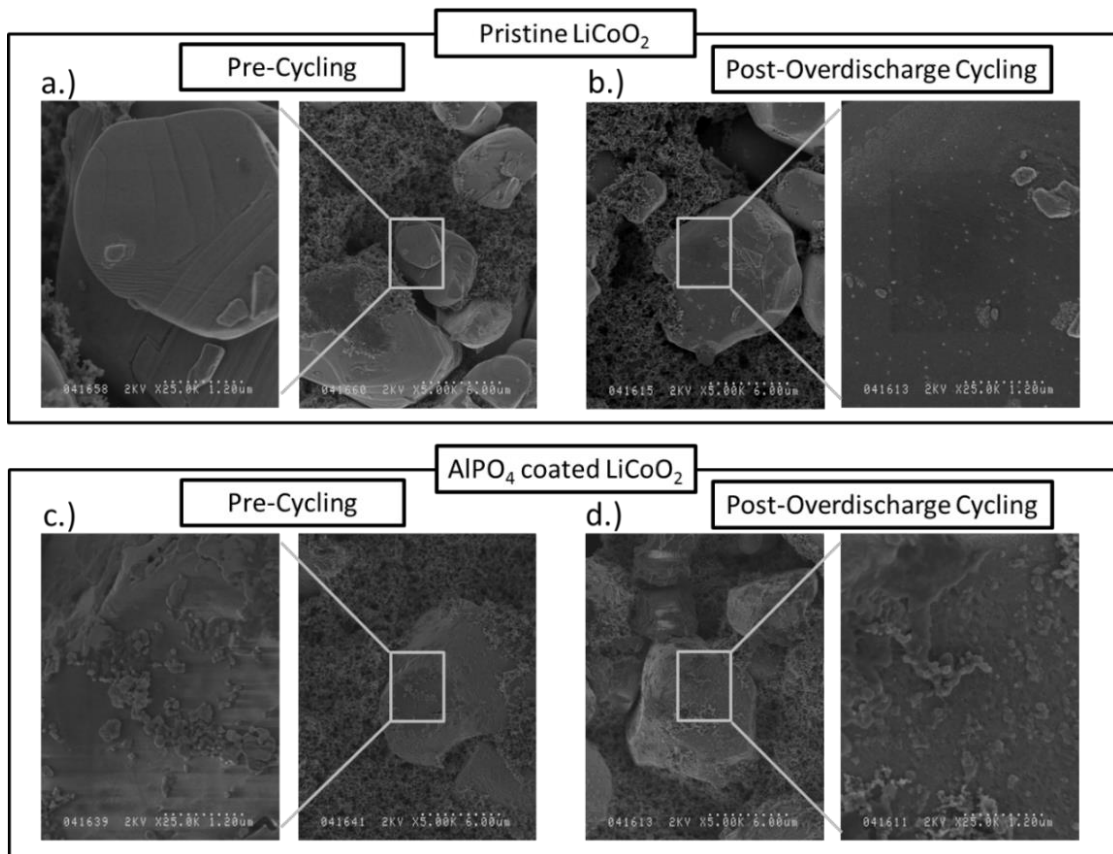


Figure 66: (a) SEM micrographs of pristine LiCoO_2 prior to cycling and after cycling (20 cycles including 10, 5% over-insertion steps by fixed resistive load after discharge to 3.0 V vs. Li/Li^+). (b) SEM micrographs of AlPO_4 coated LiCoO_2 prior to cycling and after cycling (20 cycles including 10, 5% over-insertion steps by fixed resistive load after discharge to 3.0 V vs. Li/Li^+).

of the surface film and nanoparticle deposits. Regardless, SEM micrographs indicate that microscale cracking is not a contributor to discharge voltage fade.

Figure 66c shows SEM micrographs of AlPO_4 coated LiCoO_2 cathode composite before the 5% over-insertion cycle testing. As shown, like the pristine LiCoO_2 , no microscale cracking or dislocations of the AlPO_4 coated LiCoO_2 particles are observed. There is some apparent surface roughening, but no nanoparticle depositions or burn off due to the electron beam of the SEM, in contrast to the pristine LiCoO_2 . Further studies are necessary to fully understand the surface depositions.

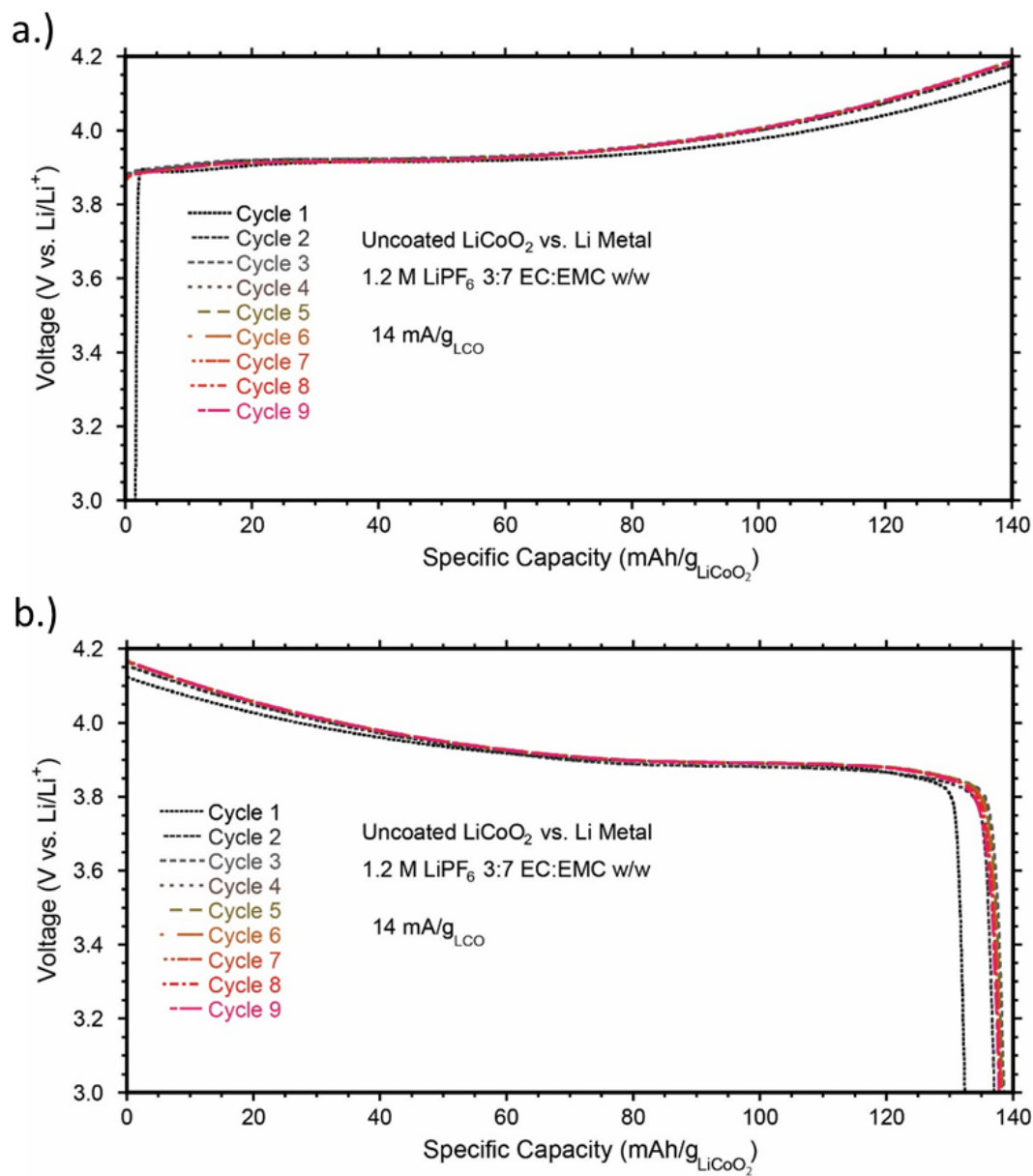


Figure 67:(a) Voltage profiles of cycles 1-9 of charge of as-received LiCoO₂ with a constant current of 14 mA/g_{LiCoO₂} to a limit of 140 mAh/g_{LiCoO₂}. (b) Voltage profiles of cycles 1-9 of discharge of as-received LiCoO₂ with a constant current of 14 mA/g_{LiCoO₂} to 3.0 V vs. Li/Li⁺.

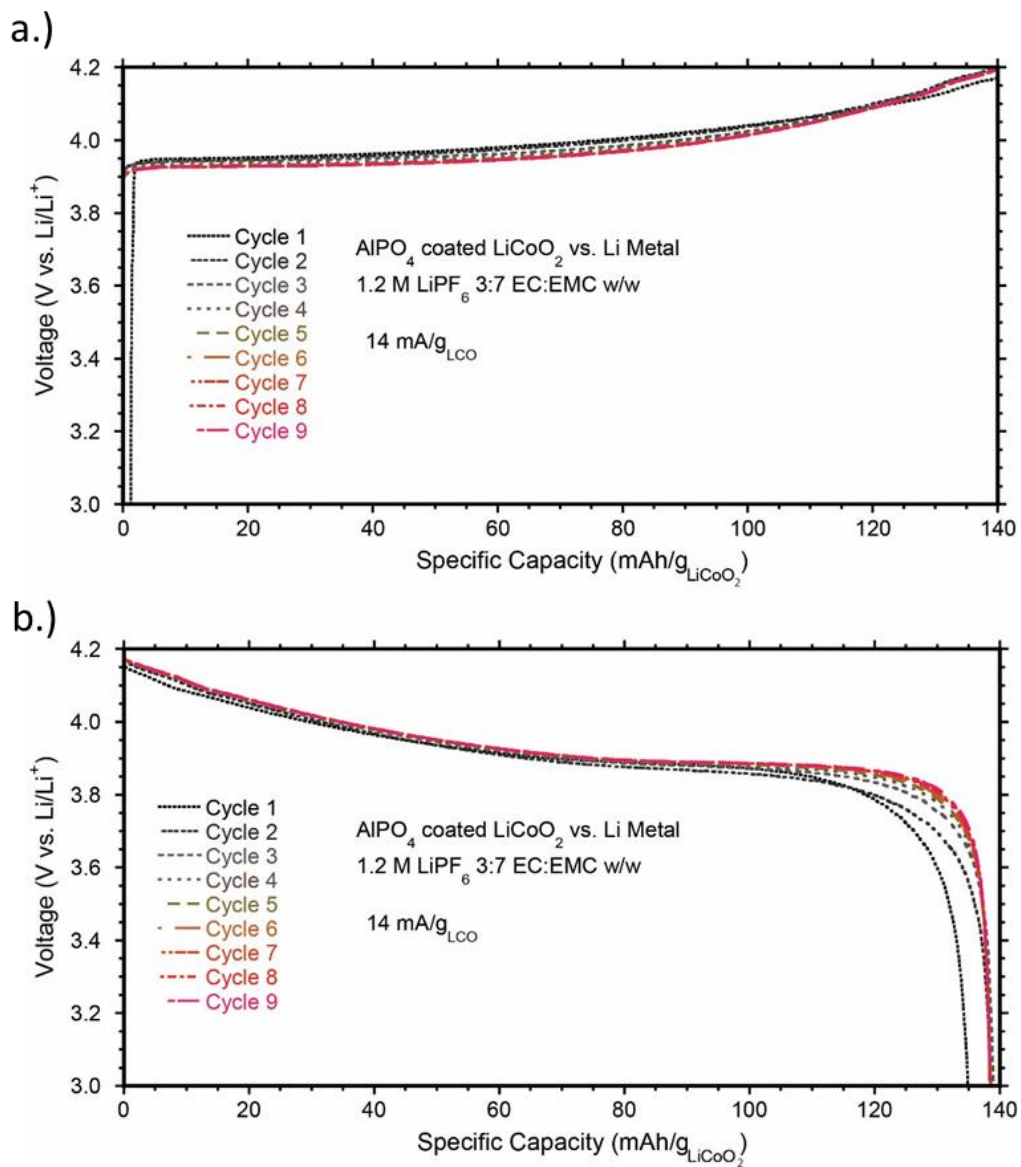


Figure 68: (a) Voltage profiles of cycles 1-9 of charge of 1 wt% AlPO_4 coated LiCoO_2 with a constant current of 14 $\text{mA/g}_{\text{LiCoO}_2}$ to a limit of 140 $\text{mAh/g}_{\text{LiCoO}_2}$. (b) Voltage profiles of cycles 1-9 of discharge of 1 wt% AlPO_4 coated LiCoO_2 with a constant current of 14 $\text{mA/g}_{\text{LiCoO}_2}$ to 3.0 V vs. Li/Li^+ .

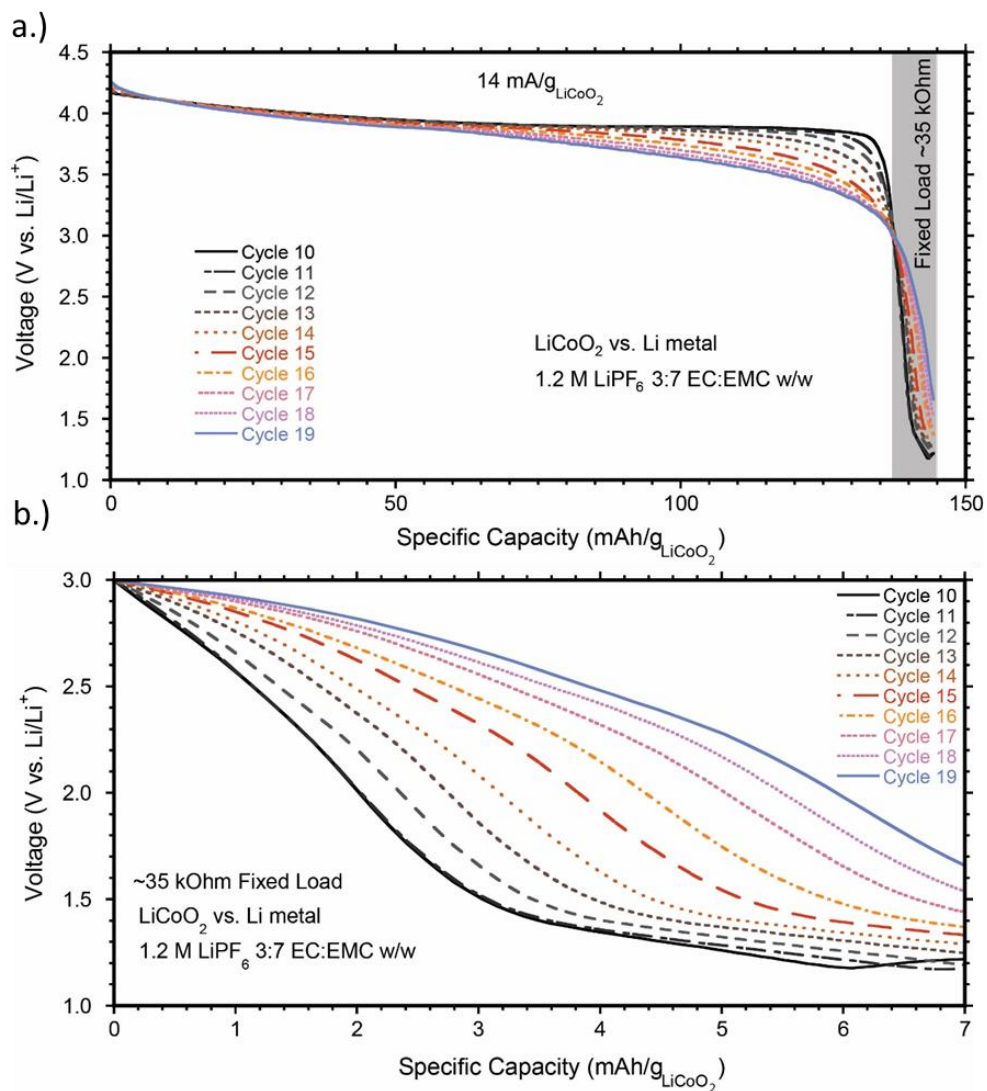


Figure 69: (a) Constant current discharge curve to 3.0 V vs. Li/Li^+ of cycle 10-19 for coin cell with as-received LiCoO_2 cathode vs. Lithium metal (b) Fixed resistive load, 5% ($7 \text{ mAh/g}_{\text{LiCoO}_2}$) over-insertion step of cycles 10-19 for coin cell with as-received LiCoO_2 cathode vs. Lithium metal.

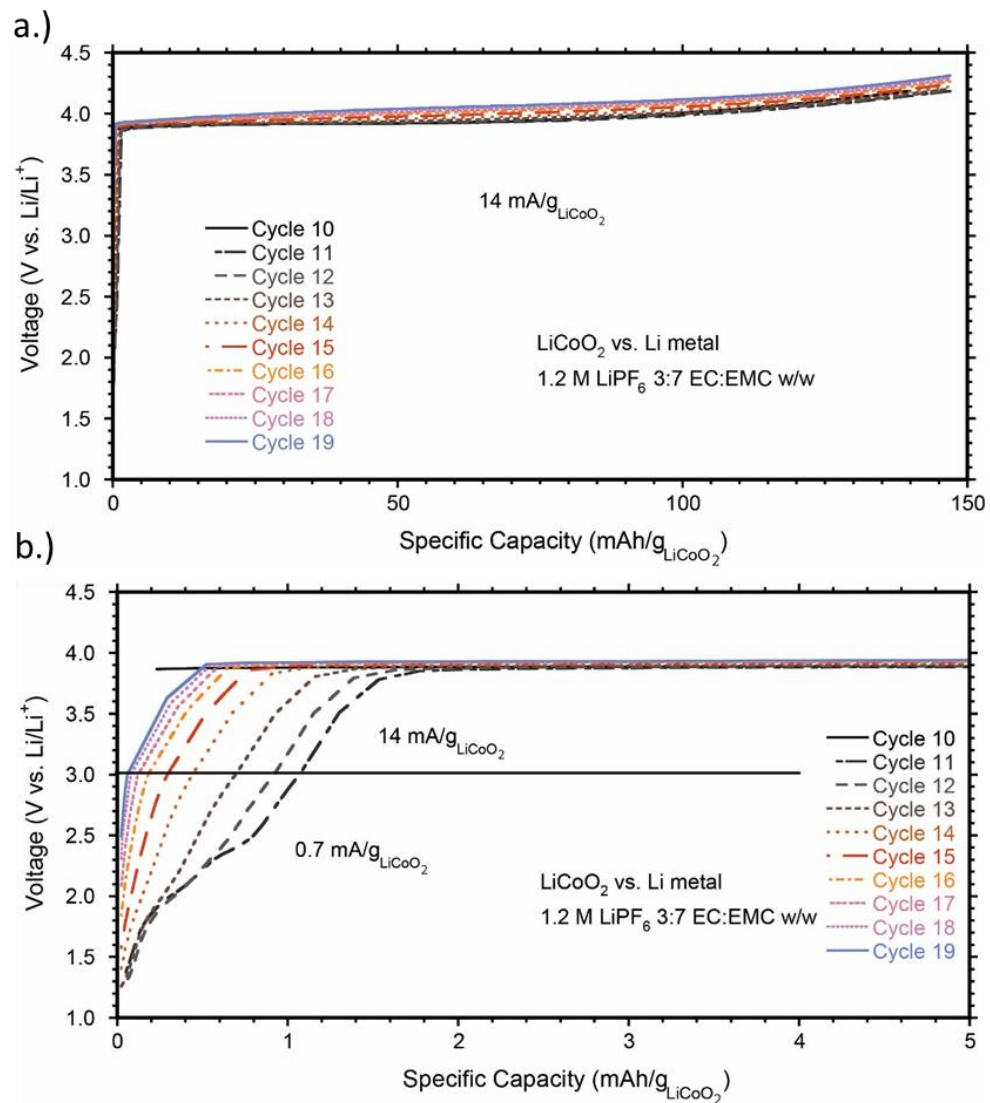


Figure 70: (a) Constant current $0.7 \text{ mA/g}_{\text{LiCoO}_2}$ charge to 3.0 V vs. Li/Li^+ and $14 \text{ mA/g}_{\text{LiCoO}_2}$ charge to $147 \text{ mAh/g}_{\text{LiCoO}_2}$ of cycles 10-19 for coin cell with as-received LiCoO_2 cathode vs. Lithium metal. (b) Zoom in of the first $5 \text{ mAh/g}_{\text{LiCoO}_2}$ of recharge of as-received LiCoO_2 for cycles 10-19.

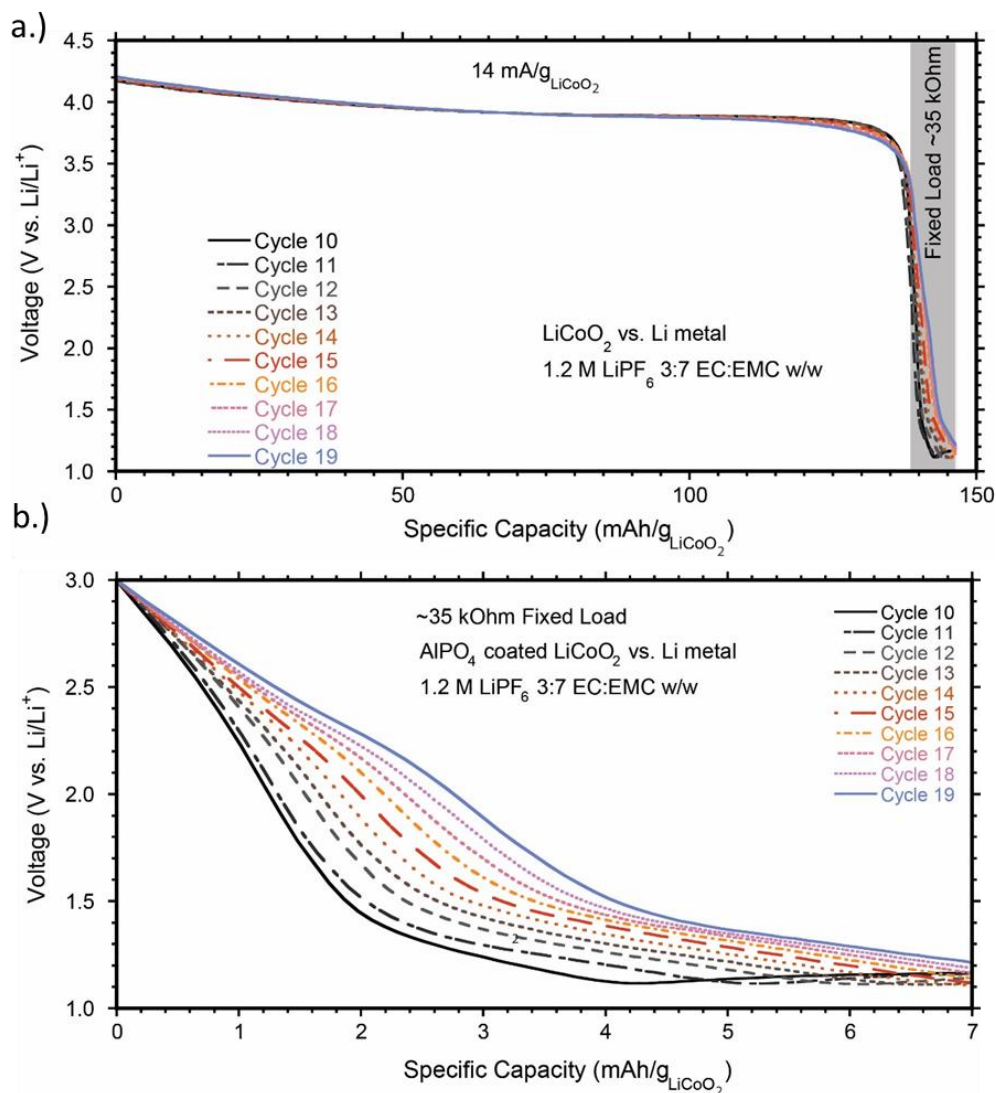


Figure 71: (a) Constant current discharge curve to 3.0 V vs. Li/Li⁺ of cycle 10-19 for coin cell with 1 w% AlPO₄ coated LiCoO₂ cathode vs. Lithium metal (b) Fixed resistive load, 5% (7mAh/g_{LiCoO₂}) over-insertion step of cycles 10-19 for coin cell with 1 w% AlPO₄ coated LiCoO₂ cathode vs. Lithium metal.

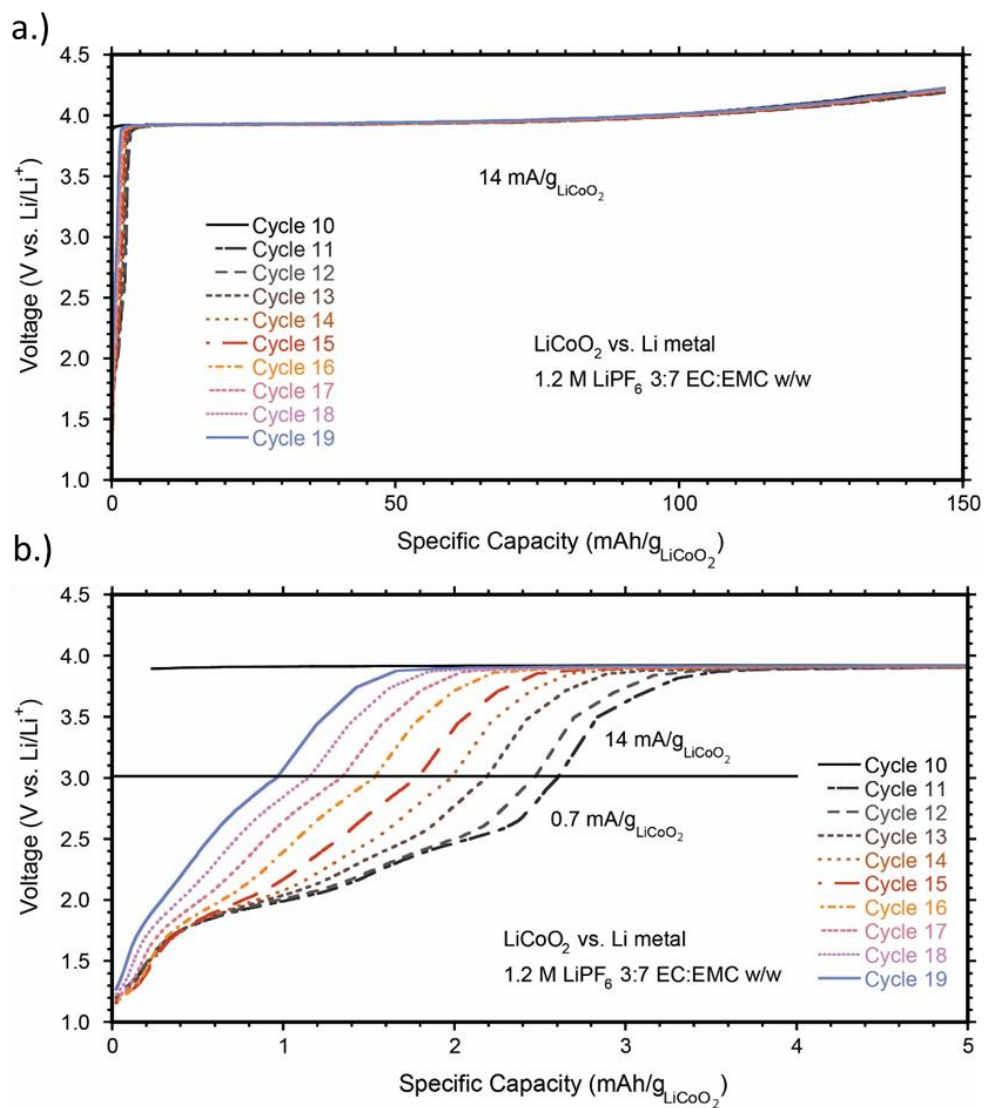


Figure 72: (a) Constant current 0.7 mA/g_{LiCoO₂} charge to 3.0 V vs. Li/Li⁺ and 14 mA/g_{LiCoO₂} charge to 147 mAh/g_{LiCoO₂} of cycles 10-19 for coin cell with 1 w% AlPO₄ coated LiCoO₂ cathode vs. Lithium metal. (b) Zoom in of the first 5 mAh/g_{LiCoO₂} of recharge of 1 w% AlPO₄ coated LiCoO₂ for cycles 10-19.

10. Appendix C: Optical Cell study of lithium metal deposition

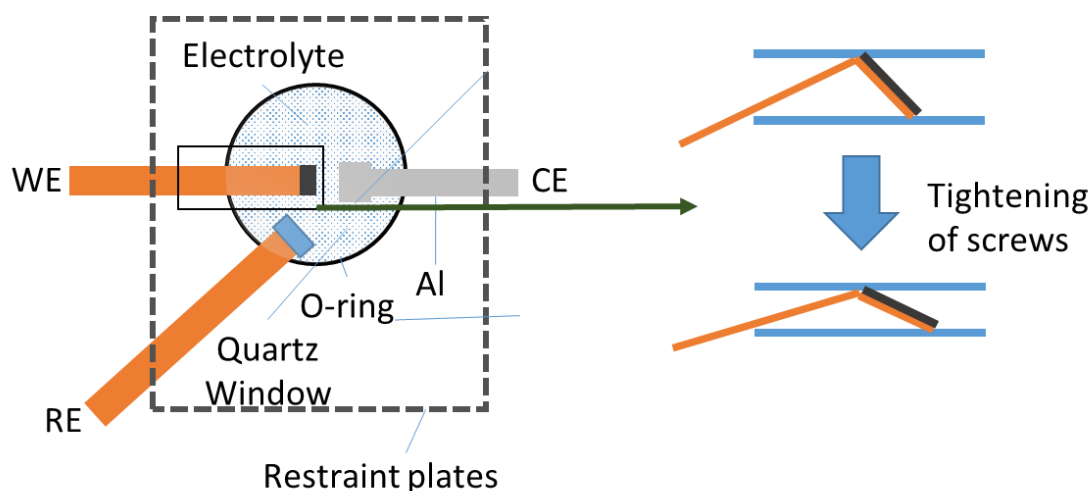


Figure 73: Diagram of optical cell setup, the WE on the left is a graphite composite coated onto copper foil, the CE on the right is a LiCoO_2 composite that is oversized so as to be used as a lithium source. The RE on the left is a lithium chip pressed onto copper foil.

Optical cells were constructed in order to study lithium plating on graphite through direct correlation of optical cell images and electrochemical potential measurements. As shown in Figure 73, the optical cells were constructed by compressing two quartz windows together via restraint plates with an O-ring between them for sealing. Metal tabs connecting electrodes were fed between the O-ring and the quartz window. All cell construction was done inside an argon glovebox maintained at <1 ppm oxygens and <1 ppm water.

The electrodes consisted of a LiCoO_2 composite coated on aluminum foil as the Counter Electrode (CE), a MesoCarbon MicroBead (MCMB) composite coated on a copper foil as the working electrode (WE) and lithium metal pressed onto copper foil as a reference electrode (RE). During testing, the potential between the RE and WE was monitored by the voltage sense leads of an Arbin BT2000 cycler while current was applied between the WE and CE. The WE electrode was cycled at 0.05 mA ($\sim\text{C}/12$) between

0.005-1.5 V vs. Li/Li⁺ 5 times. After the 5th discharge to 0.005 V vs. Li/Li⁺, a constant voltage step with a current limit of xxx was applied to ensure full lithiation of the active material of the WE was fully lithiated.

Following the constant voltage step, a constant current of 0.05 mA was applied for 10 hours. This step will herein be referred to as the “plating step”. The full voltage profile is shown on the right side of Figure 74 and Figure 75. Figure 74a shows the optical microscope image of the MCMB WE corresponding to the time when the potential of the WE reaches a minimum at -28 mV vs. Li/Li⁺. While not readily apparent in the lithium deposits have begun to form on the electrode at this stage. The initial dip in the potential of the WE electrode is consistent with previous studies[223,224] and is attributed to nucleation of lithium deposits. As shown in Figure 74b, after the electrode potential has increased to -24 mV vs. Li/Li⁺ at 0.75 hours, lithium depositions become readily apparent as the electrode potential increases. The increasing electrode potential is due to a transition from the nucleation to growth phase, where the latter has a smaller activation energy than the former[223]. Figure 74c shows the optical image of the WE after 1 hour of the plating step after the potential has increased to -22 mV vs. Li/Li⁺. As shown, the lithium deposits have grown in discretely separated positions compared to the depositions at 0.75 hours of the plating step.

Figure 75a shows the optical image of the working electrode after 2 hours of the plating step where the electrode potential has increased to about -20 mV vs. Li/Li⁺ and has begun to plateau. The plateau indicates that the lithium deposition has almost completely transitioned from nucleation to growth[223]. The lithium depositions have continued to grow outwards away from the composite and have a dendritic micron-scale morphology.

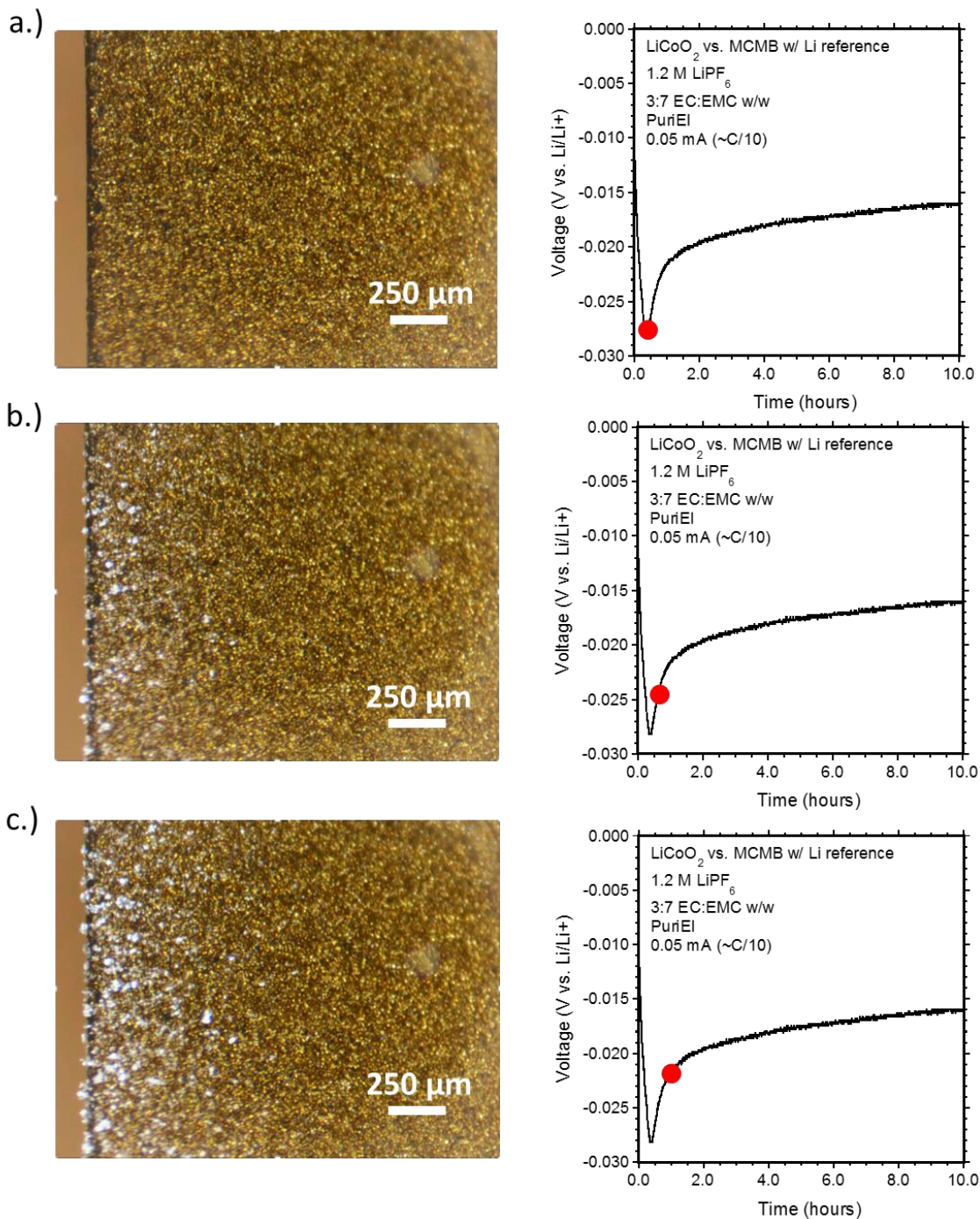


Figure 74: a.) Optical image (left) and corresponding electrochemical potential (right, red dot shows location of curve that corresponds to optical image) for cell as the electrochemical potential reaches a minimum at ~ 0.4 hours. b.) Optical image (left) and corresponding electrochemical potential (right, red dot shows location of curve that corresponds to optical image) for cell at 0.75 hours. Optical image (left) and corresponding electrochemical potential (right, red dot shows location of curve that corresponds to optical image) for cell at 1 hour.

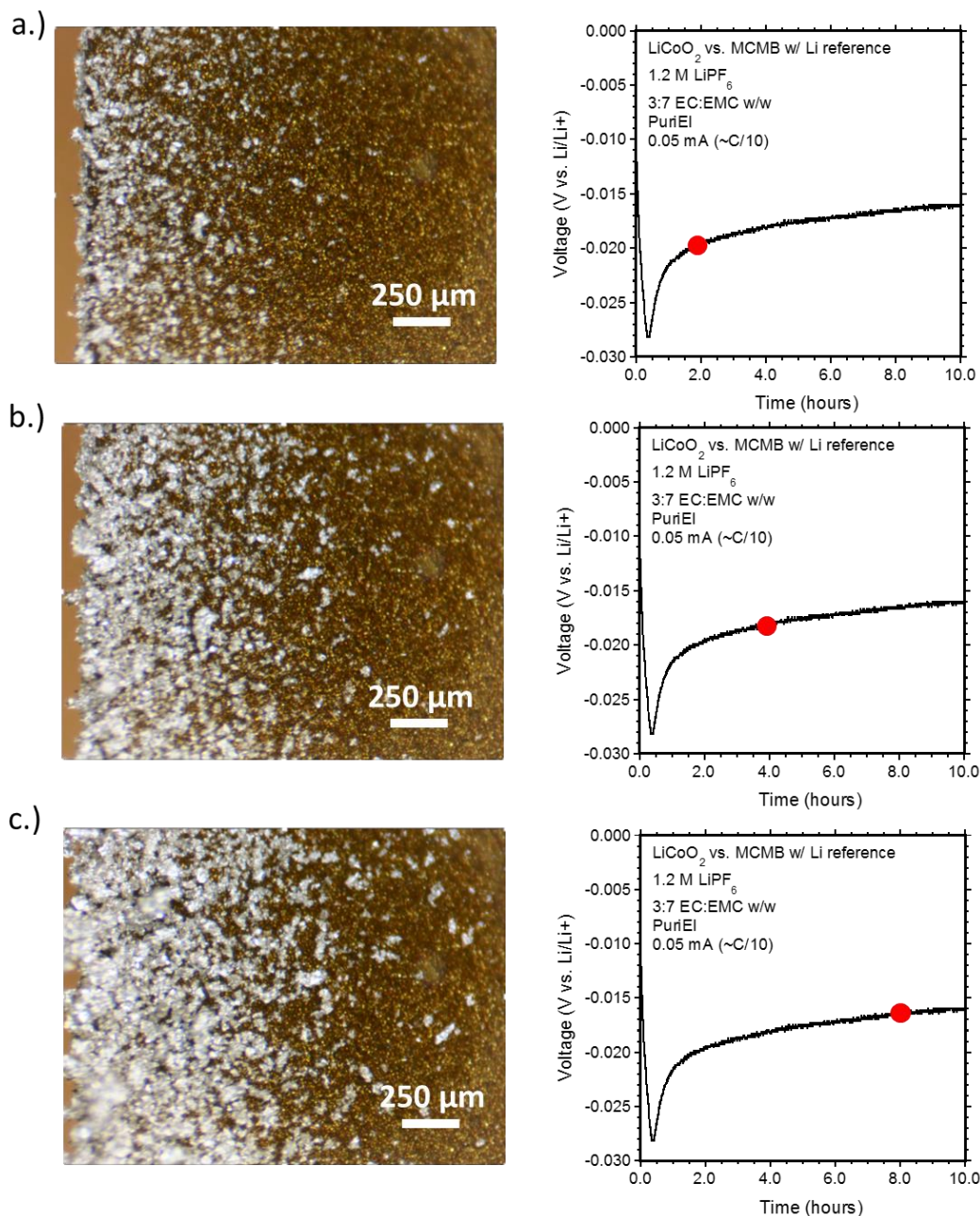


Figure 75: a.) Optical image (left) and corresponding electrochemical potential (right, red dot shows location of curve that corresponds to optical image) for cell 2 hours. b.) Optical image (left) and corresponding electrochemical potential (right, red dot shows location of curve that corresponds to optical image) for cell at 4 hours. Optical image (left) and corresponding electrochemical potential (right, red dot shows location of curve that corresponds to optical image) for cell at 8 hours.

Figure 75b shows the optical image of the WE after 4 hours of the plating step where the electrode potential has increased to -19 mV vs. Li/Li⁺. As shown, the micron scale morphology of the lithium depositions continues to be dendritic as they grown

outwards away from WE surface. Figure 75c shows the optical image of the WE after 8 hours of the deposition step, where the electrode potential has increased to -18 mV vs. Li/Li⁺. Based on the image, the lithium depositions have grown over 100 μm in length while maintaining a discrete, highly granular morphology.

Overall, the results shown in this chapter indicate that for lithium plating to occur on an MCMB anode composite, the measured electrochemical potential must decrease to less than 0.0 V vs. Li/Li⁺, to as low as -28 mV vs. Li/Li⁺. Thus, in experimental three-electrode cells, it can be concluded with reasonable certainty that as long as the measured electrochemical potential of the graphite anode does not decrease to <0.0 V vs. Li/Li⁺, no deposition of lithium metal is occurring.

11. Publications, Presentations and Awards

11.1 Journal Publications

- N. D. Cox, J. E. Rossi, C. D. Cress, A. Merrill, **K. R. Crompton**, and B. J. Landi, “Spatially Selective Au Nanoparticle Deposition and Raman Analysis of Ion-Irradiated Single-Wall Carbon Nanotubes,” 2014.
- **K. R. Crompton** and B. J. Landi, “Opportunities for near zero volt storage of lithium ion batteries,” *Energy Environ. Sci.*, vol. 9, pp. 2219–2239, 2016.
- **K. R. Crompton**, J. W. Staub, M. P. Hladky, and B. J. Landi, “Lithium rich cathode/graphite anode combination for lithium ion cells with high tolerance to near zero volt storage,” *J. Power Sources*, vol. 343, pp. 109–118, 2017.
- **K. R. Crompton**, M. P. Hladky, J. W. Staub, and B. J. Landi, “Enhanced Overdischarge Stability of LiCoO₂ by a solution deposited AlPO₄ coating” *Manuscript in preparation*
- **K. R. Crompton**, M. P. Hladky, C.T. Love, and B. J. Landi, “Lithium ion capacity of carbon nanotube paper electrodes coated with nanometer scale Al₂O₃ by atomic layer deposition ” *Manuscript in preparation*

11.2 Patents

- Crompton, Landi U.S. Serial No. 15/481115, application.

11.3 Major Conference Presentations

- **K.R. Crompton**, B.J. Landi. Lithium rich cathode/graphite anode combination for lithium ion cells with high tolerance to near zero volt storage. Oral Presentation Presented at the 35th annual International Space Power Workshop 2017 Apr 18; Manhattan Beach, CA
- **K.R. Crompton**, B.J. Landi. Near zero volt tolerant lithium ion cells that can impact safety during storage and shipping as well as reliability of restricted access cells in elevated temperature environments such as medical implants. Oral Presentation at the ECS PRiME 2016 Oct 3; Honolulu, HI
- **K.R. Crompton**, B.J. Landi. Designs Enabling Near Zero Volt Storage Tolerance in Lithium ion Batteries Using Conventional Materials. Oral Presentation Presented at the 34th annual International Space Power Workshop 2016 Apr 21; Manhattan Beach, CA
- **K.R. Crompton**, J. W. Staud, B. J. Landi. Carbon Nanotube Enabled 300 Wh/kg Battery. Poster Session Presented at: NY BEST Energy Storage Technology Conference; 2015 Nov 12; Rochester, NY Best Student Poster Selection

11.4 Awards

- Selected for ASEE S.M.A.R.T. Scholarship program in 2014
- Phi Kappa Phi – 2014
- NSF GRFP honorable mention- 2014

12. References

- [1] M. Endo, C. Kim, K. Nishimura, T. Fujino, K. Miyashita, *Carbon N. Y.* 38 (2000) 183–197.
- [2] G.M. Ehrlich, *Lithium-Ion Batteries*, in *Handbook of Batteries*, 3rd ed., 2002.
- [3] E. Stura, C. Nicolini, *Anal. Chim. Acta* 568 (2006) 57–64.
- [4] E.M. Erickson, C. Ghanty, D. Aurbach, *J. Phys. Chem. Lett.* 5 (2014) 3313–3324.
- [5] T.R.B. Association, (2016).
- [6] A.J. Bard, L.R. Faulkner, *ELECTROCHEMICAL METHODS Fundamentals and Applications*, 2001.
- [7] E. Tatsukawa, K. Tamura, *Electrochim. Acta* 115 (2014) 75–85.
- [8] A. Cresce, S.M. Russell, D.R. Baker, K.J. Gaskell, K. Xu, *Nano Lett.* 14 (2014) 1405–1412.
- [9] P. Lu, C. Li, E.W. Schneider, S.J. Harris, *J. Phys. Chem. C* 118 (2014) 896–903.
- [10] M.B. Pinson, M.Z. Bazant, *J. Electrochem. Soc.* 160 (2012) A243–A250.
- [11] M. Tang, J. Newman, *J. Electrochem. Soc.* 158 (2011) A530.
- [12] P. Verma, P. Maire, P. Novák, *Electrochim. Acta* 55 (2010) 6332–6341.
- [13] V.A. Agubra, J.W. Fergus, *J. Power Sources* 268 (2014) 153–162.
- [14] M. Kummer, J.P. Badillo, a. Schmitz, H.-G. Bredas, M. Winter, C. Schulz, H. Wiggers, *J. Electrochem. Soc.* 161 (2013) A40–A45.
- [15] M. Kummer, J.P. Badillo, a. Schmitz, H.-G. Bredas, M. Winter, C. Schulz, H. Wiggers, *J. Electrochem. Soc.* 161 (2013) A40–A45.
- [16] I. Kovalenko, B. Zdyrko, A. Magasinski, B. Hertzberg, Z. Milicev, R. Burtovyy, I. Luzinov, G. Yushin, *Science* (80-.). 334 (2011) 75–79.
- [17] L. Leveau, B. Laïk, J.-P. Pereira-Ramos, A. Gohier, P. Tran-Van, C.-S. Cojocaru, *Electrochim. Acta* 157 (2015) 218–224.
- [18] D. Ma, Z. Cao, A. Hu, *Nano-Micro Lett.* 6 (2014) 347–358.
- [19] H. Wu, G. Yu, L. Pan, N. Liu, M.T. McDowell, Z. Bao, Y. Cui, *Nat. Commun.* 4 (2013) 1943.
- [20] T.D. Bogart, A.M. Chockla, B. a Korgel, *Curr. Opin. Chem. Eng.* 2 (2013) 286–293.
- [21] M.W. Forney, R. a. DiLeo, A. Raisanen, M.J. Ganter, J.W. Staub, R.E. Rogers, R.D. Ridgley, B.J. Landi, *J. Power Sources* 228 (2013) 270–280.
- [22] M.K.Y. Chan, B.R. Long, A. a. Gewirth, J.P. Greeley, *J. Phys. Chem. Lett.* 2 (2011) 3092–3095.
- [23] R.A. DiLeo, M.J. Ganter, B.J. Landi, R.P. Raffaele, *J. Mater. Res.* 25 (2011) 1441–1446.
- [24] R.A. Dileo, S. Frisco, M.J. Ganter, R.E. Rogers, R.P. Ra, B.J. Landi, *J. Phys. Chem. C* 115 (2011) 22609–22614.
- [25] M.W. Forney, M.J. Dzara, A.L. Doucett, M.J. Ganter, J.W. Staub, R.D. Ridgley, B.J. Landi, *J. Mater. Chem. A* 2 (2014) 14528–14535.
- [26] G.-H. Kim, A. Pesaran, R. Spotnitz, *J. Power Sources* 170 (2007) 476–489.
- [27] Y.F. Chen, J.W. Evans, *J. Electrochem. Soc.* 143 (1996) 2708–2712.
- [28] S. Al-Hallaj, H. Maleki, J.S. Hong, J.R. Selman, *J. Power Sources* 83 (1999) 1–8.
- [29] R. Spotnitz, J. Franklin, *J. Power Sources* 113 (2003) 81–100.
- [30] T.M. Bandhauer, S. Garimella, T.F. Fuller, *J. Electrochem. Soc.* 158 (2011) R1.
- [31] H. Maleki, *J. Electrochem. Soc.* 146 (1999) 3224.

- [32] T.G. Zavalis, M. Behm, G. Lindbergh, *J. Electrochem. Soc.* 159 (2012) A848.
- [33] M. Reichert, J. Haetge, D. Berghus, C. Wendt, V. Meier, U. Rodehorst, S. Passerini, F. Schappacher, M. Winter, *ECS Trans.* 61 (2014) 87–103.
- [34] A.W. Golubkov, S. Scheikl, R. Planteu, G. Voitic, H. Wiltse, C. Stangl, G. Fauler, A. Thaler, V. Hacker, *RSC Adv.* 5 (2015) 57171–57186.
- [35] O.S. Mendoza-hernandez, H. Ishikawa, Y. Nishikawa, Y. Maruyama, M. Umeda, *J. Power Sources* 280 (2015) 499–504.
- [36] A. Hammami, N. Raymond, M. Arman, *Nature* 424 (2003) 635–636.
- [37] H. Maleki, G. Deng, A. Anani, J. Howard, *J. Electrochem. Soc.* 146 (1999) 3224–3229.
- [38] H. Yang, H. Bang, K. Amine, J. Prakash, *J. Electrochem. Soc.* 152 (2005) A73.
- [39] Q. Wang, P. Ping, X. Zhao, G. Chu, J. Sun, C. Chen, *J. Power Sources* 208 (2012) 210–224.
- [40] J. Lamb, C.J. Orendorff, L.A.M. Steele, S.W. Spangler, *J. Power Sources* 283 (2014) 517–523.
- [41] P. Ping, Q. Wang, P. Huang, K. Li, J. Sun, D. Kong, C. Chen, *J. Power Sources* 285 (2015) 80–89.
- [42] D. Doughty, E.P. Roth, *Electrochem. Soc. Interface* (2012) 37–44.
- [43] P.G. Balakrishnan, R. Ramesh, T. Prem Kumar, *J. Power Sources* 155 (2006) 401–414.
- [44] H. Lee, M. Yanilmaz, O. Toprakci, K. Fu, X. Zhang, *Energy Environ. Sci.* 7 (2014) 3857–3886.
- [45] C.-C. Lin, H.-C. Wu, J.-P. Pan, C.-Y. Su, T.-H. Wang, H.-S. Sheu, N.-L. Wu, *Electrochim. Acta* 101 (2013) 11–17.
- [46] J. Cho, T.G. Kim, C. Kim, J.G. Lee, Y.W. Kim, B. Park, *J. Power Sources* 146 (2005) 58–64.
- [47] J. Cho, *J. Power Sources* 126 (2004) 186–189.
- [48] J. Cho, *Electrochim. Acta* 48 (2003) 2807–2811.
- [49] J.Y. Shi, C.W. Yi, K. Kim, *J. Power Sources* 195 (2010) 6860–6866.
- [50] G. Nagasubramanian, K. Fenton, *Electrochim. Acta* 101 (2013) 3–10.
- [51] K. Xu, M.S. Ding, S. Zhang, J.L. Allen, T.R. Jow, *J. Electrochem. Soc.* 149 (2002) A622.
- [52] K. Xu, S. Zhang, J.L. Allen, T.R. Jow, *J. Electrochem. Soc.* 149 (2002) A1079.
- [53] M. Otsuki, T. Ogino, *Lithium-Ion Batter. Sci. Technol.* 121 (2009) 275–289.
- [54] H. Ota, A. Kominato, W.J. Chun, E. Yasukawa, S. Kasuya, *J. Power Sources* 119-121 (2003) 393–398.
- [55] J. Arai, *J. Appl. Electrochem.* 32 (2002) 1071–1079.
- [56] X. Wang, E. Yasukawa, S. Kasuya, *J. Electrochem. Soc.* 148 (2001) A1066.
- [57] M.S. Ding, K. Xu, T.R. Jow, *J. Electrochem. Soc.* 149 (2002) A1489.
- [58] J.R. Dahn, J. Jiang, L.M. Moshurchak, M.D. Fleischauer, C. Buhrmester, L.J. Krause, *J. Electrochem. Soc.* 152 (2005) A1283.
- [59] M.N. Golovin, *J. Electrochem. Soc.* 139 (1992) 5.
- [60] J. Chen, C. Buhrmester, J.R. Dahn, *Electrochem. Solid-State Lett.* 8 (2005) A59–A62.
- [61] T.J. Richardson, *J. Electrochem. Soc.* 143 (1996) 3992.
- [62] S.R. Narayanan, S. Surampudi, A.I. Attia, C.P. Bankston, *J. Electrochem. Soc.* 138

- (1991) 2224–2229.
- [63] C. Buhrmester, J. Chen, L. Moshurchak, J. Jiang, R.L. Wang, J.R. Dahn, J. Electrochem. Soc. 152 (2005) A2390.
- [64] M. Adachi, J. Electrochem. Soc. 146 (1999) 1256.
- [65] C. Buhrmester, L. Moshurchak, R.L. Wang, J.R. Dahn, J. Electrochem. Soc. 153 (2006) A288.
- [66] J. Li, Z. Zhang, X. Guo, Y. Yang, Solid State Ionics 177 (2006) 1509–1516.
- [67] D. Choi, J. Xiao, Y.J. Choi, J.S. Hardy, M. Vijayakumar, M.S. Bhuvaneshwari, J. Liu, W. Xu, W. Wang, Z. Yang, G.L. Graff, J.-G. Zhang, Energy Environ. Sci. 4 (2011) 4560.
- [68] Y. Baba, S. Okada, J.I. Yamaki, Solid State Ionics 148 (2002) 311–316.
- [69] J. ichi Yamaki, H. Takatsuji, T. Kawamura, M. Egashira, Solid State Ionics 148 (2002) 241–245.
- [70] Y.H. Chiang, W.Y. Sean, J.C. Ke, J. Power Sources 196 (2011) 3921–3932.
- [71] S. Lee, J. Kim, J. Lee, B.H. Cho, J. Power Sources 185 (2008) 1367–1373.
- [72] J.P. Schmidt, A. Weber, E. Ivers-Tiffée, J. Power Sources 274 (2015) 1231–1238.
- [73] M.D. Levi, C. Wang, D. Aurbach, J. Electrochem. Soc. 151 (2004) A781.
- [74] E. Markevich, M.D. Levi, D. Aurbach, J. Electrochem. Soc. 152 (2005) A778.
- [75] R. Yazami, Y.F. Reynier, Electrochim. Acta 47 (2002) 1217–1223.
- [76] C. Wang, X.W. Zhang, a. J. Appleby, X. Chen, F.E. Little, J. Power Sources 112 (2002) 98–104.
- [77] E. Sarasketa-Zabala, I. Gandiaga, L.M. Rodriguez-Martinez, I. Villarreal, J. Power Sources 272 (2014) 45–57.
- [78] J. Wang, J. Purewal, P. Liu, J. Hicks-Garner, S. Soukazian, E. Sherman, A. Sorenson, L. Vu, H. Tataria, M.W. Verbrugge, J. Power Sources 269 (2014) 937–948.
- [79] S. Käbitz, J.B. Gerschler, M. Ecker, Y. Yurdagel, B. Emmermacher, D. André, T. Mitsch, D.U. Sauer, J. Power Sources 239 (2013) 572–583.
- [80] G. Pistoia, a. Antonini, R. Rosati, D. Zane, Electrochim. Acta 41 (1996) 2683–2689.
- [81] S.H. Choi, J. Kim, Y.S. Yoon, J. Power Sources 138 (2004) 283–287.
- [82] A. Blyr, C. Sigala, G. Amatucci, D. Guyomard, Y. Chabre, J.-M. Tarascon, J. Electrochem. Soc. 145 (1998) 194–209.
- [83] T. Utsunomiya, O. Hatozaki, N. Yoshimoto, M. Egashira, M. Morita, J. Power Sources 196 (2011) 8598–8603.
- [84] R. Yazami, Y. Ozawa, J. Power Sources 153 (2006) 251–257.
- [85] L. Zhang, Y. Ma, X. Cheng, C. Du, T. Guan, Y. Cui, S. Sun, P. Zuo, Y. Gao, G. Yin, J. Power Sources 293 (2015) 1006–1015.
- [86] H. Maleki, J.N. Howard, J. Power Sources 160 (2006) 1395–1402.
- [87] Y. Liu, Q. Liu, Z. Li, Y. Ren, J. Xie, H. He, F. Xu, J. Electrochem. Soc. 161 (2014) A620–A632.
- [88] H.F. Li, J.K. Gao, S.L. Zhang, Chinese J. Chem. 26 (2008) 1585–1588.
- [89] Y.-S. Kim, S.-H. Lee, M.-Y. Son, Y.M. Jung, H.-K. Song, H. Lee, ACS Appl. Mater. Interfaces 6 (2014) 2039–43.
- [90] H. Lee, S.K. Chang, E.Y. Goh, J.Y. Jeong, J.H. Lee, H.J. Kim, J.J. Cho, S.T. Hong, Chem. Mater. 20 (2008) 5–7.

- [91] S. Erol, M.E. Orazem, R.P. Muller, *J. Power Sources* 270 (2014) 92–100.
- [92] T. Yamahira, H. Kato, M. Anzai, *Nonaqueous Electrolyte Secondary Battery*, US 5053297, 1991.
- [93] S.T. Myung, Y. Sasaki, S. Sakurada, Y.K. Sun, H. Yashiro, *Electrochim. Acta* 55 (2009) 288–297.
- [94] S.-T. Myung, Y. Hitoshi, Y.-K. Sun, *J. Mater. Chem.* 21 (2011) 9891–9911.
- [95] M. Zhao, H.D. Dewald, F.R. Lemke, R.J. Staniewicz, *J. Electrochem. Soc.* 147 (2000) 3983.
- [96] W.G. Howard, C.L. Schmidt, E.R. Scott, *Lithium-Ion Battery*, US 7563541 B2, 2008.
- [97] H. Tsukamoto, C. Kishiyama, M. Nagata, H. Nakahara, T. Piao, *Lithium Ion Battery Capable of Being Discharged to Zero Volts*, US 6596439 B1, 2003.
- [98] C. Kishiyama, M. Nagata, T. Piao, J. Dodd, P. Lam, H. Tsukamoto, in: *Abs. 425, 204th Meet. Electrochem. Soc. Inc*, 2003.
- [99] K.-S. Park, D. Im, A. Benayad, A. Dylla, K.J. Stevenson, J.B. Goodenough, *Chem. Mater.* 24 (2012) 2673–2683.
- [100] X. Zhang, B. Winget, M. Doeff, J.W. Evans, T.M. Devine, *J. Electrochem. Soc.* 152 (2005) B448–B454.
- [101] J.W. Braithwaite, *J. Electrochem. Soc.* 146 (1999) 448.
- [102] Z. Chen, J. Qian, X. Ai, Y. Cao, H. Yang, *Electrochim. Acta* 54 (2009) 4118–4122.
- [103] Y. Hamon, T. Brousse, F. Jousse, P. Topart, P. Buvat, D.M. Schleich, *J. Power Sources* 98 (2001) 185–187.
- [104] G.-J. Jeong, Y.. Kim, H.-J. Sohn, T. Kang, *J. Power Sources* 101 (2001) 201–205.
- [105] S.P. Kuksenko, *Russ. J. Electrochem.* 49 (2013) 67–75.
- [106] M.J. Lindsay, G.X. Wang, H.K. Liu, *J. Power Sources* 119-121 (2003) 84–87.
- [107] H. Tsukamoto, in: *NASA Aerosp. Batter. Work.*, 2005.
- [108] F.H. (Sam) Froes, M.N. Gungor, M.A. Imam, *JOM* 59 (2007) 28–31.
- [109] B.J. Landi, M.J. Ganter, C.D. Cress, R. a. DiLeo, R.P. Raffaele, *Energy Environ. Sci.* 2 (2009) 638.
- [110] B.J. Landi, M.J. Ganter, C.M. Schauerman, C.D. Cress, R.P. Raffaele, *J. Phys. Chem. C* 112 (2008) 7509–7515.
- [111] J.R. Dahn, U. Vonsacken, M.W. Juzkow, H. Aljanaby, *J. Electrochem. Soc.* 138 (1991) 2207–2211.
- [112] S. Hossain, Y. Saleh, R. Loutfy, *J. Power Sources* 96 (2001) 5–13.
- [113] G.-Y. Kim, R. Petibon, J.R. Dahn, *J. Electrochem. Soc.* 161 (2014) A506–A512.
- [114] Y.S. Kim, S.H. Ahn, M.Y. Son, *Copper Collector for Secondary Battery Comprising Cu-Nitril Compound Complex Formed on Surface Thereof*, US 8192872B2 B2, 2012.
- [115] J. Kim, Y. Lee, *Rechargeable Lithium Battery*, US 2009/0325072 A1, 2009.
- [116] W.G. Howard, C.L. Schmidt, E.R. Scott, *Medical Device Having Lithium-Ion Battery*, US 7337010 B2, 2010.
- [117] M.M. Thackeray, *J. Electrochem. Soc.* 142 (1995) 2558–2563.
- [118] M.G. Kim, J. Cho, *J. Mater. Chem.* 18 (2008) 5880.
- [119] H. Park, T. Yoon, Y.-U. Kim, J.H. Ryu, S.M. Oh, *Electrochim. Acta* 108 (2013) 591–595.

- [120] C.K. Back, R.-Z. Yin, S.-J. Shin, Y.-S. Lee, W. Choi, Y.-S. Kim, *J. Electrochem. Soc.* 159 (2012) A887.
- [121] H. Lee, S.K. Chang, E.Y. Goh, J.Y. Jeong, J.H. Lee, H.J. Kim, J.J. Cho, S.T. Hong, *Chem. Mater.* 20 (2008) 5–7.
- [122] M. Noh, J. Cho, *J. Electrochem. Soc.* 159 (2012) A1329–A1334.
- [123] Y. Sun, H.-W. Lee, Z.W. Seh, N. Liu, J. Sun, Y. Li, Y. Cui, *Nat. Energy* 1 (2016) 15008.
- [124] L. Wang, Y. Fu, V.S. Battaglia, G. Liu, *RSC Adv.* 3 (2013) 15022.
- [125] Y. Li, B. Fitch, *Electrochem. Commun.* 13 (2011) 664–667.
- [126] C.R. Jarvis, M.J. Lain, M. V. Yakovleva, Y. Gao, *J. Power Sources* 162 (2006) 800–802.
- [127] Z. Wang, Y. Fu, Z. Zhang, S. Yuan, K. Amine, V. Battaglia, G. Liu, *J. Power Sources* 260 (2014) 57–61.
- [128] Y. Gao, J.L.I. Burba, J.F. Engel, M. V. Yakovleva, *Lithium Metal Dispersion in Secondary Battery Anodes*, US8980477, 2015.
- [129] M.W. Forney, M.J. Ganter, J.W. Staub, R.D. Ridgley, B.J. Landi, *Nano Lett.* 13 (2013) 4158–63.
- [130] R.W. Grant, M. Sweetland, A.M. Acharige, R. Wohl, *Phased Introduction of Lithium Into the Pre-Lithiated Anode of a Lithium Ion Electrochemical Cell*, U S2014/0310951 A1, 2014.
- [131] D.H. Choi, H.S. Min, H.C. Jung, B.K. Kim, *DOPING BATH FOR FABRICATING THE*, US 2011/0278161 A1, 2011.
- [132] R.W. Grant, M. Sweetland, A.M. Acharige, *Method for Alkaliating Anodes*, US 2013/0327648 A1, 2013.
- [133] R. V Bugga, M.C. Smart, *ECS Trans.* 25 (2010) 241–252.
- [134] J. Kikkawa, S. Terada, A. Gunji, T. Nagai, K. Kurashima, K. Kimoto, *J. Phys. Chem. C* 119 (2015) 15823–15830.
- [135] Robert Huggins, *Advanced Batteries: Materials Science Aspect*, 2009.
- [136] J. Shu, M. Shui, F. Huang, Y. Ren, Q. Wang, D. Xu, L. Hou, *J. Phys. Chem. C* 114 (2010) 3323–3328.
- [137] H. Nakahara, *2013 NASA Aerosp. Batter. Work.* (2013).
- [138] H.H. Lee, C.C. Wan, Y.Y. Wang, *J. Electrochem. Soc.* 151 (2004) A542.
- [139] M. Tang, K. Miyazaki, T. Abe, J. Newman, *J. Electrochem. Soc.* 159 (2012) A634.
- [140] J.C. Burns, R. Petibon, K.J. Nelson, N.N. Sinha, A. Kassam, B.M. Way, J.R. Dahn, *J. Electrochem. Soc.* 160 (2013) A1668–A1674.
- [141] L. Chen, K. Wang, X. Xie, J. Xie, *J. Power Sources* 174 (2007) 538–543.
- [142] L. Hu, Z. Xue, K. Amine, Z. Zhang, *J. Electrochem. Soc.* 161 (2014) A1777–A1781.
- [143] O. Matsuoka, a. Hiwara, T. Omi, M. Toriida, T. Hayashi, C. Tanaka, Y. Saito, T. Ishida, H. Tan, S.S. Ono, S. Yamamoto, *J. Power Sources* 108 (2002) 128–138.
- [144] M. Nie, J. Demeaux, B.T. Young, D.R. Heskett, Y. Chen, A. Bose, J.C. Woicik, B.L. Lucht, *J. Electrochem. Soc.* 162 (2015) A7008–A7014.
- [145] R. Petibon, E.C. Henry, J.C. Burns, N.N. Sinha, J.R. Dahn, *J. Electrochem. Soc.* 161 (2013) A66–A74.
- [146] A. Bordes, K. Eom, T.F. Fuller, *J. Power Sources* 257 (2014) 163–169.
- [147] N.-S. Choi, K.H. Yew, K.Y. Lee, M. Sung, H. Kim, S.-S. Kim, *J. Power Sources*

- 161 (2006) 1254–1259.
- [148] V. Etacheri, O. Haik, Y. Goffer, G. a Roberts, I.C. Stefan, R. Fasching, D. Aurbach, *Langmuir* 28 (2012) 965–76.
- [149] G.-B. Han, M.-H. Ryou, K.Y. Cho, Y.M. Lee, J.-K. Park, *J. Power Sources* 195 (2010) 3709–3714.
- [150] S. Jeong, M. Inaba, R. Mogi, Y. Iriyama, T. Abe, *Langmuir* 17 (2001) 8281–8286.
- [151] K.C. Klavetter, S.M. Wood, Y.-M. Lin, J.L. Snider, N.C. Davy, A.M. Chockla, D.K. Romanovicz, B. a. Korgel, J.-W. Lee, A. Heller, C.B. Mullins, *J. Power Sources* 238 (2013) 123–136.
- [152] K. Leung, S.B. Rempe, M.E. Foster, Y. Ma, J.M. Martinez del la Hoz, N. Sai, P.B. Balbuena, *J. Electrochem. Soc.* 161 (2013) A213–A221.
- [153] Y.-M. Lin, K.C. Klavetter, P.R. Abel, N.C. Davy, J.L. Snider, A. Heller, C.B. Mullins, *Chem. Commun. (Camb)*. 48 (2012) 7268–70.
- [154] H. Nakai, T. Kubota, A. Kita, A. Kawashima, *J. Electrochem. Soc.* 158 (2011) A798.
- [155] C.C. Nguyen, B.L. Lucht, *J. Electrochem. Soc.* 161 (2014) A1933–A1938.
- [156] I.A. Profatilova, S.-S. Kim, N.-S. Choi, *Electrochim. Acta* 54 (2009) 4445–4450.
- [157] R. Petibon, L.M. Rotermund, J.R. Dahn, *J. Power Sources* 287 (2015) 184–195.
- [158] E.G. Shim, T.H. Nam, J.G. Kim, H.S. Kim, S.I. Moon, *J. Power Sources* 172 (2007) 901–907.
- [159] J. Xia, J.E. Harlow, R. Petibon, J.C. Burns, L.P. Chen, J.R. Dahn, *J. Electrochem. Soc.* 161 (2014) A547–A553.
- [160] S.S. Zhang, *J. Power Sources* 162 (2006) 1379–1394.
- [161] H.M. Jung, S.-H. Park, J. Jeon, Y. Choi, S. Yoon, J.-J. Cho, S. Oh, S. Kang, Y.-K. Han, H. Lee, *J. Mater. Chem. A* 1 (2013) 11975.
- [162] J.Y. Eom, I.H. Jung, J.H. Lee, *J. Power Sources* 196 (2011) 9810–9814.
- [163] J. Liu, A. Manthiram, *Chem. Mater.* 21 (2009) 1695–1707.
- [164] J. Cho, T.-J. Kim, J. Kim, M. Noh, B. Park, *J. Electrochem. Soc.* 151 (2004) A1899.
- [165] Y. Wu, a. Vadivel Murugan, a. Manthiram, *J. Electrochem. Soc.* 155 (2008) A635.
- [166] Y. Zeng, J. He, *J. Power Sources* 189 (2009) 519–521.
- [167] A.T. Appapillai, A.N. Mansour, J. Cho, Y. Shao-Horn, *Chem. Mater.* 19 (2007) 5748–5757.
- [168] J. Cho, B. Kim, J.-G. Lee, Y.-W. Kim, B. Park, *J. Electrochem. Soc.* 152 (2005) A32.
- [169] J. Cho, H. Kim, B. Park, *J. Electrochem. Soc.* 151 (2004) A1707.
- [170] B. Kim, C. Kim, T.-G. Kim, D. Ahn, B. Park, *J. Electrochem. Soc.* 153 (2006) A1773.
- [171] J.-G. Lee, B. Kim, J. Cho, Y.-W. Kim, B. Park, *J. Electrochem. Soc.* 151 (2004) A801.
- [172] Y.C. Lu, A.N. Mansour, N. Yabuuchi, Y. Shao-Horn, *Chem. Mater.* 21 (2009) 4408–4424.
- [173] K.R. Crompton, B.J. Landi, *Energy Environ. Sci.* 9 (2016) 2219–2239.
- [174] H. Wang, Y. Jang, B. Huang, D.R. Sadoway, Y. Chiang, *J. Electrochem. Soc.* 146 (1999) 473–480.

- [175] R.J. Gummow, M.M. Thackeray, D.W.I. F., S. Hull, *Mater. Res. Bull.* 27 (1992) 327–337.
- [176] J.R. Dahn, *Phys. Rev. B* 44 (1991) 9170–9177.
- [177] N. Nitta, F. Wu, J.T. Lee, G. Yushin, *Mater. Today* 18 (2015) 252–264.
- [178] S. Hy, H. Liu, D. Qian, M. Zhang, B.J. Hwang, Y.S. Meng, *Energy Environ. Sci.* 9 (2016) 1931–1954.
- [179] D. Ahn, Y. Koo, M.G. Kim, N. Shin, J. Park, J. Eom, J. Cho, T.J. Shin, *J. Phys. Chem. C* 114 (2010) 3675–3680.
- [180] M.N. Ates, Q. Jia, a. Shah, a. Busnaina, S. Mukerjee, K.M. Abraham, *J. Electrochem. Soc.* 161 (2013) A290–A301.
- [181] M.N. Ates, S. Mukerjee, K.M. Abraham, *J. Electrochem. Soc.* 161 (2014) A355–A363.
- [182] C. Ban, Z. Li, Z. Wu, M.J. Kirkham, L. Chen, Y.S. Jung, E.A. Payzant, Y. Yan, M.S. Whittingham, A.C. Dillon, *Adv. Energy Mater.* 1 (2011) 58–62.
- [183] D. -h. Cho, H. Yashiro, Y.-K. Sun, S.-T. Myung, *J. Electrochem. Soc.* 161 (2013) A142–A148.
- [184] Z. Chen, S. Ji, H. Zhu, S. Pasupathi, B. Bladergroen, V. Linkov, (2008) 157–161.
- [185] Y. Cho, P. Oh, J. Cho, *Nano Lett.* 13 (2013) 1145–52.
- [186] X. He, J. Wang, R. Kloepsch, S. Krueger, H. Jia, H. Liu, B. Vortmann, J. Li, *Nano Res.* 7 (2013) 110–118.
- [187] Y. Hou, Y. Cheng, T. Hobson, J. Liu, *Nano Lett.* 10 (2010) 2727–33.
- [188] K. a. Jarvis, Z. Deng, L.F. Allard, A. Manthiram, P.J. Ferreira, *J. Mater. Chem.* 22 (2012) 11550.
- [189] Y. Jiang, Z. Yang, W. Luo, X. Hu, Y. Huang, *Phys. Chem. Chem. Phys.* 15 (2013) 2954–60.
- [190] Y.-J. Kang, J.-H. Kim, S.-W. Lee, Y.-K. Sun, *Electrochim. Acta* 50 (2005) 4784–4791.
- [191] F. Li, S.-X. Zhao, Y.-C. Wang, K.-Z. Wang, B.-H. Li, C.-W. Nan, *J. Electrochem. Soc.* 161 (2013) A102–A108.
- [192] J. Liu, A. Manthiram, *J. Mater. Chem.* 20 (2010) 3961.
- [193] S.K. Martha, J. Nanda, Y. Kim, R.R. Unocic, S. Pannala, N.J. Dudney, *J. Mater. Chem. A* 1 (2013) 5587.
- [194] S.K. Martha, J. Nanda, G.M. Veith, N.J. Dudney, *J. Power Sources* 199 (2012) 220–226.
- [195] D. Mohanty, S. Kalnaus, R. a. Meisner, K.J. Rhodes, J. Li, E.A. Payzant, D.L. Wood, C. Daniel, *J. Power Sources* 229 (2013) 239–248.
- [196] B. Song, M.O. Lai, Z. Liu, H. Liu, L. Lu, *J. Mater. Chem. A* 1 (2013) 9954.
- [197] D. Wang, I. Belharouak, G. Zhou, K. Amine, *J. Electrochem. Soc.* 160 (2013) A3108–A3112.
- [198] M.S. Whittingham, *Chem. Rev.* 104 (2004) 4271–301.
- [199] J. Zhang, X. Guo, S. Yao, W. Zhu, X. Qiu, *J. Power Sources* 238 (2013) 245–250.
- [200] L. Zhang, B. Wu, N. Li, D. Mu, C. Zhang, F. Wu, *J. Power Sources* 240 (2013) 644–652.
- [201] C. Zhao, R. Liu, X. Liu, X. Wang, F. Feng, Q. Shen, *J. Nanoparticle Res.* 15 (2013) 2064.
- [202] T. Zhao, L. Li, S. Chen, R. Chen, X. Zhang, J. Lu, F. Wu, K. Amine, *J. Power*

- Sources 245 (2014) 898–907.
- [203] L. Zhou, D. Zhao, X. Lou, *Angew. Chem. Int. Ed. Engl.* 51 (2012) 239–41.
- [204] Y. Jang, Li-Ion Battery Cathode Materials with Over-Discharge Protection, US 2011/0244324 A1, 2011.
- [205] W. He, H. Tian, F. Xin, W. Han, *J. Mater. Chem. A* 3 (2015) 17956–17962.
- [206] Y. Yang, J.-G. Ren, X. Wang, Y.-S. Chui, Q.-H. Wu, X. Chen, W. Zhang, *Nanoscale* 5 (2013) 8689–94.
- [207] M.W. Forney, M.J. Dzara, A.L. Doucett, M.J. Ganter, J.W. Staub, R.D. Ridgley, 65 (2014) 1–2.
- [208] Y.-M. Lin, K.C. Klavetter, P.R. Abel, N.C. Davy, J.L. Snider, A. Heller, C.B. Mullins, *Chem. Commun. (Camb.)* 48 (2012) 7268–70.
- [209] G. Radhakrishnan, P.M. Adams, B. Foran, M. V. Quinzio, M.J. Brodie, *APL Mater.* 1 (2013) 062103.
- [210] X.H. Liu, L.Q. Zhang, L. Zhong, Y. Liu, H. Zheng, J.W. Wang, J.-H. Cho, S. a Dayeh, S.T. Picraux, J.P. Sullivan, S.X. Mao, Z.Z. Ye, J.Y. Huang, *Nano Lett.* 11 (2011) 2251–8.
- [211] B.R. Long, M.K.Y. Chan, P. Greeley, A.A. Gewirth, (2011) 18916–18921.
- [212] X.H. Liu, Y. Liu, A. Kushima, S. Zhang, T. Zhu, J. Li, J.Y. Huang, *Adv. Energy Mater.* 2 (2012) 722–741.
- [213] A. Kohandehghan, K. Cui, M. Kupsta, E. Memarzadeh, P. Kalisvaart, D. Mitlin, *J. Mater. Chem. A* 2 (2014) 11261.
- [214] a Magasinski, P. Dixon, B. Hertzberg, a Kvit, J. Ayala, G. Yushin, *Nat. Mater.* 9 (2010) 353–8.
- [215] R.A. Dileo, A. Castiglia, M.J. Ganter, R.E. Rogers, C.D. Cress, R.P. Raffaele, B.J. Landi, *ACS Nano* 4 (2010) 6121–6131.
- [216] R. a. DiLeo, M.J. Ganter, M.N. Thone, M.W. Forney, J.W. Staub, R.E. Rogers, B.J. Landi, *Nano Energy* 2 (2013) 268–275.
- [217] R. Dileo, *The Development of Nanomaterials for High Performance Lithium Ion Battery Anodes*, Rochester Institute of Technology, 2012.
- [218] R. a. DiLeo, B.J. Landi, R.P. Raffaele, *J. Appl. Phys.* 101 (2007) 064307.
- [219] J.S. Lee, B. Min, K. Cho, S. Kim, J. Park, Y.T. Lee, N.S. Kim, M.S. Lee, S.O. Park, J.T. Moon, *J. Cryst. Growth* 254 (2003) 443–448.
- [220] C.R. Becker, S.M. Prokes, C.T. Love, *ACS Appl. Mater. Interfaces* 8 (2016) 530–537.
- [221] M. Tang, J. Newman, *J. Electrochem. Soc.* 159 (2012) A1922–A1927.
- [222] R. Saito, A. Gruneis, G.G. Samsonidze, V.W. Brar, G. Dresselhaus, M. Dresselhaus, A. Jorio, L. Cancado, C. Fantini, M. Pimenta, A. Souza Filho, *New J. Phys.* 157 (2003) 0–15.
- [223] K.N. Wood, E. Kazyak, A.F. Chadwick, K.-H. Chen, J.-G. Zhang, K. Thornton, N.P. Dasgupta, *ACS Cent. Sci.* (2016).
- [224] G. Bieker, M. Winter, P. Bieker, *Phys. Chem. Chem. Phys.* 17 (2015) 8670–9.